CONTENTS

	Page
Foreword	iii 1/A7
Chapter I - STELLAR EVOLUTION FROM MAIN SEQUENCE STAR TO WHITE DWARF, NEUTRON STAR OR BLACK HOLE by William K. Rose	1 1/A9
Introduction	1 1/A9
Main-Sequence Stars	3 1/A11
Red Giants	4 1/A12
Planetary Nebulae and the Final State of the Sun	9 1/B3
Production of Magnetic Fields in Stellar Interiors	10 1/B4
Stellar Collapse to Neutron Star on Black Hole	13 1/B7
Chapter II - PULSARS by D. C. Backer	15 1/B9
Introduction	15 1/B9
Spin Properties	17 1/B11
Average Waveform	21 1/C1
Radio Spectrum	24 1/C4
Fluctuation Waveform	29 1/C9
Interstellar Medium	40 1/D6
Conclusion	43 1/D9
Short Topical Bibliography	46 1/D12
Appendix II-A - Listing of Data on 147 Pulsars	49 1/E1
Chapter III - BINARY STARS AND COMPACT X-RAY SOURCES by William K. Rose	55 1/E7
Binary Stars	55 1/E7
Stellar Evolution in Close Binary Systems	59 1/E11
Novae	61 1/E13
Mass Accretion onto Neutron Stars	64 1/F2
Mass Accretion onto Black Holes	68 1/F6
Bibliography	74 1/F12

Page

Chapter IV - X-RAY SIGNATURES OF COMPACT OBJECTS
by Elihu Boldt 75 1/F13

Introduction 75 1/F13
X-Ray Scales for Compact Objects 76 1/F14
Electromagnetic Radiation Limits 77 1/G1
Accretion 81 1/G5
Radiative Transfer 82 1/G6
Some Observations 85 1/G9
Acknowledgments 96 2/A9

Chapter V - GAMMA RAYS FROM COMPACT OBJECTS
by Hakki Ögelman 99 2/A12

Introduction 99 2/A12
Observations 101 2/A14
Pulsar Environments and Gamma Ray Production 109 2/B8
Contribution of Pulsars to the Galactic Gamma Ray Emission 115 2/B14
Bibliography 122 2/C7

Chapter VI - TEMPORAL ANALYSIS OF X-RAY DATA
by Richard Rothschild 125 2/C10

What do the Data Look Like? 125 2/C10
What do we do with the Data? 127 2/C12
What do the Results Mean? 149 2/E6
Appendix VI-A 151 2/E8
Appendix VI-B 166 2/F9
Bibliography 170 2/F13

Chapter VII - RECOGNITION OF COMPACT ASTROPHYSICAL OBJECTS IN THE BINARY PULSAR PSR 1913 + 16
by Steven Detweiler 173 2/G2

The Parameters of PSR 1913 + 16 ..... 173 2/G2
The Nature of the Companion 175 2/G4
The Determination of the Masses of the Binary System 176 2/G5
Effects of General Relativity 179 2/G8
Bibliography 180 2/G9

Page

Chapter VIII - PULSAR THEORY
by William K. Rose and Philip Hardee 181 2/G10

Bibliography 194 3/A12

NAS1.21:421

OCT 20 1977

Recognition of Compact Astrophysical Objects

COMPLETED ORIGINAL

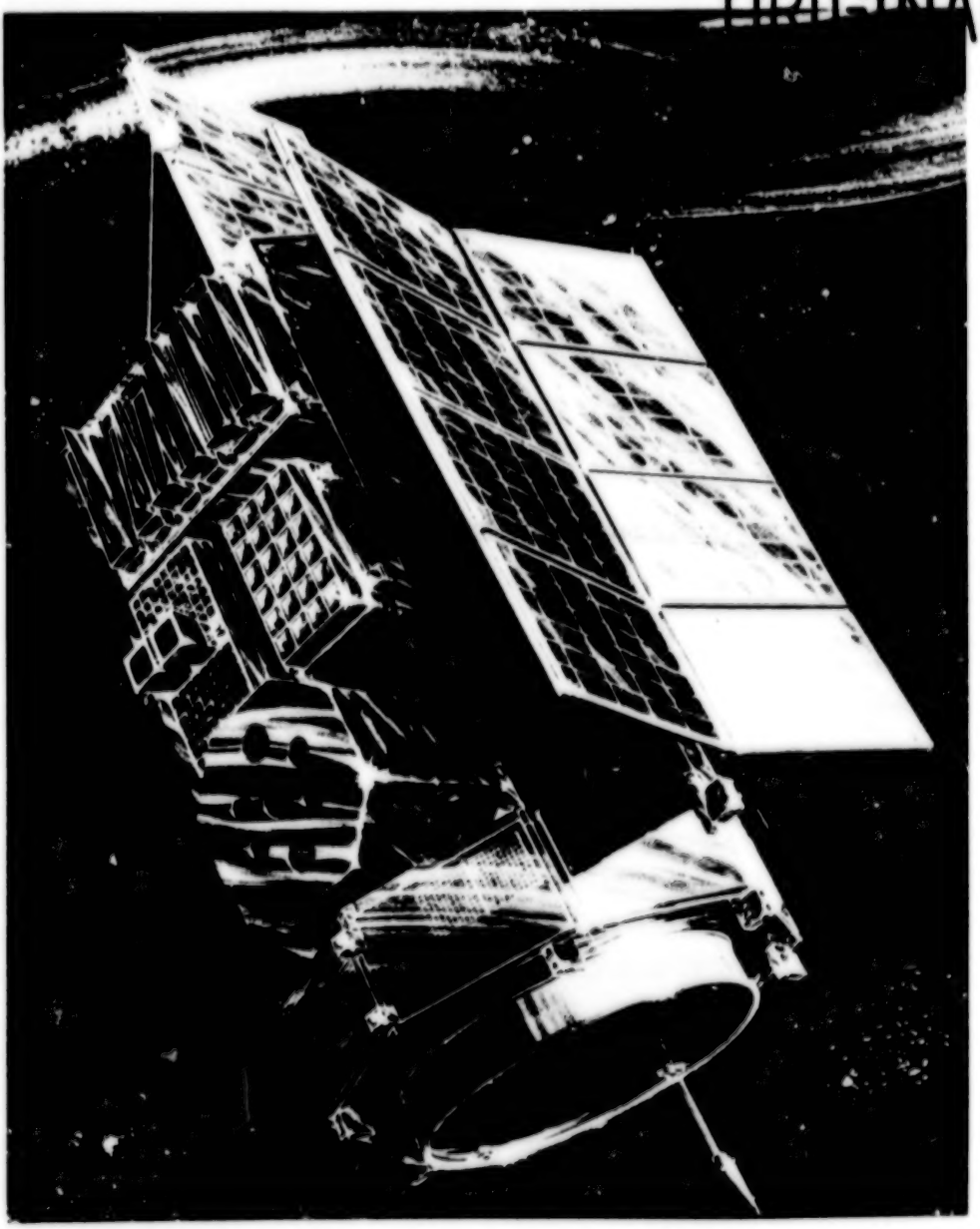

NATIONAL AERONAUTICS AND SPACE ADMINISTRATION

Item 930-I NAS1.21:42

NASA SP-421

Recognition of Compact Astrophysical Objects

Edited by
H. Ögelman and R. Rothschild

Prepared by
NASA Goddard Space Flight Center

Scientific and Technical Information Office
NATIONAL AERONAUTICS AND SPACE ADMINISTRATION
Washington, D.C.
1977

For sale by the National Technical Information Service
Springfield, Virginia 22161
Price – $7.50

FOREWORD

In the summer of 1975, the Laboratory for High Energy Astrophysics at NASA's Goddard Space Flight Center and the Department of Physics and Astronomy of the University of Maryland collaborated on a graduate level course, "Recognition of Compact Astrophysical Objects." This course was given at the University of Maryland in the Summer of 1975, and notes were distributed as the basic text. This publication is an edited version of those notes.

H. Ögelman
Goddard Space Flight Center
and
Middle East Technical University
Ankara, Turkey

R. Rothschild
Goddard Space Flight Center
Greenbelt, Md.

Blank

CHAPTER I
STELLAR EVOLUTION FROM MAIN SEQUENCE STAR TO WHITE DWARF, NEUTRON STAR OR BLACK HOLE

William K. Rose
University of Maryland
College Park, Maryland

". . . it is reasonable to hope that in a not too distant future we shall be competent to understand so simple a thing as a star."

A. S. Eddington (1926)

INTRODUCTION

Even a cursory observation of the night sky reveals that the apparent brightnesses and colors of individual stars are not the same. This basic observation is explained by the circumstance that the distances and intrinsic physical properties of individual stars vary widely. In spite of the conspicuous richness of the starry sky, the notion that stars are simple objects persisted until observations showed that their physical properties are very complex.

Early astronomy was strongly influenced by Euclidean geometry. The development of geometry led to the belief that because the sphere was the most perfect shape, the Earth, sun and stars were also spherical. The trajectories of heavenly bodies were believed to represent the changeless order of the heavens. Until Tycho Brahe and Kepler discovered supernovae, celestial bodies were pictured as perfect objects that did not change or evolve. The discovery of supernovae represented one of the most important steps in the development of our present view of the heavens.

At the present time, there is little doubt that the same laws of physics that explain natural phenomena on Earth can also explain the physical properties of stars. This circumstance leads inevitably to the conclusion that stars are not static but change with time. A major goal of modern astronomy is to explain the observations of stars in such a manner that their complex behavior can be understood as a natural consequence of the laws of physics. The development of satisfactory theories of pulsars and compact x-ray stars now represents perhaps the most fundamental problems in stellar astrophysics. The remarkable discovery of these objects has shown that stellar evolution is far more complex and interesting than many astronomers, such as Eddington, had believed.

Nuclear and gravitational energy are the two principal energy sources for the radiation that we observe from stars. For normal stars such as the sun, nuclear energy is the predominant source: Even if the sun were to contract and its radius decrease by a factor of two, the gravitational energy release would only be $\simeq 10^{-3}$ times the energy available by the fusion of protons to form helium. However, the predominance of nuclear energy sources is correct only for stars with normal stellar radii. For compact stars, gravitational energy release may predominate. To compare the relative importance of gravitational and nuclear energy we compare the nuclear energy available from hydrogen ($\simeq 6 \times 10^{18}$ erg s^{-1} g^{-1}) with the gravitational energy of matter on the surface of the sun, of a white dwarf, and of a neutron star (see Table I-1). It can readily be seen that if hydrogen is accreted onto the surface of a white dwarf, the energy release due to hydrogen burning would be $\simeq 50$ times greater than the kinetic energy of the infalling matter. On the other hand, for the case of matter that is accreted onto the surface of a neutron star, the gravitational energy release can exceed the nuclear energy release by more than a factor of 10.

Table I-1.

Nuclear Energy Release (hydrogen burning)	Gravitation Energy Release GM/R	
	White dwarf	Neutron Star
$\simeq 6 \times 10^{18}$ erg g^{-1}	$\simeq 2 \times 10^{17}$ erg g^{-1}	$\simeq 10^{20}$ erg g^{-1}

A black hole is a concentration of mass that is undergoing perpetual collapse. An observer who falls into a black hole will – in a finite time, as measured by his own clock – reach a point in space that is arbitrarily close to the center of the black hole. The event horizon of a spherical black hole is the Schwarzschild radius, $R_S = 2GM/c^2$. An observer inside this radius cannot communicate with an observer outside the black hole. As measured by the clock of an outside observer, it will take the infalling observer an infinite time to reach R_S because radiation emitted just outside R_S is strongly redshifted as it emerges from the vicinity of the black hole. The total energy that can be emitted by a mass m that falls into a black hole is always less than $E = mc^2$. This upper limit on the amount of energy that can be emitted from collapsing matter follows from the physical requirement that no region in which the total energy density is negative can exist in nature. Although in principle a collapsing star of mass M could emit as much energy as $E = Mc^2$, it is likely that the efficiency of energy release is such that no more than 10% of this available energy is ever radiated away by a collapsing star (or by matter that

is falling into a black hole). It is widely believed that the x-rays observed from most compact x-ray sources come from matter that is falling onto the surface of a neutron star, or falling into a black hole from an accretion disk. Matter falling onto the surface of a white dwarf could also produce significant x-ray emission.

The discoveries of pulsars and compact x-ray sources demonstrate that very strong gravitational fields exist in certain regions of space. In such a physical environment the Newtonian theory of gravitation is no longer correct, and the general theory of relativity must be used to describe the physical state of matter. Although there is as yet no direct experimental evidence that general relativity correctly describes the behavior of matter in very strong gravitational fields, there is great confidence in the theory because it enables us to predict the motions of planets about the sun with very great precision.

MAIN-SEQUENCE STARS

If the luminosities of stars are plotted versus their surface temperatures, most stars are found to occupy one of three principal regions of this diagram, which is called the Hertzsprung-Russell diagram. These three groups of stars are called main-sequence stars, red giants, and white dwarfs.

Main-sequence stars are stars of approximately uniform chemical composition that are burning hydrogen in their cores. The main-sequence is a mass sequence. Stars of large mass are luminous and hot, while stars of lower mass are relatively less luminous and have lower surface temperatures. It can be shown from the equations of stellar interiors that main-sequence stars satisfy a luminosity-mass relation which can be expressed in the form

$$L = K M^x$$

where x varies from $\simeq 4.5$ for $1M_\odot$ stars to about $\simeq 3$ for $15M_\odot$ stars. The mass-luminosity relation implies that high mass stars have much shorter lifetimes than stars of lower mass. The main-sequence lifetime of the sun is $\simeq 10^{10}$ years while that of a $5M_\odot$ star is $\simeq 10^8$ years. Moreover, low mass stars are formed more frequently than stars of higher mass. It follows that massive stars are much less common in nature than stars of lower mass. This circumstance is of great importance from the standpoint of the formation of pulsars and compact x-ray sources. The small number of such objects results in part because they are the end products of the evolution of relatively massive stars ($\gtrsim 5M_\odot$). Therefore their rate of formation is much less than that of white dwarfs (the end product of the evolution of less massive stars).

A star begins to evolve off of the main sequence after approximately 10% of the mass of its core has been converted from hydrogen to helium. At this point the core of the star contracts and a thick hydrogen-burning shell is formed. The thickness of this shell source decreases as the radius of the star expands until the star reaches the red giant branch.

RED GIANTS

Red giants are stars with relatively high luminosities and large radii. Stellar interiors calculations show that their luminosities are primarily determined by the masses of their hydrogen-deficient cores. As more hydrogen-deficient mass is added interior to their hydrogen-burning shells their luminosities increase. The evolution up the red giant branch continues until the central temperature is high enough ($\gtrsim 10^8$ K) for He^4 to burn to C^{12} and O^{16} by means of the triple alpha reactions. The luminosity of a red giant decreases after the ignition of core helium burning and remains relatively constant until helium is exhausted from the core and shell helium burning begins. At this point the star evolves up the red giant branch for the second time.

Physical conditions in the cores of red giants are very similar to those in the interiors of very hot white dwarfs. In the cores of red giants the density is sufficiently high for matter to be degenerate, and the temperatures are sufficiently high for neutrino emission processes to play a major role in determining the temperature of the core. Stars lose significant amounts of their mass during the red giant phase of their evolution. Moreover, many elements are synthesized and ejected into interstellar space by red giants. See Figure I-1a, b for most significant properties of a typical red giant.

WHITE DWARFS

Astronomers use the Hertzsprung - Russell diagram to classify stars according to their luminosities and surface temperatures. When stars are classified in this manner, it is found that there are numerous stars, called white dwarfs, with temperatures greater than or equal to that of the sun but with much lower luminosities. Since the luminosity and surface temperature of a star are related by the equation

$$L = 4\pi R^2 \sigma T^4$$

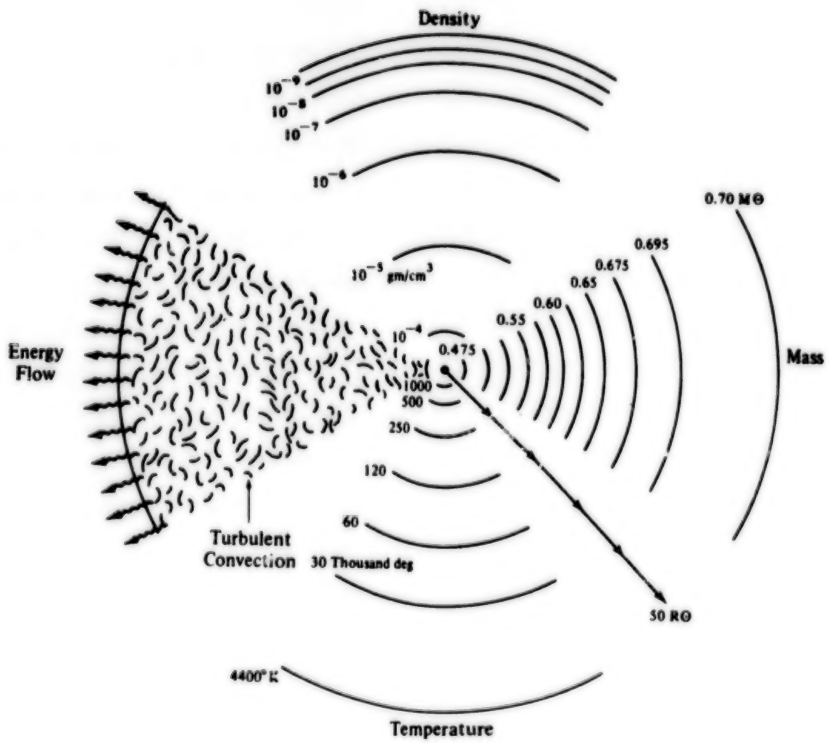

(a) Red Giant Envelope

Figure I-1a. Some important physical properties of the interior of a red giant are shown schematically (based on calculations by I. I. Iben). (source: Iben, I. I., 1967, Ann. Rev. Ay. Ap. 5, 571).

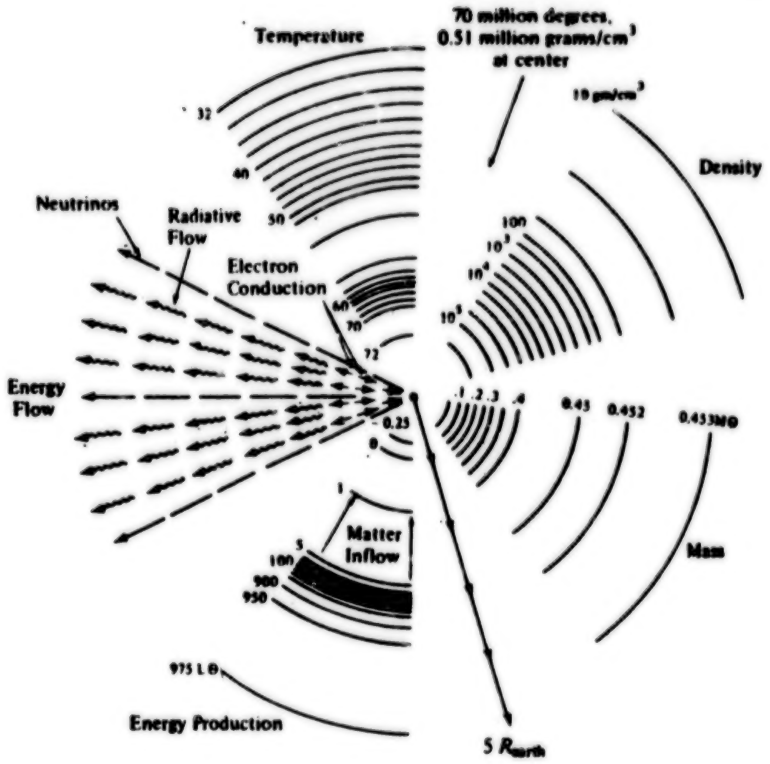

(b) Core of Red Giant

Figure I-1b. Some important physical properties of the interior of a red giant are shown schematically (based on calculations by I. I. Iben). (source: Iben, I. I., 1967, Ann. Rev. Ay. Ap. 5, 571).

where R is the radius of the stars, T is the effective temperature and σ is the radiation constant, it follows that these objectives must have much smaller radii than the sun. The radii of white dwarfs are typically one percent of the solar radius.

Before the nature of white dwarfs can be understood, it is necessary to determine their mass. Fortunately, several white dwarfs that are relatively close to the sun are in binary systems, including the white dwarf companion of Sirius A. It is possible to determine their masses directly.

The discovery that the masses of white dwarfs were comparable to the mass of the sun posed a dilemma to astronomers. Since the surface gravitational field is

$$g = \frac{GM}{R^2}$$

it follows that white dwarfs must have very strong gravitational fields. Since they are exceedingly stable, the inward force of gravity must be balanced by some outward pressure. What is responsible for this pressure? If the state of matter in the interior of a white dwarf were similar to that in the interior of the sun, very high temperatures would be required to produce the pressure gradients necessary to balance gravity. Such high interior temperatures would produce a very large outflow of radiation, and consequently white dwarfs would be very luminous. Since their luminosities are generally very low, the state of matter in their interiors cannot be that of a non-degenerate gas.

It is well known that electrons (and other spin ½ particles) obey fermi statistics and consequently only a limited number of electrons with energies less than some specified value can occupy a given volume of space. It follows that if matter is compressed to the high densities that must exist in the interior of a white dwarf ($\rho \simeq 10^6$ g cm^{-3}) most of the electrons will have high kinetic energies even if the interior temperature is relatively low.

In a white dwarf, the pressure gradients that are necessary to balance the strong gravitational field are produced by the zero point kinetic energy of a degenerate electron gas. Because the pressure in the interior depends almost entirely on the density and is nearly independent of density, it is possible to predict a relation between the mass and the radius of a white dwarf. Observations of white dwarfs show that this predicted mass-radius relation shown in Figure I-2 is nearly correct.

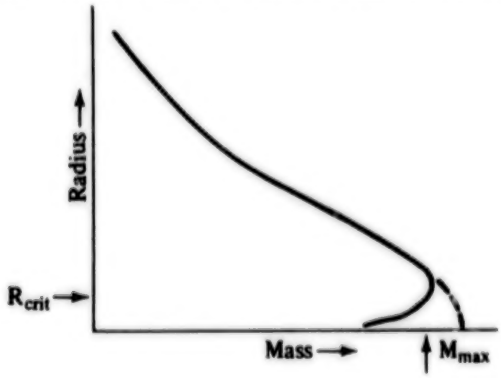

Figure I-2. The mass-radius relation is shown for a white dwarf. The dashed line would apply if inverse beta decay could be neglected (Rose, W. K., 1973, Astrophysics, Holt, Rinehart, and Winston: New York).

Although a degenerate electron gas can balance the gravitational field of a solar mass white dwarf, it is impossible to form white dwarfs with masses greater than approximately 1.4 $M_\odot$. This fundamental result indicates that a star exceeding this limit after it has exhausted its nuclear energy sources must collapse and become either a neutron star or a black hole. The existence of an upper limit to the mass of a white dwarf arises because a degenerate electron gas becomes relativistically degenerate at high densities ($\rho \gtrsim 10^6$ g cm^{-3}). The pressure-density relation for a relativistically degenerate electron gas is $P = K\rho^{4/3}$. If we use this equation of state and the equations of hydrostatic equilibrium,

$$\frac{dP}{dr} = -\rho \frac{GM(r)}{r^2},$$

and mass conservation,

$$\frac{dM(r)}{dr} = 4\pi r^2 \rho,$$

we find the dimensional relation

$$\frac{KM^{4/3}}{R^5} \simeq \frac{GM^2}{R^5}.$$

This relation tells us that for sufficiently large M, gravitation will dominate pressure for arbitrarily small values of R.

PLANETARY NEBULAE AND THE FINAL STATE OF THE SUN

A planetary nebula is a mass shell that expands away from the hot central star at a velocity that is typically 20 km sec^{-1}. Most of the visual radiation emitted by planetary nebulae comes from emission lines. The excitation of this radiation is caused by ultraviolet photons radiated by the central star. Planetary nebulae are hydrogen-rich and have masses that range from $\simeq .1M_{\odot}$ to $\simeq 1.0M_{\odot}$. If we can infer its diameter from its measured distance and angular diameter, we can use the measured velocity of expansion to estimate the time at which a nebula was ejected from the central star. It is found that the central stars of planetary nebulae follow an evolutionary path (see Figure 3) in which their positions in the Hertzsprung-Russell diagram are determined by the age of the nebulae. Young nebulae have luminosities that are $\gtrsim 10^4\ L_{\odot}$ while those older than $\simeq 2 \times 10^4$ years have luminosities $\lesssim 10^2\ L_{\odot}$. (See Figure I-3.)

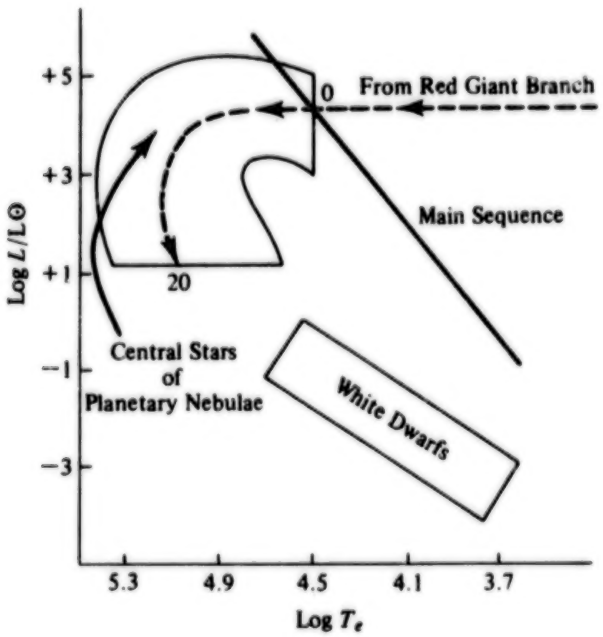

Figure I-3. The evolution of a star from the red giant branch into the white dwarf state is shown in the Hertzsprung-Russell diagram. It takes approximately 20,000 years for a star to evolve from the position denoted 0 to 20. (source: Rose, W. K., 1973, Astrophysics, Holt, Rinehart, and Winston: New York).

From their inferred lifetimes and total number in the galaxy, it can be estimated that $\simeq 3$ planetary nebulae are produced each year in our galaxy. This production rate is comparable to the rate of production of white dwarfs and it is likely that most stars (including the sun) will pass through a planetery nebula phase before they become white dwarfs.

The surface temperatures of the central stars of planetary nebulae are typically $\gtrsim 50{,}000$ K. Such hot stars must be hydrogen deficient. It is natural to ask what kind of star we would produce if we constructed a stellar model from the hot, hydrogen-deficient central star and the hydrogen-rich mass shell. The only stellar model that can be constructed with these components is a luminous red giant. It follows that red giants must be the progenitors of planetary nebulae and that planetary nebulae represent a phase of significant mass loss that occurs in the history of a star soon before it becomes a white dwarf.

The existence of planetary nebulae and other evidence for mass loss from red giants make it clear that stars lose very significant amounts of mass before they evolve into their final states. It is likely that even main sequence stars as massive as $\simeq 5M_{\odot}$ will lose sufficient mass as red giants to become white dwarfs (i.e. final mass $\leqslant 1.4M_{\odot}$), rather than neutron stars or black holes.

The theory of stellar evolution provides an explanation for the formation of planetary nebulae. Stellar model calculations show that when a red giant evolves to the evolutionary phase in which it has both a hydrogen and a helium burning shell surrounding a degenerate core, the helium burning shell is characterized by a series of thermal pulses (i.e. thermonuclear "runaways"). The violence of these thermonuclear runaways increase as the star evolves. Eventually they lead to luminosities at the base of the red giant envelope that are sufficient to eject much (in some cases all) of the red giant envelope. Observations of the planetary nebula FG Sagittae provide strong evidence that thermal pulses arise in evolved stars.

PRODUCTION OF MAGNETIC FIELDS IN STELLAR INTERIORS

Although some stellar magnetic fields are probably fossil fields (i.e. magnetic fields that were trapped in the star at the time it was formed), most of the strong magnetic fields associated with stars were probably formed by means of hydromagnetic dynamos that were produced during the stars' evolution. As will be argued below, such magnetic fields may be produced if a region of a star is non-uniformly rotating and thermally convecting over several density scale heights. (See Figure I-4.)

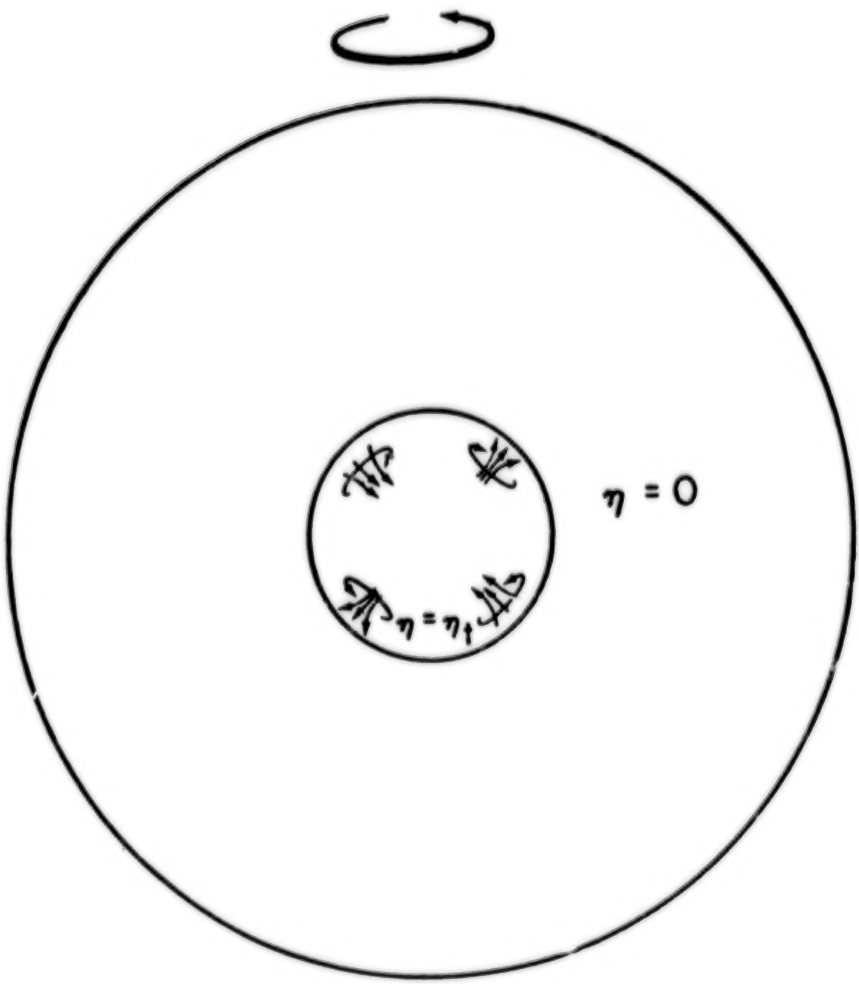

Figure I-4. An idealized model consisting of a differentially rotating convecting core surrounded by a stationary medium with infinite electrical conductivity (i.e. $\eta = 0$). The resistivity of the convecting core is $\eta_t \simeq .15\ V_t\ \ell$ (source: Levy, E. H. and Rose, W. K. 1974, Ap. J., 193, 419).

A dimensionless parameter called the dynamo number determines whether there are solutions to the dynamo equations, which describe the generation of stellar magnetic fields. The dynamo number N is defined as

$$N \equiv \frac{\gamma_0\, V_{cyl}\, R^3}{\eta_t^2} \sim -(.15)^2 \frac{R^2}{\ell^2} \left(\frac{V_\phi\, V_{cyl}}{\langle V_t^2 \rangle} \right)$$

where $\eta_t \simeq .15\ V_t \ell$ (V_t = turbulent convective velocity, ℓ = density scale height) is the turbulent magnetic diffusivity; R is the radius of the convective core or thickness of the convective envelope; $\gamma_0 \simeq V_\phi/R$ is the rate of non-uniform rotation; and V_{cyl} is the cyclonic velocity of the turbulently convecting region. If |N| becomes sufficiently large, the production of magnetic fields by means of a hydromagnetic dynamo is predicted.

The maximum magnetic field strength that can be produced by a hydromagnetic dynamo can be estimated once it is recognized that Coriolis force on convecting fluid elements is responsible for the efficient production of a dynamo magnetic field. For this reason, it is plausible to assume that when magnetic stress becomes comparable to the Coriolis force and thereby inhibits the motions of the fluid, the maximum magnetic field will be attained. We write

$$\frac{\langle B_p\ B_t \rangle}{4\pi R} \sim \rho\ V_t\ \Omega,$$

where B_p and B_t are the poloidal and toroidal components of the magnetic field respectively, $\bar{\rho}$ is the mean mass density, V_t is the turbulent velocity of the convecting fluid and Ω is the angular velocity of the convective region.

Where are the most likely sites for the production of stellar dynamo fields? Stellar magnetic fields are produced in the convective envelopes of stars (e.g., in the convective envelope of the sun). Convective regions produced as a result of thermonuclear runaways in helium burning shells and carbon burning cores are plausible sites for the production of those magnetic fields that are observed in magnetic white dwarfs ($\simeq 10^6 - 10^7$ gauss) and in pulsars ($\simeq 10^{12}$ gauss).

Main sequence stars more massive than about $1.5 M_\odot$ have surface angular velocities that are typically 30 times greater than that of the sun. If the angular momentum per unit mass were conserved during the evolution of such stars, the angular velocities of their interiors would become very high when their interior densities had become comparable to those of white dwarfs ($\rho \simeq 10^6$ g cm^{-3}). However, the observations of white dwarfs that have evolved from massive stars show that they have relatively low angular velocities. Stellar model calculations make is plausible to assume that magnetic fields in stellar interiors are responsible for the transport of angular momentum that is required to explain the observed low velocities of white dwarfs.

We can estimate the spin-down time scale of a rotating star in the following manner. Suppose that a stellar core of radius R is rotating with angular velocity Ω with respect to some external region. The magnetic field exerts a torque $\langle B_p\ B_t \rangle\ R^3$ which acts to reduce the relative angular velocity between the core and the external region. Since $I\Omega \simeq \bar{\rho}\ R^5 \Omega$, we can write

$$\frac{dI\Omega}{dt} \simeq \bar{\rho}\ R^5 \frac{d\Omega}{dt} \simeq \langle B_p\ B_t \rangle\ R^3.$$

From this equation, it follows that the spin-down time for the rotating stellar core is

$$\tau \simeq \bar{\rho}\ R^2 \Omega / \langle B_p\ B_t \rangle.$$

STELLAR COLLAPSE TO NEUTRON STAR OR BLACK HOLE

Supernovae occur when the core of a star collapses to form a neutron star or black hole. Such collapse can occur when the core mass of a red giant exceeds $\simeq 1.4\ M_\odot$ the upper mass limit for a white dwarf. In our previous discussion we have emphasized that the relative infrequency of supernovae explosions as compared to the rate of production of planetary nebulae is primarily the result of mass loss from red giants. We have argued that the cores of red giants probably do not rotate as rapidly as they would if angular momentum per unit mass were conserved during the evolution of a star. If this were not the case, the differentially rotating cores of red giants could exceed $1.4\ M_\odot$ by a significanf factor before collapse.

A neutron star (see Figure 5) is a degenerate star whose interior density is comparable with or greater than the density inside the atomic nucleus ($\rho \simeq 2.5 \times 10^{14}$ g cm^{-3}). If matter is compressed to such high densities it will form a degenerate (mostly) neutron gas. Neutrons, unlike electrons, strongly interact and therefore their equation of state is not that of a free fermion gas. In order to compute the equation of state of such a gas one must understand the forces between neutrons. If these forces are primarily repulsive, the equation of state will be stiffer than that of a free neutron gas. The reverse will be true if the forces are primarily attractive.

The best available equations of state for neutron matter show that attractive interactions dominate for neutron densities $\lesssim 3 \times 10^{14}$ g cm^{-3}, but at that at somewhat higher densities repulsive interactions dominate and consequently

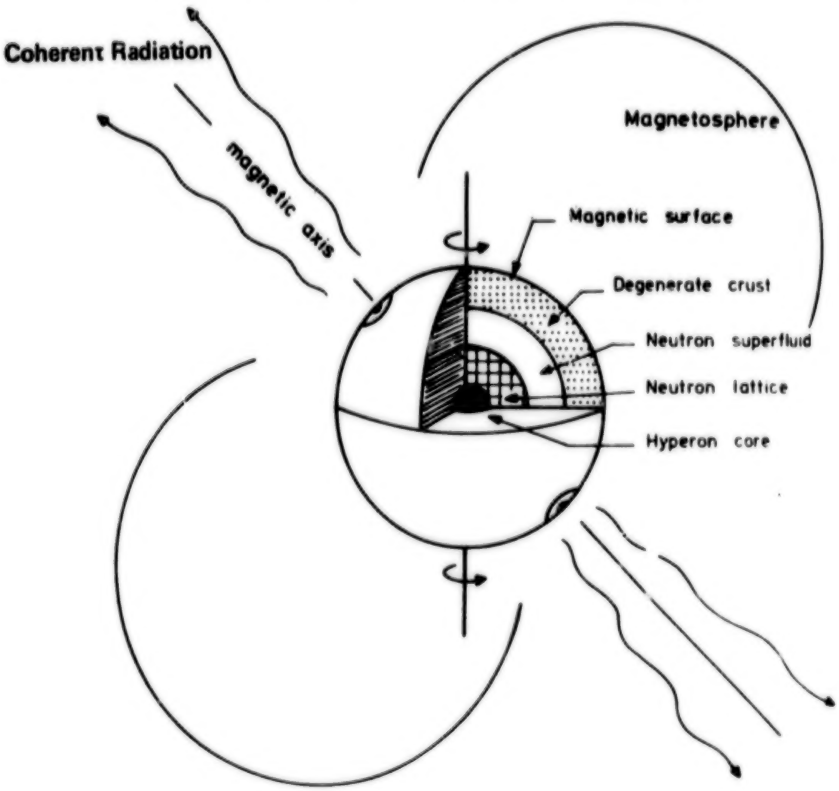

Figure I-5. Model of a neutron star (source: Hewish, A., 1975, Rev. Mod. Phys. 47, 570).

the equation of state becomes $P = K \rho^{\gamma}$ with $\gamma > 5/3$. This result implies that neutron stars more massive than that allowable for a free neutron gas (i.e. $\simeq .7\ M_{\odot}$) can be formed. This is an extremely important result since the collapsing cores of red giants are predicted to have masses that are $\gtrsim 1.4\ M_{\odot}$. It follows that neutron stars, and therefore pulsars, would probably not be formed at all if the pressure of matter did not become greater than that of a free neutron gas at high density.

Because neutron stars with relatively high mass ($M \gtrsim 1.4\ M_{\odot}$) can probably exist, it follows that it is difficult to form black holes by means of stellar collapse. Black holes are likely to be formed during the collapse of a very massive star or if mass is accreted onto the surface of a neutron star that is a member of a close binary system. It is interesting to speculate that the black hole candidate Cygnus X-1 might have been formed by the latter mechanism.

CHAPTER II
PULSARS

D. C. Backer
*NASA Goddard Space Flight Center**
Greenbelt, Maryland

and

Radio Astronomy Laboratory
University of California
Berkeley, California

INTRODUCTION

The definitive history of pulsars will be a truly fascinating account of the visionaries, Zwicky and Landau, who postulated the existence of neutron stars only one or two years after Chadwick discovered the first neutral atomic particle; of the theoreticians, Oppenheimer and his students, who came to understand neutron – star structure in the years before they built the atomic bomb; of the astrophysicists, Woltjer, Hoyle, and Pacini, who worked on the nonobservable (!) consequences of neutron stars in the Fifties and early Sixties; of the discoverers, Hewish and his colleagues, whose persistence in completely exploring scintillation of radio sources, led them to detect the pulsating radio sources; and finally, of the many scientists who, in February 1968 and the months thereafter, rushed to the telescopes around the globe or to their copies of Landau and Lifshitz Classical Theory of Fields, often treading on the less hardy, to explore the details of the pulsar phenomenon.

This history has not been written. It will not be given here. There are however many progress reports on the pulsars in the open literature, some of which are tabulated chronologically in Table II-1.

In this account it is assumed that a pulsar is a collapsed remnant at the very end of its stellar evolution path (see the discussion by Rose in Chapter I). with the angular momentum and magnetic flux of a common star, $10^{41\text{-}43}$ kg m^2 s^{-1} and $10^{22\text{-}24}$ Mx, respectively. The collapse of a common star to neutron star dimensions, 10 km in radius, with angular momentum and magnetic flux conservation, can produce spin frequencies well over 1 Hz and surface magnetic fields of 10^{11} gauss, values which lead to many consistency arguments concerning fundamental observations:

*NAS/NRC Resident Research Associate

Table II-1
Brief Chronology of Pulsar Investigations

REVIEW PAPERS

Hewish, A., et al., 1968, Nature, **217**, 709 (the discovery).
Maran, S. P., and Cameron, A. G. W., 1968, Physics Today, **21**, 41.
Hewish, A., 1969, Endeavor, **28**, 55.
Radhakrishnan, V., 1969, Proc. ASA, **1**, 254.
Ginzburg, V. I., Zheleznyakov, V. V., and Zaitsev, V. V., 1969. Ap. Sp. Sci, **4**, 464.
Hewish, A., 1960, Ann. Rev. Ay. Ap., **8**, 265.
Drake, F. D., 1971, McGraw-Hill Encyclopedia, "Pulsar", 95-97.
Tilson, S., 1970, IEEE Spectrum, **7**, 43.
Ostriker, J. P., 1971, Scientific American, **224**, No. 1, 48.
Ruderman, M., 1971, Scientific American, **224**, No. 2, 24.
Smith, F. G., 1971, Rep. Prog. Phys., **35**, 399.
ter Haar, D., 1972, Physics Reports (Sec. C), **3**, 57.
Ruderman, M., 1972, Ann. Rev. Ay. Ap., **10**, 427.
Manchester, R. N., 1973, Proc. IEEE, **61**, 1205.
Hewish, A., 1975, Science, **188**, 1079 (Nobel lecture).
ter Haar, D., 1975, Contemp. Physics, **16**, 243.
Ginzburg, V. L., and Zhelezniakov, V. V., 1975, Ann. Rev. Ay. Ap., **13**, 511.

MAJOR CONFERENCES

1968 New York: Maran, S. P., 1968, Sky Tel., **36**, 4.
1969 Flagstaff: Misc., 1969, Publ. Astr. Soc. Pacific, **82**, 375.
1969 Rome: unpublished (?).
1970 Jodrell Bank: Davies, R. D., and Smith, F G., 1971, IAU Symposium No. 46.
1970 Brighton: Ginzburg, V. L., 1971, Highlights of Astronomy, **2**, 3. Hewish, A., 1971, Highlights of Astronomy, **2**, 3.
1974 Stanford: Manchester, R. N., 1974, Science, **186**, 66.

(1) the range of spin frequencies (Ω);
(2) the decrease of spin frequencies with time due to rotational energy loss;
(3) the Poynting flux of the magnetic field through the "light cylinder" (a cylinder aligned with the rotation axis and with radius $r_c = c/\Omega$) which satisfies the energy source needed to maintain the Crab nebula.
(4) an oblique dipole moment of the field which provides a natural source of asymmetry for the low duty-cycle pulsar emission, as well as a source of high-energy particles through unipolar induction.

The following sections will cover many of the areas of observational knowledge and occasionally elaborate on the simple physical picture outlined above. They will stay closer to what we know, than to what we would like to know or what we presently conjecture about pulsating radio stars.

SPIN PROPERTIES

A narrow bandwidth sample of pulsar radiation is, to first order, a sequence of delta functions, not unlike the clock pulses from a good atomic standard. In an hour one might count 5000 pulses and know the arrival times of the first and last pulses referred to an atomic standard to a few ms. This leads to a period determination accurate to about 1μs, or 1 part in 10^6. Repeating this over several months would lead one, as it led Hewish, to discover a Doppler pattern in the succession of period determinations due to the Earth's velocity about the sun. To investigate the nature of an extra-solar system periodic signal, it is necessary to reduce one's observations to an inertial frame of reference. This is done by correcting topocentric pulse arrival time (t_a) at the telescope to barycentric arrival time (t_b) at the gravitational center of the solar system, a point often just outside the solar surface. The correction is

$$t_b = t_a + (\mathbf{R}_\oplus(t_a) + \mathbf{R}_0(t_a)) \cdot \mathbf{S}(t_a) + K(t_a), \qquad (1)$$

where $\mathbf{R}_\oplus$ is the position of the earth center of mass with respect to the solar system barycenter, $\mathbf{R}_0$ is the position of the observatory on – or, for terrestrial satellites above – the earth, S is the position of the source on the celestial sphere as viewed from the barycenter, and K is a correction for the error in the terrestrial clock as it moves in and out of the gravitational potential well of the solar system. Since errors in t_a may be as small as 100 μs, one needs errors in $\underset{\sim}{R}$ to be of order 10μs, or 3 km.

To measure t_a it is necessary to average many pulses summed synchronously with an accurate period of date both to obtain a stable waveform and to have high sensitivity. With a set of barycentric arrival times distributed over a year or more for any pulsar (t_b^i) one can investigate the stability of the spin by comparing the values t_b^i to the best estimate for the spin frequency (Ω) and its derivative ($\dot{\Omega}$) to obtain a residual "phase"

$$\phi^i = \Omega\,(t_b^i - t_b^0) + \frac{1}{2}\dot{\Omega}\,(t_b^i - t_b^0)^2 - N^i, \qquad (2)$$

where N^i is the integer which reduces ϕ^i to a value less than 0.5. The phase residuals are then fit in a least-squares sense to errors in **S** (in Eq. (1), Ω, $\dot{\Omega}$, and perhaps $\ddot{\Omega}$. The standard equation of condition is

$$\phi^i = \mathbf{R}^i \cdot [\Delta\mathbf{S}_0 + \mu\,(t_b^i - t_b^0)] + \Delta\Omega\,(t_b^i - t_b^0) + \frac{1}{2}\Delta\dot{\Omega}\,(t_b^i - t_b^0)^2, \qquad (3)$$

where $\Delta\mathbf{S}_0$ is the vector position error at t_b^0, $(\Delta\alpha, \Delta\delta)$, and μ is the apparent proper motion of the pulsar, (μ_α, μ_δ). The effect of annual parallax is below the accuracy of present experiments. The final residual phase after the fitting procedure reflects any systematic variations of pulsar spin from the model. Observed values are $1.8 < \Omega < 180\ s^{-1}$ and $0^- > \dot{\Omega}/\Omega^2 > -4 \times 10^{-13}$. Examples of systematic variations are (A) discontinuities of the spin, most frequently observed as a sudden fractional increase of Ω by 10^{-6} to 10^{-8} and a decrease of $\dot{\Omega}$, and (B) slower wanderings of the residual phase by small fractions of a pulse period over time scales of months. These have been interpreted as sudden and slow changes in the moment of inertia of the star.

Much has been written about the spin properties of pulsars. The rotational energy of a pulsar is

$$E = \frac{1}{2} I \Omega^2, \qquad (4)$$

where I is the moment of inertia obtained from neutron star structure calculations, roughly 10^{38} kg m^2. The rotational energy loss rate is

$$\dot{E} = -I\Omega\dot{\Omega}, \qquad (4)$$

and varies between 10^{22} and 10^{32} J s^{-1}. Theories of the pulsars predict a spin dependence of $\dot{E} \propto \Omega^m$ with $3 < m < 5$. Measurements of $\ddot{\Omega}$ of a pulsar. available now only for the Crab nebula pulsar, lead to a value of

$$m = 1 + \frac{\Omega\ddot{\Omega}}{\dot{\Omega}} \sim 3.6 \qquad (6)$$

A correlation of observed values of Ω and $\dot{\Omega}$ (Figure 1) leads to a similar value for m, but the scatter is large and it is not clear that all objects belong to a single statistical sample.

The ratio of Ω and $\dot{\Omega}$ gives a time scale for evolution of the spin frequency:

$$t_e = \Omega/\dot{\Omega}\,, \qquad (7)$$

which is twice the age of a pulsar if m = 4 and if the magnetic dipole field does not decay with time. The evolution time is as small as 10^4 yr, but a more typical value is 10^6 yr. We view the relation of t_e and age with caution today because of the irregular variations of Ω and $\dot{\Omega}$ mentioned above and of the existence of an object with $t_e < 4 \times 10^9$ yr.

Finally we mention that, in models of pulsars which spin down as a consequence of dipole radiation from an oblique magnetic field, the perpendicular component of the dipole field at the surface can be related to the spin properties by

$$B_{S\perp} \propto (\Omega\dot{\Omega})^{1/2}. \qquad (8)$$

Much labor has been spent relating one pulsar property to another within the context of the models we have described. Very few attempts have been made to account for the lack of independence of quantities such as $\dot{E}$, t_e, and $B_{S\perp}$ due to their derivation from the same observables, Ω and $\dot{\Omega}$. An important contribution in this regard has recently appeared (Lyne et al., 1975). They find no correlation between $P_1 (= 2\pi/\Omega)$ and $\dot{P}_1$ $(= 2\pi\dot{\Omega}/\Omega^2)$, their observables, but they do find correlations with 408-MHz luminosity, equivalent width of the average pulse and galactic Z distance of

$$\left.\begin{aligned} L_{408} &\propto P_1^{-1.8}\ \dot{P}_1^{+0.88} && \text{(correlation} \cdot 0.43 \pm 0.05),\\ W &\propto P_1^{-0.46}\ \dot{P}_1^{-0.23} && (-0.57 \pm 0.07),\\ Z &\propto P_1^{1.43}\ \dot{P}_1^{+0.36} && (0.17 \pm 0.10), \end{aligned}\right\} \qquad (9)$$

respectively.

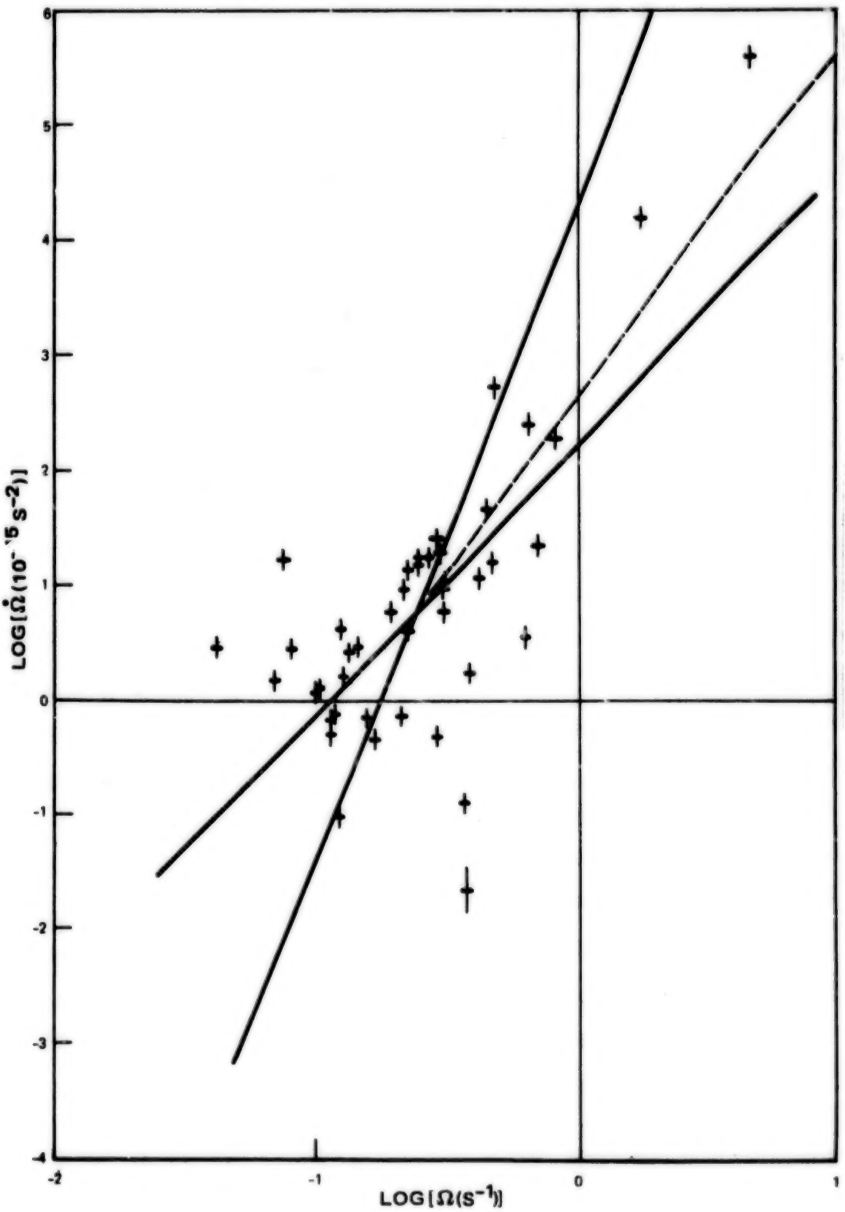

Figure II-1. Spin properties of pulsars. A scatter plot of pulsar spin frequency (Ω) against the time derivative of the spin frequency ($\dot{\Omega}$).

AVERAGE WAVEFORM

In fact pulsar radiation is not a sequence of delta functions. An intensity-time series of samples of the total power output of a narrow-band signal received by a radio telescope, when folded modulo the apparent period, displays a waveform with a typical width of $0.04\ P_1$. There are a number of properties of the total-power waveforms of the ensemble of pulsars:

(1) Taken as an ensemble, there is no time asymmetry of the waveforms.

(2) The waveforms indicate the presence of separate "components" either by resolved peaks or by inflection points which suggest unresolved "components".

(3) In the shortest-period objects there is a high incidence for components at two points in the pulse period separated by 0.50 ± 0.15 periods – a main pulse and an interpulse – and in two cases for a low level "bridge" of radiation extending throughout the narrower gap between the two regions of emission.

(4) The component-to-component peak-intensity ratios can vary with radio frequency to such a degree that one may effectively disappear.

(5) The widths and separations of components frequently decrease monotonically with radio frequency.

(6) The two-component objects do not appear to be the sum of two independent components, but rather are single double-peaked beams.

These properties, excepting (3), are consistent with a model for the average pulsar beam which is, most frequently, an oblique, rotating hollow-cone of outer dimension 10°. An observer with a polar angle within 5° of the polar angle of the cone axis views a single cut through the cone – a single-peaked waveform when far from the axis and a double-peaked one when near the axis. When the cone axis and the observer are near the rotation axis, a broad pulse is observed with identical morphology. This scaling of morphology is exhibited in figures 2 and 3, which include a category of triple-peaked waveforms that appear to arise from a hollow cone with a central, and somewhat unrelated, pencil beam added to the more common double-peaked waveform. Two beams spaced at 180° in the equatorial plane are required to explain interpulse components.

Pulsar radiation is strongly polarized. A complete average waveform then requires four Stokes parameters: the total intensity I discussed above; the linear polarization parameters Q and U, which are differences of power received by probes of the radiation field at respective position angles of 0°

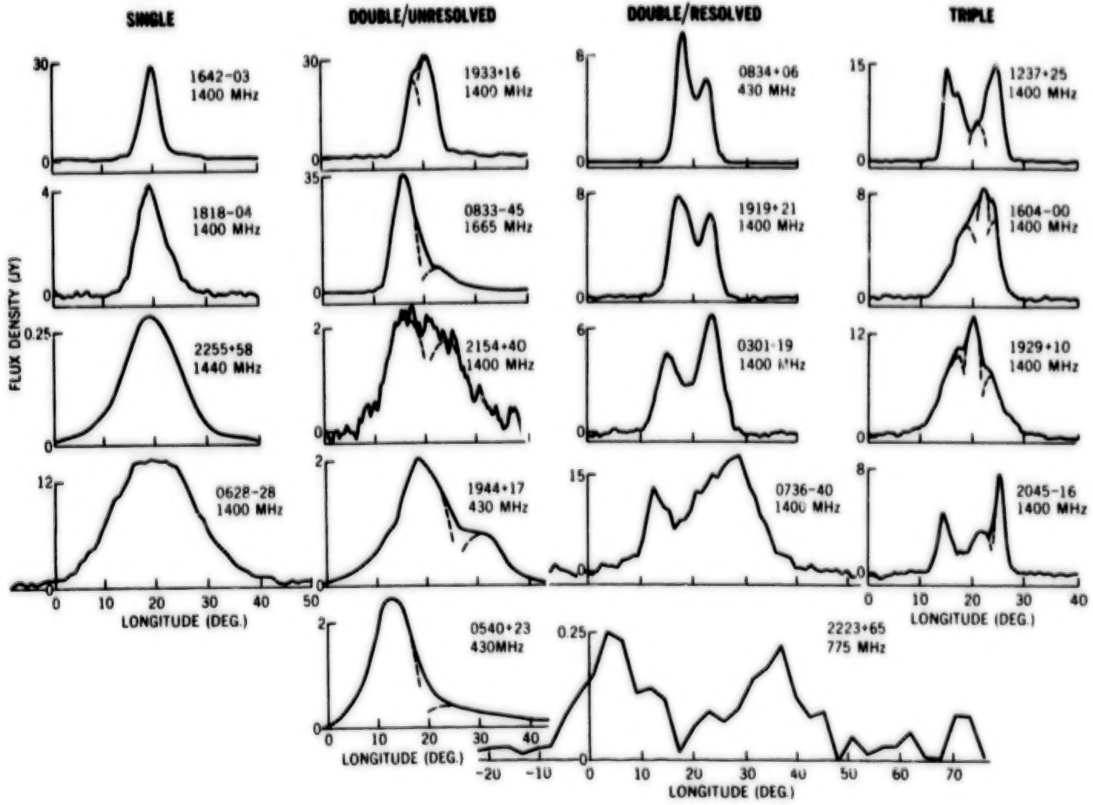

Figure II-2. Average waveform morphology. Total-intensity waveforms of pulsars with SINGLE, DOUBLE/UNRESOLVED, DOUBLE/RESOLVED and TRIPLE component morphology which displays the scaling of profiles with longitude expected for random orientation of observer and hollow-cone beam axes with respect to the rotation axis (source: Backer, 1976).

22.

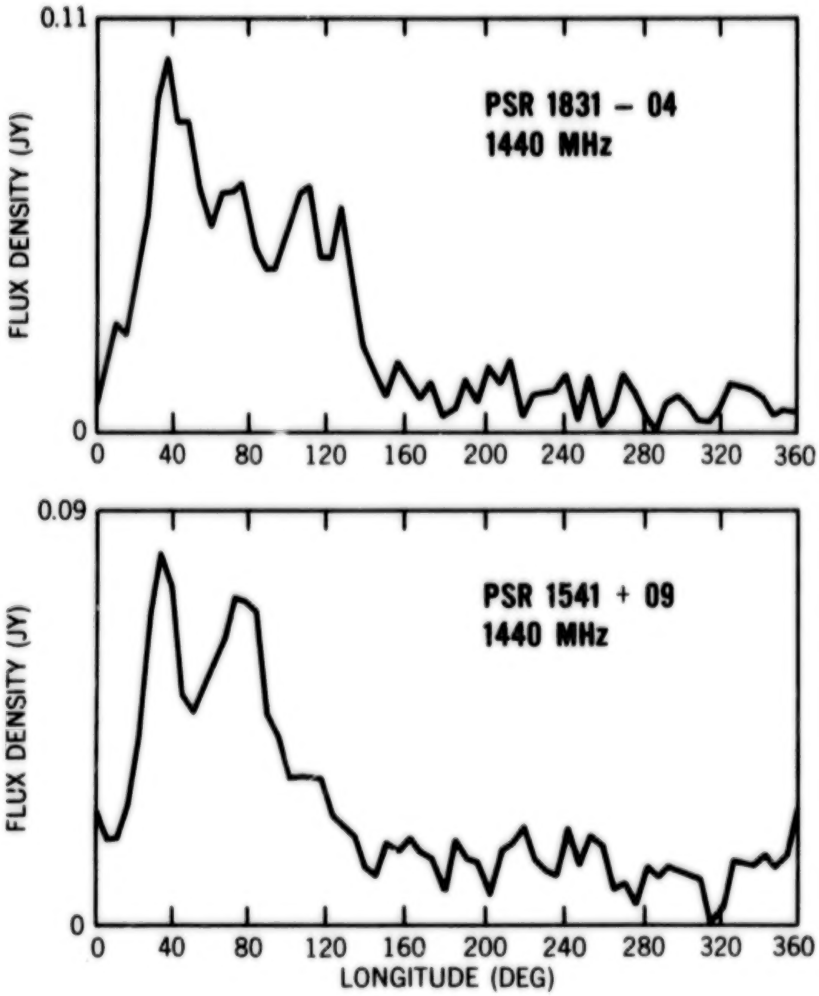

Figure II-3. Average waveform morphology. (See comments to Figure II-2.)

and 90° and 45° and 135°; and the circular polarization parameter V which is the power difference of probes sensitive to left and right circular polarization. It is common to display waveforms of the linear polarization $P = (Q^2 + U^2)^{1/2}$, the position angle of the linear polarization $A = 1/2 \tan^{-1} (U/Q)$ and V. The same quantities are sometimes given with intensive quantities normalized by the total intensity.

Average values of P/I range from 0 to very near 100% in various parts of various objects. The angle often rotates monotonically through the waveform. Values of V/I are generally less than 40%. Some polarization waveforms are given in Figure 4 – from observations at 430 MHz made with the Arecibo telescope. The polarization angle rotation is often consistent with the rotation expected for emission in the plane defined by the observer and cone axis vectors – which is the original concept that led to hollow-cone model. Examples of the polarization angle rotation for this model are given in Figure 5. Radiation from relativistic particles being accelerated along the axial field lines of an oblique magnetic dipole could provide the required beam geometry for both total intensity and the polarization angle.

RADIO SPECTRUM

The height of the total-intensity waveform averaged over the entire period is the flux-density of the equivalent continuum source. The low average flux densities of pulsars, a few Janskys at meter wavelengths, is the reason that these radio stars were not catalogued and investigated earlier. The one exception is the Crab nebula pulsar, which was discovered and studied, especially by Hewish and his colleagues, in pre-pulsar years. However, at the long wavelengths where the Crab pulsar is detectable, it does not pulse regularly because of a smearing of the pulse by multipath propagation effects (see the section on Interstellar Medium). The flux density spectra have steep, power-law decreases at cm wavelengths, with indices between -1 and -3 and a range of m-wavelength morphologies from continued power laws to a second, flatter power law, to sharp cutoffs. Figure 6 displays several examples. The radio luminosities of pulsars, calculated with distances estimated from the thermal plasma column densities (see the section on Interstellar Medium) and based on the conical beam model, range from $L_r = 10^{18}$ to 10^{23} W, or $10^{16\text{-}21}$ Joules per pulse. The ratio $L_r/\dot{E}$ is always less than 10^{-3}. By comparison, laboratory lasers have only recently attained the megajoule level for pulses of nanosecond duration: 10^{15} W.

At a single frequency, radiation brightness temperatures inferred from the peak flux-density in the average waveform and the 10° beamwidth are near 20^{25} K. This emission, with $h\nu \approx 10^{-26}$ J and with $kT_b \approx 10^2$ J on average (!), constitutes the greatest thermodynamic imbalance known to man. For contrast, the radiation from compact extragalactic sources has $h\nu \simeq 10^{-23}$ J with $kT_b < 10^{-8}$ J. The radiation mechanism must involve the coherent action of a large number of charges with no perturbing influences that would open up channels with $h\nu$ closer to kT_b. Coherent radiation processes are in

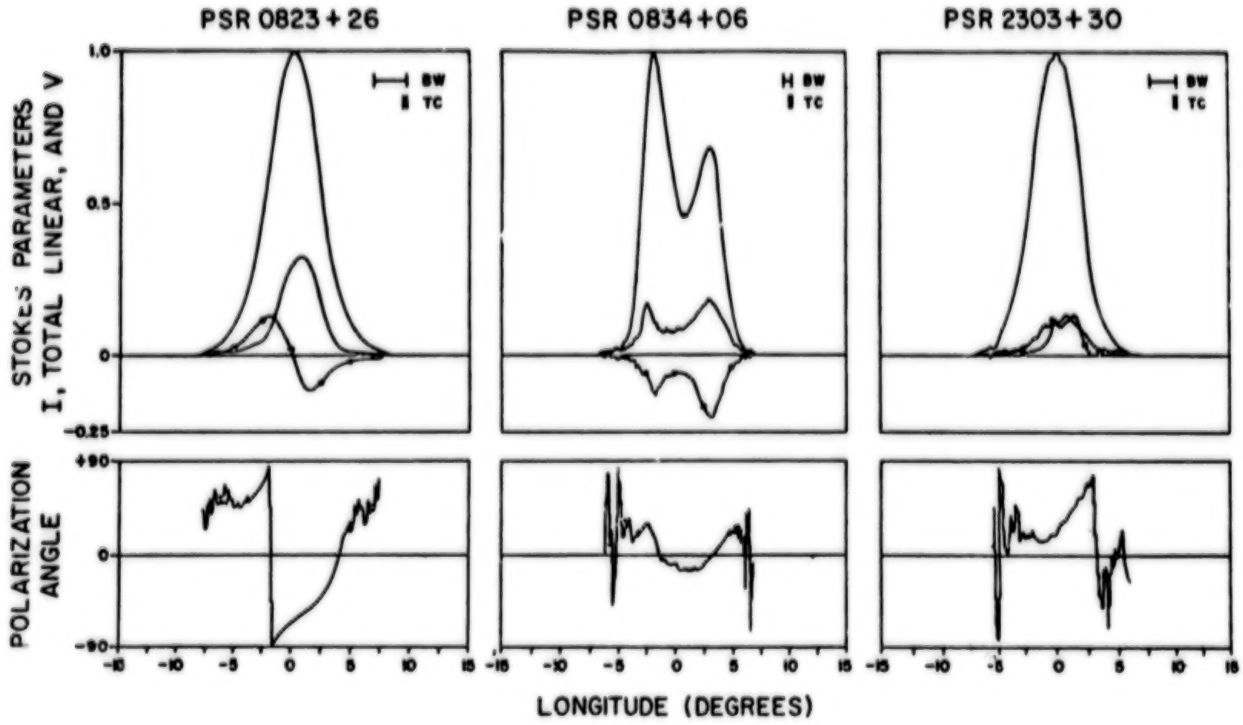

Figure II-4. Polarization average waveforms. Waveforms of total intensity (I), $(Q^2 + U^2)^{1/2}$, V (line with points on it) and, below, $\frac{1}{2} \tan^{-1}$ (U/Q). The intensive quantities have been normalized so that the maximum I is unity. Resolutions in longitude provided by the time constant (TC) and by the dispersion within the bandwidth (BW) are indicated (source: Rankin et al., 1974).

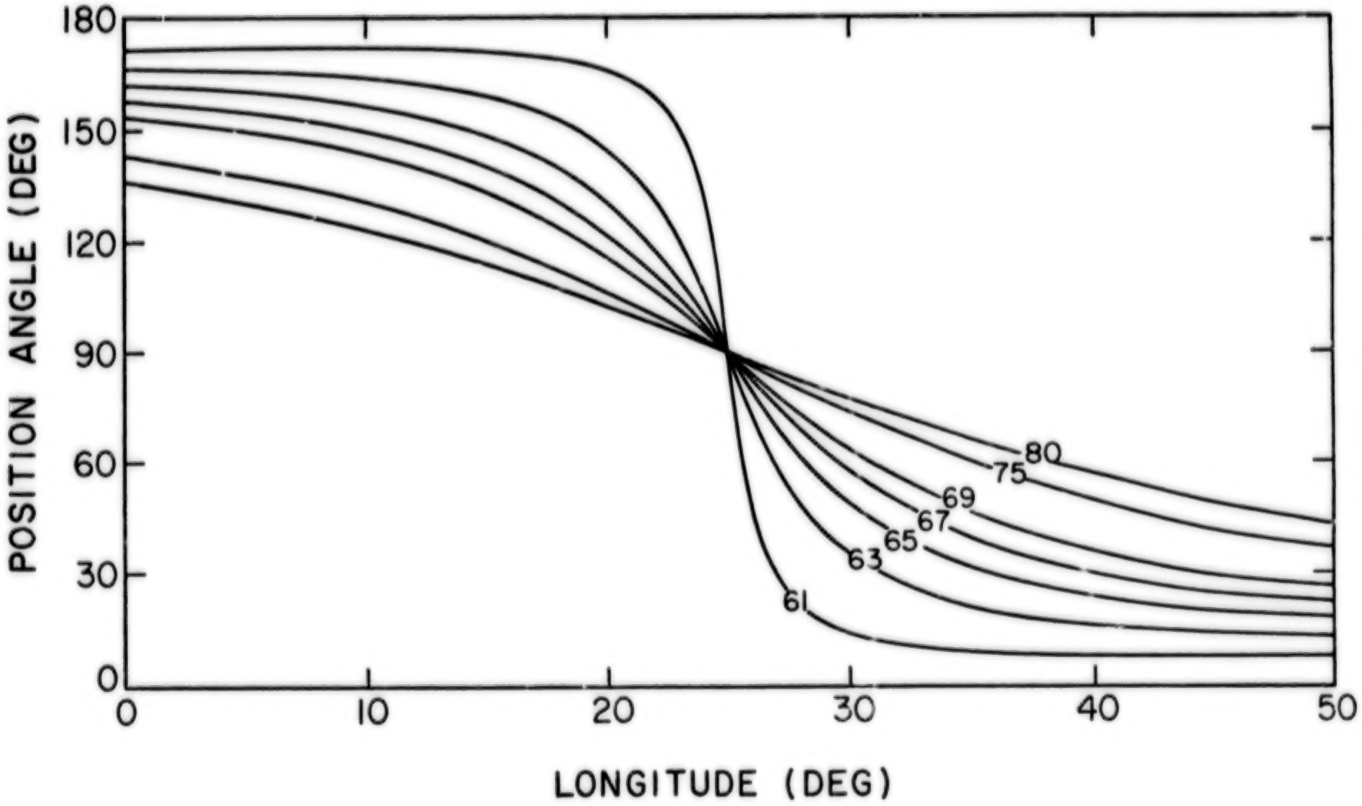

Figure II-5. Model polarization angle waveforms. For a pole at 60° from the rotation axis we show its position angle relative to the observer – rotation axis plane – for a number of observer polar angles. Cf. Figures II-4 and II-12.
(Source: Backer, Rankin and Campbell, 1976).

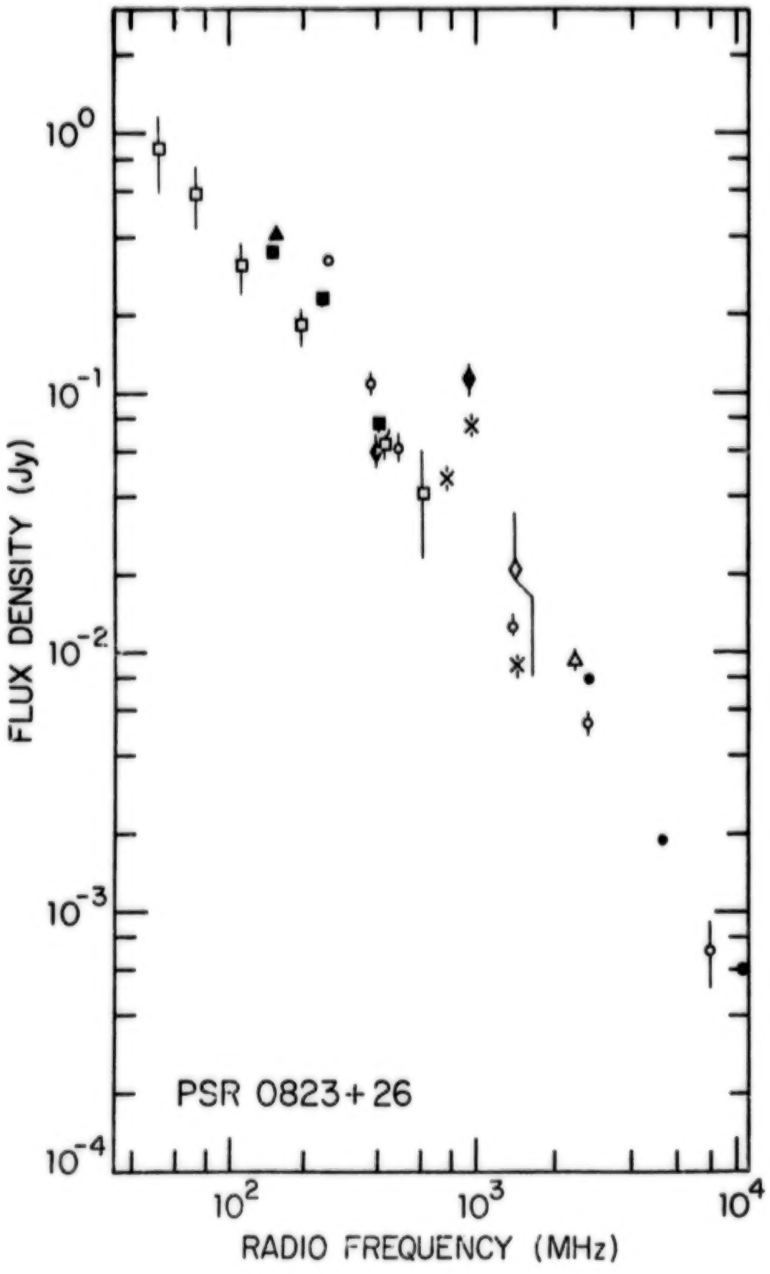

Figure II-6(a). Flux-density spectra. Observations of two pulsars at different epochs are summarized indicating the existing of stable spectra (source: Backer and Fisher, 1976).

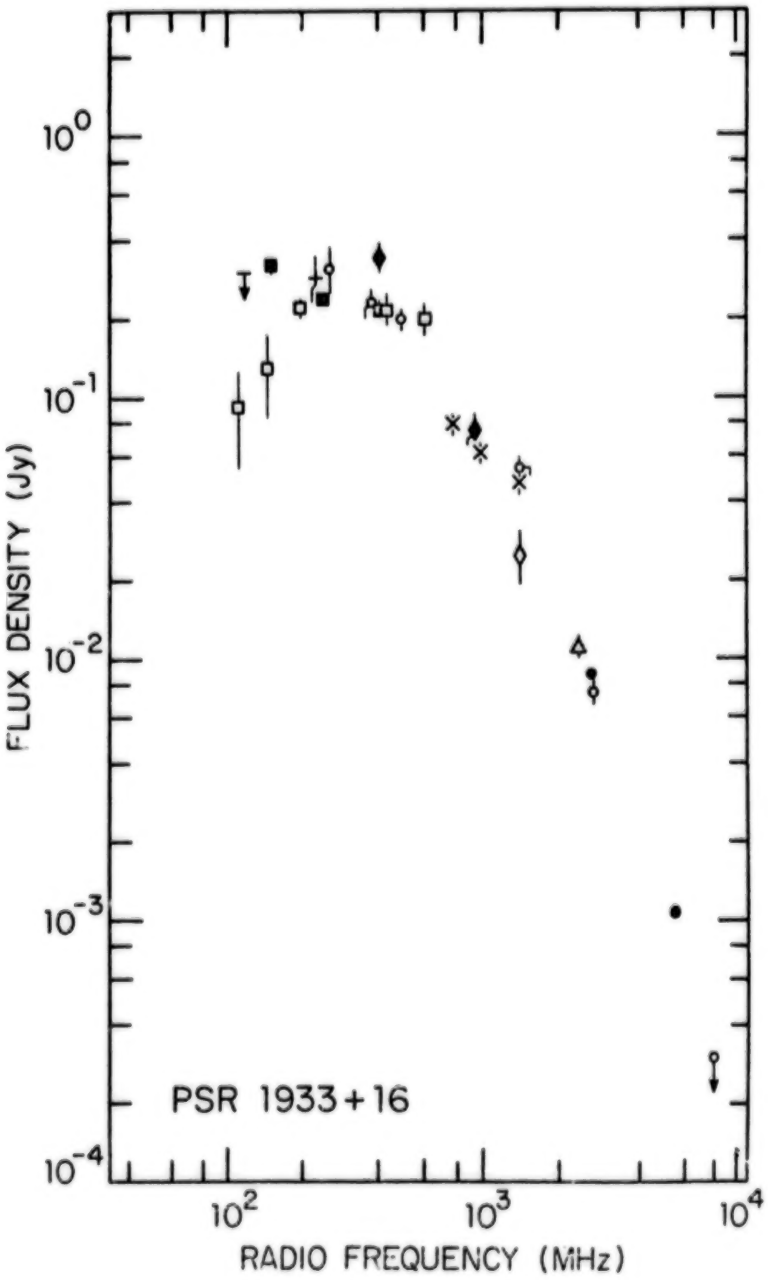

Figure II-6(b). Flux-density spectra. Observations of two pulsars at different epochs are summarized indicating the existing of stable spectra (source: Backer and Fisher, 1976).

principle, narrow bandwidth since many particles must transfer their free energy to radiation in unison. Perhaps as much as a decade bandwidth would be possible for processes like coherent magnetic bremsstrahlung radiation. However, the spectra of pulsars extend over two decades at comparable levels; in particular, the power-law form of the spectra suggests a distribution of parameters governing the center frequency of the coherent process in the emission which extends the spectrum over the observed bandwidth.

FLUCTUATION WAVEFORM

The individual pulses are seldom similar to the average waveform, either in total intensity or in polarization state. We deal at first with the total intensity fluctuations, and approach the matter as through a microscope, with increasing time resolution.

As we have described in the preceding section, repeated measurements of the flux density have shown 2 to 1 variations at meter wavelengths with a characteristic time

$$t_{slow} \simeq 40 \text{ days.} \tag{10}$$

Present evidence suggests that this modulation is more severe at longer wavelengths, which could imply a propagation effect or could relate to the higher degree of coherence required for the stronger radiation at long wavelengths (the degree of coherence should scale with the radiation brightness temperature which increases with $\lambda^{3\text{-}5}$ for pulsars). At present no source of memory for the slow variations has been identified.

We now focus on variations over roughly 100-1000 pulses, an increase of resolution by several orders of magnitude, but we are still concerned with the average flux density, or perhaps the average waveform. Above a few hundred MHz we have also hurdled over a domain of intensity variations imposed by variable refraction in the intervening medium. (See the section on Interstellar Medium.) In the 100 - 1000 P_1 domain, many objects have a "bursty" intensity-time sequence, and a few exhibit sudden changes in the average waveform between one of two "modes". In relation to the latter effects, there are also abrupt changes in emission patterns within sequences of individual pulses, again between one of several modes. Since these variations are much longer than the pulse-to-pulse changes, we can label them according to their frequency character:

$$100\, P_1 < t_{red} < 1000\, P_1. \tag{11}$$

A sequence of pulse energies unaffected by propagation effects has a fluctuation spectrum composed of several elements:

(a) the "red" fluctuations mentioned above,
(c) a uniform level of "white" fluctuations, and
(b,d) one or more features indicating a quasi-periodic process in the data. (See Figure 7.)

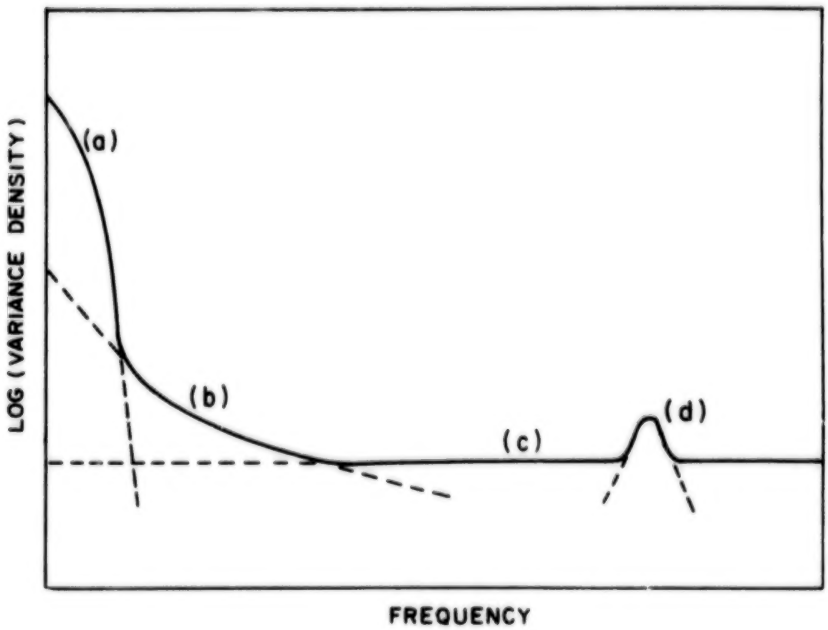

Figure II-7. Fluctuation waveform. Schematic of the typical fluctuation spectrum of pulsar data from a single longitude point. The components are (a) a low-frequency rise due to interstellar scintillation; (c) a "white" noise level arising from random subpulse/micropulse variations; and (b,d) features indicating the presence of a quasi periodic process of a quasi periodic process in the data (source: Backer, 1975).

The presence of a quasi periodic process leads us to increase our resolution another several orders of magnitude, from 1 P_1 to 10^{-3} P_1. We find that individual pulses are often narrower than the average waveform and very erratic from one pulse to the next. To the extent that there are well-defined peaks in individual pulses, we can identify "subpulses" which many identify as a cut through the fundamental instantaneous beam of the emission from one or a few coherent groups of particles:

$$t_{subpulse} \simeq 10^{-2} P_1. \qquad (12)$$

The random statistics of the subpulse emission is responsible for the "white" fluctuations introduced above.

In most objects there is a definite correlation of the subpulse emission from one pulse to the next. This may take the form of short bursts of pulses; of a loosely defined pattern of subpulses on and off in different regions of the pulse that is replicated with a pattern period which one detects as a quasi periodicity in fluctuation spectra; or of a highly organized pattern of regularly spaced subpulses which, in the simplest case, appear to drift through the average waveform with a drift rate D, a separation within the pulse P_2, and a pattern repetition period $P_3 = D P_2$ (see Figure II-8). A high degree of random behavior is expected in pulsars, since the level of radiation is a very sensitive function of the number of particles and of their arrangement along the line of sight. It is less easy to understand the organized behavior. There is a need for a short-term memory in the emission mechanism which allows it to generate for several periods at a time in the most random objects, and to create a periodic array of beams which slip slowly out of view over tens of periods in the organized objects.

One attractive explanation for these effects is the creation of an array of subpulse beams periodically distributed in a circle around the axis of the hollow-cone average beam discussed earlier in the Average Waveform section (Figure II-9). If these beams rotate slowly around the axis because of electromagnetic body forces on the current producing the radiation, then many of the correlated subpulse phenomena outlined above could be modeled; e.g., subpulses which drift in a nonlinear manner, subpulses in double-component objects which disappear in the mid-pulse region, and sudden changes of D and P_3.

In calling this section Fluctuation Waveform we refer not just to the waveform of an individual pulse which deviates from the average, but also to summaries of how statistical properties of the second moment of the intensity data vary across the pulse. We are identifying the data as $I_{jk} = I(\phi_j, t_k)$ where ϕ_j is the relative position within the average waveform, or relative longitude of the sub-earth point of the underlying star, and $t_k \simeq kP_1$. This may be transformed to fluctuation spectra:

$$P(f_k, \phi_j) = |\mathcal{I}(f_k, \phi_j)|^2 / \langle I_{jk} \rangle_k^2, \qquad (12)$$

where $\mathcal{I}_{kj}$ and I_{jk} are a Fourier transform pair and $\langle I_{jk} \rangle_k$ is the average intensity at longitude ϕ_j. An example of P_{kj} for PSR 1237 + 25 is given in Figure 10 which displays a remarkable symmetry about the midpulse point. A histogram analysis can give an idea of the probability-density function for intensities

$$p(I_k|\phi_j) = h(I_k|\phi_j)/N, \qquad (13)$$

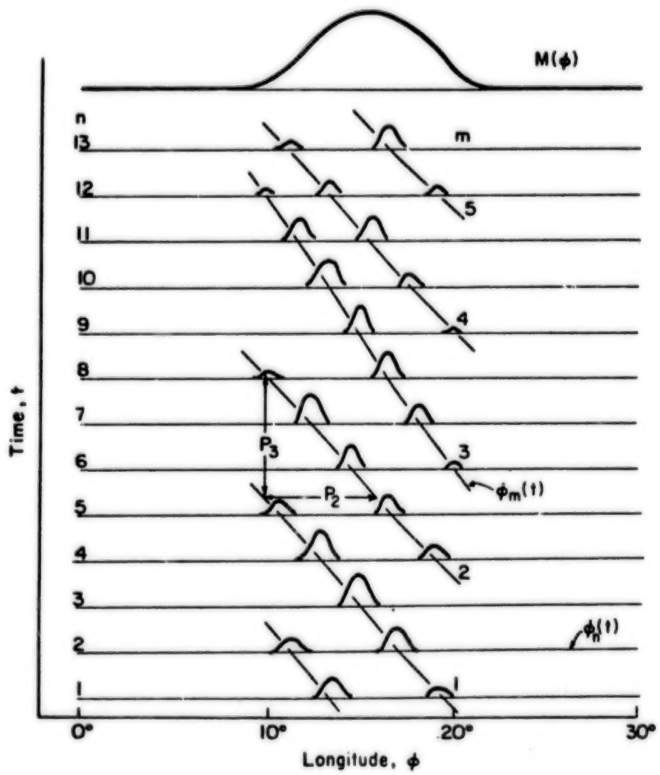

Figure II-8. Drifting subpulses. A schematic of the data from a pulsar with drifting subpulses (source: Backer, 1973).

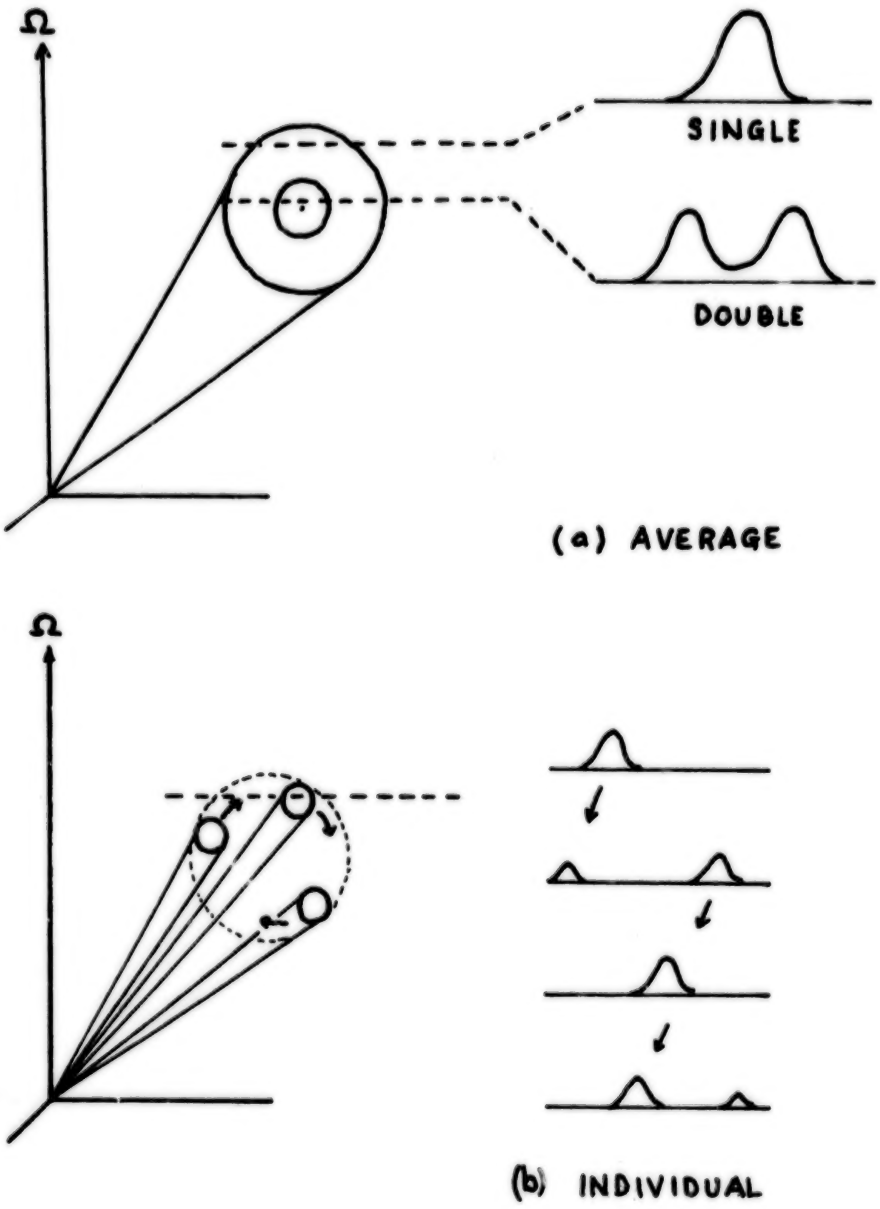

Figure II-9. (a) Hollow-cone beam model. (b) One two-dimensional beam pattern which is consistent with many of the observational details discussed in this section and the section on average waveforms.

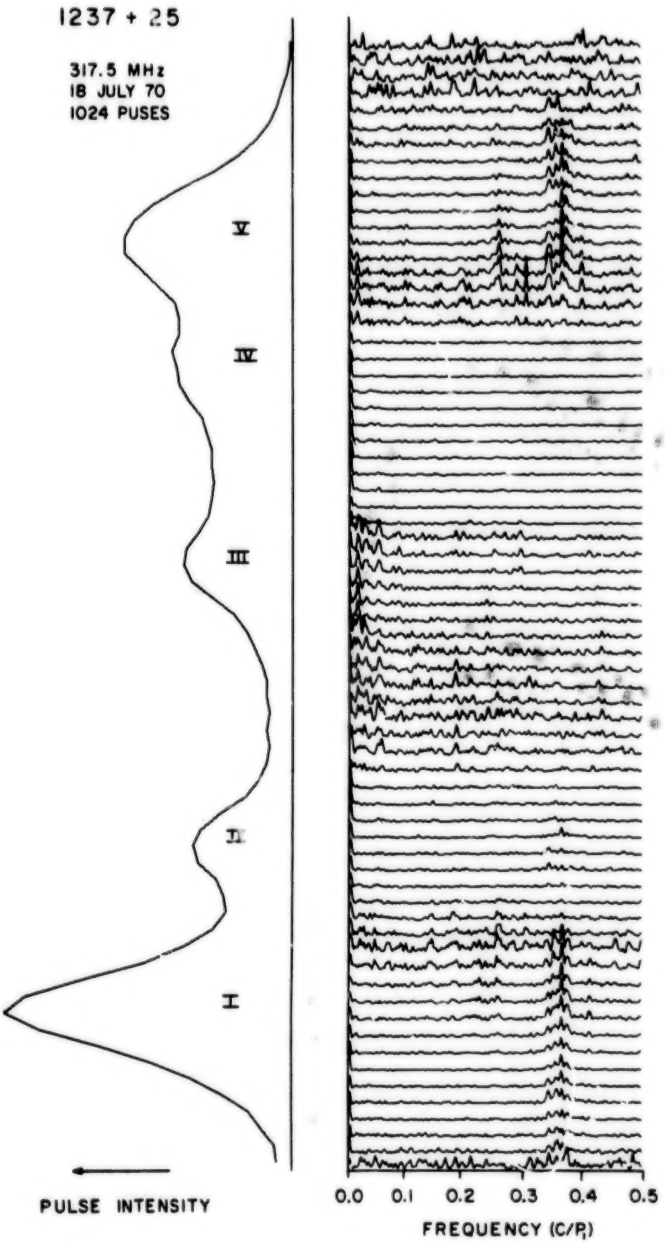

Figure II-10. Fluctuation waveform. A sequence of fixed-longitude fluctuation spectra (right) obtained from the sequence of longitudes whose average intensities are plotted to the left. Five components are noted in Roman numerals. The data display a remarkable mirror symmetry about the midpulse point (source: Backer, 1973).

where h is the frequency of occurrence histogram of intensities at longitude ϕ_j and N is the number of pulses analyzed. An example of p_{kj} is given in Figure 11 for PSR 0950 + 08. From these two summaries of intensity fluctuations, one can form simple waveforms of the rms intensity fluctuation about the mean:

$$\sigma(\phi_j) = \left[\sum_k (I_k - \langle I_{jk} \rangle_k)^2 \, p(I_k | \phi_j) \right]^{1/2}, \tag{14}$$

$$\sigma(\phi_j) = \left[\sum_k P(f_k, \phi_j) \right]^{1/2} \tag{15}$$

In addition one can form "fractional" rms measures from P_{kj} by summing over only one of the several elements of fluctuation mentioned above; e.g. σ_{red}, σ_{white}, $\sigma_{feature}$. Finally, it is possible to use the phase information in the transform $\mathcal{S}(f_{kj}\, \phi_j)$ near $f_k \simeq 1/P_3$ to quantize the most regular drifting-subpulse patterns.

Pulsar radiation has strong elliptical polarization. The polarization state of individual pulses – $Q(\phi_j, t_k)$, $U(\phi_j, t_k)$, and $V(\phi_j, t_k)$ – is *not* identical to the average state multiplied by the variable total intensity waveform. Variations in linear polarization $A(\phi_j, t_k) = (Q^2(\phi_j, t_k) + U^2(\phi_j, t_k))^{1/2}$ range from a minimum of about 30% about the mean to a total range of 0% to 100%. The polarization angles

$$\theta(\phi_j, t_k) = \frac{1}{2} \tan^{-1} \left(\frac{U(\phi_j, t_k)}{Q(\phi_j, t_k)} \right) \tag{16}$$

often fluctuate 30° about the most probable values, *with*, however, a small probability of being 90° ± 20° away. There are objects, or regions of objects, which have a nearly random angle distribution. And the circular polarization may fluctuate by 30% about the mean, which is most frequently less than 30%. Figure 12 is an extension of the histogram analysis mentioned above to the polarization state for PSR 0525 + 21. Moving across the displays one finds j, ϕ_j with 360° = P_1, the total intensity $\langle I \rangle = \langle I(\phi_j, t_k) \rangle_k$; the vector-averaged linear polarization $P_\perp = (\langle Q(\phi_j, t_k) \rangle_k^2 + \langle U(\phi_j, t_k)_k \rangle^2)^{1/2}$; the average linear

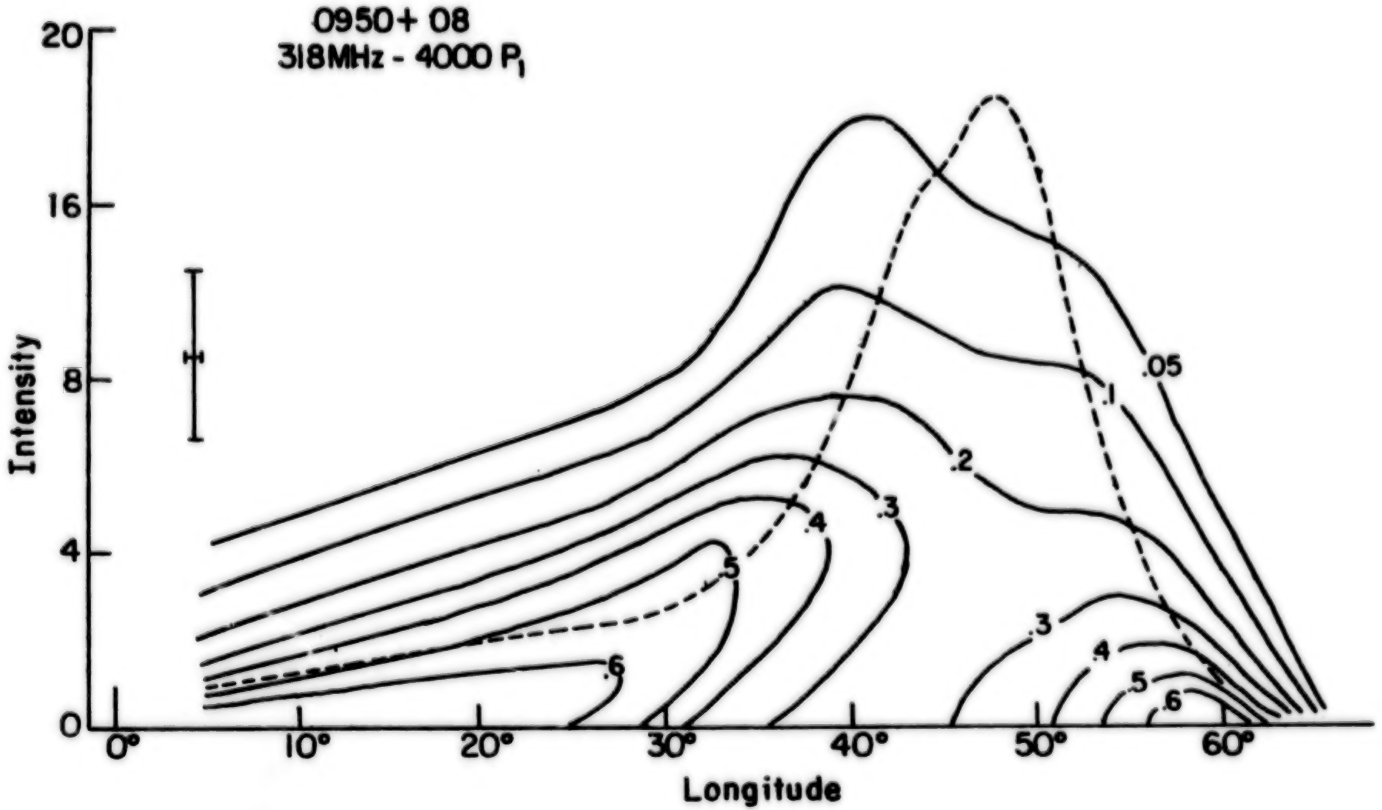

Figure II-11. Fluctuation waveform. Probability density map of data from PSR 0950 + 08. The cell size for the probabilities is given by the error bars to the left. The average profile is indicated by the dashed line.

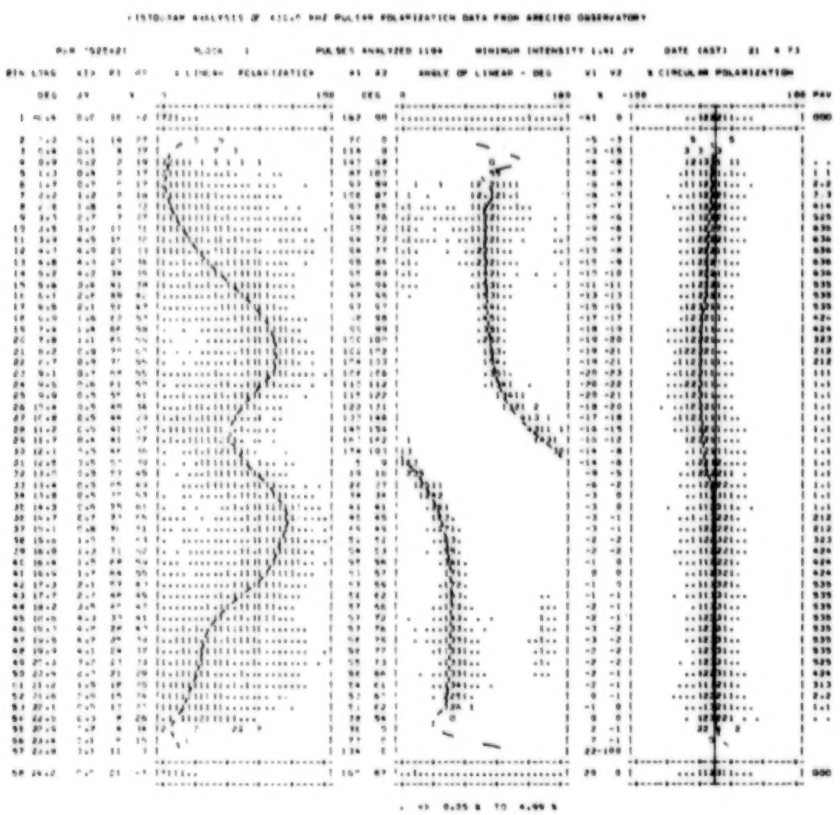

Figure II-12. Fluctuation waveform. Probability density "map" of the polarization data from PSR 0525 + 21.

polarization P2 = $\langle (Q^2(\phi_j, t_k) + U^2(\phi_j, t_k))^{1/2} \rangle_k$, an intensity map of the probability of linear polarization with an overlay of the vector-averaged quantities; the analagous quantities for the polarization angle and the circular polarization; and ten times the fraction of data at ϕ_j which was above a threshold suitable for including the data in the three probability maps.

The most striking property of the individual pulse polarization data is the double-valued angle state at angles differing by nearly 90°. It is the relative probabilities of these two states which often lead to the complex polarization angle waveforms mentioned in the Average Waveform section. By taking these two states into account, we find that the monotonic angle rotation across the pulse is common to *most* objects – giving further support to the hollow-cone emission beam model. In addition, we find that (a) in many cases the occurrence of the two angle states in the data has a pattern bearing

a fixed relationship to the correlated subpulse phenomena mentioned above; (b) the transition between angle states in an individual pulse is very rapid and at a point of low linear polarization; and (c) the two states often occur with opposite senses of circular polarization.

There is no physical explanation for this phenomenon at present. The data suggest a subpulse beam with positive and negative lobes of linear and circular polarization, with the linear polarization solely in one Stokes parameter (see the discussion of Stokes parameters in Average Waveform section). If this beam drifts as described above and shown in Figure 13 for the drifters and objects with periodic subpulse patterns, and has a fixed orientation for other objects, then we can satisfactorily model the polarization data. It is curious that the hypothetical beam is precisely the beam of an ultra-relativistic charge accelerated along a circle with the *symmetric* linear Stokes parameter attenuated. While Stokes parameters are a convenient parametric expression of the state of polarization of radiation for calculations of radiative transfer (Chandrasekhar, 1963), they do not constitute orthogonal modes of the radiation. However, guided by the observational requirement of a single linear-polarization Stokes parameter, one needs to look for radiative processes that emit or, very importantly, perhaps amplify, one or the other orthogonal components of the electric field depending on the orientation within the total-intensity beam. Finally, we note that the polarization transition described above is a rapid reflection of the polarization state through the origin of the Poincaré sphere (whose Cartesian axes are Q, U and V).

Now for one final increase in time resolution – by about two orders of magnitude – to $10^{-5}\ P_1$. In a number of objects one finds another regime of deep fluctuations, micropulses, with a typical time scale, determined from autocorrelation analysis, of 100 μs:

$$t_{\mu\text{pulse}} \simeq 10^{-4}\ P_1. \tag{17}$$

Statistical analyses of this form of data have found it to be consistent with nearly random Gaussian noise amplitude-modulated by the subpulse pattern. The "nearly" used above is a qualification needed because in PSR 2016 + 28 there are often periodic micropulses with $P_5 \simeq 1$ ms ($P_4 \simeq DP_1 = P_3P_1/P_2$ is the time for drifting subpulses to cycle around the star *if* that is their orbit and *if* P_2 and P_3 are constant along the orbit). The simple picture for micropulses is either individual coherent emissions or random interference between independent coherent emissions. There is little information at present on the polarization properties of micropulses.

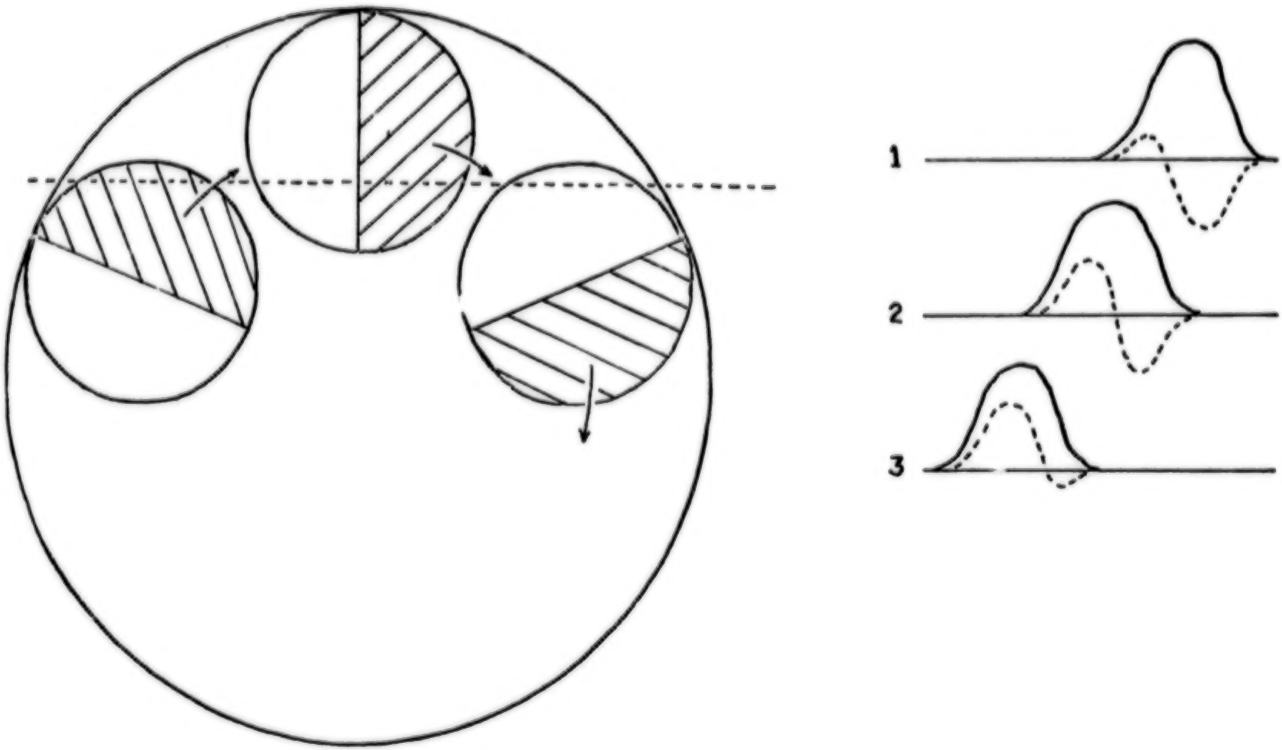

Figure II-13. Hollow-cone beam model; see caption of Figure II-9. Here we have added polarization lobes – positive (blank) and negative (hatched) – to the subpulses with a fixed orientation with respect to the position angle of the cone axis.

INTERSTELLAR MEDIUM

The interstellar medium contains three components which affect pulsar radiation: thermal electrons, a weak magnetic field, and neutral hydrogen. In a few objects there is or may be a circumstellar cloud of electrons and field, but in general such an effect is not important and it will not be discussed further here. The thermal electrons alter the group velocity of the radiation, yielding a dispersed signal. The arrival time of the pulse is given by

$$t_a \sim 0.4\ \mathrm{DM}\ \nu_8^{-2} \tag{18}$$

relative to infinite frequency where ν_8 is the signal frequency in units of 10^8 Hz and DM is thermal electron column density in units of electrons pc cm^{-3}

$$\mathrm{DM} = \int_{\text{earth}}^{\text{PSR}} n_e\, d\ell. \tag{19}$$

This signal dispersion necessitates either the use of narrow bandwidths to obtain 10^{-3} P_1 resolution for the studies described in previous sections,

$$B \simeq 0.12\, P_1\, \nu_8^3\ \mathrm{DM}^{-1}\ \mathrm{MHz}, \tag{20}$$

or a multi-bandwidth "antidispersion" device. Dispersion sets a time resolution limit on direct observations of micropulses of

$$\left|\frac{dt_a}{d\nu}\right| B_0 \simeq 1/B_0, \tag{21}$$

$$B_0^2 \simeq 2.4 \times 10^{-4}\, \nu_8^3\ \mathrm{DM}^{-1}\ \mathrm{MHz}^2.$$

Micropulse studies mentioned in the previous section used antidispersion techniques to explore the radiation down to 10μs ($B_0 \sim 100$ KHz) at $\nu_8 \sim 1$ The column densities measured by pulse dispersion have led to a revision of the astronomer's understanding of the interstellar medium.

In a dilute plasma threaded by a weak magnetic field the orthogonal propagation modes of electromagnetic radiation are circularly polarized. The phase velocities of the two modes differ by minute amounts and, as a result, the polarization angle rotates with decreasing frequency. The rate of rotation is called the rotation measure

$$\frac{d\theta}{d\lambda^2} = RM = 0.81 \int_{earth}^{PSR} B_{||}\ n_e\ d\ell. \qquad (22)$$

where $B_{||}$ is the component of the interstellar magnetic field directed toward the observer in microgauss. The ensemble of pulsar rotation measures have been used to investigate the large scale structure of the galactic magnetic field.

It has been known for many years that the interstellar gas is not homogeneous. There are arms (spiral or otherwise), isolated clouds of dust which absorb optical radiation at Doppler-shifted frequencies of atomic lines, and clouds of neutral hydrogen which emit and absorb at frequencies near 1420 MHz. Within a year after pulsars were discovered it was clear that the electron gas in the interstellar medium was perturbed by parts in 10^2 on a scale of 10^{11} cm, ten orders of magnitude smaller than the neutral clouds known previously. The observation that led to this understanding was the existence of deep modulation of the pulsar emission over a scale of many kHz at meter wavelengths which persisted for a thousand periods. Recall that this modulation was neglected in the preceding section. Without any further information, this observation led one to think of diffraction effects from scattered radiation rather than properties of the coherent emission mechanism. The straightforward dimensional analysis of the phenomenon led to the prediction of strong frequency dependences of the spectral and temporal scale lengths of the modulation, as well as a number of associated phenomena.

Envision a layer of thickness Z filled with minute perturbations of size *a* and electron density deviation δn. From a random walk argument the rms perturbation of the phase of a wavefront will be

$$\delta\phi \propto \left(\frac{Z}{a}\right)^{1/2} \delta n\, \lambda. \qquad (23)$$

At meter wavelengths $\delta\phi$ is many radians. This will scatter the radiation by the angle

$$\delta\theta \propto \lambda/\ell_\phi \qquad (24)$$

where ℓ_ϕ is the typical distance over which the phase differs by a radian, roughly $a/\delta\phi$, and produce a Fraunhofer diffraction pattern at distances

$$Z > \ell_\phi/\delta\theta = \ell_\phi^2/\lambda. \qquad (25)$$

The delay between direct and scattered radiation is

$$\tau_b \propto Z\,\delta\theta^2 = Z\,\lambda^2\,\ell_\phi^{-2}, \tag{26}$$

which can become observable at meter wavelengths. Since $\delta\phi >> 1$, ℓ_ϕ scales as λ^{-1} and hence $\tau_b \propto \lambda^4$. Recall the mention in the introduction that the Crab nebula pulsar was known as a compact *continuum* source at decametric wavelengths, due to scattering, in the years before the pulsar discovery. Adding random phase data together with delays of τ_b will result in destructive interference with a scale

$$B_s \propto 1/\tau_b. \tag{27}$$

Now if we allow the configuration of pulsar, irregular medium, and observer to change slowly because of relative velocities, the diffraction viewed by an observer with a narrow bandwidth ($B < B_s$) receiver will change in a time

$$\tau_s \approx \ell_\phi / v_t, \tag{28}$$

where v_t is the transverse component of the velocity of the line of sight relative to the scattering medium. As mentioned above, ℓ_ϕ scales as λ^{-1} and hence $\tau_s \propto \lambda^{-1}$. The frequency dependences of $\delta\theta$, τ_b, B_s, and τ_s from these simple dimensional arguments have been observed. If the neutral electrons are uniformly distributed in the interstellar medium and if $\delta n/n$ is constant everywhere, then the scattering observables should scale with dispersion measure, $Z \propto DM$. However, the observed dependences of τ_s and B_s (or τ_b) are stronger functions of dispersion measure than are predicted.

$$\begin{aligned} \tau_s &\propto DM \qquad \text{not} \qquad DM^{1/2}, \\ B_s &\propto DM^{3\text{-}4} \qquad \text{not} \qquad DM^2 \end{aligned} \tag{29}$$

It is suggested that Z *is* proportional to DM, but that δn grows with Z because of the growing probability of encountering ever stronger perturbations of electron density as a line of sight extends into the interstellar medium. The quantity $(Z/a)^{1/2}\,\delta n$ is a measure of the scattering.

At meter wavelengths experiments with observatories spaced by $10^{8\text{-}9}$ cm have been performed to attempt a measurement of the drift velocity v_t of the diffraction pattern since ℓ_ϕ is near $10^{9\text{-}10}$ cm. These experiments have not been very successful owing to the short length of recordings (measured in units of τ_s) and to instabilities in the pattern indicating that the medium

rearranges itself within a few τ_s. The experiments do indicate velocity components v_t as high as 300 km s^{-1}, although a typical value is 50 km s^{-1}. These velocities are consistent with the hypothesis that pulsars receive a momentum impulse at birth from an asymmetric explosion, a binary disruption, or radiation reaction.

At frequencies near 1420 MHz pulsar signals are absorbed by neutral hydrogen clouds along the line of sight. A comparison of absorption spectrum features to emission spectrum features, observed when the pulsed signal is zero, leads to distance estimates for a pulsar based on a velocity model for the galaxy. Distance estimates from neutral hydrogen measurements – and, for the Crab nebula pulsar, from properties of the nebula – provide a crude calibration of the dispersion measure-distance relation. Further precision in the DM-Z relation must await parallax measurements using long-baseline interferometry.

By using the present cude DM-Z relation we can explore the space distribution of pulsars. This is given in Figures 14 and 15, scatter plots in cartesian galactic coordinates X and Y and X and Z. One finds a distribution in Z of ±150 pc and a general confinement to the inner 12 kpc of the galaxy.

CONCLUSION

We have covered most of the territory mapped out by radio astronomers since 1968. We have omitted, unfortunately, the large amount of theoretical work done on the magnetosphere electrodynamics and internal solid state physics of rapidly rotating, highly magnetized compact stars. At the present level of mathematical sophistication, much of this work has been unable to relate to the details of pulsar radiation. The results of more speculative theoretical work have been included in the preceding sections.

Where are we going? In the coming years we will have firmer knowledge of the space distribution and motion of pulsars. Sensitive surveys are being conducted to find new objects, and long-baseline-interferometry studies have begun to determine proper motions and parallaxes. These results as well as complementary studies of X-ray stars (see the discussion in following chapters) will tie pulsars into the overall picture of stellar evolution in the galaxy. While every form of statistical analysis has not been attempted on pulsar radiation, it is not clear that the specification of more details of subpulse phenomena is in order, with the important exception of curious polarization effects. Certainly the micropulse phenomenon is worth further probes

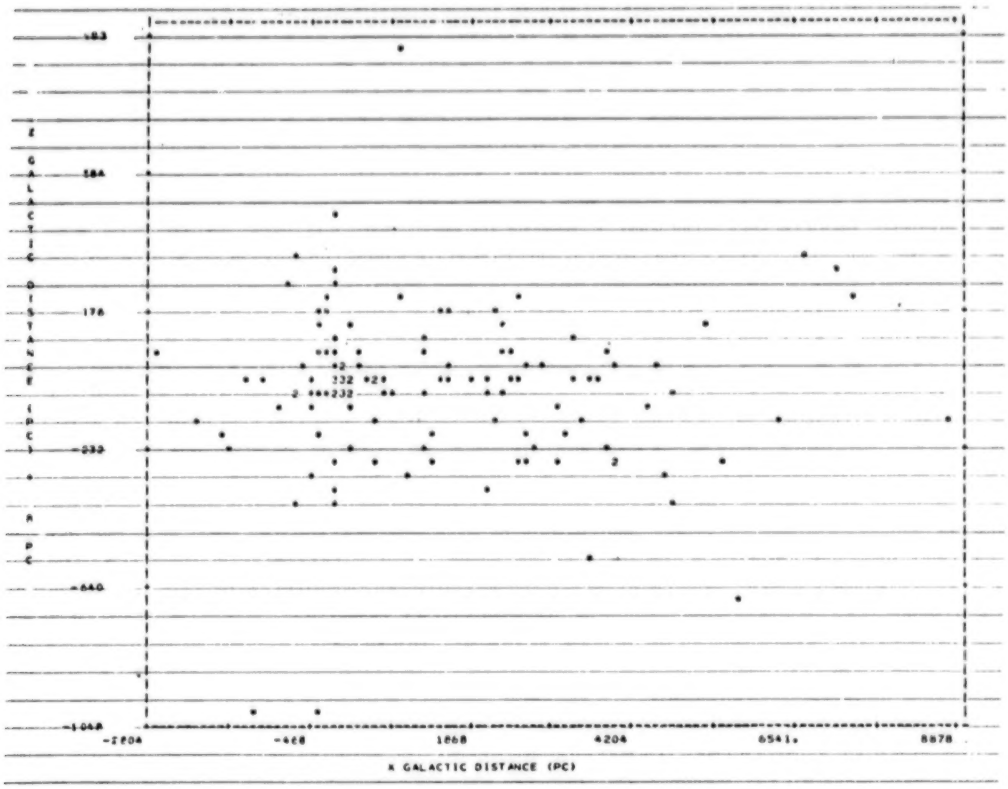

Figure II-14. Spatial distribution. Scatter plot of pulsars in X and Z galactic cartesian coordinates using the pulsar dispersion measures and a model of the galactic electron gas to obtain radial distances.

44.

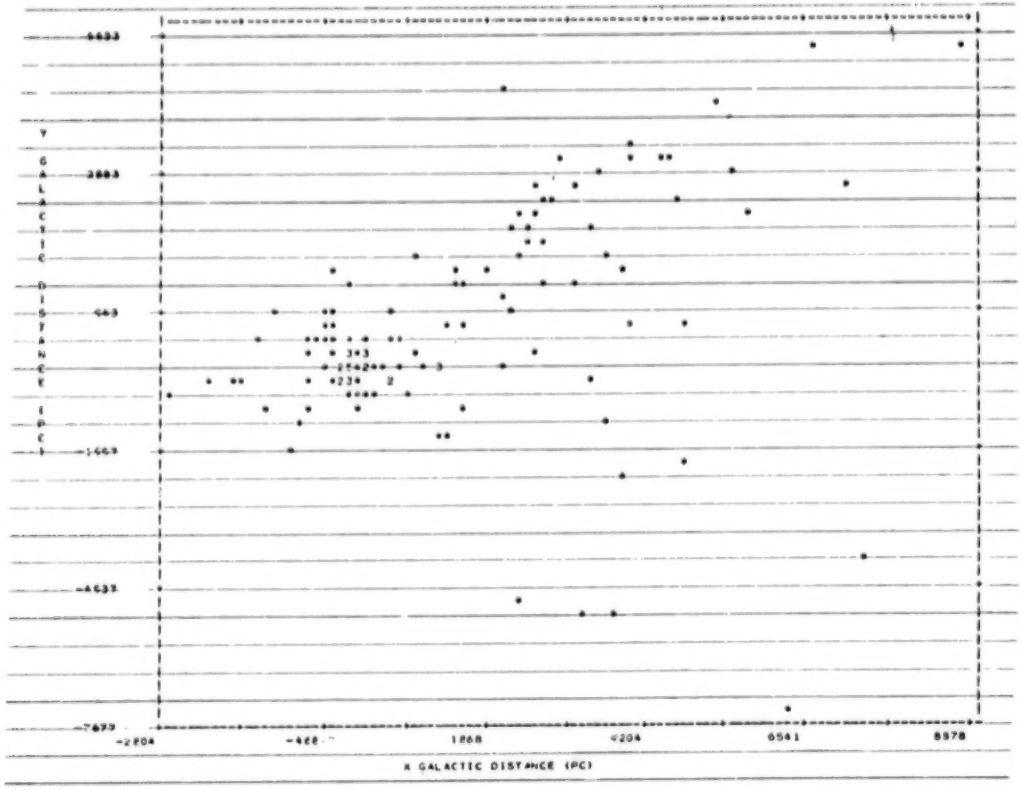

Figure II-15. Spatial distribution. Scatter plot of pulsars in X and Y galactic cartesian coordinates.

to assess its "true" character; of particular importance in this regard is an investigation of the polarization properties of micropulses. In at least one object, PSR 2016 + 28, there is an indication of a polarization signature to the micropulses within a subpulse – a fact which suggests that the micropulse is a beam of radiation, and not merely random amplitude modulation within the subpulse envelope. By dealing with the properties of individual beams, it seems that the observers and theoreticians may be able to make progress in communicating with each other.

It is clear also that in the coming years we will have a better understanding of the interstellar medium through "column measure" observations of pulsars, combined with parallax determinations, high energy photon observations of the interstellar medium (Hα, UV etc), and theoretical work. With pulsar proper motions and parallaxes in hand, we can return to doing scattering diffraction pattern studies and hope to isolate medium effects from pulsar transverse velocity effects.

Following is a short bibliography; further references may be found in the review articles in Table II-1 or in the NASA/STAR volumes. Appendix A of this chapter is a listing of data on 147 pulsars kindly provided by Y. Terzian.

SHORT TOPICAL BIBLIOGRAPHY

Introduction

(see review articles in Table 1)
(also two volumes of early Nature letters and articles entitled Pulsars)

Spin Properties

Boynton, P. E., Groth, E. J., IIP, Partridge, R. B., and Wilkinson, D. T., 1969, Ap. J. 157, L197 (Crab).
Hunt, G. C., 1971, MNRAS, 153, 119.
Manchester, R. N., and Peters, W. L., 1972, Ap. J., 173, 221.
Manchester, R. N., and Taylor, J. H., 1974, Ap. J., 191, L63.
Papaliolios, C., Carleton, N. P., and Horowitz, P., 1970, Nature, 228, 445,
Reichley, P. E., Downs, G. S., and Morris, G. A., 1970, Ap. J. (Letters), 159, L35.
Reichley, P. E., and Downs, G. S., 1971, Nature P. S., 234, 48 (Vela).
Richards, D. W., Rankin, J. M., and Zeissig, G. A., 1974, Nature, 251, 37.

Average Waveform

Backer, D. C., 1976, to be pub. in Ap. J., November, 1976.
Backer, D. C., Boriakoff, V., and Manchester, R. N., 1973, Nature P.S., 243, 77.
Komesaroff, M. M., Morris, D., and Cooke, D. J., 1970, Ap. Letters, 5, 37.
Lyne, A. G., Smith, F. G., and Graham, D. A., 1971, MNRAS, 153, 337.
Manchester, R. N., 1971, Ap. J. (Suppl.) 23, 283.

Radio Spectrum

Backer, D. C., and Fisher, J. R., 1974, Ap. J., 189, 137.
Backer, D. C., and Fisher, J. R., 1976, in preparation.
McLean, A. I. O., 1973, MNRAS, 165, 133.
Sieber, W., 1973, Astron. Astrophys., 28, 237.

Fluctuation Waveform

Backer, D. C., 1973, Ap. J., 182, 245.
Backer, D. C., Rankin, J. M., and Campbell, D. B., 1976, Nature, 263, 202.
Hankins, T. H., 1972, Ap. J. (Letters), 177, L11.
Huguenin, G. R., Taylor, J. H., and Helfand, D. J., 1973, Ap. J., 181, L139.
Manchester, R. N., Taylor, J. H., and Huquenin, G. R., 1975, Ap. J., 196, 83.
Rankin, J. M., Campbell, D. B., and Backer, D. C., 1974, Ap. J., 188, 609.
Taylor, J. H., and Huguenin, G. R., 1971, Ap. J., 167, 273.
Taylor, J. H., Manchester, R. H., and Huguenin, G. R., 1975, Ap. J., 195, 513.

Interstellar Medium

Backer, D. C., 1975, Astron. Astrophys., 43, 395 (Scattering).
Gomez-Gonzalez, J., and Guelin, M., 1974, Astron. Astrophys., 32, 441 (HI).
Gordon, K. J., and Gordon, C. P., 1973, Astron. Astrophys., 27, 119 (HI).
Gordon, K. J., and Gordon, C. P., 1975, Astron. Astrophys., 40, 27 (HI).
Komesaroff, M. M., Hamiton, P. A., and Ables, J. G., 1972, Aust. J. Phys. 25, 759, (Scattering).
Lang, K. R., 1971, Ap. J., 164, 249 (Scattering).
Lazareff, B., 1975, Astron. Astrophys., 42, 25 (HI).
Manchester, R. N., 1972, Ap. J., 172, 43 (RM, DM).
Mutel, R. L., Broderick, J. J., Carr, T. D., Lynch, M., Desch, M., Warnock, W. W., and Klemperer, W. K., 1974, Ap. J., 193, 279 (Scattering).
Rickett, B. J., 1970, MNRAS, 150, 67 (Scattering).
Salpeter, E. E., 1969, Nature, 221, 31 (Scattering).
Scheuer, P. A. G., 1968, Nature, 218, 920, (Scattering).

Slee, O. B., Ables, J. G., Batchelor, R. A., Krishna-Mohan, S., Venugopal, V. R., and Swarup, G., 1974, MNRAS, 167, 31 (Scattering).
Sutton, J. M., 1971, MNRAS, 155, 51 (Scattering).

Evolution and Models

Backer, D. C., and Sramek, R. A., 1976, A. J., 81, 430.
Ginzburg, V. L., and Zheleznyakov, V. V., 1970, Comments Ap. Sp. Sci., 2, 167.
Huguenin, G. R., Manchester, R. N., and Taylor, J. H., 1971, Ap. J., 169, 97.
Hulse, R., and Taylor, J. H., 1975, Ap. J. (Letters), 195, L51.
Prentice, A. J. R., and ter Haar, D., 1969, MNRAS, 146, 423.
Manchester, R. N., Taylor, J. H., and Van, Y. Y., 1974, Ap. J. (Letters), 189, L119.

APPENDIX II-A

LISTING OF DATA ON 147 PULSARS

VERVANT TERZIAN NAIC AND CASA CORNELL UNIVERSITY *PULSARS* JULY 1,1975 TOTAL NUMBER= 147 PAGE 1

PULSAR DESIGNATION	PULSAR	R.A. H.M.S.	DECL. DEG.	'	"	L II DEG.	B II DEG.	PERIOD (SEC)	EPOCH (J.D.24+)	1/2 PULSE WIDTH (MSEC)	DISPERSION MEASURE (PARSEC/CM3)	PERIOD CHANGE (NSEC/DAY)	APP.AGE P/(DP/DT) (YRS)	REFERENCES
P0031-07	MP0031	0 31 34	-07 38 26			110.4	-49.8	0.9429507566	40690	51	10	0.0366	7.1E+07	3
P0105+65	PSR0105+65	1 05 00	65 50 00			124.6	3.3	1.2836506982	42006	(29)	30	1.074	3.3E+06	11,17
P0138+59	PSR0138+59	1 38 20	59 52 00			129.1	-2.3	1.2229480053	42006	35	35	(0.015)	(2.2E+08)	10,16,17
P0153+61	PSR0153+61	1 53 0C	61 55 00			130.5	0.2	2.3516185238	42006	(43)	60	16.358	3.9E+05	11,17
P0254-54	MP0254	2 54 24	-54			270.9	-54.9	0.4476	(41347)	10	10			3
P0301+19	PSR0301+19	3 01 42	19 21 12			161.1	-33.3	1.3875835779433	41544	27	16	0.1118	3.4E+07	2,10
P0329+54	CP0329	3 29 11	54 24 38			145.0	-1.2	0.714518642+4	40622	6	27	0.177	1.1E+07	3
P0355+54	PSR0355+54	3 55 00	54 05 00			148.2	0.8	0.1563802120	42006	4	57	0.379	1.1E+06	9,16,17
P0450-18	MP0450	4 50 22	-18 04 14			217.1	-34.1	0.5489359406	41639	19	40	0.363	4.0E+06	3,7,10
P0525+21	MP0525	5 25 52	21 58 18			183.8	-6.9	3.7454934468	40957	181	51	3.461	2.9E+06	3,10
P0531+21	MP0531	5 31 31	21 58 55			184.6	-5.8	0.0331296454	41221	3	57	36.926	2.5E+03	3
P0540+23	PSR0540+23	5 40 07	23 28 15			184.4	-3.3	0.2459851594092	41709	10	72	1.333	5.1E+05	2,9,11
P0611+22	PSR0611+22	6 11 16	22 31 42			188.8	2.4	0.3349190191183	41709	6	97	5.161	1.8E+05	2,9,10
P0628-28	PSR0628-28	6 28 51	-28 34 08			237.0	-16.8	1.2444148959981	40242	(50)	34	0.217	1.6E+07	3
P0736-40	MP0736	7 36 51	-40 35 18			254.2	-9.2	0.376918586	41639	22	161	<1.728	>5.9E+05	3,7
P0740-28	PSR0740-28	7 40 48	-28 15 16			243.8	-2.6	0.1667511118	41639	8	74	1.443	3.1E+05	3,7
P0809+74	CP0809	8 09 03	74 30 10			140.0	31.6	1.2922612052	40689	41	6	0.0138	2.5E+08	3
P0818-13	MP0818	8 18 06	-13 41 23			239.9	12.6	1.2381282107?6	41006	22	41	0.1820	1.9E+07	3,10
P0823+26	AP0823+26	8 23 51	26 47 18			197.0	31.7	0.5306595999042	40242	6	19	0.144	1.0E+07	3
P0833-45	PSR0833-45	8 33 39	-45 00 19			263.6	-2.8	0.089210747?9	40307	2	69	10.823	2.3E+04	3,15
P0834+06	CP0834	8 34 26	06 20 47			219.7	36.3	1.2737634?9759	40626	24	13	0.587	5.9E+06	3
P0835-41	MP0835	8 35 34	-41 24 54			260.9	-8.3	0.7514208897	41639	10	148			3,7
P0904+77	PSR0904+77	9 04	77 40			135.3	33.7	1.57905	(40222)	<80				3
P0940-55	MP0940	9 40 40	-55 30			278.5	-2.1	0.6643868	(41835)	30	149			3,13
P0943+10	PP0943	9 43 27	10 05 50			225.4	43.1	1.09770363972	41666	50	15	0.3052	9.9E+06	2,3
P0950+08	CP0950	9 50 31	08 09 43			228.9	43.7	0.2530650?317	40622	9	3	0.0198	3.5E+07	3
P0959-54	MP0959	9 59 51	-54 37			280.1	0.3	1.436951	40553	50	131			3,7
P1055-51	MP1055-51	10 55 49	-51 40			286.0	7.0	0.1971065	(41347)		24			3,7
P1112+50	PSR1112+50	11 12 49	50 46 30			154.4	60.4	1.65645381814	42006	18	9	0.224	2.2E+07	9,10,17
P1133+16	CP1133	11 33 28	16 07 33			241.9	69.2	1.187911144405	40622	28	5	0.323	1.0E+07	3
P1154-62	MP1154	11 54 45	-62 08 36			296.7	-0.2	0.400520293	41639		267			3,7
P1221-63	PSR1221-63	12 21 4C	-63 47			300.0	-1.3	0.216475	(41835)		92			6
P1237+25	AP1237+25	12 37 12	25 10 17			252.2	86.5	1.382448571?5	40626	50	9	0.0825	4.6E+07	3
P1240-64	MP1240	12 40 20	-64 07 12			302.1	-1.6	0.3884790	(41347)	60	297			3,7
P1323-62	PSR1323-62	13 23 42	-62 03			307.1	0.3	0.529054	41733		310			6
P1354-62	PSR1354-62	13 54 10	-62 13			310.5	-0.6	0.4355740	41733		400			6
P1359-50	MP1359	13 59 43	-50			314.5	11.0	0.690	(40585)	20	20			3
P1426-66	MP1426	14 26 34	-66 09 54			312.3	-6.3	0.7854625	(41347)	10	65			3,7
P1449-65	MP1449	14 49 22	-65			315.3	-5.3	0.17940353	41639	(5)	71			3,7
P1451-68	PSR1451-68	14 51 29	-68 32			313.9	-8.6	0.263376771	41639	25	9	<0.259	>2.8E+06	3,7
P1508+55	MP1508	15 08 04	55 42 56			91.3	52.3	0.739677876?0	40626	10	20	0.433	4.7E+06	3
P1530-53	MP1530	15 30 23	-53 30			325.7	1.9	1.368881	40553	25	25			3,7
P1541+09	PSR1541+09	15 41 14	09 38 48			17.8	45.8	0.7484481888	42006	63	35	(0.038)	(5.4E+07)	3,17
P1556-44	MP1556	15 56 12	-44 31 30			334.5	6.4	0.2570553	(41347)		59			3,7
P1557-50	PSR1557-50	15 57 05	-50 36			330.7	1.6	0.194598	(41835)		270			6

YERVANT TERZIAN NAIC AND CASA CORNELL UNIVERSITY *PULSARS* JULY 1, 1975 TOTAL NUMBER= 147 PAGE 4

PULSAR DESIGNATION	PULSAR	R.A. H.M.S.	DECL. DEG. ' "	L II DEG.	B II DEG.	PERIOD (SEC)	EPOCH (J.D.24+)	1/2 PULSE WIDTH (MSEC)	DISPERSION MEASURE (PARSEC/CM3)	PERIOD CHANGE (MSEC/DAY)	APP.AGE P/(DP/DT) (YRS)	REFERENCES
P1558-50	PSR1558-50	15 58 46	-50 49	330.7	1.3	0.864192	41733		165			6
P1601-52	PSR1601-52	16 01 58	-52 56	329.7	-0.6	0.675953	41733		30			6
P1604-00	MP1604	16 04 38	-00 24 41	10.7	35.5	0.421816075 79	41005	15	11	0.0265	4.4E+07	3,10
P1641-45	PSR1641-45	16 41 11	-45 53 33	339.2	-0.2	0.455052	41733		450			6
P1642-03	PSR1642-03	16 42 24	-03 12 31	14.1	26.1	0.387688779 65	40622	4	34	0.154	6.9E+06	3,16
P1700-32	PSR1700-32	17 00 00	-32 40 00	351.7	5.4	1.211784686 4	42005		103	0.059	5.6E+07	8,17
P1703-18	MP1700-18	17 00 56	-18	4.0	14.0	0.802	(41347)		<40			3
P1706-16	MP1706	17 06 33	-16 37 21	5.8	13.7	0.653050454 37	40622	12	25	0.550	3.3E+06	3
P1717-29	PSR1717-29	17 17 10	-29 32 00	356.5	4.3	0.620447906 9	42005	(32)	45	0.065	2.6E+07	11,17
P1718-32	PSR1718-32	17 18 40	-32 05 00	354.5	2.5	0.477157098 7	42005	(35)	120	0.059	2.2E+07	11,17
P1727-47	MP1727	17 27 50	-47 42 18	342.6	-7.6	0.829699077	41639	30	122	15.55	1.4E+05	3,7
P1730-22	PSR1730-22	17 30 15	-22 29 00	4.0	5.8	0.871682858 5	42005		45	(0.002)	(1.2E+09)	8,17
P1742-30	PSR1742-30	17 42 45	-30 43 00	358.5	-1.0	0.367421488 6	42005		84	0.921	1.1E+06	6,17
P1747-46	MP1747	17 47 56	-46 56 12	345.0	-10.2	0.742351809	41639	20	21	6.05	3.3E+05	3,7
P1749-28	PSR1749-28	17 49 49	-28 06 01	1.5	-1.0	0.562553168 299	40127	6	51	0.705	2.2E+06	3
P1754-24	PSR1754-24	17 54 37	-24 21 00	5.3	0.0	0.234091	(42200)		188			1
P1813-26	PSR1813-26	18 13 10	-26 50 00	5.2	-4.8	0.592885148 3	42005		90	(-0.025)		8,17
P1818-04	MP1818	18 18 14	-04 29 03	25.5	4.7	0.598072621 83	40622	10	84	0.545	3.0E+06	3
P1819-22	PSR1819-22	18 19 50	-22 53 00	9.4	-4.3	1.87426779 52	42005	(76)	140	0.050	1.0E+08	11,17
P1822-09	PSR1822-09	18 22 40	-09 36 00	21.4	1.3	0.768950592 1	42004	11	19	4.512	4.7E+05	10,17
P1826-17	PSR1826-17	18 26 15	-17 54 00	16.6	-3.3	0.307129250 1	42005	(59)	207	0.483	1.7E+06	11,16,17
P1831-03	PSR1831-03	18 31 00	-03 40 00	27.7	2.3	0.686676834 3	42004	(32)	235	3.582	5.3E+05	10,11,17
P1831-04	PSR1831-04	18 31 40	-04 31 00	27.0	1.8	0.290108159 9	42004		68	(0.009)	(8.8E+07)	8,17
P1845-04	PSR1845-04	18 45 10	-04 05 32	28.9	-1.0	0.597738993 7	42004	20	142	4.480	3.7E+05	3,17
P1845-01	PSR1845-01	18 45 30	-01 27 00	31.3	0.1	0.659428490 0	42005	(80)	163	0.453	4.0E+06	3,5,17
P1846-06	PSR1846-06	18 46 07	-06 43 00	26.7	-2.4	1.451292705 0	42005	(38)	152	3.949	1.0E+06	11,17
P1857-26	PSR1857-26	18 57 44	-26 04 49	10.5	-13.5	0.612209076 5	42005	25	35	(0.014)	(1.2E+08)	3,17
P1859+03	JP1858	18 59 02	03 26 46	37.2	-0.6	0.655444707 516	41471	(170)	402	0.6482	2.8E+06	2,3
P1900+05	PSR1900+05	19 00 15	05 52	39.5	0.2	0.746568	(42314)	30	170			4
P1900-06	PSR1900-06	19 00 30	-06 35 00	28.5	-5.6	0.431884782 8	42005	(14)	180	0.298	4.0E+06	11,17
P1900+01	PSR1900+01	19 00 50	01 34 00	35.8	-1.9	0.729301559 39	42005		228	0.356	5.6E+06	8,17
P1901+10	PSR1901+10	19 01 40	10 00	43.3	1.8	1.856568	(42322)	90	120			1
P1904+12	PSR1904+12	19 04 57	12 40	46.7	2.3	0.827096	(42322)	30	260			1
P1906+09	PSR1906+09	19 06 40	09 10	43.2	0.3	0.830271	(42322)	45	240			1
P1906+00	PSR1906+00	19 06 45	00 05 00	35.1	-3.9	1.016945246 4	42005		111	0.467	6.0E+06	8,17
P1907+02	PSR1907+02	19 07 08	02 49 56	37.6	-2.7	0.499491370 926	41768	(11)	190	0.2386	5.7E+06	2,11
P1907+10	PSR1907+10	19 07 30	10 55 00	44.8	1.0	0.283638557 5	42004		144	0.232	3.3E+06	8,17
P1908+12	PSR1908+12	19 08 06	12 28	46.2	1.6	1.44173	(42322)	40	260			1
P1910+20	PSR1910+20	19 10 20	20 55 00	54.0	5.0	2.232496312 89	42006		84	0.825	7.4E+06	8,17
P1910+10	PSR1910+10	19 10 30	10 30	44.8	0.1	0.409338	(42322)	25	140			1
P1911+13	PSR1911+13	19 11 10	13 34 00	47.9	1.6	0.521472	(42314)	25	140			4
P1911-04	MP1911	19 11 15	-04 45 59	31.3	-7.1	0.825933665 03	(40624)	8	89	0.351	6.5E+06	3
P1911+09	PSR1911+09	19 11 30	09 30	44.0	-0.6	1.24197	(42322)	45	140			1
P1911+03	PSR1911+03	19 11 48	03 54	39.1	-3.2	2.3303	(42322)	480	35			1,14
P1911+11	PSR1911+11	19 11 57	11 15	45.6	0.2	0.600997	(42322)	20	90			1

VERVANT TERZIAN NAIC AND CRSR CORNELL UNIVERSITY *PULSARS* JULY 1,1975 TOTAL NUMBER= 147 PAGE 3

PULSAR DESIGNATION	PULSAR	R.A. H.M.S.	DECL. DEG.	L II DEG.	B II DEG.	PERIOD (SEC)	EPOCH (J.D.24+)	1/2 PULSE WIDTH (MSEC)	DISPERSION MEASURE (PARSEC/CM3)	PERIOD CHANGE (MSEC/DAY)	APP.AGE P/(DP/DT) (YRS)	REFERENCES
P1913+10	PSR1913+10	19 13 05	10 05	44.7	-0.6	0.404531	(42322)	35	240			1
P1913+16A	PSR1913+16	19 13 10	16 40	50.5	2.4	1.616239	(42322)	45	60			1
P1913+16B	PSR1913+16	19 13 13	16 00 24	50.0	2.1	0.059030	(42322)	10	167			1
P1914+13	PSR1914+13	19 14 40	13 06	47.6	0.4	0.281840	(42314)	20	230			4
P1915+09	PSR1915+09	19 15 00	09 40	44.6	-1.2	0.270252	(42314)	20	40			4
P1915+13	OP1914+13	19 15 22	13 48 29	48.3	0.6	0.194625883200	41566	15	94	0.6222	8.6E+05	2,3,10
P1916+14	PSR1916+14	19 16 00	14 40	49.1	0.9	1.180883	(42314)	30	30			4
P1917+00	PSR1917+00	19 17 17	00 16 03	36.5	-6.2	1.27225529554	41768	(27)	85	0.6630	5.3E+06	2,11
P1918+19	PSR1918+19	19 18 50	19 43 00	53.9	2.7	0.8210345766	42005		140	0.065	3.5E+07	8,17
P1919+14	PSR1919+14	19 19 10	14 12	49.0	0.0	0.618180	(42316)	30	90			4
P1919+21	CP1919	19 19 36	21 47 17	55.8	3.5	1.33730115212	40690	31	12	0.116	3.2E+07	3
P1919+20	PSR1919+20	19 19 40	20 00	54.2	2.6	0.760682	(42322)		80			1
P1920+20	PSR1920+20	19 20 08	20 10	54.4	2.6	1.172760	(42322)		200			1
P1920+21	PSR1920+21	19 20 36	21 08 00	55.3	3.0	1.07791188561	42006		220	0.706	4.2E+06	8,17
P1921+17	PSR1921+17	19 21 06	17 00	51.7	0.9	0.5472209	(42322)		140			1
P1922+20	PSR1922+20	19 22 30	20 30	55.0	2.3	0.237790	(42322)		220			1
P1924+19	PSR1924+19	19 24 16	19 20	54.1	1.4	1.346012	(42322)		420			1
P1924+16	PSR1924+16	19 24 30	16 42	51.9	0.1	0.579811	(42314)	25	165			4
P1924+14	PSR1924+14	19 24 35	14 30	49.9	-1.0	1.324922	(42314)	40	205			4
P1925+18A	PSR1925+18	19 25 00	18 50	53.8	1.0	0.482766	(42322)		240			1
P1925+22	PSR1925+22	19 25 08	22 30	57.0	2.7	1.43107	(42322)	90	200			1
P1925+18B	PSR1925+18	19 25 27	18 50	53.8	0.9	0.298312	(42322)		80			1
P1927+18	PSR1927+18	19 27 18	18 40	53.9	0.4	1.220446	(42322)		100			1
P1927+13	PSR1927+13	19 27 35	13 10	49.1	-2.3	0.760001	(42322)	15	200			1
P1929+15	PSR1929+15	19 29 30	15 30	51.4	-1.6	0.314351	(42314)	30	140			4
P1929+10	PSR1929+10	19 29 52	10 53 03	47.4	-3.9	0.22651703833	40625	5	3	0.100	6.2E+06	3
P1930+20	PSR1930+20	19 30 00	20 23	55.7	0.7	0.268210	(42314)	20	200			4
P1930+22	PSR1930+22	19 30 30	22 15	57.4	1.5	0.1444258	(42322)	8	219			1
P1930+13	PSR1930+13	19 30 58	13 00	49.4	-3.1	0.928325	(42322)	35	160			1
P1933+17	PSR1933+17	19 33 15	17 40	53.7	-1.3	0.634408	(42322)		200			1
P1933+16	JP1933+16	19 33 32	16 09 58	52.4	-2.1	0.35873542051	40690	8	159	0.519	1.9E+06	3
P1933+15	PSR1933+15	19 33 40	15 30	51.9	-2.4	0.967339	(42314)	30	160			4
P1939+17	PSR1939+17	19 39 47	17 40	54.5	-2.7	0.696261	(42322)		180			1
P1942+17	PSR1942+17	19 42 15	17 50	54.9	-3.1	1.996098	(42322)		160			1
P1943+18	PSR1943+18	19 43 18	18 30	55.6	-3.0	1.068707	(42322)		240			1
P1944+22	PSR1944+22	19 44 16	22 40	59.3	-1.0	1.334451	(42322)	30	150			1
P1944+17	HP1944	19 44 39	17 58 15	55.3	-3.9	0.440618461656	41671	30	16	0.002108	5.7E+08	2,3,10
P1946+35	JP1946	19 46 34	35 32 38	70.7	5.0	0.717306326897	41502	21	129	0.6096	3.2E+06	2,3
P1952+29	JP1953	19 52 22	29 15 22	65.9	0.8	0.426676758565	41720	13	20	0.000294	4.0E+09	2,3
P2002+31	JP2003	20 02 54	31 28 34	69.0	0.0	2.111211178283	41502	15	233	6.444	9.0E+05	2,10
P2016+28	AP2016+28	20 16 00	28 30 31	68.1	-4.0	0.557953339053	40689	14	14	0.0129	1.2E+08	3
P2020+28	PSR2020+29	20 20 33	28 44 43	68.9	-4.7	0.343400843442	41665	7	25	0.1638	5.7E+06	2,10
P2021+51	JP2021	20 21 25	51 45 08	87.9	8.4	0.529195331221	40626	7	23	0.263	5.9E+06	3
P2024+21	PSR2024+21	20 24 55	21 40	63.6	-9.5	0.398173	(42322)	15	100			1
P2028+22	PSR2028+22	20 28 24	22 20	64.6	-9.8	0.630512	(42322)	20	70			1

52.

PULSAR DESIGNATION	PULSAR	R.A. H.M.S.	DECL. DEG.	I *	L II DEG.	B II DEG.	PERIOD (SEC)	EPOCH (J.D.24+)	1/2 PULSE WIDTH (MSEC)	DISPERSION MEASURE (PARSEC/CM3)	PERIOD CHANGE (NSEC/DAY)	APP.AGE P/(DP/DT) (YRS)	REFERENCES
P2045-16	PSR2045-16	20 45 47	-16 27 48	30.5	-33.1	1.961566482076	40695	79	12	0.945	5.7E+06	3	
P2106+44	PSR2106+44	21 06 30	44 30 00	86.9	-2.0	0.4148704908	42007		129	(0.005)	(2.3E+08)	8,17	
P2111+46	JP2111	21 11 37	46 31 42	89.0	-1.3	1.014684444509	41006	29	141	0.0620	4.5E+06	3,10,16	
P2148+63	PSR2148+63	21 48 40	63 15 00	104.1	7.4	0.3801403094	42006	15	125	0.014	7.4E+07	9,11,17	
P2154+40	PSR2154+40	21 54 56	40 02 30	90.5	-11.4	1.5252634548	42006	52	71	0.283	1.5E+07	10,17	
P2217+47	PSR2217+47	22 17 46	47 39 48	98.4	-7.6	0.538467737844	40624	8	44	0.239	6.2E+06	3	
P2223+65	PSR2223+65	22 23 30	65 22 00	108.7	7.0	0.6825333245	42006			0.825	2.3E+06	8,17	
P2255+58	PSR2255+58	22 55 46	58 54 30	108.8	-0.7	0.3682433246	42006	13	148	0.497	2.0E+06	9,10,17	
P2303+30	PSR2303+30	23 03 34	30 43 49	97.7	-26.7	1.5738846617	42006	26	50	0.236	1.7E+07	3,17	
P2305+55	PSR2305+55	23 05 00	55 26 00	108.6	-4.2	0.4750674553	42006	(27)	45	(0.006)	(2.2E+08)	11,17	
P2319+60	PSR2319+60	23 19 42	60 07 30	112.1	-0.6	2.256483560l	42006	68	96	0.588	1.1E+07	9,16,17	
P2324+60	PSR2324+60	23 24 00	60 55 00	112.9	0.0	0.2336517104	42006		120	0.031	2.1E+07	8,17	

REFERENCES:

1. HULSE,R.A., TAYLOR,J.H.,UNIVERSITY OF MASSACHUSETTS, PREPRINT, 1975.
2. RICHARDS,D.W., RANKIN,J., ZEISSIG,G.A., "NATURE", VOL.251, PP.37-39, SEPTEMBER 6,1974.
3. TERZIAN,Y., "EARTH AND EXTRATERRESTRIAL SCIENCES", VOL.2, PP.63-68, 1972.
4. HULSE,R.A., TAYLOR,J.H., "THE ASTROPHYSICAL JOURNAL", VOL.191, L59-L61, JULY 15,1974.
5. RUDNICK,L., DEPT. OF PHYSICS, PRINCETON UNIVERSITY, PERSONAL COMMUNICATION TO Y. TERZIAN, APRIL 1,1974
6. KONESAROFF,H.M., ABLES,J.G., COOKE,D.J., HAMILTON,P.A., MCCULLOCH,P.M., "ASTROPHYSICAL LETTERS", VOL.15, PP.1-6, 1973.
7. MCCULLOCH,P.M., KONESAROFF,H.M., ABLES,J.G., HAMILTON,P.A.,RANKIN,J.M., "ASTROPHYSICAL LETTERS", VOL.14, PP.169-170, 1973.
8. DAVIES,J.G., LYNE,A.G., SEIRADAKIS,J.H., "NATURE PHYSICAL SCIENCE", VOL.244, PP.84-85, AUGUST 6,1973.
9. GRAHAM,D., HUNT,G.C., "NATURE PHYSICAL SCIENCE", VOL. 242, PP.86-87, APRIL 9,1973.
10. MANCHESTER,R.N., TAYLOR,J.H.,HUGUENIN,G.R., "NATURE PHYSICAL SCIENCE", VOL.240, PP.74-75, NOVEMBER 27,1972.
11. DAVIES,J.G., LYNE,A.G., SEIRADAKIS,J.H., "NATURE", VOL.240, PP.229-230, NOVEMBER 24,1972.
12. SMITH,F.G., "REPORTS ON PROGRESS IN PHYSICS", VOL.35, PP.450-458, 1972.
13. CENTRAL BUREAU FOR ASTRONOMICAL TELEGRAMS, INTERNATIONAL ASTRONOMICAL UNION, CIRCULAR NO. 2563.
14. MUHANTY,D.K., BALASUBRAMANIAN,V., "MONTHLY NOTICES OF THE ROYAL ASTRONOMICAL SOCIETY", SHORT COMMUNICATION, VOL.171, PP.17P-18P, MAY,1975.
15. KONESAROFF,H.M., HAPILTON,P.A., ABLES,J.G., "AUSTRALIAN JOURNAL OF PHYSICS", VOL.25, PG.759, 1972.
16. GRAHAM,D.A., HEBOLD,U., HESSE,K.H., HILLS,D.L., WIELEBINSKI,R., "ASTRONOMY AND ASTROPHYSICS", VOL.37, PP.405-410, 1974.
17. LYNE,A.G., RITCHINGS,R.T., SMITH,F.G., "MONTHLY NOTICES OF THE ROYAL ASTRONOMICAL SOCIETY", VOL.171, PP.579-597,1975.

Blank
Page

CHAPTER III
BINARY STARS AND COMPACT X-RAY SOURCES

William K. Rose
University of Maryland
College Park, Maryland

BINARY STARS

More than half the stars in the sky are probably members of binary systems. Kepler's third law implies that the orbital period P and distance between stars are related by

$$\left(\frac{2\pi}{P}\right)^2 a^3 = G(M_1 + M_2) \tag{1}$$

where a is the distance between the centers of the components, and M_1 and M_2 are their masses.

Visual binaries are systems whose components are usually sufficiently distant from one another (i.e. $\gtrsim 100$ times the diameters of individual stars) that the evolution of one component is practically unaffected by the presence of the other. On the other hand, in close binary systems the distances between components are comparable to the radii of individual components and the evolution of the components is affected by the transfer of mass between them. Close binary systems are also spectroscopic binaries, since the orbital motions of the components have velocities $\simeq 100$ kms^{-1} and consequently their motions can be inferred from the Doppler effect. Eclipses are observed whenever the orbital plane of the binary system forms a sufficiently small angle with respect to the line of sight. Observations show that the outer layers of the components are distorted because of tidal interactions.

In many binary systems (Cygnus X-1 is a very important example) the spectral lines of only one component can be observed. For such systems the masses of the components cannot be determined without additional information and all we determine is the mass function

$$f(M) = \frac{M_2^3 \sin^3 i}{(M_1 + M_2)^2} \tag{2}$$

where M_1 is the mass of the primary and i is the complement of the angle between the line of sight and the orbital plane. For an eclipsing binary system the angle i is close to 90 degrees. In order to find the masses of the stars in a single line binary system it is necessary to have additional information such as knowledge that one component is a main sequence star or supergiant of known mass.

Calculations of the evolution of stars in close binary systems are almost always based on the assumption that mass transfer occurs when the radius of one component exceeds some critical value, which is generally taken to be the radius of the Roche lobe. For this reason, it is important to derive an expression for this critical radius in any given binary system.

The orbital angular velocity is

$$\omega^2 = \frac{G(M_1 + M_2)}{a^3}. \tag{3}$$

We define a coordinate system that is rotating with angular velocity ω and whose origin is at the center of mass of the system. The equation of motion for a small point mass m is this coordinate system is

$$m\frac{d^2r}{dt^2} = F_1 + F_2 - m\omega \times (\omega \times r) - 2m\omega \times \dot{r} \tag{4}$$

where F_1 and F_2 are the gravitational forces of M_1 and M_2 on m. If we define the direction of ω to be along the z axis and let the x axis lie along the line separating the two masses, the x and y components of the above equations become

$$\ddot{x} = \frac{-GM_1(x - x_1)}{[(x-x_1)^2+y^2]^{3/2}} - \frac{GM_2(x - x_2)}{[(x-x_2)^2+y^2]^{3/2}} + \frac{G(M_1 + M_2)x}{a^3} + 2\omega\dot{y} \tag{5}$$

$$\ddot{y} = \frac{GM_1 y}{[(x - x_1)^2 + y^2]^{3/2}} - \frac{GM_2 y}{[(x-x_2)^2+y^2]^{3/2}} + \frac{G(M_1 + M_2)y}{a^3} - 2\omega\dot{x} \tag{6}$$

where

$$x_1 = \frac{M_2}{M_1 + M_2}a; \quad x_2 = \frac{-M_1}{M_1 + M_2}a,$$

are the positions of M_1 and M_2 along the x axis.

In the rotating frame of reference the total energy is a constant of the motion. To show this we note that the centrifugal force can be derived from the potential

$$V_c = -\frac{1}{2} m\omega^2 (x^2 + y^2) \tag{7}$$

and the Coriolis force, since it is perpendicular to the velocity can do no work in the rotating frame. It follows that in the rotating frame the total energy can be written

$$E = \frac{1}{2} m (\dot{x}^2 + \dot{y}^2) + V \tag{8}$$

with

$$V = \frac{-GmM_1}{[(x - x_1)^2 + y^2]^{1/2}} - \frac{GmM_2}{[(x - x_2)^2 + y^2]^{1/2}} - \frac{Gm(M_1 + M_2)(x^2 + y^2)}{2a^3}$$

It is convenient to define

$$\xi = \frac{x}{a}, \qquad \eta = \frac{y}{a},$$

$$\xi_1 = \frac{M_2}{M_1 + M_2}, \qquad \xi_2 = \frac{M_1}{M_1 + M_2}.$$

In terms of these quantities, V can be expressed as

$$V = \frac{Gm(M_1 + M_2)}{a} \left[\frac{-\xi_2}{[(\xi - \xi_1)^2 + \eta^2)^{1/2}]^{1/2}} + \frac{-\xi_1}{[(\xi - \xi_2)^2 + \eta^2)^{1/2}} - \frac{1}{2}(\xi^2 + \eta^2) \right] \tag{9}$$

A plot of the function $V(\xi,0)$ is shown in Figure III-1. We note that there are three critical points (called Lagrangian points) along the ξ axis at which the potential $V(\xi,0)$ has maxima. Two additional Lagrangian points are located off the ξ axis. It can be shown by expanding the right hand members of the force equations in powers of the displacement about the Lagrangian points that motions in the vicinity of these points are unstable.

Equipotential surfaces close to either M_1 or M_2 are almost spherical. More distant surfaces become more distorted until they intersect at the inner Lagrangian point (L1) for some critical value of the potential. This equipotential surface (see Figure III-2) is called the critical Roche potential, and the lobes surrounding the two stars are called the Roche lobes. At larger values of the potential the two stars become surrounded by a common equipotential surface.

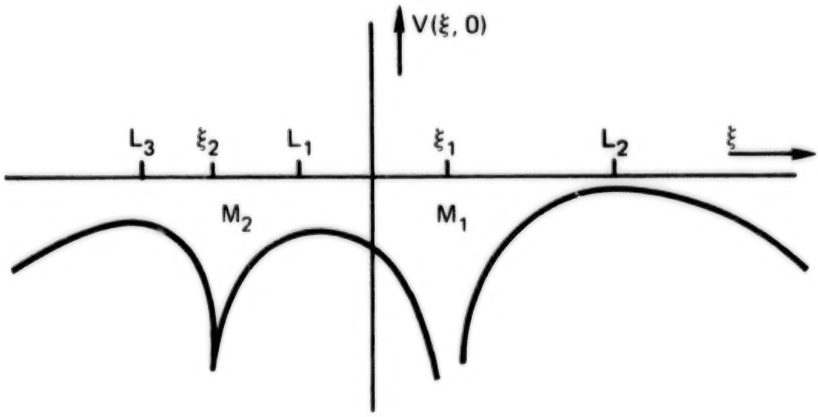

Figure III-1. $V(\xi, 0)$ is shown as a function of ξ.

An approximate value of the radius r of a Roche lobe can be obtained by setting $4/3\pi r^3$ equal to the volume with the Roche Lobe. When this is done the following useful expressions for the radii of the Roche lobes are found:

$$.8 < \frac{M_1}{M_2} < 20, \quad \frac{r_1}{a} \simeq .38 + .2 \log \frac{M_1}{M_2}, \tag{10}$$

$$0 < \frac{M_1}{M_2} < .8, \quad \frac{r_1}{a} \simeq \frac{2}{3^{4/3}} \left(\frac{M_1}{M_1 + M_2} \right)^{1/3} \tag{11}$$

The orbital angular momentum J of a binary system is

$$J^2 = \frac{G(M_1 M_2)^2 a}{M_1 + M_2} \tag{12}$$

If the total mass and angular momentum of the system are conserved during mass transfer, the distance from the centers of M_1 and M_2 are obtained from the expression

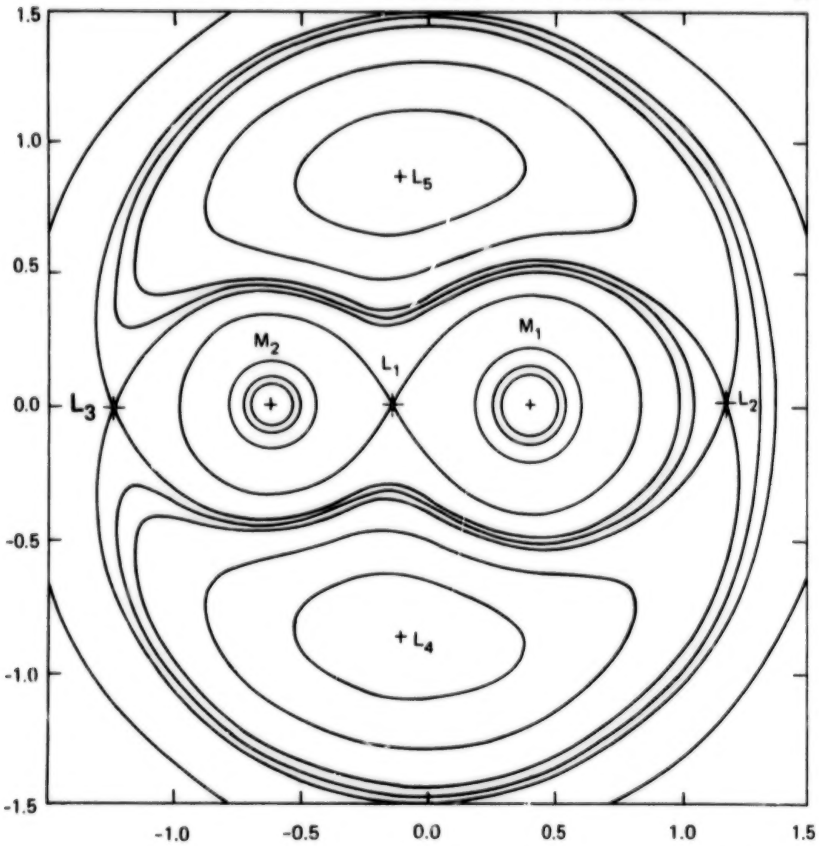

Figure III-2. A plot of the equipotential surfaces. The critical Roche equipotential surface intersects the inner Lagrangian point (L_1).

$$a = \frac{MJ^2}{G(M_1M_2)^2} = \frac{\text{Constant}}{M_1^2(M - M_1)^2}. \tag{13}$$

As a star evolves it may expand and overflow its Roche lobe. Under these circumstances it is possible to use the above equations to calculate how much mass is transferred and then to calculate the effect of this mass transfer on the binary system. It is important to emphasize that it is not possible to define a critical potential surface if the rotation of the stars is nonsynchronous

STELLAR EVOLUTION IN CLOSE BINARY SYSTEMS

Previously, we discussed the evolution of single stars. Since one known pulsar and the most interesting compact x-ray sources are members of

close binary systems, it is of considerable interest to understand how stars evolve in such systems.

The Roche equipotential surface is the critical potential surface that determines whether a point mass is gravitationally bound to a component of a binary system. If the radius of one star expands so as to fill its Roche lobe, mass will be transferred to the other star through its first Lagrangian point. There are three evolutionary phases in which a star will expand and fill its Roche lobe. In some binary systems the components are sufficiently close that mass transfer will arise before the primary (i.e., and the more massive component) has completed hydrogen core burning. Binaries of this general class have orbital periods of approximately 1-2 days. In other systems mass transfer will occur after hydrogen core exhaustion but before helium core ignition. The orbital periods of the latter binary systems will range from ~ 2 to ~ 200 days. In still more widely separated binaries mass transfer will begin only after the primary has evolved up the asymptotic giant branch (i.e., hydrogen and helium burning shells). These relatively widely separated binary systems have orbital periods of years.

For the first class of binary system discussed above, mass transfer from massive primary to the less massive secondary will cause the Roche lobe to shrink and mass transfer will continue on a thermal time scale until the mass ratios are reversed. Thereafter, mass transfer will continue on a nuclear time scale. For the second class of binary, mass transfer will continue until almost all the mass of the primary is transferred to the secondary. Stellar model calculations indicate that the mass of the primary will exceed the limiting white dwarf mass ($1.4\ M_\odot$) after mass exchange only if the initial primary mass is $\gtrsim 16\ M_\odot$. Mass transfer is expected to occur very quickly for widely separated binary systems that exchange mass when the primary is on the asymptotic giant branch. For such systems we expect that significant amounts of mass will be lost from the system.

It is of interest to ask which binary systems are likely to be the progenitors of x-ray binaries. Stellar model calculations indicate that in order to produce an x-ray binary containing a neutron star or a black hole, the initial primary mass must be $\gtrsim 16\ M_\odot$ unless a second phase of mass exchange occurs in which mass from the initially less massive star is added to the white dwarf remnant of the initial primary.

The masses and orbital periods of such x-ray binaries as Cyg X-1 and Cen X-3 can be understood on the basis of the above picture for binary evolution. However, in order to produce these x-ray binaries it is likely that considerable mass and angular momentum be lost from the binary system. It is important to note that mass exchange before mass loss does not reduce the

angular momentum per unit mass of a binary system. However, a net loss of angular momentum per unit mass may arise during the evolution of stars in a binary system. Suppose that the masses of the primary and secondary are almost the same. In this case the secondary may fill its Roche lobe as the primary is still transferring mass, and mass from both stars will be transferred through the second and third Lagrangian points. Such mass transfer will cause a considerable loss of angular momentum from the binary system. The mass transferred through the second and third Lagrangian points may flow away very quickly or it may form an envelope around the binary stars. In the latter case the binary stars will experience a drag force as they orbit inside this envelope. Such a drag force may cause the members of the binary system to move closer together.

NOVAE

Novae are stars that are observed to brighten by many orders of magnitude in a short period of time (~1 day). They are typically 10^5 times more luminous than the sun at maximum light, and occur quite frequently. Approximately 25 - 50 novae occur every year in our galaxy. It is of interest to compare the frequency of nova outbursts with the production rate of planetary nebulae and supernovae. In our previous discussion of planetary nebulae we have noted that their rate of formation is approximately equal to the rate of formation of white dwarfs ($\simeq$3 per year per galaxy). Since post-novae stars and presumably also pre-nova stars are hot white dwarfs (also called ultraviolet dwarfs) it may appear surprising that their frequency of production should exceed that of white dwarfs. However, as we shall discuss below, novae must recur many times in a single stellar system. (See Figures III-2).

Supernovae are stellar explosions that occur much less frequently than novae ($\simeq$ one supernovae per 70 years per galaxy) but are much more spectacular events. The amount of energy released in a nova outburst ($\simeq 10^{46}$ ergs) is approximately 10^5 times less than is observed in a supernova outburst. Since the binding energy of an evolved star is $\gtrsim 10^{50}$ ergs, it is clear that the amount of energy released during a nova outburst is much too small to greatly affect the entire star. Only the outer envelope of the pre-nova star is ejected into space. On the other hand, the energy released during a supernova outburst is sufficient to produce a remnant star that is fundamentally different than the pre-supernova star.

During a nova outburst a shell of matter that is approximately 10^{-5} $M_\odot$ is ejected into space at a velocity that is $\simeq$2000 km s^{-1}. The kinematics of the expanding shell can be inferred by the appearance of highly broadened emission lines and blueshifted absorption lines.

The absorption lines are blueshifted because they arise in the outer layers of the matter that is moving towards the observer. Some novae occur sufficiently close to the sun that we can measure the change in the angular diameter of the expanding gas shell. By measuring the velocity of expansion of the nova mass shell and also how rapidly its angular diameter changes with time, we can determine the distances to these novae. Since we can measure the apparent brightness of a nova, a determination of distance implies that we can infer its luminosity. Although the visual luminosities of novae at maximum light vary by a considerable factor, there is an empirical relation between the rate of decline from maximum light and the absolute brightness at light maximum. The more luminous novae tend to decline more rapidly than the less luminous. This circumstance implies that one can estimate the distance to a nova by measuring its apparent brightness at light maximum and the rate of decline of its apparent brightness. Since novae are quite luminous, they can be used to estimate the distances to galaxies. The first observational evidence for external galaxies came from observing the light curves of novae in the Andromeda galaxy (M31).

Perhaps the most important clue concerning the origin of novae comes from the observational evidence that all novae arise in binary systems. The typical nova outburst occurs in a close binary system in which one component is a white dwarf and the other a star of normal stellar diameter (most likely a subgiant or main sequence star). The observations indicate that mass is flowing from the larger star onto the surface of the white dwarf. If a nova outburst occurs each time the amount of accreted mass equals the typical amount of mass ejected ($\simeq 10^{-5}\ M_\odot$) then many thousands of nova outbursts can arise from a single stellar system before the secondary (i.e., the larger star) has exchanged much of its mass.

So far we have not discussed what effect the accreted matter will have on the white dwarf. Calculations show that as hydrogen-rich matter is accreted onto the surface of a white dwarf, the outer envelope will contract and thereby cause the interior to heat up. For plausible mass accretion rates ($10^{-8} - 10^{-10}\ M_\odot$/year) temperatures sufficiently high to ignite hydrogen burning at the base of the hydrogen-rich envelope are attained after the mass of the hydrogen-rich envelope exceeds approximately $10^{-4}\ M_\odot$. (See Figure III-4 for temperature distributions in hot white dwarf models).

The ignition of hydrogen burning in the hydrogen-rich envelope of a white dwarf will produce a thermonuclear runaway that can lead to the mass loss that is associated with the outburst. Several mechanisms for mass loss have been proposed. If the thermonuclear runaway takes place under conditions of relatively high density ($\rho > 10^3$ gm cm^{-3}) and high CN abundance, very

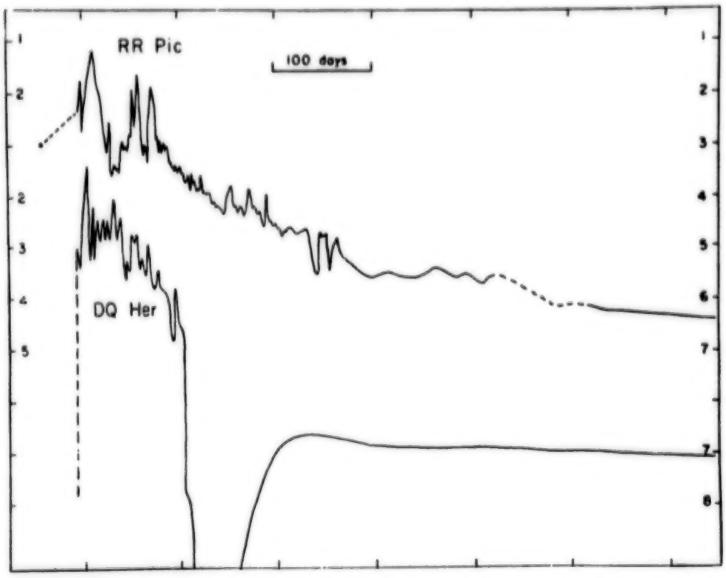

Figure III-3. Light curves of the novae DQ Her and RR Pic

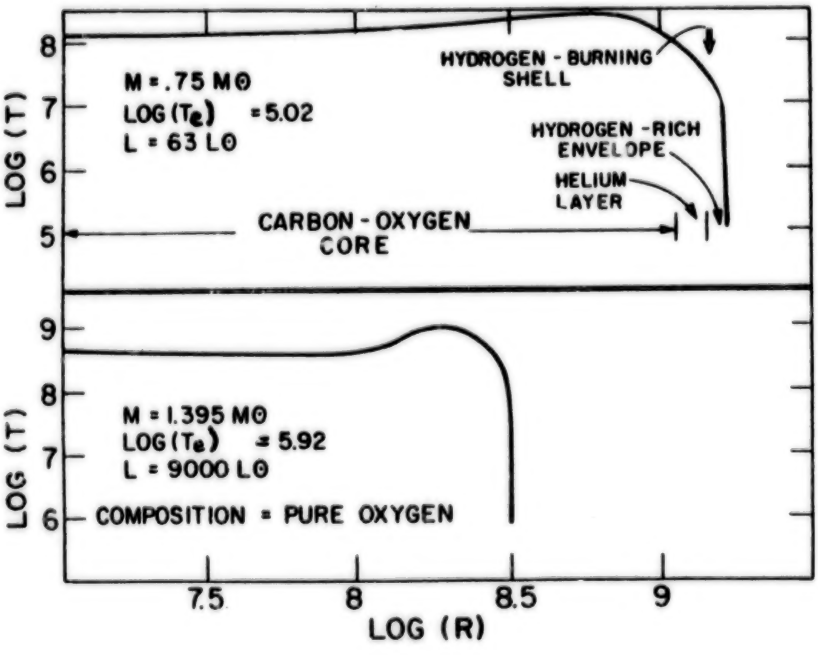

Figure III-4. The temperature (T) is shown as a function of radius (R) for 0.75 $M_{\odot}$ and 1.395 $M_{\odot}$ models of hot white dwarfs. The 1.395 $M_{\odot}$ model has a very high effective temperature (T_e) and a very steep rise in temperature near the surface (source: Rose, 1972)

high rates of nuclear energy generation may result ($\epsilon_{CN} \simeq 10^{16}$ erg g^{-1} s^{-1}). Such high burning rates can lead to an ejection of the envelope in a dynamical time scale. Pulsations provide another plausible mechanism for mass loss since the white dwarf will be pulsationally unstable shortly after the ignition of hydrogen burning. Surface magnetic fields of $10^6 - 10^7$ gauss have been inferred from the observed polarization of the light from the old nova DQ Her. Such high magnetic fields will suppress convection in the outer layers of the white dwarf envelope and therefore lead to mass loss when the stellar luminosity exceeds the Eddington limit

$$L_{crit} \simeq 10^{38} \frac{M}{M_\odot} \text{ ergs s}^{-1}. \tag{14}$$

Although mass accretion onto white dwarfs does not usually lead to strong x-ray emission, white dwarfs can be x-ray sources. This circumstance can be most readily seen if we equate the thermal energy density to the gravitational energy density on the surface of a white dwarf. We find

$$T_{surface} \sim \frac{GM}{R} \frac{m_p}{k} \sim 10^8 \text{ K} \tag{15}$$

MASS ACCRETION ONTO NEUTRON STARS

The compact x-ray sources, Her X-1 and Cen X-3, are believed to be neutron stars that are members of close binary systems in which mass accretion is responsible for the observed x-ray emission. These systems are extremely interesting because they provide an opportunity to determine the masses of neutron stars.

Her X-1, which is one of the most carefully observed x-ray sources, has three periodicities associated with it. The period of the x-ray pulsations (1.24 s) is the shortest period. This is believed to be the rotation period of an obliquely magnetized neutron star. The 1.7 day orbital period is the next longest period. Finally, the x-ray source is observed to turn on and off with a period of approximately 35 days.

The shapes of the x-ray pulses are observed to vary in time. Sometimes there is a single main pulse; at other times the main pulse has two peaks. The star Hz Her is the optically identified companion of Her X-1. Most of the optical variability of Hz Her is probably caused by x-ray heating of its exposed hemisphere. The optical light curve near minimum intensity is much narrower than

the x-ray eclipse. Optical emission from an accretion disk surrounding Her X-1 may explain this interesting effect. Such an accretion disk is predicted if matter flows from Hz Her to Her X-1 through the inner Lagrangian point. Observed x-ray absorption dips provide additional evidence for an accretion disk.

Measurements of the orbital Doppler variations of the pulsation period allow one to measure the projected orbital radius (3.95×10^{11} cm), velocity (169 km s^{-1}), and mass function

$$f(M) = \frac{M_{Hz}^3 \sin^3 i}{(M_{Hz} + M_x)^2} \simeq .85\ M_\odot. \qquad (16)$$

The optical light curve shows that the angle of inclination is $>85°$. Although x-ray heating complicates the optical determination of the mass of Hz Her, it lies in the range $1.5 - 2.5\ M_\odot$. The corresponding range in x-ray mass is $.7 - 1.7\ M_\odot$. If it is assumed that Hz Her fills its Roche lobe, it is possible to relate the mass ratio to the radius of the Roche lobe and the diameter of the occulting region. In this case the masses of the binary components become $M_{Hz} \simeq 2.2\ M_\odot$ and $M_x \simeq 1.3\ M_\odot$.

Cen X-3 is another pulsed binary x-ray source. The x-ray pulses have a periodicity of 4.8 seconds and contain more than 70% of the x-ray emission. X-ray eclipses are observed, and from the Doppler shift of the period of the pulsations it is possible to infer that the source is a member of a massive binary system whose orbital period is 2.09 days. Changes in the pulsation period are $\dot{P}/P \sim 10^{-4}$ $year^{-1}$ but are not monotonic. The x-ray spectrum, which has a possible low energy cutoff at 2–4 keV, is flat up to $\simeq$25 keV. The x-ray spectrum is harder near the peak intensity of the pulse.

The binary companion of Cen X-3 is a BO supergiant that is at a distance of approximately 10 kpc. The projected orbital radius of the binary is 1.1×10^{12} cm and the mass function $\simeq 15.4\ M_\odot$. The measured mass function implies that the optical companion has a mass greater than $15.4\ M_\odot$. Mass estimates for Cen X-3 are not as precise as for Her X-1 but do indicate that the mass of Cen X-3 is comparable to that of Her X-1.

Although Her X-1 and Cen X-3 were formed as a result of stellar collapse, they are both members of close binary systems. It is natural to ask under what physical conditions a supernova explosion can occur in a binary system without causing its disruption. We consider a binary system in which the components move in circular orbits about their center of mass. In the center

of mass frame the velocities of M_1 and M_2 are

$$V_1 = M_2 \left[\frac{G}{a(M_1 + M_2)}\right]^{1/2}, \tag{17}$$

$$V_2 = M_1 \left[\frac{G}{a(M_1 + M_2)}\right]^{1/2} \tag{18}$$

respectively. The supernova outburst is assumed to be spherically symmetric. Let $q\,M_1$ equal the mass of the stellar remnant and $(1 - q)\,M$ equal the ejected mass. Because the time scale for the supernova outburst is short as compared to the orbital period, the change in the potential and kinetic energy of the binary system is sudden. The acceleration must remain finite and consequently the velocities of M_1 and M_2 will remain constant at the time of the explosion.

Immediately after the explosion the kinetic and potential energies in the original center of mass frame are

$$T = \frac{1}{2}\,\frac{-GM_1M_2}{a(M_1 + M_2)}\,[q\,M_1 + M_2] \tag{19}$$

and

$$U = q\,\frac{-GM_1M_2}{a} \tag{20}$$

respectively. It follows that the total energy in the original center of mass frame is

$$E = \frac{GM_1M_2}{2a(M_1+M_2)}\,[M_1(1 - 2q) - M_2\,q]. \tag{21}$$

The kinetic energy associated with the motion of the center of mass is

$$\frac{p^2}{2(q\,M_1 + M_2)}$$

where

$$p = M_2V_2 - q\,M_1V_1 \tag{22}$$

is the momentum in the original center of mass frame. It follows that the total energy in the new center of mass frame is

$$E = \frac{q\,GM_1M_2}{2a(qM_1 + M_2)}\,[M_1 - M_2 - 2q\,M_1] \tag{23}$$

and therefore the binary will become unbound if

$$M_1 - M_2 > 2q\,M_1. \tag{24}$$

In most binary systems the more massive star will undergo stellar collapse before its companion has left the main sequence. Under such conditions the above equation shows that the binary system will probably become unbound since the mass of the remnant is generally a small fraction of the mass of the primary. Moreover, asymmetries in the supernova outburst itself will usually act to make a binary system unbound. These physical arguments explain why only one known pulsar is a member of a binary system. On the other hand, in a close binary system where mass exchange is important, the exploding star can be less massive than its companion at the time of a supernova explosion and consequently the binary system can readily remain bound.

After a supernova outburst, the binary orbit must be eccentric. It follows that the highly circular orbits of Her X-1 and Cen X-3 must have been circularized if a supernova outburst occurred in these systems. Although the physical mechanism for this circularization is not understood, mass exchange may act to circularize the orbit of the binary. It is interesting that the orbit of the binary pulsar PSR 1913 + 16, in which mass exchange is not significant, is highly eccentric.

The x-ray luminosities of Her X-1 and Cen X-3 are $\simeq 10^{37}$ ergs s^{-1}. The luminosity available from accretion onto the surface of a neutron star is

$$L = \frac{GM}{R}\,\frac{dM}{dt} \tag{25}$$

and consequently the required rate of mass accretion is $dM/dt \simeq 10^{-9} M_\odot$ year.

We define the Alfvén surface to be the surface below which the plasma surrounding a neutron star corotates with the star. The location of the Alfven surface is determined by the condition that the kinetic energy density of the infalling matter $(1/2\,\rho v^2)$ should be equal to the energy density of the stellar magnetic field $(B^2/8\pi)$. The Alfven surface is located at $r_A \simeq 10^8$ cm, if the surface magnetic field of the neutron star is $B \simeq 10^{12}$ gauss. The accreting matter may have sufficient angular momentum for centrifugal force to halt its infall before it reaches the Alfvén surface. In this case an accretion disk

will be formed. Viscous forces within the disk can transport angular momentum and thereby allow an infall of plasma.

Infalling plasma will induce surface currents above the Alfvén surface. Such surface currents will shield matter above the Alfvén surface from the influence of the stellar magnetic field. Magnetic fields are likely to be frozen into the infalling matter. This circumstance implies that the radial component of the field should increase as $1/r^2$ during infall, while the perpendicular component of the field will grow as $1/r^2$. Amplification of the infalling magnetic field will continue until dissipative processes cause it to decay. Such dissipation will prevent the magnetic energy density from exceeding the kinetic energy density of the infalling matter; therefore magnetic fields will not stop infall.

Since the velocity of the infalling matter is likely to be supersonic with respect to the Alfvén surface, a shock wave will probably form in front of the surface. The thickness of this shock wave will be comparable to the distance over which the plasma is deflected, i.e. the ion Larmor radius

$$r_2 = \frac{v}{\frac{eB}{m_c c}}$$

where v is the free fall velocity of the plasma. We note that this distance is less than the collisional mean free path and consequently the shock is collisionless.

Magnetic forces of the form $\mathbf{J} \times \mathbf{B}$ will inhibit the flow of plasma across magnetic field lines and the plasma will flow toward the polar regions of the neutron star. The magnetosphere is likely to be subject to Rayleigh-Taylor instability of some other macroscopic instability in the vicinity of the magnetic poles. For these reasons, the plasma may flow to the surface near the poles. The anisotropic radiation patterns necessary to explain the x-ray pulses are, therefore, produced by the anisotropic infall of plasma.

MASS ACCRETION ONTO BLACK HOLES

Among the known compact x-ray sources, Cyg X-1 is considered most likely to be a black hole. Cir X-1 is another plausible candidate. The x-ray fluxes from both these objects show variability over very short time scales. In the case of Cyg X-1 the fluctuations extend down to times less than 1 ms.

Cyg X-1 is known to have at least two x-ray states (an upper and a lower state). In the upper state the source has an excess of low energy (i.e. < 6 keV) x-rays. In 1971 a radio source appeared at the position of Cyg X-1 at the same time that the x-ray emission changed from the upper to the lower state. During this transition the 2-6 keV flux decreased by a factor of 4 and the 10-20 keV flux increased by a factor of 2. Recent (1975) x-ray observations show that Cyg X-1 has returned to its high state.

Cyg X-1 is a member of a 5.6 day spectroscopic binary. Its companion is the 9th magnitude BOI supergiant HDE 226888. Recent observations indicate that the distance to HDE 226888 is $\gtrsim 2$ kpc. This distance determination is extremely important. If HDE 226888 is more distant than 1 kpc, it must be a massive supergiant (i.e. $M \geqslant 20\ M_\odot$). A lower limit can be placed on the mass ratio M(Cyg X-1)/M(HDE 226888). It follows from this measured lower limit that Cyg X-1 must have a mass $\gtrsim 4M_\odot$. This mass is probably too high for a neutron star or white dwarf, and consequently Cyg X-1 is probably a black hole. Attempts to interrupt the x-ray emission have assumed that the x-rays are coming from an accretion disk that surrounds a black hole ($M \geqslant 4\ M_\odot$). A mass accretion rate of $10^{-9}\ M_\odot$/yr may be sufficient to produce the required x-ray emission. It is important to point out that spherical accretion is a very inefficient means of producing radiation, since only a small fraction of the available energy is emitted during infall. Moreover, spherical accretion does not produce strong 1-10 keV x-ray sources. For this reason, accretion disks are the only known plausible models for intense 1-10 keV x-ray emission from black holes.

Two basic types of mass accretion can arise in close binary systems. For the case of Roche lobe overflow, the infalling matter has a great deal of angular momentum and consequently an extensive accretion disk will be formed. In the second type of mass accretion, mass transfer occurs as a result of a stellar wind. In this case it is touch and go whether or not the infalling matter has sufficient angular momentum to form an accretion disk.

The above discussion makes it clear that before we can understand x-ray emission from black holes we must understand the physical properties of accretion disks. Such disks must have outer and inner boundaries. The location of the outer boundary is determined by the specific angular momentum of the accreting matter. The location of the inner boundary is determined by the circumstance that, by general relativity, it is impossible for stable particle orbits to exist closer than $\simeq 3r_s$ ($r_s = 2GM/c^2$) to a black hole. In discussing the structures of accretion disks we will assume that mass accretion is steady and that matter in an accretion disk is in Keplerian orbits (i.e., centrifugal force balances gravity in the radial direction).

We assume that dM/dt is the rate at which gas is added to an accretion disk. The specific angular momentum at a radius r from the center of a black hole is

$$L = \left(\frac{GM}{r}\right)^{1/2} r = (GMr)^{1/2}. \tag{26}$$

An element of mass must lose almost all of its angular momentum before it reaches the inner radius. For this reason, angular momentum must be continuously transported away from the outer boundary of the accretion disk by infalling gas under steady state conditions. The rate of removal of angular momentum is

$$\frac{dJ}{dt} = \frac{dM}{dt} (GMr_0)^{1/2}, \tag{27}$$

where r_0 is the radius of the outer boundary.

The surface density of matter in the disk is

$$\Sigma = 2h\rho \tag{28}$$

where h is the thickness of the disk and ρ is the density half-way between its two sides. The radial velocity is $v < 0$ and $v^{\phi} = \omega r = (GM/r)^{1/2}$. The viscous stress is

$$t_{\phi r} = 2\eta\sigma_{\phi r} \tag{29}$$

where η is the dynamic viscosity and the shear $\sigma_{\phi r}$ of the Keplerian orbits is

$$\sigma_{\phi r} = -\frac{3}{4}\omega = -\frac{3}{4}\left(\frac{GM}{r^3}\right)^{1/2} \tag{30}$$

From the conservation of mass, it follows that

$$\frac{dM}{dt} = 2\pi r v^r \Sigma. \tag{31}$$

At any particular time angular momentum is transported across any radius r by the infall of mass. In order to conserve angular momentum outwards. Angular momentum conservation implies

$$\frac{dM}{dt}(GMr)^{1/2} = 2\pi r\, 2h t_{\phi r}\, r + \dot{j}_c . \tag{32}$$

The left hand side of the above equation represents the rate at which angular momentum is transported inward through a radius r and

$$\dot{j}_c \simeq \frac{dM}{dt}(GMr_I)^{1/2} \tag{33}$$

(where r_I is the inner boundary of the disk) is the rate at which angular momentum is deposited on the black hole. The remaining term represents the rate at which viscous stresses transport angular momentum outwards.

The above equations imply that the viscous stress $t_{\phi r}$ is determined by the mass accretion rate and the mass of the black hole. Solving for the viscous stress, we find

$$2h\, t_{\phi r} = \frac{\dfrac{dM}{dt}}{2\pi r^2}\left[(GMr)^{1/2} - (GMr_I)^{1/2}\right]. \tag{34}$$

If at any r, $2h t_{\phi r}$ is smaller than given in the above equation, the viscous stresses will not be sufficiently strong to allow the mass flow dM/dt and consequently mass accumulation will take place. Mass accumulation in the outer regions of the disk will lead to an increase in its radius.

The rate of generation of heat per unit area in the disk is

$$2h\epsilon = -4h\, t_{\phi r}\, \sigma_{\phi r} \simeq \frac{3}{4\pi r^2}\frac{dM}{dt}\frac{GM}{r}, \quad (r \gg r_I), \tag{35}$$

and consequently the rate of generation of heat between r_1 and r_2 is

$$\int_{r_1}^{r_2} 2h\epsilon\, 2\pi r\, dr \simeq \frac{3}{2}\frac{dM}{dt}\left(\frac{GM}{r_1} - \frac{GM}{r_2}\right), \tag{36}$$

$$r_2 > r_1 \gg r_I$$

As shown below, heat is produced in the disk by viscous stresses as well as gravitational energy release. Gravitational energy is released between r_1 and r_2 at the rate

$$\frac{dM}{dt}\left(\frac{GM}{r_1}-\frac{GM}{r_2}\right) \tag{37}$$

It follows from the virial theorem that 1/2 of this energy goes into heat and 1/2 into orbital kinetic energy; therefore viscous forces which transport angular momentum outwards deposit heat between r_1 and r_2 at the rate that is 2/3 the total rate of generation of heat given in equation 36.

The rate at which energy is transported across a radius r is

$$E = \omega J \simeq \frac{3}{2}\frac{dM}{dt}\frac{GM}{r} \tag{38}$$

The energy flux from the top and bottom of the disk is 2F, where

$$F \simeq \frac{3}{8\pi r^2}\frac{dM}{dt}\frac{GM}{r}. \tag{39}$$

We note that F is independent of the viscosity and depends on r, the mass accretion rate, and the mass of the black hole. The total luminosity from the disk is obtained from the expression

$$L = \int_{r_I}^{\infty} 2F\, 2\pi r dr. \tag{40}$$

The minimum disk temperature $T_{min}(r)$ at a given radius r is achieved if the disk radiates as a blackbody; i.e.,

$$\frac{1}{4}a\,T_{min}^4 = F(r). \tag{41}$$

On the other hand, the maximum value for T(r) is determined by the relation

$$T_{max} \simeq \frac{GM}{r_1}\frac{m_p}{k} = \frac{m_p c^2}{6} \tag{42}$$

The x-ray observations of Cygnus X-1 indicate that the hottest electron temperature T_e in the disk surrounding Cygnus X-1 is $T_e \simeq 10^9$ K, which is between T_{min} and T_{max}.

The vertical structure of an accretion disk is much less well determined than the radial structure, since the determination depends on a knowledge of the viscous stresses in the disk. It is plausible to assume that

$$t_{\phi r} = \alpha P$$

If α were known, then the vertical structure could be determined by the condition of hydrostatic equilibrium

$$\frac{P}{h} = \rho \left(\frac{GM}{r^3} \right) h, \tag{43}$$

the equation of state

$$P = \frac{\rho k (T_i + T_e)}{m_p}, \tag{44}$$

some assumption about the relative magnitudes of T_i and T_e, and angular momentum conservation. It has been suggested that $T_i >> T_e$ in the inner portion of the accretion disk surrounding Cygnus X-1. In this picture the inner part of the disk bulges because $T_i > 10^{11}$ K but T_e is kept $\leqslant 10^9$ K as a result of Comptonization of relatively soft x-rays (<6 keV) emitted by the outer regions of the disk. This theory explains the spectrum of the hard x-rays (>10 keV) from Cygnus X-1.

According to general relativity the motion of a particle moving about a spherically symmetric black hole (i.e., moving in a Schwarzschild field) can be written in the form

$$\left(\frac{dr}{d\tau} \right)^2 = 2E + \frac{r_S}{r} - \frac{h^2}{r^2} + \frac{r_S h^2}{r^3}, \tag{45}$$

where

$$r_S = \frac{2GM}{c^2},$$

and

$$h = r^2 \dot{\phi} = \text{constant}$$

is the specific angular momentum and τ is the proper time. The above expression differs from the corresponding Newtonian result in that as a result of the last two terms on the right hand side of the equation, the effective potential

energy becomes large and negative for sufficiently small r. Thus, in general relativity gravitational capture is possible in the absence of tidal forces, and stable orbits about a black hole are impossible for sufficiently small r (or sufficiently high E and fixed h).

ACKNOWLEDGMENTS

The author thanks Dr. Brian Flannery for reading the manuscript and offering many helpful comments.

BIBLIOGRAPHY

Davidson, K. and Ostriker, J. P. 1973, Ap. J., 179, 585.

Kippenhahn, R. and Weigert, A. 1967, Z. Ap., 65, 251.

Lauterborn, D. 1970, Astro. and Ap., 7, 150.

Lamb, F. K., Pethick, C. J. and Pines, D. 1973, Ap. J., 184, 271.

McLaughlin, 1960, Stellar Atmospheres, ed. by J. Greenstein (University of Chicago Press: Chicago).

Novikov, I. D. and Thorne, K. S. 1973, in Black Holes, Les Houches, eds. DeWitt and DeWitt (Gordon and Breach: N.Y.).

Paczynski, B. 1971, Ann. Rev. Astro. and Ap., 9, 183.

Prendergast, K. H. 1960, Ap. J., 132, 162.

Pringle, J. E. and Rees, M. J. 1972, Astro and Ap., 21, 1.

Rose, W. K. 1968, Ap. J., 152, 245.

Rose, W. K., 1972. Stellar Evolution, ed. by H-Y Chiu and A. Muriel (MIT Press: Cambridge. Mass.)

Rose, W. K. 1973, Astrophysics (Holt, Rinehart and Winston: N.Y.).

Shakura, N. I. and Sunyaev, R. A. 1973, Astro. and Ap., 24, 337.

Shapiro, S. L., Lightman, A. P. and Eardley, D. M. 1975, Preprint.

CHAPTER IV
X-RAY SIGNATURES OF COMPACT OBJECTS

Elihu Boldt
Goddard Space Flight Center
Greenbelt, Maryland

INTRODUCTION

Although the concept of an extremely compact stellar object (i.e., neutron star or black hole) has existed as a theoretical curiosity for a long time, the fundamental observational consequence of detectable X-radiation was somehow overlooked prior to the advent of experimental X-ray astronomy. We recall what a surprise it was to find that X-ray astronomy is even possible, in the sense that there are any detectable signals at all from beyond the solar system. Then there was the greater surprise that over a hundred stellar sources within our own galaxy each radiate X-rays at more than 10^{36} ergs/s (i.e. the luminosity of a thousand suns, in X-radiation alone). Now, after looking at the temporal and spectral signatures of several of the brightest sources, we suspect that most of the strongest sources, if not all, are associated with compact objects. Hence, we have come to realize that the main reason X-ray astronomy is flourishing is that compact stellar objects do in fact exist and that intense X-radiation is a direct consequence of energetic processes fundamental to them.

We can now go back and do the homework we should have done about twenty years ago. That is, we can see how far we could have gone in discussing the potential X-ray characteristics of compact stellar objects without knowing anything other than the most basic theoretical parameters of compact objects and some elementary laws of physics. Of course, given the advantage of knowing something about the actual X-ray data, this procedure is obviously artificial. Nevertheless, it may help to give us the kind of background needed for interpreting these data in a discriminating way and extracting the genuinely new information they must carry. We will try this out in practice later by examining some specific data which from the work of the x-ray astronomy group at Goddard Space Flight Center; provide us with a good challenge for three of the most interesting objects yet discovered, viz: Cyg X-1, Cyg X-3 and Her X-1.

II. X-RAY SCALES FOR COMPACT OBJECTS

As was indicated by Dr. Rose in Chapter I, a neutron star is expected to have a mass approximately that of the sun and a radius of about 10^6 cm. Hence, we introduce the dimensionless parameters M and R_6 defined by:

$$M \equiv M/M_\odot$$

$$R_6 \equiv R/(10^6 \text{ cm}).$$

The velocity (v_{ff}) of freely falling matter, as measured at R, is always given by

$$v_{ff} = (2GM/R)^{1/2} \tag{1}$$

Expressed in our dimensionless parameters, this becomes

$$v_{ff} = 0.542\, c(M/R_6)^{1/2}. \tag{2}$$

In other words, for a typical neutron star, the free fall velocity is about half the velocity of light. Hence, we note immediately that collisions with ambient matter will give rise to bremsstrahlung radiation in the X-ray band. Specifically, the endpoint for the bremsstrahlung spectrum of photons observed at infinity, emerging from the collisions of matter falling to the surface of a neutron star, is given (with m_0 the electron rest mass) as

$$(h\nu)_\infty = m_0 c^2 \left\{[1 - (v/c)^2]^{-1/2} - 1\right\} \left\{1 - (v_{ff}/c)^2\right\}^{1/2}. \tag{3}$$

For $M = R_6$ and $v = v_{ff}$ this gives 82 keV as the endpoint, placing the bulk of the emission in the usual hard X-ray region. On the other hand, for $M \geqslant 3.4\, R_6$, $v_{ff} = c$ and Equation (3) shows that $(h\nu)_\infty = 0$. Hence, if $R_6 \simeq$ is fundamental for a neutron star, then the mass cannot exceed 3 $M_\odot$ without the object becoming a black hole. X-radiation from near the surface of a compact object is then quite natural for a neutron star but impossible for a black hole. For a non-spinning black hole (Schwarschild metric), the orbital velocity for the innermost stable circular Keplerian orbit (Kepler radius $R_6 = 0.88\, M$) is precisely half the velocity of light and we again have conditions natural for collisional production of X-rays, but well above the surface of the star (Schwarschild radius $R_6 = 0.29\, M$).

The other basic parameter we consider is the magnetic field (H). A field of 10^6 - 10^7 G for a white dwarf or the core of a red giant would, with flux conservation, become a field on the order of 10^{12} - 10^{13} G when the object

collapses to a neutron star. Again we introduce a dimensionless parameter

$$H_{12} \equiv H/(10^{12}\ G)$$

The quantum of the magnetic field (i.e., the energy of cyclotron photons) is then

$$\hbar \frac{e}{mc} H = H_{12}\ (11.6\ KeV). \tag{4}$$

This is obviously in the X-ray band and implies important emission and absorption effects, as we shall describe later. Curiously enough, this huge magnetic field disappears as stellar collapse approaches the Schwarzschild radius and these magnetic effects are strictly absent for black holes.

III. ELECTROMAGNETIC RADIATION LIMITS

The general classical expression for the rate of energy radiated by an electron of velocity (v) in a field (**E**, **H**) is given by

$$\dot{W}_r = \frac{\sigma_o}{4\pi} \left[\left(\mathbf{E} + \frac{\mathbf{v}}{c} \times \mathbf{H}\right)^2 - \frac{1}{c^2} (\mathbf{E} \cdot \mathbf{v})^2\right] \gamma^2 c, \tag{5}$$

where

$$\gamma^2 \equiv [1 - (v/c)^2]^{-1} \text{ and } \sigma_o \equiv \frac{8}{3}\pi\ e^2/mc^2)^2$$

is the well known Thomson cross-section. We consider an electromagnetic environment of photons to obtain the results appropriate to inverse Compton scattering. We specify an ambient photon propagation direction by a unit wave vector (**k**) such that

$$\mathbf{H} = \mathbf{k} \times \mathbf{E}, \quad \mathbf{k} \cdot \mathbf{E} = 0. \tag{6}$$

Equation 5 may now be written

$$\dot{W}_r = \sigma_o\ U_{EH}\, c\, [1 - (\mathbf{k} \cdot \mathbf{v}/c)]^2/[1 - (v/c)^2] \tag{7}$$

where $U_{EH} \equiv E^2/8\pi$ is the energy density of such photons. In order to investigate the "force" exerted by these ambient photons we note that the rate of radiated momentum is $\dot{W}_r\, v/c^2$ and that of absorbed momentum is $\dot{W}_a k/c$, where W_a is the energy absorbed. Using energy and momentum conservation,

we find that the force in the k direction is (for $v^2 \ll c^2$), given by

$$F_k = \sigma_o U_{EH} [1 - 2(\mathbf{k} \cdot \mathbf{v}/c)]. \tag{8}$$

Averaging over photon propagation directions we get the net force arising from all ambient photons, as follows

$$\langle \mathbf{F} \rangle = \sigma_o U_{EH} \left[\langle \mathbf{k} \rangle - 2 \left\langle \frac{\mathbf{v} \cdot \mathbf{k}}{c} \mathbf{k} \right\rangle \right]. \tag{9}$$

For particles falling onto a compact object the second term is always negative; hence

$$\langle \mathbf{F} \rangle \geqslant \sigma_o U_{EH} \langle \mathbf{k} \rangle, \tag{10}$$

and the net total force inward (gravitational minus this electromagnetic radiation force) is always

$$|F_{net}| \leqslant \left[\frac{GMm}{R^2} - \frac{\sigma_o L}{4\pi R^2 c} \right] \tag{11}$$

where L is the luminosity, given by

$$L = 4\pi U_{EH} c \langle \mathbf{k} \cdot \mathbf{R} \rangle R. \tag{12}$$

This net total force vanishes when

$$L = (4\pi GMmc)/\sigma_o \equiv L_E, \tag{13}$$

where L_E is so defined (i.e., the Eddington luminosity limit).

The net total force may then be rewritten as

$$|F_{net}| \leqslant m\left(\frac{GM}{R^2}\right)\left(1 - \frac{L}{L_E}\right). \tag{14}$$

That is, in effect, the gravitational source term (GM) is reduced by the factor $(1 - L/L_E)$.

Because of the charge neutrality of the infalling plasma, the total mass per electron is essentially one atomic mass unit (amu); the protons couple to the gravitational field, the electrons couple to the ambient radiation field, and

Coulomb attraction couples the electrons and protons. Hence the mass (m) in Equation 13 refers to a mass of 1 amu, and the Eddington limit so evaluated is

$$L_E = 1.3 \times 10^{38}\ M\ \text{erg/s}. \tag{15}$$

It is convenient, therefore, to measure luminosity in units of 10^{38} ergs/s and define a dimensionless luminosity parameter (L_8) as

$$L_8 \equiv L/10^{38}\ \text{ergs/s})$$

If this limiting luminosity (i.e., Equation 15) arises from blackbody emission, the temperature is given by

$$T = 2.0\, M^{1/4}\, (R_6)^{1/2} \times 10^7\ \text{K}, \tag{16}$$

providing a spectrum that resides well within the X-ray region. Measuring temperature in units of 10^7 K, we define

$$T_7 \equiv T/(10^7\ \text{K})$$

and obtain the general blackbody expression for temperature in terms of luminosity and size as

$$T_7 = 1.9\, L_8^{1/4}\, R_6^{-1/2}. \tag{17}$$

For optically thin emission, the Eddington limit places restrictions on the population of radiating particles. For an ambient magnetic field ($H \neq 0$, $E = 0$), Equation 5 gives (with $\beta \equiv v/c$)

$$\dot{W}_r = \frac{4}{3}\, \sigma_o\, U_H\, \beta^2\, (1 - \beta^2)^{-1}. \tag{18}$$

Since the number of radiating particles is

$$N = L/\dot{W}_r \tag{19}$$

the Eddington limit (i.e., Equation 15) and Equation 18 give

$$N \leqslant 4 \times 10^{39}\, M\, (H_{12})^{-2}\, \beta^{-2} \tag{20}$$

where equation 4 implies that the electron velocity (β) in Equation 20 needs to exceed a minimum value, given by

$$\beta^2 > 0.045\ H_{12}. \tag{21}$$

Hence,

$$N \leqslant 9 \times 10^{40}\, M\, H_{12}^{-3} \tag{22}$$

The upper limit on the kinetic energy content W_e of electrons corresponding to Equation 19 is

$$W_e \leqslant 2 \times 10^{33}\, M\, H_{12}^{-2}\ \text{ergs}. \tag{23}$$

This upper limit will be particularly important when we examine the energy content of flare events associated with some of the compact sources.

For bremsstrahlung radiation, we use Equation 5 to give the radiation rate under the condition that

$$\langle (\mathbf{v} \cdot \mathbf{E})^2 \rangle = \frac{1}{3} E^2 v^2, \tag{24}$$

obtaining

$$\dot{W}_r = 2\sigma_c\, c \left(1 - \frac{\beta^2}{3}\right) U_E, \tag{25}$$

where the electric field energy density U_E is given (with $\alpha \equiv 1/137$) by

$$U_E = Z^2\, m_o c^2\, \beta n/(137\pi), \tag{26}$$

n being the number density of nuclei (charge Ze). Considering an equal number density of electrons and protons, the Eddington limit here puts a limit on the emission measure of the emitting region:

$$\int \dot{W}_r\, n\, d\,(\text{vol.}) < L_E \tag{27}$$

which, with Equations 25 and 26, may be expressed

$$\int n^2\, d\,(\text{vol.}) < 1.7 \times 10^{60}\, M \left(1 - \frac{\beta^2}{3}\right)^{-1} \beta^{-1}\ \text{cm}^{-3} \tag{28}$$

where, for the X-ray region, we require $\beta \simeq 0.05 - 0.5$. Since $\langle n^2 \rangle$ is always greater than $\langle n \rangle^2$ we may rewrite Equation 28 as

$$N^2/(\text{volume}) < 1.7 \times 10^{60} M \left(1 - \frac{\beta^2}{3}\right)^{-1} \beta^{-1} \text{ cm}^{-3}. \quad (29)$$

In terms of the energy content W of radiating particles, Equation 29 yields

$$W < 7 \times 10^{29} M^{1/2} \left(1 - \frac{\beta^2}{3}\right)^{-1/2} \beta^{3/2} (\text{volume})^{1/2} \text{ m c}^2. \quad (30)$$

This will help us isolate the particle population responsible for the burst events seen in Cygnus X-1 (a black hole candidate).

IV. ACCRETION

For emission driven by an accretion process with matter initially at rest, the luminosity is given by

$$L = \left(\frac{dM}{dt}\right) \frac{GM}{R} (1 - L/L_E), \quad (31)$$

where the rate of mass accretion (dM/dt) is given by

$$\frac{dM}{dt} = 4\pi\rho R^{3/2} \eta \, [2GM (1 - L/L_E)]^{1/2} \quad (32)$$

with η the ratio of infall velocity to free-fall velocity,

$$\eta = \langle (v \cdot R/R) \rangle \, [2GM (1 - L/L_E)/R]^{-1/2}. \quad (33)$$

From the above equations we obtain a lower limit on the density, given by

$$\rho \geq 3.7 \times 10^{-6} L_8 M^{-3/2} R_6^{-1/2} \text{ g/cm}^3 \quad (34)$$

(i.e., obtained for $\eta = 1$, $L \ll L_E$).

For a plasma at a temperature T_7, this may be used to infer a lower limit on the thermal kinetic energy density as

$$U_T \equiv \frac{3}{2} kT \left(\frac{\rho}{m}\right) \geq 29 \times 10^{20} T_7 M^{-3/2} R_6^{-1/2} \text{ eV/cm}^3. \quad (35)$$

For free-fall, the kinetic energy density U_{ff} would be given by

$$U_{ff} = \rho c^2 \left[\left(1 - 0.194 \frac{M}{R_6} \right)^{1/2} \right] \simeq \rho c^2 \left(0.15 \frac{M}{R_6} \right). \qquad (36)$$

From Equation 36 we note that $U_{ff} \simeq 0.2\ \rho c^2$ near the surface of a neutron star or the innermost stable orbit of a Schwarschild metric black hole, and $U_{ff} \simeq \rho c^2$ near the Schwarschild radius of a black hole.

From Equation 34, we get

$$\rho c^2 \geqslant 21 \times 10^{26}\ L_8\, M^{-3/2}\, R_6^{-1/2}\ \text{eV/cm}^3. \qquad (37)$$

For comparison, the energy density of the magnetic field is

$$U_H = 25 \times 10^{33}\ H_{12}^2\ \text{eV/cm}^3. \qquad (38)$$

Considering a dipole field (i.e. $H \propto R^{-3}$), the minimal kinetic energy density (Equations 36-37) would equal that in the magnetic field at a radius approximately $10 - 10^2$ times that for the maximum field strength. Hence, particle motion in this inner region is likely to be dominated by magnetic effects, leading to beaming and pulsed modulation as the dipole rotates. At a radius approximately $(10^5/T_7)$ that of a neutron star, we expect (from Equations 35 and 36) that the accreting plasma is dominated by thermal and/or external effects. The vast intermediate region is of course dominated by the gravitational field of the compact object.

V. RADIATIVE TRANSFER

Having established a lower limit to the density of accreting matter as a function of radius (see Equation 34) we are now in a position to evaluate a lower limit to the column density of the entire accreting atmosphere through which we might view the X-ray emission, viz:

$$\int_{R_6}^{\infty} \rho dr \geqslant 7.4\ R_6^{1/2}\ L_8\, M^{-3/2}\, (\Gamma^{1/2} - 1)\ \text{g/cm}^2 \qquad (39)$$

where we have assumed that this atmosphere extends to at least ΓR_6. First we notice the remarkable feature that this immediately implies a highly ionized atmosphere, for otherwise photoelectric absorption would render the source

invisible in the usual X-ray region (i.e., below $\simeq$ 20 keV). Even if the gas were so hot that all elements of lower Z than iron were completely ionized, the K shell electrons of iron at cosmic abundance alone would cause an appreciable absorption dip at about 9 keV. Hence, the temperature of the gas in this atmosphere is likely to be greater than 10^8 K and is almost certainly greater than 10^7 K.

Using Equation 34 for density, we evaluate the optical depth for free-free absorption as (τ_ν) as

$$\tau_\nu \geqslant 6 \times 10^{-5} (T_7)^{-7/2} \left(\frac{1 - e^{-x}}{x^3}\right) (L_8)^2 M^{-1} \ell n \Gamma \qquad (40)$$

where $x \equiv h\nu/kT$ and Γ is the ratio of the outer radius to the inner radius defining the atmosphere considered. For $T_7 \geqslant 1$, Equation 40 implies that the atmosphere could be extremely thin to emission and absorption. This is a lower limit to the optical depth, due mainly to the fact that we took $\eta = 1$ in evaluating the lower limit for density given in Equation 34. However, it is not likely that η would be smaller than about 10^{-3}. Although this would increase the optical depth by about three orders of magnitude, it would still be less than unity (i.e., optically thin).

The optical depth for Thomson scattering is (τ_s)

$$\tau_s = 2.9 R_6^{1/2} (\Gamma^{1/2} - 1) L_8 M^{-3/2} \qquad (41)$$

where R_6 is the radius of the source and $\Gamma(R_6)$ is the outer radius of the scattering atmosphere. It is quite likely, therefore, that this atmosphere be optically thick to Thomson scattering. We note, however, that Thomson scattering may be substantially altered in the presence of a strong magnetic field, since the transfer of energy to electron motion normal to the field is quantized at intervals $\hbar\omega = H_{12} \times 11.6$ keV and thus is severely restricted. The modified cross section (σ_H) may be expressed in terms of the Thomson cross section (σ_H) as follows:

$$\sigma_H^{\pm} (\theta) = \sigma_0 \left[\left(\frac{h\nu}{h\nu \pm 11.6 \text{ keV } H_{12}}\right)^2 + \frac{1}{2} \sin^2\theta\right], \qquad (42)$$

where θ is the angle between the field direction and the direction of photon propagation. For $h\nu << 11.6$ keV H_{12}, Equation 42 shows that the cross section at small angles can become much smaller than the value given by the unperturbed Thomson cross section. This opens up the interesting possibility

of an optically thin direction along the dipole axis even though the atmosphere in general might be optically thick to electron scattering.

An atmosphere that is optically thin for free-free absorption but thick for electron scattering has a rather novel consequence. If the electrons in this atmosphere are at a temperature T, then photons which come into thermal equilibrium with them by elastic Thomson scattering will acquire a Boltzmann energy distribution (*not* Planckian) given by

$$\frac{dN}{d\nu} \propto \nu^2 \exp(-h\nu/kT). \tag{43}$$

Monochromatic photons passing through a plasma of temperature T transfer an average energy per collision

$$\langle \Delta E_e \rangle = (h\nu/m_0c^2)(h\nu - 4kT). \tag{44}$$

When $h\nu \ll 4kT$, the photon energies get boosted by the collisions and the radiation is "Comptonized." If $h\nu > 4kT$, the photons heat the gas until $kT = h\nu/4$ and then emerge with the Boltzmann distribution, for which

$$\langle h\nu \rangle = 3kT, \ \langle (h\nu)^2 \rangle = 12\,(kT)^2, \tag{45}$$

and hence the expectation value for energy transfer (given by Equation 44) goes to zero.

For a black body source

$$\langle h\nu \rangle = 2.68\ kT_{BB}, \ \langle (h\nu)^2 \rangle = 10.1\ (kT_{BB})^2, \tag{46}$$

the condition of zero average energy transfer would (see Equation 44) imply that

$$T = \langle (h\nu)^2 \rangle / (4 \langle h\nu \rangle = 0.94\ T_{BB}. \tag{47}$$

Finally, we compare the Boltzmann and Planck distributions at the same T:

$$\frac{(dN/d\nu)_{Boltzmann}}{(dN/d\nu)_{Planck}} = [1 - \exp(-h\nu/kT)]; \tag{48}$$

This shows that they deviate from each other significantly only when

$$k\nu < kT.$$

VI. SOME OBSERVATIONS

Dr. Rose has already discussed, in Chapter 1, two well studied X-ray pulsars in eclipsing binary systems, Her X-1 and Cen X-3. Most of the X-ray data used in the interpretation of their binary behavior are temporal in character (e.g. Doppler variations of the pulsation period) and indicate that the compact member in each of these cases is a neutron star. We shall now emphasize the information provided by the X-ray spectra themselves. In addition to Her X-1, we shall describe some spectra obtained by the Goddard X-ray group for two compact objects which appear quite different, Cyg X-1 and Cyg X-3.

The data we shall describe were all obtained with the same complement of X-ray detectors during two rocket-borne experiments with launch dates separated by a year (October 4, 1973 and October 3, 1974). As is shown in Figure IV-1, the first of these flights examined Her X-1, Cyg X-3, and Cyg X-1 in that order, with exposures on the order of a minute each. We note the remarkable constrast in temporal behavior among the sources exhibited in this figure. For Her X-1 we see the pronounced periodic signal of the 1.24s pulsar. For Cyg X-3 the variations are strictly statistical (i.e., on such a small time scale the 4.8 hour periodicity produces negligible systematic effects). For Cyg X-1, rapid temporal variations are most pronounced and chaotic on time scales down to a millisecond (Figure IV-2).

The spectrum of Her X-1 is extremely simple (see Figure IV-3). The photon number spectrum follows a rather strict power law of unit index (i.e., $dN/d(h\nu) \propto (h\nu)^{-1}$) from somewhat below 2 keV to somewhat above 20 keV. Observations at higher energies indicate that the harder emission might not be pulsed.

We pursue the suggestion that the emission from Her X-1 comes from accretion onto the magnetic poles. Due to the suppression of Coulomb collision losses in the environment of intense magnetic fields, the particles falling onto the neutron star are stopped by nuclear collisions. The resulting penetration amounts to an optical depth for usual Thomson scattering of $\gtrsim 10$. However, as we have seen in the last section (see Equation 41), Thomson scattering along the field is also highly suppressed (i.e., along the dipole axis for regions near the poles) for $h\nu << (11.6 \text{ keV})H_{12}$. Hence, we expect the intensity near the dipole direction to vary as follows:

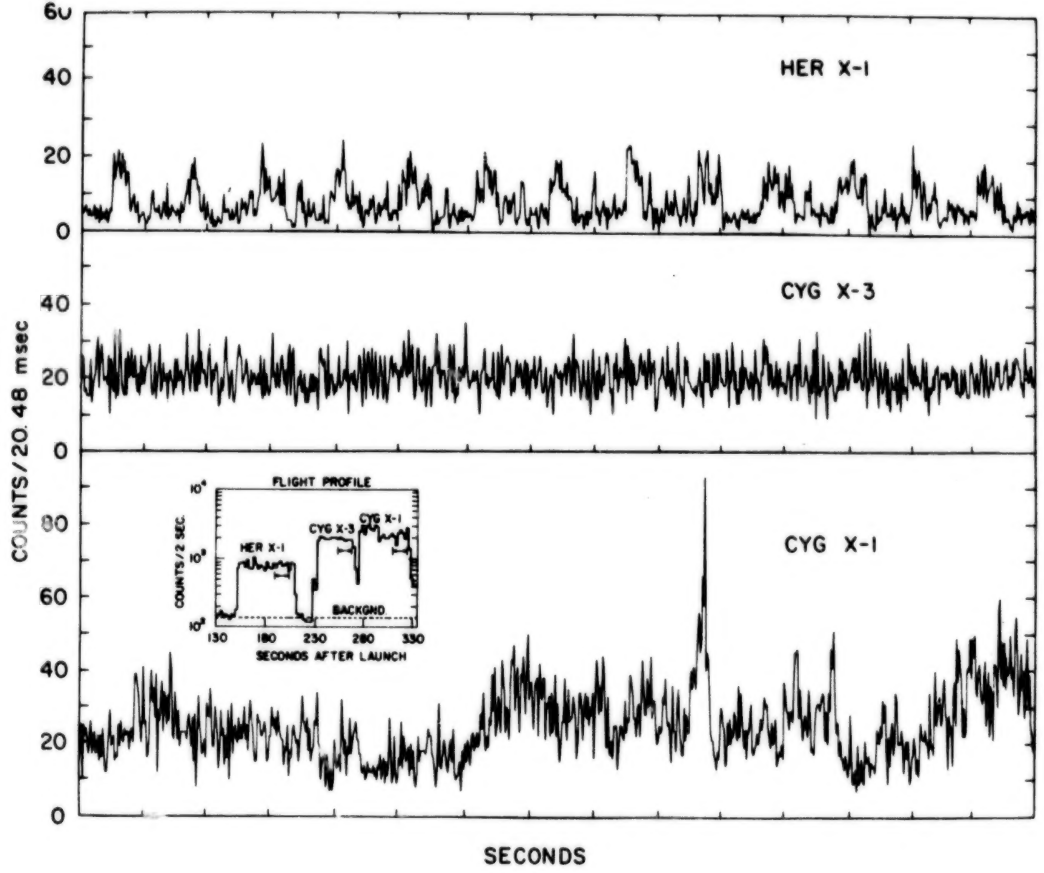

Figure IV-1. The count rate profiles binned every 20.48 ms, for Her X-1. Cyg X-3 and Cyg X-1 during 15-second exposure samples of each source obtained during the same rocket-borne experiment on October 4, 1973 (GSFC Flight 13.010). The inset shows the overall flight profile in counts per 2-second interval versus time after launch (in seconds). The arrows indicate when the 15-second data samples occurred relative to the full exposure.

86.

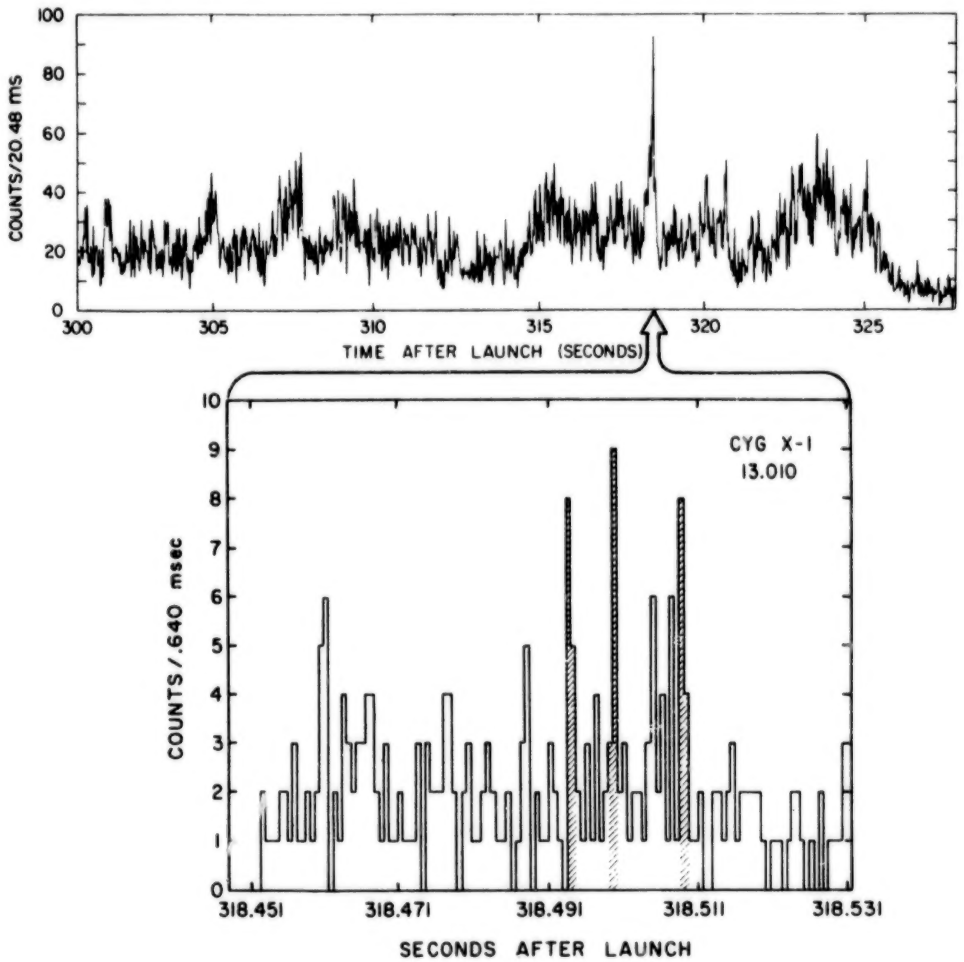

Figure IV-2. High time resolution data on Cyg X-1 obtained in GSFC Flight 13.010. The lower portion is an expansion of the peak of the "flare" at about 318.5 seconds after launch. The shaded elements correspond to statistically significant bursts of millisecond duration.

87.

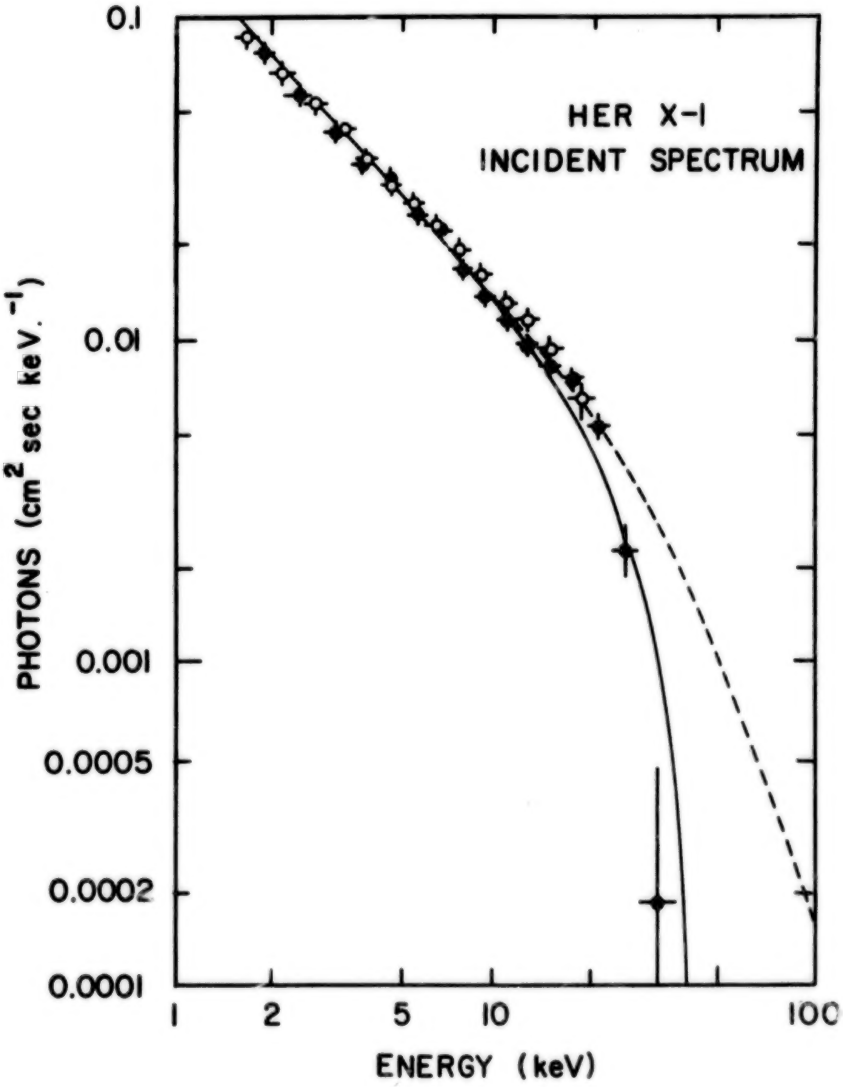

Figure IV-3. The average spectrum for Her X-1 obtained during GSFC Flight 13.010. The open symbols are taken from the argon-filled counter, and the closed symbols from the Xenon-filled counter. The dashed curve corresponds to attenuation of a pencil beam in the ordinary mode whereas the solid line corresponds to the extra-ordinary mode (with $\tau_s = 10$ and $H_{12} = 10$, in Equation 41).

$$I(h\nu, \theta) \approx I_0 (h\nu) \exp\left[-\frac{\tau_s}{2} \sin^2\theta - \tau_s \left(\frac{h\nu}{11.6 \text{ keV } H_{12}}\right)^2\right] \quad (49)$$

We see that the exponential factor only becomes a significant attenuator for

$$\sin\theta \geq [2/\tau_s]^{1/2} \quad (50)$$

and/or

$$h\nu \geq [(11.6 \text{ keV})H_{12}]/\tau_s^{1/2}. \quad (51)$$

For $\tau_s = 10$, Equation 50 implies $\theta \geq 27°$, consistent with the half-width of the pulsed beam. For $H_{12} = 10$, Equation 51 implies that spectral attenuation sets in at $h\nu \geq 37$ keV. This leads us to believe that the high energy cutoff behavior for Her X-1 at about 24 keV may be obtained via Equation 41, suitably fine tuning the parameters $\tau_s \gtrsim 10$ and $H_{12} \approx 10$. A source spectrum of the form $I_0 \propto (h\nu)^{-1}$ is not surprising for $h\nu$ small compared with any of the possible characteristic driving energies (e.g. > 100 keV for kT, 11.6 keV(H_{12}) or free-fall bremsstrahlung end point). As shown in Figure IV-3, we obtain a remarkably good fit for attenuation that is dominated by the extraordinary mode (i.e., minus sign for Equation 42), which is to be expected for $\tau_s(h\nu)/(11.6 \text{ keV}) H_{12} > 1$.

Figure 4 shows the spectrum obtained for Cyg X-3 on October 4, 1973. Considering data below 10 keV, it is well fit by a blackbody spectrum of kT = 1.24 keV (a high energy tail above 10 keV cannot be excluded). Normalized to a distance of 10 kpc, the apparent source luminosity is L(1.7 - 40 keV) = 8.8×10^{37} ergs/s, whereas the blackbody luminosity at the inferred temperature ($T_7 = 1.4$) is $L = 7.2 \times 10^{37}$ ergs/s. Since 10 kpc is a likely lower limit to the distance, we note that the luminosity is close to the Eddington limit. Using Equation 15, we obtain

$$M \geq 0.7.$$

From Equation 17 we obtain the blackbody radius as

$$R_6 = \frac{(1.9)^2 L_8^{1/2}}{1.4^2} = 1.84\, L_8^{1/2} \gtrsim 1.6.$$

Hence, the mass and radius of the blackbody are comparable to those expected for a neutron star.

Figure IV-5 shows the spectrum obtained for Cyg X-3 one year later (October 3, 1974). The differences may be summarized as follows:

(1) At energies of about 4 keV the new spectrum is depleted of photons by an order or magnitude, but at energies above about 15 keV it becomes harder than the earlier spectrum.

(2) The second spectrum shows a strong spectral feature near the energy region where iron K-line emission would be expected.

Acceptable fits may be obtained for the spectrum of Figure IV-5 by assuming optically thin thermal emission with $kT \geqslant 17$ keV and a line at 6.7 keV with an equivalent continuum width of 1.2 keV (i.e. for kT = 17 keV, the power in the line is 7% of the total power in the continuum). The apparent source luminosity is $L(1.7 - 40\ \text{keV}) = 4.2 \times 10^{37}$ ergs/s. However, this is a lower limit since the spectrum may still have an appreciable contribution from beyond 40 keV. Further, since this observation was taken near zero phase of the 4.8 hour periodicity (i.e., at an intensity minimum) it needs to be normalized upward for comparison with the earlier observation which occurred at a phase 0.8. We conclude, therefore, that both luminosities are about the same and are at or very near the Eddington luminosity. As we have seen in Section IV, the accretion rates and density profiles may change appreciably near the Eddington limit, thereby producing a variety of spectra at the same luminosity.

To what extent could the optically thin spectrum be considered that for the source of the optically thick spectrum seen through an optically dense atmosphere? It is interesting to note, in this connection, that the optically thick spectrum of Figure IV-4 could be as well fit by a Boltzmann distribution (see Equation 43) as by a blackbody (both at the same temperature), since there were in fact no observations below kT = 1.24 keV, and even if there had been they would have been severely modified by interstellar absorption effects. As described in the last section, the atmosphere for a source near the Eddington limit is likely to be optically thick for electron scattering, but thin for free-free absorption.

What sort of inputs are permissible for an emerging Boltzmann spectrum at kT = 1.24 keV? From Equation 45 we note that

$$\langle (h\nu)^2 \rangle / \langle (h\nu) \rangle = 4\ kT \approx 5\ \text{keV}.$$

Hence, for example, a single line at 5 keV would be one possibility, but that is not what was seen. For a spectrum of the form

CONTENTS

	Page
Foreword	iii 1/A7
Chapter I - STELLAR EVOLUTION FROM MAIN SEQUENCE STAR TO WHITE DWARF, NEUTRON STAR OR BLACK HOLE by William K. Rose	1 1/A9
Introduction	1 1/A9
Main-Sequence Stars	3 1/A11
Red Giants	4 1/A12
Planetary Nebulae and the Final State of the Sun	9 1/B3
Production of Magnetic Fields in Stellar Interiors	10 1/B4
Stellar Collapse to Neutron Star on Black Hole	13 1/B7
Chapter II - PULSARS by D. C. Backer	15 1/B9
Introduction	15 1/B9
Spin Properties	17 1/B11
Average Waveform	21 1/C1
Radio Spectrum	24 1/C4
Fluctuation Waveform	29 1/C9
Interstellar Medium	40 1/D6
Conclusion	43 1/D9
Short Topical Bibliography	46 1/D12
Appendix II-A - Listing of Data on 147 Pulsars	49 1/E1
Chapter III - BINARY STARS AND COMPACT X-RAY SOURCES by William K. Rose	55 1/E7
Binary Stars	55 1/E7
Stellar Evolution in Close Binary Systems	59 1/E11
Novae	61 1/E13
Mass Accretion onto Neutron Stars	64 1/F2
Mass Accretion onto Black Holes	68 1/F6
Bibliography	74 1/F12

Page

Chapter IV - X-RAY SIGNATURES OF COMPACT OBJECTS
by Elihu Boldt 75 1/F13

Introduction 75 1/F13
X-Ray Scales for Compact Objects 76 1/F14
Electromagnetic Radiation Limits 77 1/G1
Accretion 81 1/G5
Radiative Transfer 82 1/G6
Some Observations 85 1/G9
Acknowledgments 96 2/A9

Chapter V - GAMMA RAYS FROM COMPACT OBJECTS
by Hakki Ögelman 99 2/A12

Introduction 99 2/A12
Observations 101 2/A14
Pulsar Environments and Gamma Ray Production 109 2/B8
Contribution of Pulsars to the Galactic Gamma Ray Emission 115 2/B14
Bibliography 122 2/C7

Chapter VI - TEMPORAL ANALYSIS OF X-RAY DATA
by Richard Rothschild 125 2/C10

What do the Data Look Like? 125 2/C10
What do we do with the Data? 127 2/C12
What do the Results Mean? 149 2/E6
Appendix VI-A 151 2/E8
Appendix VI-B 166 2/F9
Bibliography 170 2/F13

Chapter VII - RECOGNITION OF COMPACT ASTROPHYSICAL OBJECTS IN THE BINARY PULSAR PSR 1913 + 16
by Steven Detweiler 173 2/G2

The Parameters of PSR 1913 + 16 ..... 173 2/G2
The Nature of the Companion 175 2/G4
The Determination of the Masses of the Binary System 176 2/G5
Effects of General Relativity 179 2/G8
Bibliography 180 2/G9

Page

Chapter VIII - PULSAR THEORY
by William K. Rose and Philip Hardee 181 2/G10

Bibliography 194 3/A12

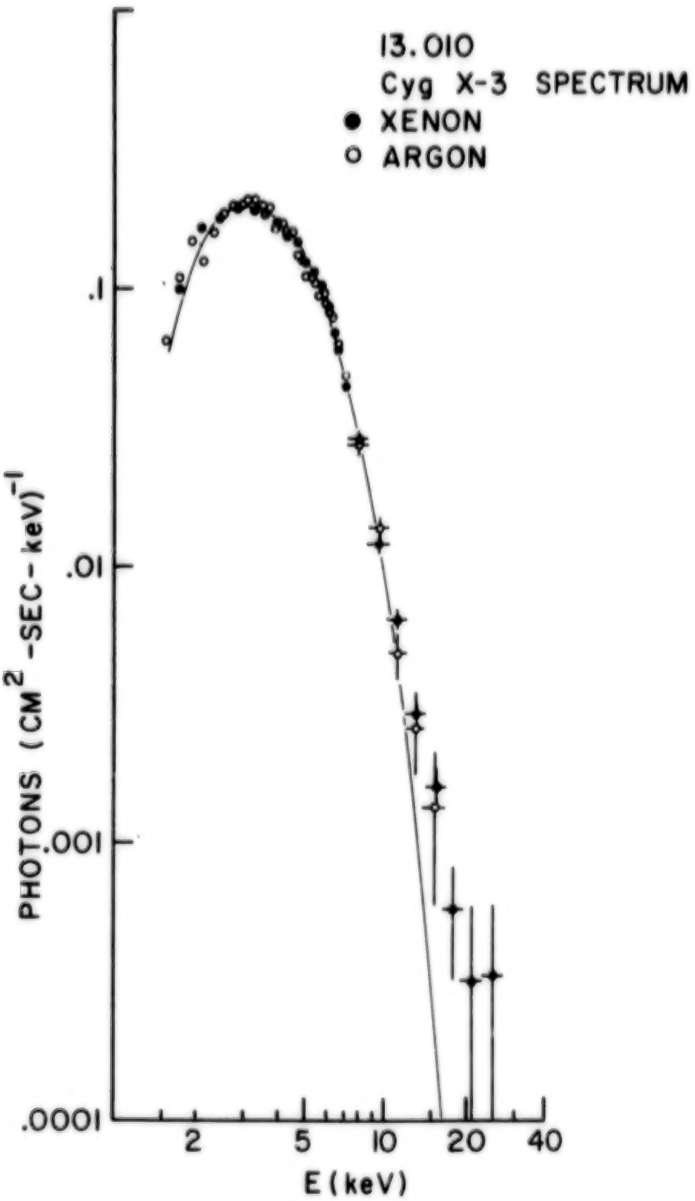

Figure IV-4. The spectrum obtained for Cyg X-3 on 4 October 1973 (GSFC Flight 13.010).

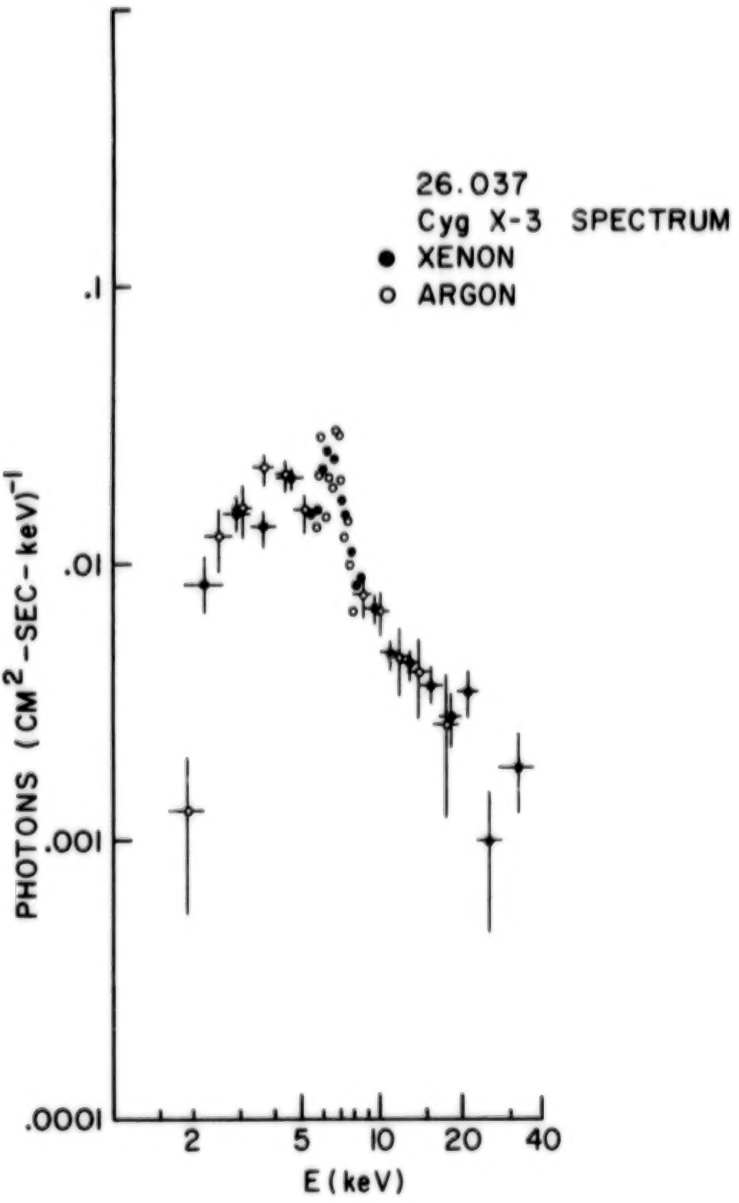

Figure IV-5. The spectrum obtained for Cyg X-3 on 3 October 1974 (GSFC Flight 26.037).

$$\frac{dN}{dh\nu} \propto (h\nu)^{-1} \exp(-h\nu/kT')$$

we have

$$\frac{\langle (h\nu)^2 \rangle}{\langle h\nu \rangle} = kT'. \tag{52}$$

This implies $kT' = 5$ keV, clearly less than the lower limit of 17 keV obtained for the spectrum of Figure IV-5. For a power-law spectrum of number index Γ and end-point E_0 we find

$$\frac{\langle (h\nu)^2 \rangle}{\langle h\nu \rangle} = \left(\frac{2-\Gamma}{3-\Gamma}\right) E_0. \tag{53}$$

Taking kT for the Boltzmann Equation, then Equations 45 and 53 imply

$$\frac{2-\Gamma}{3-\Gamma} = \frac{4kT}{E_0}. \tag{54}$$

For $kT = 1.24$ keV and $E_0 = 40$ keV this implies $\Gamma \approx 1.9$, which is steeper than the optically thin spectrum observed. Finally, let us consider a blackbody as the source spectrum. From equation 46 we find that the corresponding blackbody source would be one for which $kT = 1.4$ keV, not much different from that already considered.

Although the spectrum of Cyg X-1 is notorius for variations, it is in fact the most stable in X-ray astronomy. From the first detection of radio emission in March 1971 to the apparent transition in April 1975 (i.e., ~4 years) the spectrum remained remarkably constant. For example, the two spectra (Figures IV-6 and IV-7) obtained one year apart with the same instrument are both statistically significant and indistinguishable for the band covered ($\simeq 1.5 - 40$ keV). They both yield a power-law spectrum of number index 1.57, presumably highly characteristic of this emission from an accretion disk. Normalizing to a minimum distance of 2.5 kpc, we find the luminosity to be $L \geq 2.9 \times 10^{36} E_0^{0.43}$ ergs/s, where E_0 is the upper end of this power law spectrum. Since $E_0 \geq 40$ keV, we obtain

$$L > 1.4 \times 10^{37} \text{ ergs/s.}$$

Since this source is probably several solar masses (i.e., a black hole), the luminosity might very well be much below the Eddington limit.

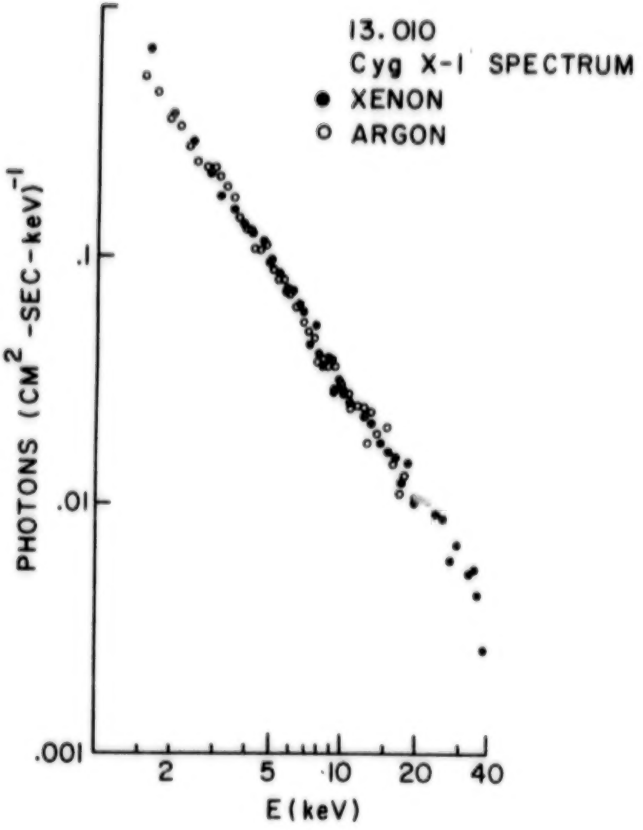

Figure IV-6. The spectrum obtained for Cyg X-1 on 4 October 1973 (GSFC Flight 13.010).

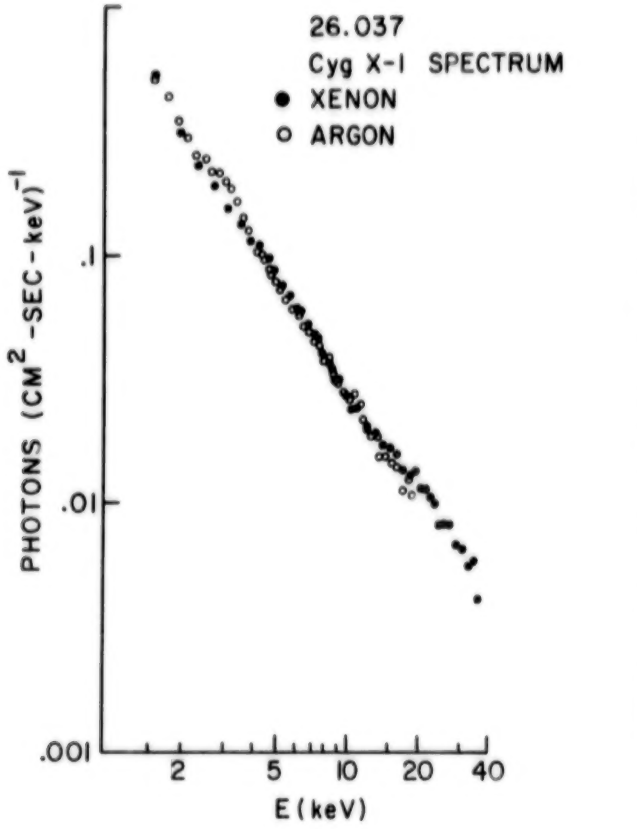

Figure IV-7. The spectrum obtained for Cyg X-1 on 3 October 1974 (GSFC Flight 26.037).

As Dr. Rothschild will discuss in detail in Chapter 6, the bulk of this emission may be characterized by randomly occurring events (i.e., shot noise) of comparable magnitude, such that we might express the average luminosity as

$$L = W\lambda$$

where W is the mean energy per event and $\lambda \lesssim 20\ s^{-1}$ is the average rate of events (at least during the two observations considered here). Hence we conclude that

$$W \geqslant 7 \times 10^{35}\ \text{ergs}.$$

Following the arguments of Section III, we conclude that

$$W_e \leqslant 1.5 \times 10^{33}\ L_8/H_{12}^2 .$$

Hence, the lower limit to the energy per event places an upper limit on the magnetic field associated with electrons radiating cyclotron radiation in this band. This yields $H_{12} < 2 \times 10^{-2}$.

For bremsstrahlung radiation we have the condition

$$W < \quad 6 \times 10^{29} \sqrt{L_8}\ \frac{\beta^{3/2}}{(1-\beta^2/3)^{1/2}}\ (\text{Vol.})^{1/2}\ \ m\,c^2.$$

Since the duration of these events is a fraction of a second and $\beta \leqslant 0.5$ we have that the emitting volume $< 3 \times 10^{30}\ cm^3$. Hence

$$W < 10^{38}\ [m/m_{(\text{electron})}]\ \text{ergs},$$

and we do not obtain a significant restriction (i.e., the shot noise events are well under 10^{38} ergs each). However, the millisecond bursts have an energy of $\gtrsim 1.4 \times 10^{35}$ ergs each. For millisecond bursts the maximum emitting volume is down by a factor of about 10^{-9} relative to "one second" events, and we obtain the corresponding constraint

$$W < 3 \times 10^{33}\ [m/m_{(\text{electron})}]\ \text{ergs}.$$

This tells us that the radiating particles must be more massive than electrons (for example, the energy content in protons could be as high as 6×10^{36} ergs).

So far we have restricted ourselves to some data below 40 keV, the region of the spectrum accessible from rocket-borne proportional counters. The larger exposures and extended response needed for examining the harder emission from compact X-ray sources is best supplied by satellite-borne scintillation counters and solid state detectors. Results from one such pioneering experiment are summarized in Figure IV-8. These spectra represent long-term averages and give us a rather simple picture for characterizing the gross spectral properties for the X-ray emission from sources in binary systems. Expressed as energy spectra (i.e., keV/keV), they are remarkably flat at low energies ($\leqslant$10 keV) and then fall off rather abruptly at a few tens of kilovolts, with essentially no detectable emission for energies above about 50 keV. As we noted in Section II, such energy scales are to be expected for compact objects such as neutron stars and black holes.

ACKNOWLEDGMENTS

The notion of an "effective" gravitational source term $GM(1 - L/L_E)$ is based upon a point of view of the Eddington limit given to me by Professor E. Schatzman.

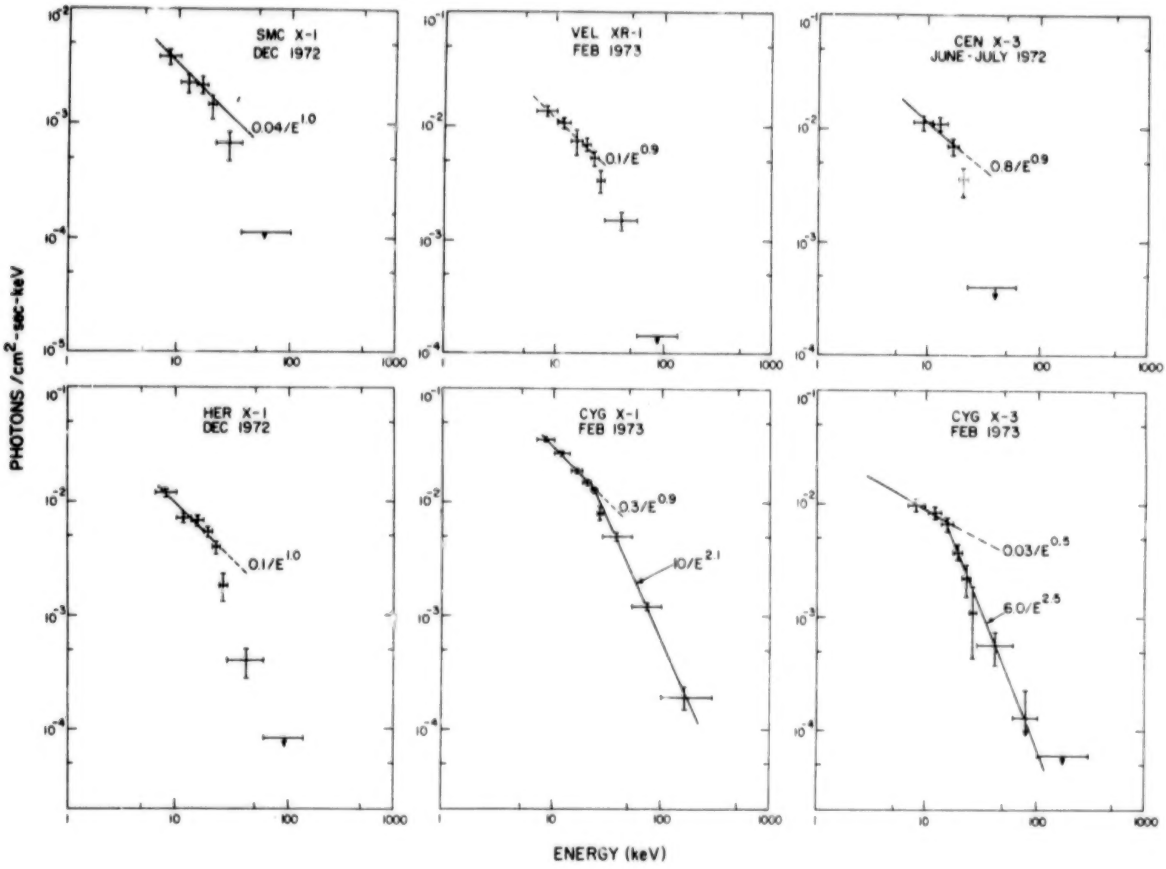

Figure IV-8. Spectra derived from observations with the USCD OSO-7 x-ray telescope (Source: Ulmer, 1975). The spectral index for Cyg X-3 (below the break) indicated here is a correction to the original figure.

M. M. Basko and R. A. Sunyaev, "Radiative Transfer In a Strong Magnetic Field and Accreting X-ray Pulsars" 1975, Ay. and Ap., 42, 311 Institute for Space Research, Moscow.

E. Boldt "Cosmic Ray Photons," Chapter IV in "Lectures In High Energy Astrophysics," (ed. H. Ogelman and J. R. Wayland) 1969, NASA SP-199, Washington, D. C.

H. Gursky and E. P. J. van den Heuvel, "X-ray Emitting Double Stars" 1975, Scientific American Vol. 232, No. 3 (March) p. 24.

S. Holt, "Galactic X-ray Sources," Chapter VII in "High Energy Particles and Quanta in Astrophysics" (ed. F. B. McDonald and C. E. Fichtel 1974. The MIT Press, Cambridge, Mass.

S. S. Holt, E. A. Boldt, R. E. Rothschild and P. J. Serlemitsos, "A New Measurement of the Her X-1 X-ray Pulse Profile" 1974, Ap. J., 190, L109.

Landau and E. Lifshitz, "The Classical Theory of Fields" 1951, Addison-Wesley, Reading, Mass.

S. Lodenquai, V. Canuto, M. Ruderman and S. Tsuruta, "Photon Opacity In Surfaces of Magnetic Neutron Stars" 1974, Ap. J. 190, 141.

L. Maraschi, C. Reina and A. Treves, "On Spherical Accretion near the Eddington Luminosity" 1974, Ay. and Ap. 35, 389.

I. D. Novikov and K. S. Thorne, "Astrophysics of Black Holes" p. 343-450 in "Black Holes" (ed. C. and B. S. DeWitt) 1973, Gordon and Breach, New York.

R. E. Rothschild, E. A. Boldt, S. S. Holt and P. S. Serlemitsos, "Millisecond Temporal Structure in Cygnus X-1" 1974, Ap. J., 189, L13.

P. J. Serlemitsos, E. A. Boldt, S. S. Holt and R. E. Rothschild, "Spectral Variability of Cyg X-3" 1975, Ap. J. (Letters) 201, L9.

M. P. Ulmer, "Galactic X-ray Sources" Proceedings of International Conference on X-rays In Space, 1975 (U. of Calgary: Calgary) p. 128.

Ya. B. Zeldovich and I. D. Novikov, "Relativistic Astrophysics," Vol. 1, "Stars and Relativity," 1971, University of Chicago Press.

CHAPTER V
GAMMA RAYS FROM COMPACT OBJECTS

Hakki Ögelman*
Goddard Space Flight Center
Greenbelt, Maryland

I. INTRODUCTION

In contrast to radio and x-ray emission studies from compact objects, the gamma ray observations, at best, can be classified as "underdeveloped." If we examine the productivity of these regions of the electromagnetic spectrum we see that about 150 compact objects (pulsars) have been discovered in the radio, and about 40 in the x-ray region (mass-accreting neutron stars). The gamma ray region, on the other hand, has two compact objects on its inventory. Furthermore, of these two, the Crab Nebula and Vela pulsars were initially discovered in the radio region. We need not be too apologetic, however, since in the rest of the electromagnetic spectrum the Crab pulsar is the only object seen in other than the radio, X-ray, and gamma ray regions.

Two of the strongest gamma ray sources which the present level of experimental sophistication allows us to see are compact objects. This is similar to the history of x-ray astronomy, in which the strongest sources detected initially, are now interpreted as mass-accreting compact objects. In contrast, the two strongest radio sources first discovered were a supernova remnant and another galaxy. Today pulsars are a small set of thousands of radio sources, whereas compact x-ray sources constitute about 30% of all the sources observed in x-rays. The conclusion we can draw from this type of data is that as gamma ray astronomy techniques develop we can hope to see compact objects emerging as the main component of sources emitting in this energy region. The expectations of the future, then, justify a discussion of the implications of just two gamma-ray sources in our understanding of the physical processes that take place in compact objects.

We may ask, what is special about gamma rays and compact objects? In the previous lectures we have heard about radio emission from pulsars and x-ray emission from neutron stars in close binary pairs. These emissions reflect quite different conditions. The radio emission from pulsars signifies a non-thermal process requiring strong magnetic fields and very energetic electrons. In such emission processes we have to have a very tenuous medium, vacant of

*NAS-NRC Senior Postdoctoral Research Associate at GSFC, on leave from Middle East Technical University, Ankara, Turkey.

any significant material, so as to prevent the energetic electrons from thermalizing in the medium. In contrast, the proposed emission mechanism for x-ray-emitting compact objects is thermal emission of material that gets heated up as it falls into the gravitational potential well of a neutron star. As we have seen, the rate of energy release in this well if related to the size of neutron star, has an effective temperature that causes emission in the x-ray binaries. We would then expect to encounter a material starved, magnetic field rich emission process. Our first response would be that under these circumstances, nothing very special should happen in the gamma ray region. The electromagnetic emission spectrum in magnetic fields more or less follows the trend in the electron spectrum; if anything, it steepens with respect to the normal trend at high energies. Since, *a priori*, we expect the energetic electrons in pulsars to have some form of power law distribution that gives rise to all the emission, we should not expect any special enhancement in our simplistic approach. Indeed, the spectrum observed for the Crab Nebula pulsar does justify this notion; however, the Vela pulsar is not observable between the radio and gamma ray regions. Actually, a source is observed in the 2–10 keV range which appears to show pulsations occasionally. Certainly, the two objects behave quite differently in the region between 10^{-3} to 10^{7} eV.

One process that lends special importance to gamma rays around 100 MeV is the production of π° mesons in high energy interactions of nucleons with matter. Subsequently the π° mesons decay into two gamma rays with $\simeq$70 MeV energy each in the π° reference system. The geometry of the collisions with respect to the observer doppler-broaden this in the laboratory frame; however, the peak of the distribution is always centered around 70 MeV. Effectively, then, gamma rays around this energy are the characteristic quanta that high energy nuclei emit in material, just as thermal activity is indicated by emission lines of the atoms. However, as we shall discuss later, the pulsars are believed to have very little material in their magnetospheres and the π° production mechanism does not appear to be effective.

Turning back to the material starved, electromagnetically rich pulsar magnetosphere, we can speculate on how we might get special emphasis in the emission around the gamma ray region. As a beginning, consider observations of secondary gamma rays at sea level in the earth's atmosphere. If we performed such an experiment, we could notice an excess of gamma rays around 100 MeV. Although the details of the individual interactions are complex we can guess roughly why the energetic photons cluster around 100 MeV. Initially we start on top of the atmosphere with a very energetic gas of cosmic rays. The atmosphere is many interaction mean-free-paths thick both to this hot gas and to its secondary components. The energetic protons quickly interact, producing π-mesons which immediately decay into electrons, positrons,

and gamma rays. The electrons predominantly lose their energy by bremsstrahlung to photons of comparable energy, and the photons pair-produce and create electrons with similar energies. The electromagnetic cascade thus multiplies and grows. When the average energy drops to around 100 MeV, the electrons start losing their energy predominantly by ionization and the photons by Compton processes. At this stage the electron and photon components can no longer sustain each other and the shower stops growing. Furthermore, around 100 MeV the photons have their minimum cross section and they can emerge more readily at sea level. We may expect a similar situation in the pulsar magnetospheres. In this case, although there is no material, the electrons and photons are coupled to each other through the intense magnetic fields. In particular, the photons anihilate with the characteristic photons of energy $\hbar eB/mc$ of the magnetic fields, and produce electron-positron pairs. The threshold of this process is around 25 MeV on the surface where $B \simeq 10^{13}$ eV at the speed of light cylinder. In a simplistic approach then, we can suspect that energetic electrons and photons will create a shower wherein the emerging flux of photons would have energies in the range indicated, which conveniently falls into the gamma ray range; thus we have a gamma ray biased emission.

With these general considerations we shall proceed to examine the gamma ray data in Section II, and gamma ray production in pulsars in Section III. In Section IV we shall try to estimate the relation of gamma rays from pulsars to the total galactic gamma ray emission.

The discussion of the data will be limited to the energy region 35 MeV to 100 MeV and we shall primarily discuss the results from the SAS-2 satellite, since at present it offers the most complete self-consistent survey of the galaxy in this energy region.

II. OBSERVATIONS

The first compact source discovered in gamma rays is the pulsar NP0531 in Crab Nebula. The energy range in which this object is detected extends from radio photons to 10^9 eV and possibly up to 10^{12} eV. The electromagnetic spectrum in the range 10^5 to 10^9 eV is shown in Figure V-1. The dashed line represents the intensity of the Crab Nebula supernova remnant. As can be inferred from the figure, while in the 1–10 keV range the pulsar emission is about 10% of the total nebulosity; above 10 MeV the pulsar emission dominates over the supernova remnant. Figure V-2, shows the phase distribution of gamma ray events above 35 MeV as measured by SAS-2 detector folded modulo of NP0531 radio period. Also shown on the same figure are the

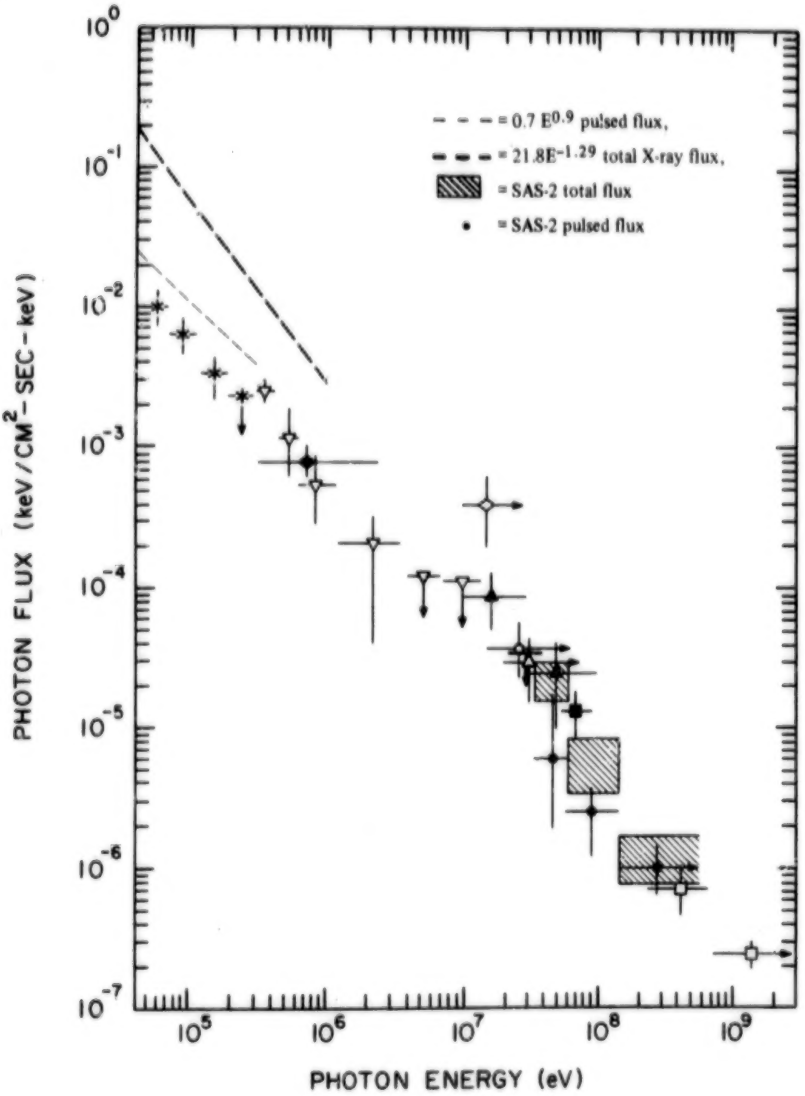

Figure V-1. Spectral distribution of fluxes observed from the region of the Crab nebula. The lower dashed line is the pulsed flux ($0.7E^{-0.9}$), the upper dashed line is the total x-ray flux ($21.8\ E^{-1.24}$), the hatched boxes are the SAS-2 total flux measurements, and the solid dots are the SAS-2 pulsed flux (Source: Kniffen et al., 1974).

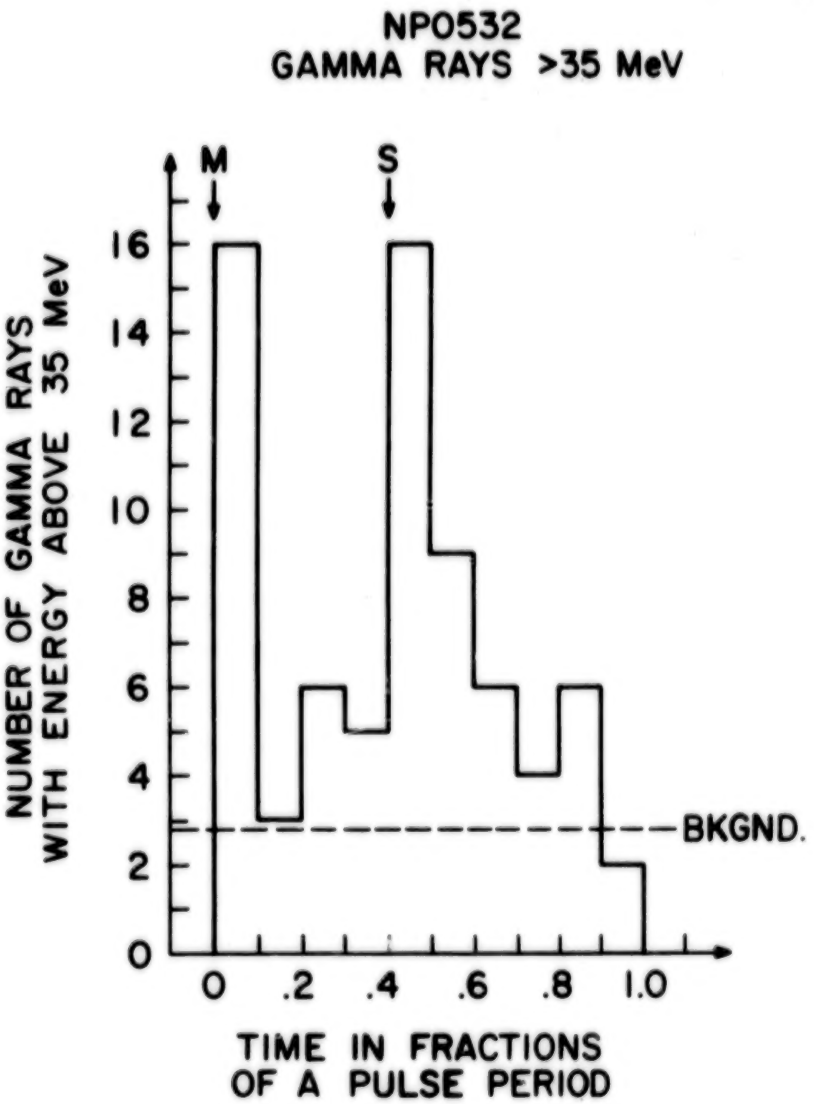

Figure V-2. The phase distribution of gamma ray events above 35 MeV as measured by SAS-2 detector folded modulus of NP0531 radio period. The arrival times of the main (M) and secondary (S) radio pulses corrected for interstellar dispersion are marked (Source: Kniffen et al., 1974).

arrival times of the main (M) and secondary (S) radio pulses, corrected for interstellar dispersion. The gamma ray distribution shows two peaks which are coincidental with the corresponding radio features. The statistical probability of getting this phase distribution is around 10^{-5}. The flux of pulsed gamma rays above 35 MeV is $(6.2 \pm 2.8) \times 10^{-6}$ photons cm^{-2} s^{-1}, and above 100 MeV it is $(2.2 \pm 0.7) \times 10^{-6}$ photons cm^{-2} s^{-1}.

Since the Crab pulsar, with its 33 ms period is the fastest known pulsar, it is natural to go down the line and examine other pulsars. The second fastest pulsar, PSR1913 + 16, has a period of 59 ms. However, it is a binary pulsar and its period and orbit parameters are not known accurately enough to permit gamma ray pulsation analysis. The third fastest pulsar is PSR0833-45, the Vela pulsar, which is located four times closer than the Crab pulsar. Indeed, SAS-2 results of the gamma ray emission of Vela show a strongly pulsed flux with the 89 ms period of the radio pulsar. Figure V-3 shows the phase plot of these gamma rays. One strange feature of the gamma ray phase distribution is that, unlike its radio counterpart, it shows two peaks. For the radio observations there is only an upper limit to a second pulse away from the main pulse amplitude. In the gamma ray region the second pulse is almost as intense as the main one. Moreover, the radio peak does not coincide with either of the gamma ray peaks. The pulsed flux above 35 MeV is $(15.1 \pm 2.4) \times 10^{-6}$ photons cm^{-2} s^{-1}. In the wavelength region between radio and gamma rays, the features of the Vela pulsar differ from that of the Crab Nebula pulsar. The intrinsic luminosity ratio of Crab to Vela pulsars, L_{Crab}/L_{Vela}, is 8 around 100 MeV, 80-100 around X-ray energies, and >5000 at optical wavelengths. As far as gamma rays are concerned there is hardly any difference in the phase plots of these pulsars. Figure V-4 shows the pulse shape of these two pulsars in various energy bands.

The various observational features of these two pulsars are summarized in Table V-1.

In addition to the positive results we can set upper limits to a variety of pulsars that have accurate enough period and period derivative information. The preliminary results of such an effort are summarized in Table V-2. What has been done in the analysis is the following: Gamma rays arriving from the proper position of the pulsar, within about 2σ of the angular accuracy of the measurements, were folded modulus of the pulsar period at the solar system barycenter. The phase distribution was then examined in bins of 0.1 period phase. Since we do not have, *a priori*, a good estimate of what pulse shape to expect (remember that the phase plot of gamma rays from Vela pulsar does not look like its radio counter part), we merely check the χ^2 analysis of the phase distribution's compatibility with random data. Since none of

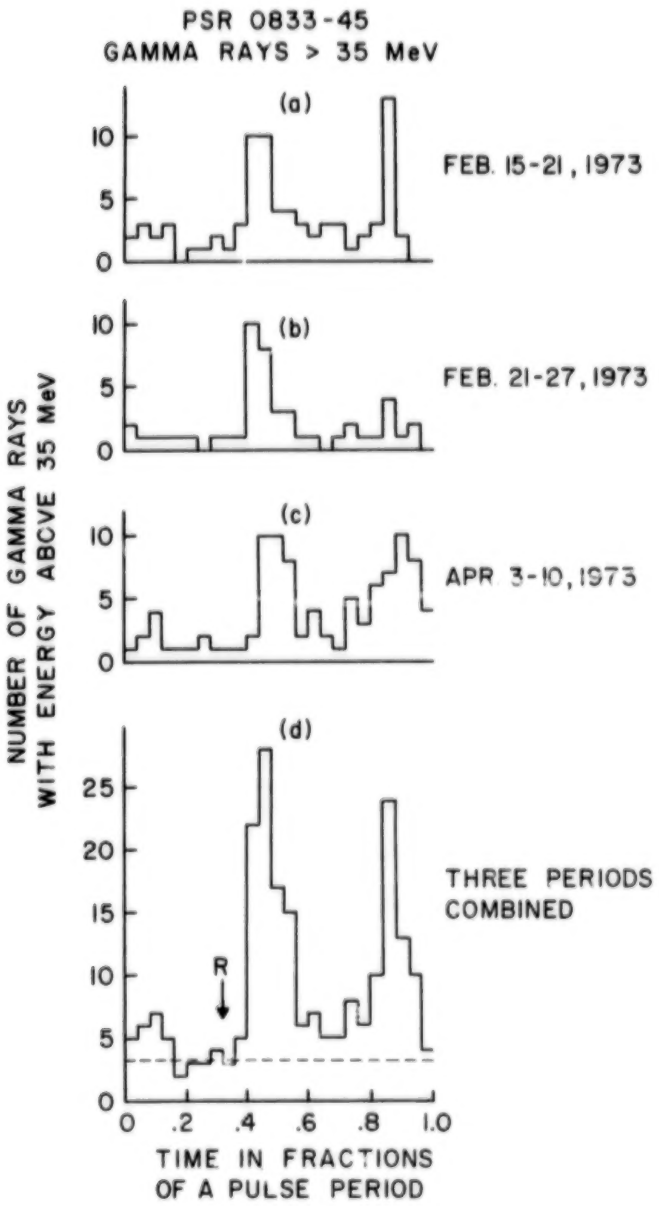

Figure V-3. Phase plot of gamma rays from Vela pulsar using 89 ms period (Source: Thompson et al., 1975).

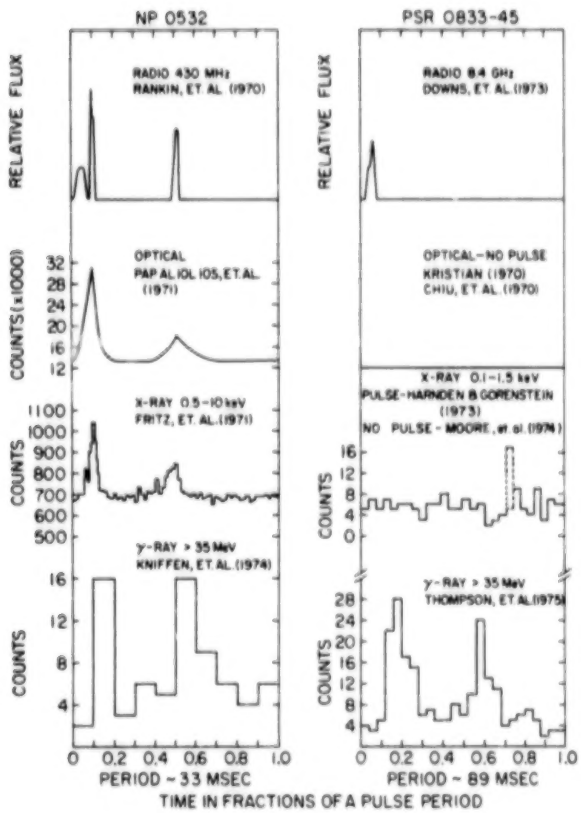

Figure V-4. Pulse shape of the Crab and Vela pulsars at various energy ranges.

Table V-1
Summary of NP0531 and PSR0833-45 Data

Source	Period (sec)	Drst. (pc)	Apparent Age $P/2\dot{P}$ (yr)	Pulsed γ-Rays >35 MeV			Rotational* Energy Loss Rate (ergs s^{-1})
				Flux (cm^{-2} s^{-1})	Lum† (ph. s^{-1})	Lum† (ergs s^{-1}	
NP 0531	.03313	2000	1.2×10^3	$(6.2 + 2.8) \times 10^{-6}$	$(3.0 \pm 1.4) \times 10^{38}$	5×10^{34}	4.5×10^{38}
PSR-0833-45	.08922	500	1.1×10^4	$(15.1 \pm 2.4) \times 10^{-6}$	$(4.6 \pm .7) \times 10^{37}$	7×10^{33}	7×10^{36}

*I assumed to be 10^{45} g · cm^2

†The emission solid angle of the pulsar assumed to be 0.4π sr.

Table V-2
Summary of Data on Pulsars with Upper Limits to
γ-Ray Flux above 35 MeV

Pulsar	χ^2 (9 deg. of freedom	3σ limit of pulsed flux (cm^{-2} s^{-1})	P(sec)	$P/2\dot{P}$ (yr)	D (pc)	γ Luminosity† upper limits (photon s^{-1})
P0525 + 21	7.3	1.1×10^{-6}	3.745	1.5×10^{6}	1460	3.0×10^{32}
P0540 + 23	13.6	1.2×10^{-6}	.246	2.5×10^{5}	1980	5.7×10^{37}
P0611 + 22	5.9	15.5×10^{-6}	.335	9.0×10^{4}	2720	1.1×10^{38}
P0943 + 10	16.2	0.7×10^{-6}	1.098	4.9×10^{6}	300	7.8×10^{35}
P0950 + 08	4.4	0.6×10^{-6}	.253	1.8×10^{7}	80	4.9×10^{34}
P1133 + 16	17.5	0.6×10^{-6}	1.188	5.0×10^{6}	138	1.4×10^{35}
P1237 + 25	16.1	0.4×10^{-6}	1.382	2.3×10^{7}	296	4.5×10^{35}
P1451 + 68	7.9	3.7×10^{-6}	.263	$>1.4 \times 10^{6}$	222	2.2×10^{36}
P1642 - 03	16.3	0.6×10^{-6}	.387	3.4×10^{6}	125	1.2×10^{35}
P1706 - 16	7.0	1.0×10^{-6}	.653	1.7×10^{6}	131	2.1×10^{35}
P1727 - 47	6.2	1.9×10^{-6}	.830	7.7×10^{4}	3960	3.6×10^{38}
P1747 - 46	11.3	1.8×10^{-6}	.742	1.7×10^{5}	560	7.0×10^{36}
P1749 - 28	4.6	1.4×10^{-6}	.562	1.1×10^{6}	1310	2.8×10^{37}
P1818 - 04	13.6	0.9×10^{-6}	.598	1.5×10^{6}	2590	7.6×10^{37}
P1915 + 13	3.4	1.5×10^{-6}	.195	4.3×10^{5}	2480	1.1×10^{38}
P1919 + 21	7.1	1.4×10^{-6}	1.337	1.6×10^{7}	328	1.8×10^{36}
P1929 + 10	10.1	1.7×10^{-6}	.227	3.1×10^{6}	89	1.6×10^{35}
P2020 + 28	3.0	2.1×10^{-6}	.343	2.8×10^{6}	651	1.1×10^{37}
P2021 + 51	6.7	2.3×10^{-6}	.529	2.8×10^{6}	624	6.3×10^{36}
P2111 + 46	5.2	1.4×10^{-6}	1.015	2.3×10^{6}	317	1.7×10^{36}
P2217 + 47	7.0	1.1×10^{-6}	.538	3.1×10^{6}	1250	2.0×10^{37}

†The emission solid angle of the pulsar assumed to be 0.4π steradians.

of the plots showed a χ^2 more than 17.5 (Probability $> .05$ of occurring by random chance on a χ^2 distribution with 9 degrees of freedom), we have listed in Table V-2 the upper limits so the gamma ray luminosity for these objects together with assumed distances and the actual values of χ^2. The upper limits were roughly calculated by assuming that if the pulsar flux existed it would be in one bin and the limit is 3σ of the mean per bin of the phase plot. In the future a more refined analysis with actual comparison of radio arrival times may reveal that these upper limits are actually close to positive measurements, but for the time being we shall only treat them as upper limits. Since even these upper limits – when expressed as a limit to the luminosity – contain large errors due to the errors in distance determination, they should be treated cautiously. In the subsequent discussion we shall only use them as a general check on the extrapolated behavior of the Crab and Vela pulsars.

III. PULSAR ENVIRONMENTS AND GAMMA RAY PRODUCTION

As we have seen from the previous discussions on compact objects, they have the following typical parameters: $M \sim 1M_\odot$, $R \sim 10^6$ cm, $B \sim 10^{12}$ gauss; the rotation periods P cover the range .03 to 3 seconds.

From considerations of electrodynamics, a rotating dipole has to set up a large voltage between its surface and the speed of light cylinder (where the magnetic field lines can no longer loop around and so close on the surface). This is simply a consequence of the fact that near the pulsar the plasma has to co-rotate with the neutron star, and far out it cannot do so. The voltage thus developed does not depend very much on what the dipole axis inclination is with respect to the rotation axis. We can estimate the magnitude of the voltage simply by using Faraday's law of induction:

$$\phi(\text{voltage}) \sim \frac{1}{c}\frac{d}{dt}\int \mathbf{B}\cdot d\mathbf{s}. \qquad \text{(III-1)}$$

If we take $dt \simeq 1/\Omega$, $\mathbf{B}\cdot d\mathbf{S} \simeq BR^2$, then

$$E \simeq \frac{\phi}{R} \simeq \frac{\Omega BR}{c}(\text{cgs}). \qquad \text{(III-2)}$$

Substituting typical neutron star parameters, we see that the voltage ranges between 10^{12} and 10^{10} volts/cm near the surface. This potential difference is very attractive for particle acceleration. However, what fraction of this

voltage is available for particle acceleration is difficult to say, since the manner in which the magnetosphere is covered with the network of currents that create this potential has a great bearing on this question.

We can also estimate the magnitude of the currents and hence the density n of the charge-separated plasma that will provide these currents. Again let us use elementary electrodynamics. From Gauss's Law, we get

$$\nabla \cdot \mathbf{E} = 4\pi\rho = 4\pi en. \tag{III-3}$$

Using E from Equation (III-2), we get

$$n \simeq \frac{\Omega B}{4\pi ec} \tag{III-4}$$

With typical parameters we have charge-separated densities around 10^{13} cm^{-3} at the surface and 10^4 cm^{-3} at the speed of light cylinder for a Crab Nebula type pulsar where $\Omega \simeq 200$ s^{-1}. Although these densities are calculated for currents, the regions which do not partake in these currents could not have densities very different; at least we can use this n as a lower limit.

It is interesting to take the surface density of 10^{13} cm^{-3} and integrate it to infinity assuming that it falls off as R^{-3}. The result is a surprising sum of $\simeq 5 \times 10^{18}$ particles cm^{-2}. If we assume neutrality, we can multiply it by the proton mass to get the total column density of 10 micrograms – cm^{-2}!

There is an independent way of calculating this column density based on the pulsar dispersion measurements. The radio signals from pulsars show shift in arrival times as a function of frequency which is interpreted as due to the dispersion in the interstellar medium. Effectively the dispersion measure gives us $\int n_e \cdot d\ell$ between us and the radio emitting region on the pulsar. Most of the dispersion measures ranging from 10 to 500 parsec cm^{-3} can be accounted for by travel in the interstellar medium. Let us estimate that less than 5 parsec cm^{-3} of this could be intrinsic to the pulsar. This gives us

$$\int_{\text{pulsar}} n_e \, d\ell \leqslant 1.5 \times 10^{19} \text{ electron cm}^{-2}$$

which is in accord with the estimated value of 5×10^{18} cm^{-2}. It seems that pulsars have very little material above their surfaces, something around 10 to 20 micrograms cm^{-2}, a factor of 10^6 less than that Dr. Boldt has estimated for mass accreting neutron stars.

It is interesting to do a rough estimate on what mass accretion rates are expected for pulsars, inasmuch as they are neutron stars and at distances large compared to the speed of light cylinder; they should appear no different than neutron stars of x-ray binaries. Let us assume that the pulsar has a velocity v with respect to the interstellar medium. The accretion radius r_{ac} can be defined as that where the kinetic energy of the gas with respect to the moving pulsar is less than the gravitational energy at that distance, i.e.,

$$r_{ac} \simeq \frac{2GM}{v^2}. \tag{III-5}$$

The mass accretion rate is then given by

$$\frac{dM}{dt} = \pi r_{ac}^2 \rho v = \frac{\pi (2GM)^2 \rho}{v^3}, \tag{III-6}$$

where ρ is the density of the interstellar medium in which the pulsar moves. With $M \simeq 1 M_\odot$, $\rho \simeq 1$ hydrogen mass cm^{-3}, and $v \simeq 50$ km s^{-1}, we get

$$\frac{dM}{dt} \simeq 7 \times 10^9 \text{ g s}^{-1} = 7.4 \times 10^{-17} M_\odot \text{ yr}^{-1}.$$

Compared to mass accretion rates of 10^{-6} - 10^{-9} $M_\odot$ yr^{-1} for x-ray stars, this accretion rate is too small to be of any importance in generating energy. However, such a process may cause the enhancement of the material in the line of sight. To get an order of magnitude estimate of the amount of material between the speed of light cylinder r_c and the accretion radius r_{ac} let us assume $\rho_0 \sim 1$ atom cm^{-3} gets compressed as $(r_{ac}/r_c)^2$ and then it trickles on the neutron star surface. Then

$$\int_{r_{ac}}^{r_c} \rho d\ell \simeq \left(\frac{r_{ac}}{r_c} - r_{ac} \right) \rho_0. \tag{III-7}$$

With the previously assumed values and $\Omega \sim 200$ s^{-1}, we obtain 10^{-18} atoms cm^{-2}. Again, this value is in accord with the other two methods of estimation.

We have seen that the potential gradients in the magnetospheres of pulsars is sufficient to accelerate protons above the π° production threshold. However, we are also forced to the conclusion that there is very little material above the surface of the neutron star that could make π° mesons out of these photons.

As a matter of fact only about $10^{-5}/72$ of the protons would interact. To get 10^{35} ergs s^{-1} in gamma rays would require a proton energy luminosity of more than 10^{43} ergs s^{-1} which is a factor of 10^5 above the rotational energy loss rate of the pulsar.

One may speculate on the possibility of π° production by the protons of the magnetosphere accelerated towards the surface of the neutron star; in this case we do have plenty of target material. At about 1 GeV proton kinetic energy, the cross section times multiplicity of π° production is about 10^{-26} cm^2, at higher proton energies this product increases as approximately the 0.5 power of the proton kinetic energy. Roughly, GeV protons convert a few percent of their energy to gamma rays of interest. As the energy of the proton goes up, the efficiency of energy conversion to gamma rays around 100 MeV drops ($\simeq$as $T^{-1/2}$). Even in the optimum range of proton energies we need 10^{37} to 10^{38} ergs s^{-1}, or 10^{39} to 10^{40} protons s^{-1}. This is about a factor 10^6 larger than the estimated primary electron flux from the pulsar.

Let us leave protons, pions, and nuclear processes temporarily and look at the possibility of electromagnetically generating the gamma rays.

What happens to energetic electrons and photons in a medium such as that encountered in the pulsar magnetosphere?

Electrons can interact mainly in one of two ways yielding end products that are again photons. One process is synchrotron radiation, in which the energy of the radiated photon in eV is

$$E_\gamma = 5 \times 10^{-20}\, B_\perp\, E_e^2 \text{ (eV)}. \qquad \text{(III-8)}$$

The energy loss rate in eV per second, is given by

$$\frac{dE_e}{dt} = 5 \times 10^{-15}\, E_e^2 \text{ (eV)} B^2 \qquad \text{(III-9)}$$

with B in gauss. Or, we can write the mean pathlength of the electron as

$$\lambda_s \simeq \frac{cE_e}{dE_e/dt} \simeq 6 \times 10^{24}\, E_e^{-1}\, B^{-2} \text{ cm}. \qquad \text{(III-10)}$$

The other process that affects the electron is curvature radiation. In this case the energy of the radiated photon is

$$E_\gamma = 6.5 \times 10^{-23} E_e^3 \text{ (eV)} \; R_c^{-1} \text{ eV}, \tag{III 11}$$

where R_c is the radius of curvature of the trajectory in centimeters. The energy loss rate is

$$\frac{dE_e}{dt} = 5 \times 10^{-20} E_e^4 R_c^{-2} \text{ eV} \cdot \text{s}^{-1}, \tag{III-12}$$

and the mean-free-path is

$$\lambda_c \simeq 6 \times 10^{29} E_e^{-3} R_c^2 \text{ cm}. \tag{III-13}$$

We could also calculate same type of formulas for inverse Compton type interactions. But since, at the surface, the magnetic field energy density $H^2/8\pi$ is about 4×10^{22} ergs/cm^3 and photon energy density is around 2×10^{14} ergs cm^{-3} even if the object is radiating at the Eddington limit, for all practical purposes all the main energy loss mechanisms are going to be due to the magnetic field.

Now, without going into the details of the processes let us try to understand what will happen to energetic electrons trying to get out of the surface of the pulsar.

Notice that if we ask what sorts of photons will a 10^{12} eV electron radiate through synchrotron processes near the surface, where $B \simeq 10^{12}$ gauss, we get an unrealistic value like 5×10^{16} eV, this is much larger than the electron energy. The conflict is due to the fact that Equation (III-8) is a classical formula whereas we are really dealing with quantum electrodynamical regimes at such electron energies near the surface. The parameter Υ that separates the classical regime from the quantum region is given by

$$\Upsilon = \frac{E}{mc^2} \frac{B}{B_{cr}}, \tag{III-14}$$

where the critical magnetic field B_{cr} is that at which the energy of the photon with Larmor frequency $\hbar eB/mc$ exceeds the rest mass energy of the electron, $m_e c^2$:

$$B_{cr} \equiv \frac{m^2 c^3}{e\hbar} = 4.4 \times 10^{13} \text{ gauss}. \tag{III-15}$$

With these parameters we can express Υ as:

$$\Upsilon = 4.5 \times 10^{-20} \, E(eV) \, B(gauss) \qquad \text{(III-16)}$$

If Υ is less than 1 we are in the classical regime, and otherwise in the quantum mechanical regime. In our example of $E = 10^{12}$ eV and $B = 10^{12}$ gauss, the parameter $\Upsilon \simeq 4.5 \times 10^{4}$, well into the quantum mechanical regime. Synchrotron emission in such a regime is similar to bremsstrahlung emission in solid material. In contrast to the photons from a bremsstrahlung spectrum which have equal amounts of energy per logarithmic interval up to the electron energy, the magnetic bremsstrahlung has a broad peak at

$$E_\gamma \simeq E_e \left(\frac{3\Upsilon}{2 + 3\Upsilon} \right), \qquad \text{(III-17)}$$

which approaches E_e at $\Upsilon >> 1$. In the quantum regime the characteristic length over which electromagnetic interactions take place is of the order of the Compton wavelength, $\sim 4 \times 10^{-11}$ cm. Again if we apply the condition of $E_e \simeq 10^{12}$ eV and $B \simeq 10^{12}$ gauss to Equation (III-10) we see that the mean-free-path of the electron is only 15% of the Compton wavelength. The implications are then that we will get cascades like

$$e^{\pm} + B \rightarrow e^{\pm} + \text{electrons} + \text{positrons} + \text{photons} + B$$

in a very small region of the order of the Compton wavelength

Notice that the condition for pair production,

$$E_\gamma \frac{heB}{M_e c} \gtrsim (M_e c^2)^2, \qquad \text{(III-18)}$$

is equivalent to

$$\frac{E_\gamma}{M_e c^2} \frac{B}{B_{cr}} \equiv \Upsilon \geqslant 1, \qquad \text{(III-19)}$$

which is identical to the condition that electrons radiate in the quantum mechanical phenomenon with the same Feynman diagram as the bremsstrahlung.

The essential import of all of this is the following:

As long as the energies E of the photons and electrons are greater than $2 \times 10^{19}/B_{\perp}$ eV, there is a cascade growth that reaches maximum in a very short length when the average energies of the electrons and photons drop down to a critical value $E_c = 2 \times 10^{19}/B_{\perp}$. For surface fields of 10^{12} gauss, $E_c \sim 20$ MeV. Hence any acceleration process on the surface cannot yield energizing electrons or photons above this energy, and most of the emerging photons will have energies around 20 MeV. Unless there is more acceleration, these shower electrons would radiate the remainder of their energy with a spectrum similar to the magnetic bremsstrahlung of a 20 MeV electrons in fields slightly less than the surface fields of the pulsar. The shower photons would emerge from the pulsar with their ~20 MeV energy. Indeed we thus have a mechanism for generating a large number of photons around the energy of the gamma rays of interest, just as most photons in extensive air showers have the critical energy appropriate for air.

IV. CONTRIBUTION OF PULSARS TO THE GALACTIC GAMMA RAY EMISSION

Generalization based on two observations may lead to erroneous conclusions, however, scientific knowledge follows the extrapolation of existing knowledge and we cannot resist the move. Furthermore, we do have a number of upper limits that will aid our generalizations.

The intention then, is to consider the Crab, Vela and other pulsars as the manifestations of the same kind of object at different ages, from the data to determine an empirical luminosity-versus-time curve, and to examine its implications.

In Figures 5, 6, and 7 we have plotted the gamma ray luminosities for the Crab and Vela pulsars together with upper limits for the other pulsars as a function of the period P, apparent age $P/2\dot{P}$, and the total rotational energy loss rate respectively. Those upper limits which have χ^2 greater than 15 are circled as being more promising as possible positive fluxes.

The most common interpretation of the relationship of P and $\dot{P}$ is in terms of the radiation losses of a rotating dipole. In this case, the energy radiated away is proportional to P^{-4}. If we assume that the radiated energy is supplied by the rotational energy loss of the pulsar,

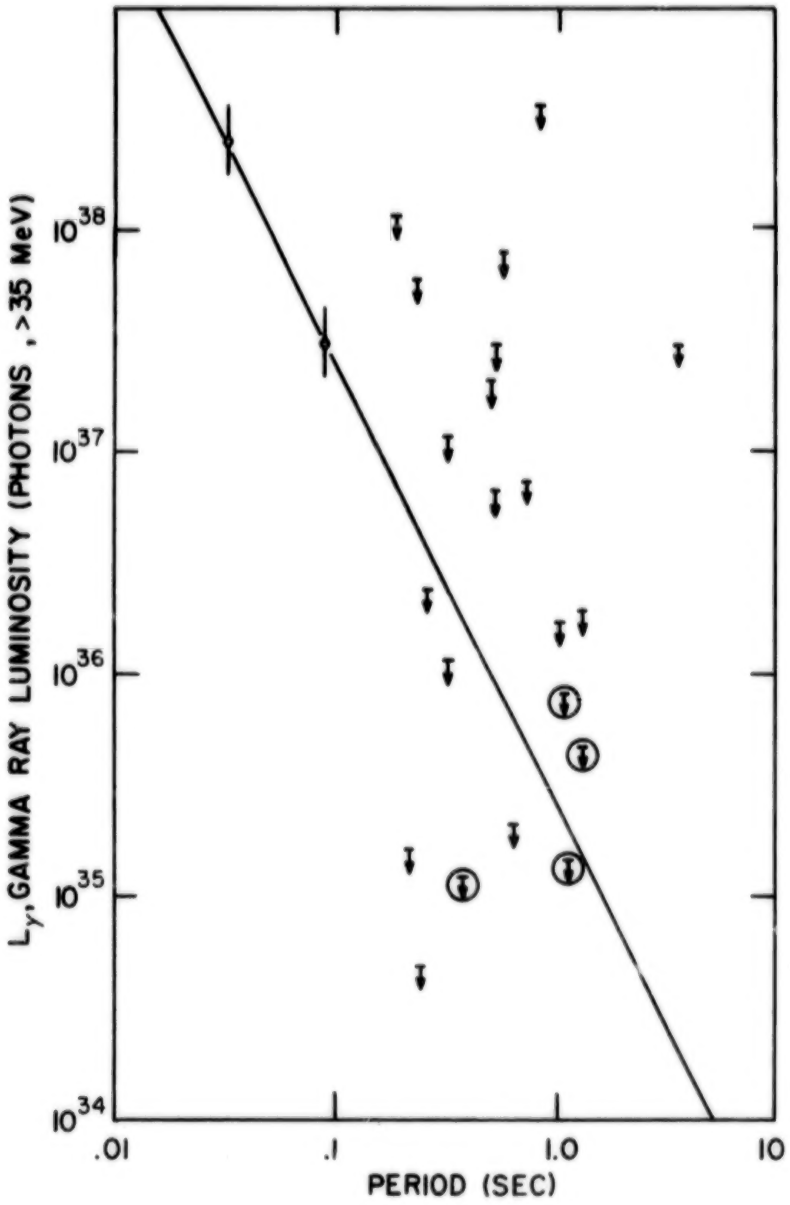

Figure V-5. Gamma ray luminosity for Crab and Vela pulsars together with upper limits for the other pulsars as a function of period (P).

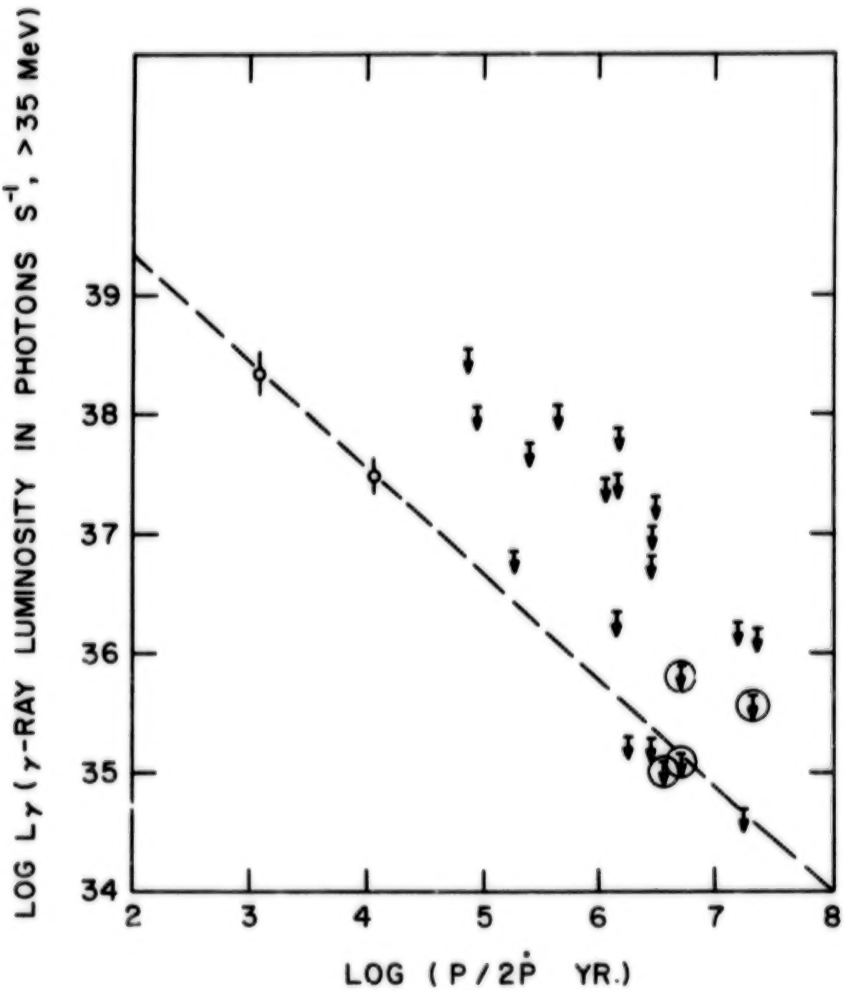

Figure V-6. Gamma ray luminosity for Crab and Vela pulsars together with upper limits for the other pulsars as a function of apparent age ($P/2\dot{P}$).

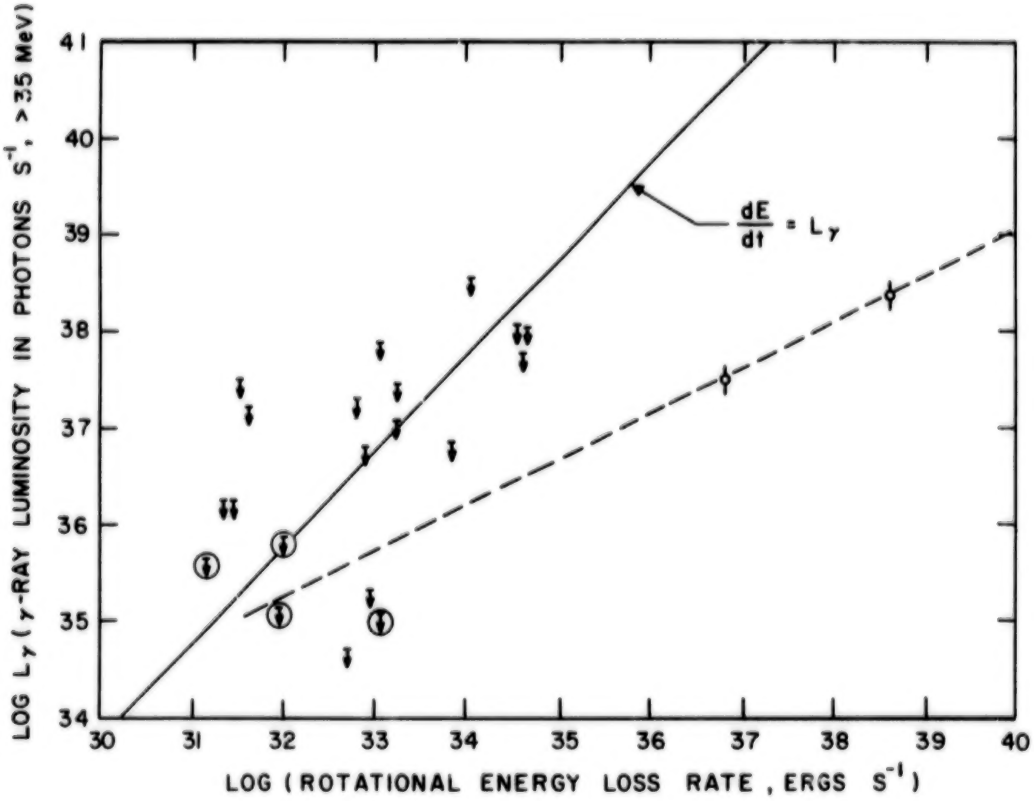

Figure V-7. Gamma ray luminosity for Crab and Vela pulsars together with upper limits for the other pulsars as a function of the total rotational energy loss rate.

$$\frac{dE^{rot}}{dt} = \frac{4\pi^2 I \dot{P}}{P^3}, \qquad \text{(IV-1)}$$

where I is the moment of inertia of the pulsar. Under these assumptions $\dot{P}$ should be proportional to P^{-1}. Furthermore, if the radio luminosity is proportional to the rotational energy loss rate, we expect L_{radio} to be proportional to P^{-4}. Experimentally, when we compare these measurements as determined in the radio region, we find that P shows no correlation with $\dot{P}$, and radio luminosities follow a $P^{-1.3}$ to $P^{-1.8}$ power law dependence. The lack of correlation between P and $\dot{P}$ can be interpreted as possibly the large variation ($\simeq$ 20) between initial parameters such as the moment of inertia and magnetic field strength for different pulsars. The relatively slow drop-off in radio luminosity as a function of period implies that in the earlier stages of the pulsar most of the dissipated rotational energy goes into other things, possibly electrons in the remnant. Progressively as the pulsar ages we get a larger fraction of the available energy out as radiation.

In the same spirit let us examine the gamma ray data. In Figure 5 we see the plot of the logarithm of gamma ray luminosity L_γ versus log P. A straight line plotted between the Crab and Vela pulsars gives

$$L_\gamma\ (>35\ \text{MeV}) = 2.8 \times 10^{35}\ P^{-2.2 \pm .5}\ \text{photon s}^{-1} \qquad \text{(IV-2)}$$

Upper limits of L_γ to pulsars P0950 + 08, P1642 - 03, and P1929 + 10 fall more than an order of magnitude below this extrapolation. However, we should bear in mind that the similar radio luminosity plots exhibit a range of two order of magnitude for pulsars with the same period. The gamma ray data are also consistent with pulsars with periods larger than 0.2 second not emitting gamma rays. This seems like an unlikely conclusion since the voltages in the magnetosphere fall off as P^{-1} and the density of material available for acceleration falls off as P^{-1}. In a rough model of gamma rays being the product of magnetospheric showers of energetic electrons, we would expect the number of gamma rays n_γ emitted at the shower maximum per energetic primary to be proportional to

$$n_\gamma\ (\text{at shower max}) \sim \frac{E_0}{E_{crit}}, \qquad \text{(IV-3)}$$

where E_0 is the energy of the shower initiating electron and E_{crit} is the energy when photons and electrons decouple. The total gamma ray luminosity L_γ should then be proportional to:

$$L_\gamma \sim n_0 \frac{E_0}{E_{crit}}, \qquad \text{(IV-4)}$$

If we estimate that E_0 will fall off as P^{-1} (Equation III-2) and n_0, the number of shower-initiating primaries, to fall off as P^{-1} (Equation III-4), and that B, which determines E_{crit}, does not change much, then $L_\gamma \propto P^{-2}$. This type of luminosity dependence on period seems to be supported by the Crab and Vela pulsars.

If we examine the L_γ versus apparent age $t = P/2\dot{P}$ plot of Figure V-6 we notice that Crab and Vela pulsars fit

$$L_\gamma\,(>35\text{ MeV}) = 4 \times 10^{37} \left(\frac{t(yr)}{10^4}\right)^{-0.9 \pm .2} \text{ photons s}^{-1}. \qquad \text{(IV-5)}$$

Although a few of the upper limits are slightly below this extrapolation, considering the uncertainties in distances, Equation (IV-5) is not in conflict with the rest of the data. Pulsars P1133 + 16 and P1642 - 03 with χ^2 values greater than 16 lie on this extrapolation.

On Figure V-7 we show the distribution of L_γ and upper limits to it as a function of the spindown enegy loss rate assuming that each pulsar has a moment of inertia $I = 10^{45}$ g cm^2. Also drawn on this figure is a line that indicates the case of all rotational energy loss going into production of gamma rays above 35 MeV. Notice that the Crab pulsar converts about 10^{-4} and Vela 10^{-3} of the rotational energy loss into gamma rays observed. The extension of Crab and Vela pulsar luminosities implies that when the gamma vary luminosities are around $1\text{-}4 \times 10^{37}$ photons s^{-1}, all of the available rotational energy loss is being used in generating gamma rays. It seems then, making use of Figure V-6, that such a power law extension must break down when the apparent age of the pulsar is around $2 - 6 \times 10^6$ years.

The SAS-2 results indicate that, with reasonable assumptions of the galactic distribution of sources, the galaxy should be emitting 10^{42} photons s^{-1} in photons above 35 MeV. What fraction of the galactic luminosity can we account for by pulsars of all ages distributed throughout the galaxy?

Let us first make some assumptions:

1. Pulsars are created during supernova explosions and the rate of generation is about 1 per 100 years in our galaxy.

2. The apparent age $P/2\dot{P}$ is a good approximation of the true age.

3. Pulsars emit gamma rays as a function of time given by the power law relationship of Figure V-6:

$$L_\gamma\ (>35\ \text{MeV}) \simeq 4 \times 10^{37} \left(\frac{t(\text{yr})}{10^4}\right)^{-0.9}$$

4. This gamma ray emission continues until the apparent age is 5×10^6 years, and then turns off or decreases its luminosity very quickly. At this stage the gamma ray luminosity is 1.5×10^{35} photons s^{-1}.

Under these assumptions we can predict the L_G, the gamma ray luminosity of the galaxy. Writing the pulsar luminosity as a function of time as

$$L_\gamma = At^{-a}, \tag{IV-6}$$

where A and a are constants appropriate for assumption 3. The pulsar generation rate per unit time dn/dt can be expressed as

$$\frac{dn}{dt} = B. \tag{IV-7}$$

The number of pulsars with gamma ray luminosity between L and L + dL is

$$\frac{dn}{dL} = \frac{dn}{dt}\,\gamma \left(\frac{dL_\gamma}{dt}\right)^{-1} = \frac{A^{1/a}B}{a}\, L_\gamma^{-(1/a+1)}, \tag{IV-8}$$

and the total galactic luminosity is

$$L_G = \int_{L_\gamma min}^{L_\gamma max} \frac{dn}{dL_\gamma} L_\gamma\, dL_\gamma = \frac{A^{1/a}B}{a(1-1/a)} \left(L_{\gamma max}^{1-1/a} - L_{\gamma min}^{1-1/a}\right). \tag{IV-9}$$

Using the constants

$A = 1.6 \times 10^{41}$ photon s^{-1} (at t = 1 yr),

$B = 10^{-2}$ supernova yr^{-1},

$L_\gamma min = 1.5 \times 10^{35}$ photon s^{-1} ($t = 5 \times 10^6$ yrs),

$$L_\gamma max = 2.5 \times 10^{39} \text{ (t = 100 years)},$$

$$a = 0.9,$$

we obtain

$$L_G \simeq 5 \times 10^{40} \text{ photons s}^{-1} \text{ (>35 MeV)}, \qquad \text{(IV-10)}$$

which is about 5% of the total measured galactic emission. Within just the errors of exponent a this value can change between 6×10^{39} and 2×10^{42} photons s^{-1}. The additional uncertainties in the "typical" behavior of Crab and Vela pulsars increases the range of L_G.

In conclusion, let us note that pulsars can provide a measurable fraction of the total galactic gamma ray emission above 35 MeV. With the advent of more sophisticated and sensitive instrumentation, not only will the history of pulsar emission or its lifetime be better estimated, but also the details of gamma ray pulse profiles from these objects can enlighten our knowledge of the pulsars significantly.

Recalling the spirit of the opening paragraph, describing the "underdeveloped" nature of the gamma ray region in terms of its "productivity" in the discovery of compact objects, let us remind ourselves that it may still hold very rich unexploited reserves.

Note added in Proof: A more refined analysis of 75 pulsars observed by SAS-2 has been compiled (Ögelman et. al., 1976) wherein PSR 1747-46 and PSR 1818-04 show positive effects at around 4σ level. The rest of the conclusions of these lectures do not change significantly.

BIBLIOGRAPHY

A. On gamma rays from Crab Pulsar

McBreen, B., Ball, S. E., Jr., Campbell, M., Greisen, K., and Koch, D., 1973, Ap. J. 184, 571-580.

Grindlay, J. E., 1972, Ap. J. (Letters), 174, L9-L17.

Fazio, G. G., Hemken, H. F., O'Mongain, E., and Weekes, T. E., 1972, Ap. J. (Letters) 175, L117-L122.

Frye, G. M., Jr., and Wang, C. P., 1969, Ap. J. 158, 925-937.

Kettering, G., Mayer-Hasselwander, H. A., Pfeffermann, E., Pinkau, K., Rothermel, H., and Sommer, M., 1976, Proc. 12th Internat. Cosmic Ray Conf. 1, 57-62 (U. of Tasmania, Hobart 1971).

Browning, R., Ramsden, D., and Wright, P. J., 1971, Nature 232, 99-101.

Albats, P., Frye, G. M., Jr., Zych, A. D., Mace, O. B., Hopper, V. D., and Thomas, J. A., 1972, Nature 240, 221-224.

Kinzer, R. L., Share, G. H., and Seeman, N., 1973, Ap. J. 180, 547-549.

Parlier, B., Agrinier, B., Forichen, M., Leray, J. P., Boella, G., Marschi, L., Bucheri, R., Robba, N. R., and Scarsi, L., 1973, Nature Phys. Sci., 242, 117-120.

Helmken, H., and Hoffman, J., 1973, Proc. 13th Internat. Cosmic Ray Conf. 1, 31-35, (U. of Denver: (Denver).

Kniffen, D. A., Hartman, R. C., Thompson, D. J., 1974, Nature 251, 397.

B. On Gamma Rays from Vela

Albats, P., Frye, G. M., Thomson, G. B., Hopper, V. D., Mace, O. B., Thomas, J. A., Staib, J. A., 1974, Nature 251, 400.

Thompson, D. J., Fichtel, C. E., Kniffen, D. A., and Ögelman, H. B., 1975, Ap. J. (Letters), 200, L79.

Ögelman, H. B., Fichtel, C. E., Kniffen, D. A., and Thompson, D. J., 1976, Ap. J. 209, 584-591.

C. Pulsars (See Chapter II)

D. Pulsars and Gamma Ray Production

Shklovskii, I. S., 1970, Ap. J. (Letters), 159, L77.

Sturrock, P. A., 1970, Ap. J. 164, 529.

Ruderman, M. A., and Sutherland, P. G., 1975, Ap. J. 196, 51.

E. High Energy Electromagnetic Processes in Intense Fields

Erber, T., 1966, Rev. Mod. Phys. 38, 626.

CHAPTER VI
TEMPORAL ANALYSIS OF X-RAY DATA

Richard Rothschild
Goddard Space Flight Center
Greenbelt, Maryland

This chapter will be broken into three main categories. The first is "What do the data look like?" We shall look at the raw data from a GSFC rocket flight in October of 1973; it dramatically shows what we are up against when we come to the matter of interpretation. The second section will cover "What do we do with the data?" Manipulation of the actual data will be discussed and results shown. The final section will cover "What do the results mean?" This will include a discussion of how the data bias the results, and also how we can interpret the results.

WHAT DO THE DATA LOOK LIKE?

Figure VI-1 is a plot of integrated counts per 20.48 ms versus time for the exposure to Her X-1, Cyg X-3, Cyg X-1, and, naturally, the diffuse background. The plot begins about 150 seconds after launch, when the doors of the rocket are open and viewing an area of the sky devoid of detectable sources. The count rate is about 75 per second. At about 160 seconds after launch, the source Her X-1 comes into view of the detectors and the rocket points at it for fifty-odd seconds. During this time the intensity is seen to rise and fall with the 1.24-second period characteristic of the pulsar. The mean rate is 4 to 5 hundred counts per second. The rocket then scanned over to Cyg X-3, viewing the diffuse background again and cutting across Cyg X-1 on the way. When Cyg X-3 entered the field of view of the detectors the payload again stopped and pointed at the source for about 35 seconds. Cyg X-3 exhibited no discernible structure at this time, and in fact the variations in count rate are consistent with those for a random source with constant mean rate. Next, the rocket began to scan over to Cyg X-1, and when the latter was in the field of view, once again the payload held its pointing for about a minute. The mean count rate here was about 1300 per second, the intensity is quite chaotic, and there seems to be flares of fraction of a second duration. Finally the doors closed, exposing a radioactive calibration source to the detectors.

On this flight our finest temporal bin was 320 μs, and exposure to galactic x-ray sources totaled some three minutes. Thus we have about a half million time bins to work with. What we did with those counts is the subject of the next section.

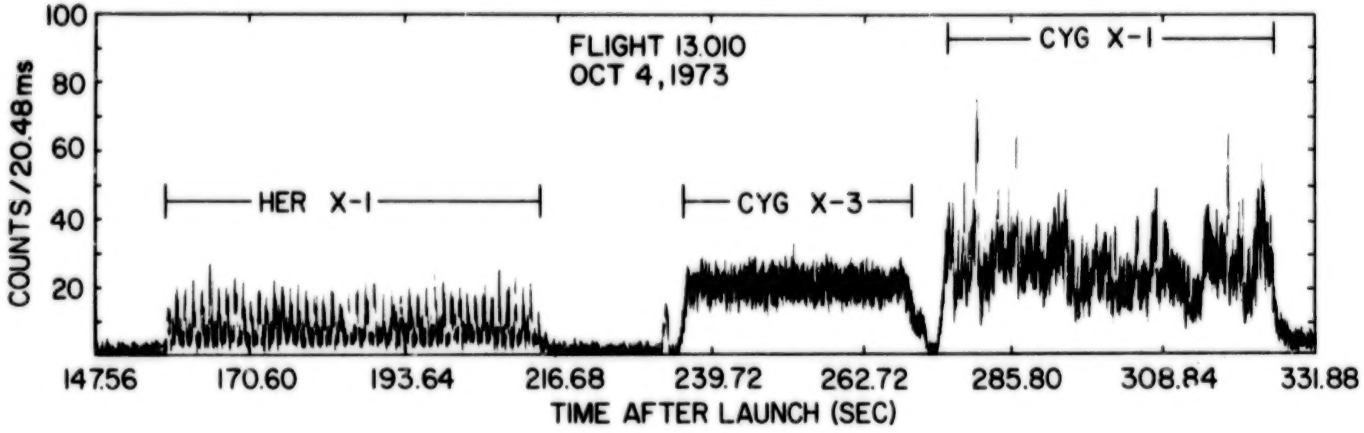

Figure VI-1. Integrated counts per 20.48 ms versus time after launch for the October 4, 1973 flight of a GSFC x-ray astronomy rocket payload. The three sources observed are labelled.

WHAT DO WE DO WITH THE DATA?

The analysis of temporal data can be naturally divided into studies of periodic and nonperiodic data. Periodic data can be studied by means of power spectrum analysis, which includes the use of the Fast Fourier Transform (FFT) algorithm, and light curves. Autocorrelation functions can also be used on periodic data, but the discussion of their use will be presented with respect to nonperiodic data. Nonperiodic data analysis will include the use of autocorrelation functions, plots of variance/integration-time versus integration-time, searches for bursting beyond Poisson prediction, computation of burst widths, and searches for "ringing" of bursts.

Power Spectrum

The power spectrum of a process is the Fourier transform of the autocovariance function, and represents the distribution of the variance with frequency. If a periodic process is being measured, the variance will exceed the overall mean variance at a given frequency whenever the frequency is an integer times the fundamental frequency. First a few definitions:

μ_x = mean value of the process x(t),

σ_x^2 = variance of the process x(t)

$\gamma_{xx}(\tau)$ = autocovariance of the process x(t)

$\rho_{xx}(\tau)$ = autocorrelation of the process x(t)

They are related as follows. If the process x(t) yields a time series of N counts x_i, then

$$\mu_x = \frac{1}{N} \sum_{i=1}^{N} x_i$$

$$\sigma_x^2 = \frac{1}{N} \sum_{i=1}^{N} (x_i - \mu_x)^2,$$

$$\gamma_{xx}(\tau) = \frac{1}{N} \sum_{i=1}^{N} (x_i - \mu_x)(x_{i+\tau} - \mu_x),$$

$$\rho_{xx}(\tau) = \gamma_{xx}(\tau)/\sigma_x^2$$

but note that $\sigma_x^2 = \gamma_{xx}(0)$. Hence

$$\rho_{xx}(\tau) = \gamma_{xx}(\tau)/\gamma_{xx}(0).$$

The power spectrum is defined as

$$\Gamma_{xx}(f) = \int_{-\infty}^{\infty} \gamma_{xx}(\tau)\, e^{-i2\pi f\tau}\, d\tau,$$

which is just the Fourier transform of $\gamma_{xx}(\tau)$. The inverse transform states

$$\gamma_{xx}(\tau) = \int_{-\infty}^{\infty} \Gamma_{xx}(f)\, e^{i2\pi f\tau}\, df,$$

If we set $\tau = 0$, we see that

$$\sigma_x^2 = \int_{-\infty}^{\infty} \Gamma_{xx}(f)\, df.$$

This just confirms what was previously stated. The power spectrum at a given frequency $\Gamma_{xx}(f)\, df$ is the contribution to the variance from frequencies f to f + df. In order to compare various sets of data, it is necessary to normalize the power spectra. This is accomplished by dividing by the variance. This result, $\Gamma_{xx}(f)/\sigma_x^2$, is the spectral density function and can be written as

$$R_{xx}(f) = \Gamma_{xx}(f)/\sigma_x^2 = \int_{-\infty}^{\infty} \rho_{xx}(\tau)\, e^{-i2\pi f\tau} d\tau.$$

An alternate method for generating power spectra is the use of the Fourier coefficients of x(t). If x(t) is digitized on N intervals of width T, such that NT is the length of the exposure, the Fourier series approximating x(t) is denoted by $\tilde{x}(t)$ and is given by

$$\tilde{x}(t) = \sum_{m=-n}^{n-1} X_m\, e^{i2\pi mt/NT},$$

where X_m is the complex Fourier coefficient, n = 1/2 N, and the fundamental frequency is $f_1 = 1/NT$. The coefficients are then given by

$$X_m = \frac{1}{N} \sum_{r=-n}^{n-1} x_r \, e^{-i2\pi mr/N},$$

where x_r are the digitized values of x(t). Then Parseval's Theorem states that the average power of the signal x_r is given by

$$\frac{1}{NT} \sum_{r=n}^{n-1} x_r^2 \, T = \sum_{m=-n}^{n-1} |X_m|^2;$$

hence

$$\Gamma_{xx}(f) = |X_m|^2$$

where

$$f = mf_1 = m/NT.$$

Consequently, we are dealing with Fourier transforms and their properties are well documented in the literature. We need not derive rigorously any of those results, but we shall use the graphic representation used by Brigham (1974) in order to illustrate some details that are important.

Since our data are digitized, so necessarily must be anything calculated directly from the data, such as the autocovariance function and consequently the power spectrum. There is a theorem called the Sampling Theorem that states how the underlying continuous power spectrum or autocovariance can be calculated from the discrete ones. We will get to this later. The main use of power spectra or spectral density functions is to determine periodicities present in data, and these methods are very powerful in revealing even weak periodic signals in the presence of a strong random signal. Hence, one must be quite careful that the analysis does not introduce any false contributions to the spectra. If the signal were continuous and of infinite duration such that $\int_{-\infty}^{\infty} x(t)\,dt$ is finite, we would have no problem in calculating power spectra. Such is not the case, however. We will start with a continuous function $\gamma(t)$ and its Fourier transform $\Gamma(f)$, as illustrated below:

We have assumed that $\Gamma(f) = 0$ for $|f| > f_c$; that is, there is a critical frequency f_c above which $\Gamma(f)$ is zero. This says that $\Gamma(f)$ is band-limited in frequency. Actually, x-ray data are band-limited in time ($x(t) = 0$, for $0 > t$ and $t > T_0$), i.e., there are only counts during the exposure. However, the results are analogous and are more easily depicted graphically for the frequency limited case. To continue, $\Gamma(f)$ is the "pure" continuous power spectrum. It has no distortions. In order first to digitize $\gamma(t)$, we multiply by d(t), which is an infinite series of delta functions spaced at intervals T. The Fourier transform of d(t) is D(f) and is three delta functions of height $1/T$ at $f = 0, \pm 1/T$. This is illustrated below:

The product $\gamma(t) \cdot d(t)$ is then a series of delta functions whose amplitude is equal to the value of $\gamma(t)$ at that value of t. The Fourier transform of $\gamma(t) \cdot d(t)$ is the convolution of $\Gamma(f)$ and D(f) which turns out to be $\Gamma(f)$ centered at each of the three delta functions D(f). The results are illustrated below;

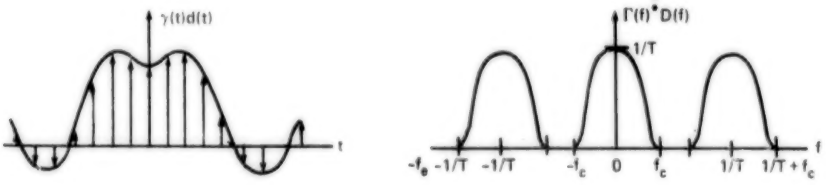

As is shown in the $\Gamma(f) * D(f)$ graph, the three $\Gamma(f)$ functions do not overlap and thus affect each other's shape. The function $\Gamma(f) * D(f)$ centered at $f = 0$ is identical to $\Gamma(f)$. Hence we have not *aliased* the data through our digitalization process. This was only because it was drawn with $1/T > 2f_c$. It is easily seen that if $1/T < 2f_c$ the central peak of the $\Gamma(f) * D(f)$ plot would no longer be identical to $\Gamma(f)$ since the overlapping with the side lobes would alter its shape. This is just the effect to be avoided. Hence, when picking the digitization period T, we make sure that $T \leq 1/2f_c$. (With x-ray data which usually is time domain band-limited, the optimum procedure is to use the smallest T possible, so that the overlap is minimized. It cannot be eliminated: there will always be some aliasing due to the high frequency side lobes. Also, when $f > f_c$ $\Gamma(f) * D(f)$ begins to repeat and no new information is generated.) This critical frequency, 1/2T, is called the Nyquist frequency. In order to avoid aliasing, or to minimize it if unavoidable, we always pick $1/T = 2f$ where T is the finest temporal bin possible. In order to remove the 1/T scale difference between $\Gamma(f)$ and $\Gamma(f) * D(f)$, $|f| < f_c$, we multiply $\Gamma(f) * D(f)$ by rectangular pulse Q(f) of height T and duration 2fc centered at $f = 0$. The inverse transform of this is q(t) and both are illustrated below

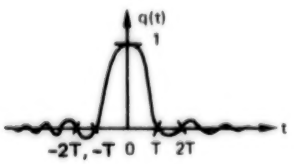

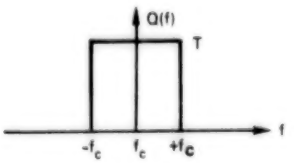

The result $(\Gamma(f) * D(f) \cdot Q(f)$ is then the same as the initial $\Gamma(f)$. Hence $(\gamma(t) \cdot d(t)) * q(t)$ is the same as the original $\gamma(t)$. All of this yields the sampling theorem. When stated for the usual case in x-ray astronomy (band-limited in time) we get that

$$\Gamma_{xx}(f) = \frac{1}{2T_c} \sum_{n=-\infty}^{\infty} \Gamma_{xx}\left(\frac{n}{2T_c}\right) \frac{\sin[2\pi T_c(f - n/2T_c)]}{\pi(f - n/2T_c)};$$

hence we can reconstruct the best estimate of the continuous power spectrum $\Gamma_{xx}(f)$ from the digitized power spectrum elements $\Gamma_{xx}(n/2T_c)$.

Another potential problem arises from the finite length of the exposure. This is equivalent to multiplying $\gamma(t)$ by a rectangle x(t) of length T_0 and height 1.

This is illustrated below:

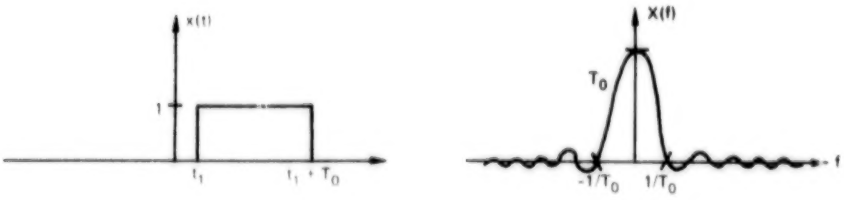

The problem is obvious: Due to the infinite extent in the frequency domain of X(f), there will be a contribution to $\Gamma_{xx}(f)$ at all frequencies. This smearing is called *leakage*. It is due to the fact that an abrupt turn-on takes an infinite amount of power. That is, a rectangular pulse is made of contributions from cosines and sines of all frequencies. In order to minimize leakage, various experimenters use other "windows" than the rectangular pulse – ones that have less steep slopes. This lessens the effect of the data in the initial and final portions of the exposure, but for a long enough exposure it can be quite valuable.

When one considers actually computing all the Fourier coefficients from the data, one is immediately presented with a problem of computer time. For determining the amplitude of N sinusoids the computer time is proportional to N^2. For even a fraction of our 5×10^5 points, this is a large number. In the early 1960s an algorithm was developed that reduced this number to N Log_2 N. Hence there was a substantial savings in time. For 5×10^5 points, $\simeq 2^{19}$ points) the ratio of $(N \log_2 N)/N^2$ is $\approx 4 \times 10^{-5}$. This is the Cooley-Tukey algorithm. Later an algorithm based on $(2^N)!$ experiments was developed and called the fast Fourier fold. These are used today for computing the power spectra. Generally the mean value of x(t) is subtracted from each data point, in order to reduce the leakage from the spike at f = 0 which is due to the transform of μ. Then the power spectrum for random data has a mean of zero, instead of one.

Figure VI-2 shows the power spectrum of 20 seconds of data from Her X-1. The four peaks are at f = .81062, and at two, three, and four times that. This frequency corresponds to a period of P = 1.234 seconds which is near the quoted value of 1.237 seconds. If we had used 40 seconds of exposure the

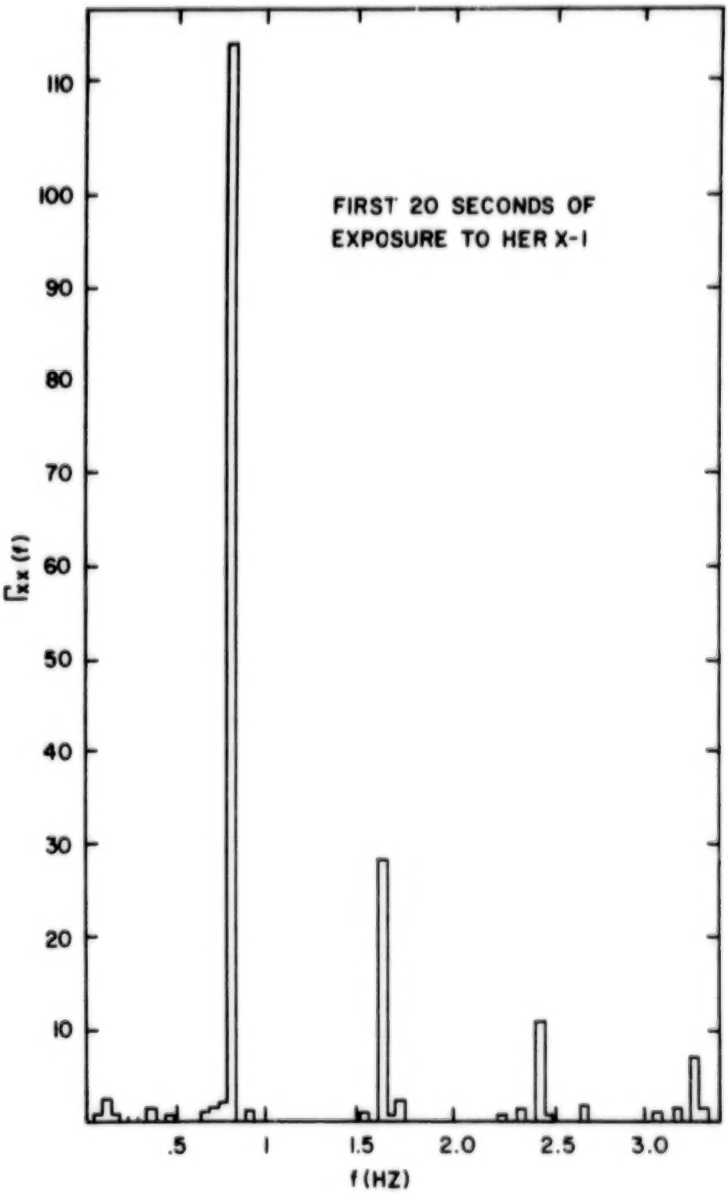

Figure VI-2. Power spectrum of 20 seconds of data from Her X-1. The four peaks are f = .81062, 2f, 3f, and 4f.

binning would be a factor of two finer and a better value of the period could be found. Note the low background in the spectrum at points away from the peaks. This is the case for proper use of the techniques explained above. In order to demonstrate the effects due to the finite length of the signal, the power spectrum was generated for data at the end of the Her X-1 exposure. It includes about 14 seconds of Her X-1 data, then 2 seconds of data when the payload was shifting off the source and about 4 seconds of background. Hence, we have included data whose average rate changed drastically during the exposure. We then would expect significant smearing of the spectrum. This spectrum is shown in Figure VI-3. Note the large low-frequency spike and the increased contribution away from the peaks. Notice also that the peaks are wider. All of this is due to smearing from the transition in the data, and points to the desirability of doing the power spectra away from the ends of the exposure where the rates are varying.

Another example of a power spectrum is shown in Figure VI-4. The 55-second exposure to Cyg X-1, a non-periodic source on this time scale, was broken into five 10-1/2 second exposures, and the principal low frequency components are shown. Along the right edge is a histogram of the combined data. There is a lot of low frequency power, the vast majority of which does not repeat from one 10-second interval to another. This is due to the steep changes in intensity over short time intervals exhibited by this source. The early observations of Cyg X-1 claimed to have found periodicities, but this could not be confirmed on later observations. This is all due to the chaotic variations in intensity which can produce quasiperiodic temporal structure that last up to a minute or two. We now know this structure can be described by a non-periodic phenomenon – shot noise, which we shall discuss later.

Light Curves

Once the period has been specified, either from a power spectrum analysis or another independent experiment, the data can be folded modulo the period. This consists of calculating the phase with respect to the period of each temporal bin or event, and then binning the data by phase. Figure VI-5 shows seven Her X-1 light curves binned by phase. The width of the bins is determined from statistical considerations. The top plot contains data from the entire exposure and has not been corrected for background. The level of the background is indicated by the black arrow labeled B. The binning is 1% of the pulse period and hence this plot has 12.4 ms resolution. Three distinct peaks can be seen: one at phase $\simeq .17$, a large one at about .65, and a third at about .90. Note that the first and second pulse are nearly 180° out of phase.

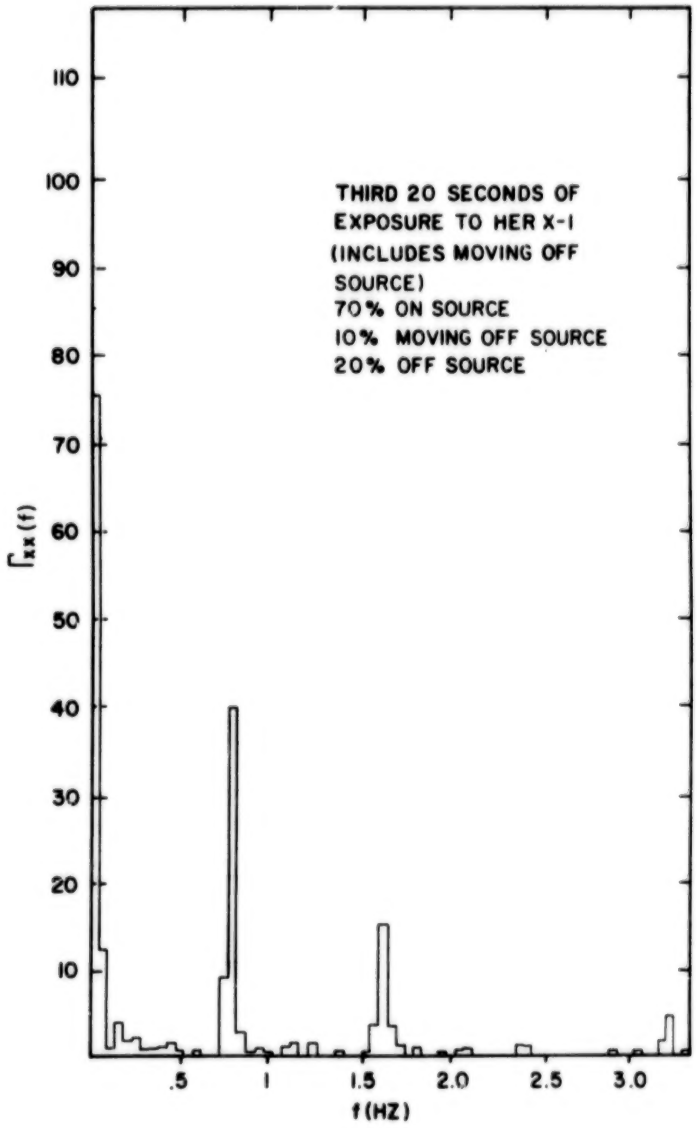

Figure VI-3. Power spectrum of 14 seconds of data from Her X-1, 2 seconds of data when the payload was moving off of the source, and 4 seconds of diffuse background data.

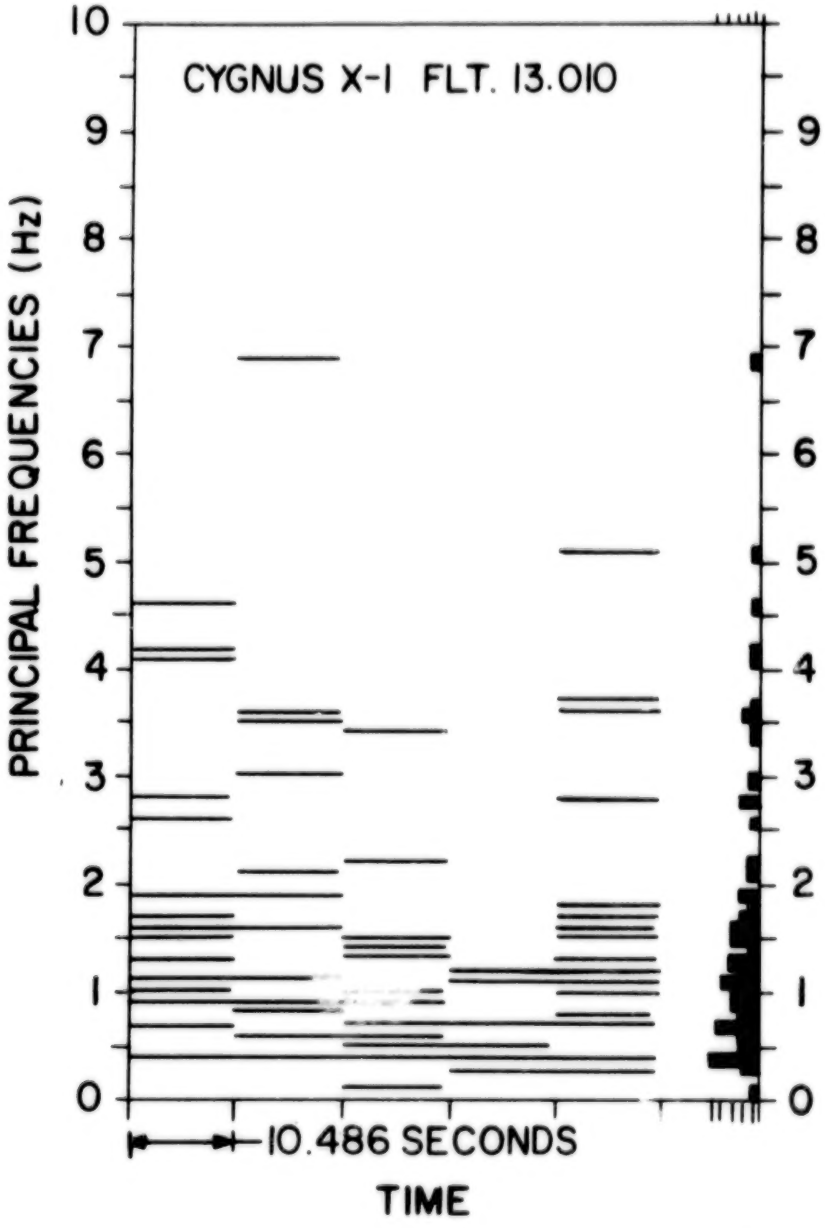

Figure VI-4. Power spectrum of five 10-1/4-second intervals of data from Cyg X-1. The principal frequencies below 10 Hz are shown. A histogram of the combined data is along the right edge. (Source: Boldt et al., 1975).

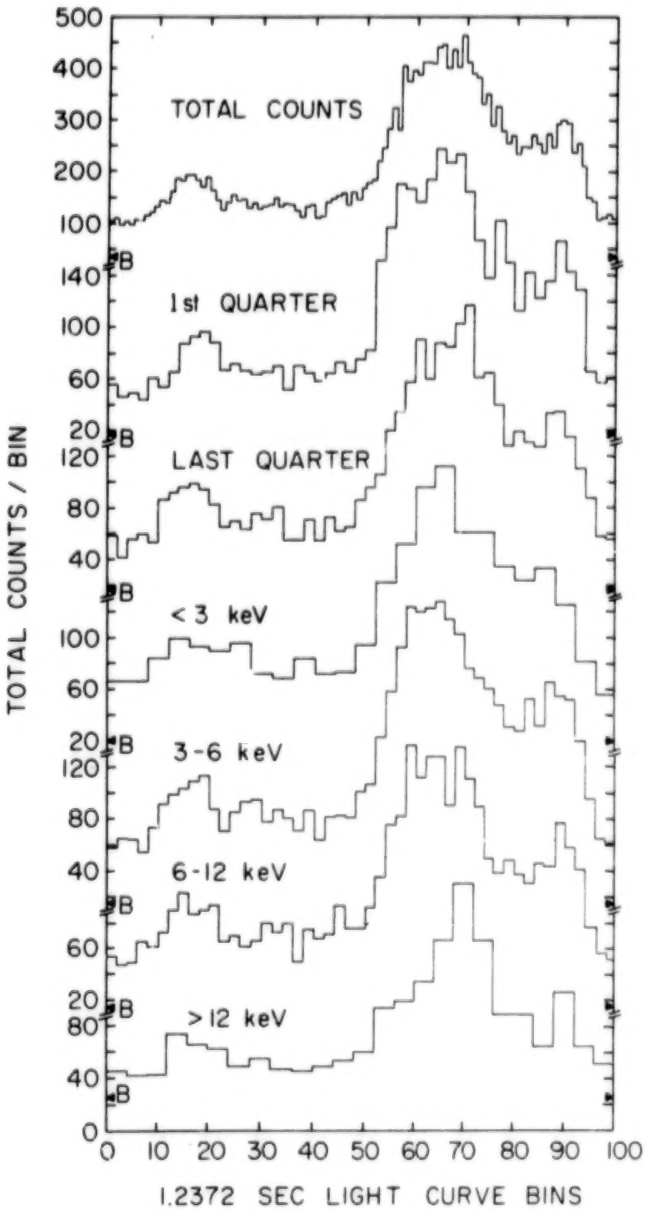

Figure VI-5. Folded light curves from Her X-1 data. The top curve includes all of the data, the next two curves include data from the first and last quarter of the exposure, and the lower four curves are for data in the energy ranges ⟨3 keV,⟩ 3–6 keV, 6–12 keV, and 12 keV. The background level for each curve is marked by the B.

The next two light curves show data from the first and last quarters of the exposure. The similarity of these two is borne out by χ^2 tests: they are the equivalent. Hence no time variability in the pulse shape on a time scale of tens of seconds. The last four show the light curves for data in various energy ranges. Statistics prevent a quantitative statement, but it would seem that the peaks narrow with energy and might even shift position slightly.

Autocorrelation Function

The autocorrelation can be used to reveal periodicities in data, but it is far less accurate in determining periods, since a knowledge of the pulse profile is necessary to fit the data. In recent years it has become useful in the analysis of non-periodic data such as Cyg X-1. Even though the intensity of a source displays no periodicities, there still can be an underlying time structure, e.g., shot noise. The autocorrelation function can reveal such structure quite vividly.

As noted previously the autocorrelation $\rho(\tau)$, where τ is the lag or shift parameter, is defined as

$$\rho(\tau) = \frac{\gamma(\tau)}{\gamma(0)},$$

where $\gamma(\tau)$ is the autocovariance. $\gamma(\tau)$ is calculated from the aspect-corrected data (corrected to counts seen at the center of the field of view, X_i. If there are N values of X_i, then

$$\gamma(\tau) = \frac{1}{N} \sum_{i=1}^{N-\tau} (x_i - \mu)(x_{i+\tau} - \mu)$$

where τ is digitized in units of temporal bins. Thus the autocorrelation function can be calculated. This, however, is a composite of two sources of signal – the x-ray source itself and the counting statistics. Some of the scatter due to statistics can be lessened by averaging $\rho(\tau)$ and $\rho(-\tau)$, since $\rho(\tau)$ is an even function and they should be equal. Still, effects due to these two sources will still be present.

Assume the signal $z(t) = x(t) + y(t)$, where $x(t)$ is the source signal and $y(t)$ is the counting statistics effect. Then, as described by Weiskopf, et al (1975),

$$\rho_z(\tau) = \gamma_{zz}(\tau)/\sigma_z^2$$

$$= \frac{\gamma_{xx}(\tau) + \gamma_{xy}(\tau) + \gamma_{yx}(\tau) + \gamma_{yy}(\tau)}{\sigma_z^2}.$$

But $\gamma_{xy} = \gamma_{yx} = 0$, since x(t) and y(t) are independent. Hence

$$\rho_z(\tau) = \frac{\gamma_{xx}(\tau) + \gamma_{yy}(\tau)}{\sigma_z^2}.$$

Since y(t) is random noise, its autocovariance is zero for $\tau \neq 0$, and $\gamma_{yy}(\tau) = \sigma_y^2$ for $\tau = 0$. Similarly $\gamma_{xx}(0) = \sigma_x^2$, and because of their independence

$$\sigma_z^2 = \sigma_x^2 + \sigma_y^2.$$

Thus we have

$$\rho_z(\tau) = \begin{cases} 1 & \tau = 0 \\ \gamma_{xx}(\tau)/\sigma_z^2 & \tau \neq 0 \end{cases};$$

But, by definition,

$$\rho_x(\tau) = \gamma_{xx}(\tau)/\sigma_x^2;$$

hence

$$\rho_z(\tau) = \begin{cases} 1 & \tau = 0 \\ \dfrac{\sigma_x^2}{\sigma_z^2}\rho_x(\tau) & \tau \neq 0 \end{cases}.$$

Inverting this gives $\rho_x(\tau)$. Noting that $\sigma_x^2 = \sigma_z^2 - \sigma_y^2$, we have

$$\rho_x(\tau) = \begin{cases} 1 & \tau = 0 \\ \dfrac{\sigma_z^2}{\sigma_z^2 - \sigma_y^2}\rho_z(\tau) & \tau \neq 0 \end{cases}.$$

Thus we have a method for modifying the observed autocorrelation function $\rho_z(\tau)$ to get the x-ray source autocorrelation function $\rho_x(\tau)$. σ_z^2 is just $\gamma_{(0)}$ and σ_y^2 is just μ.

As with the light curves, the autocorrelation functions can be performed for data in various energy ranges. The functions for various energy ranges can be compared in an effort to determine whether effects seen are energy dependent. Such an analysis was done on the data from Cyg X-1 and Cyg X-3 and the results are shown in Figure VI-6. The Cyg X-3 autocorrelation function exhibits the characteristics of random noise $\rho(0) = 1$ and $\rho(\tau) \equiv 0$ for $\tau \neq 0$. No structure is apparent. On the other hand, the Cyg X-1 autocorrelation function displays considerable structure. Even though the power spectrum yielded no periodicity, there is a definite exponential character in the data. This says that pulses from one time are correlated with pulses from another. We will discuss this in the interpretation section later, but suffice it to say that this exponential character is the shape of the shot noise pulses making up the Cyg X-1 intensity. The wavy nature of the autocorrelation function is not due to other periodicities, but due to the finite interval being sampled and to the shot noise itself.

Mean Variance

Another method exists for displaying the data from a source in such a way as to allow the identification of the presence of shot noise processes. This employs the computation of the mean variance of the data binned over intervals of duration ΔT. Then the plot of $\langle (\delta N)^2 \rangle / \Delta T$ versus ΔT can be quite revealing. Here $\langle (\delta N)^2 \rangle$ is defined as

$$\langle (\delta N)^2 \rangle = \frac{1}{J} \sum_{i=1}^{J} [x_i - \mu(\Delta T)]^2,$$

where J is the number of bins of width ΔT in the exposure being considered, x_i is the number of counts accumulated in bin i, and $\mu(\Delta T)$ is the mean value of x_i for bins of width ΔT. Then as ΔT is varied, J varies, $\mu(\Delta T)$ varies, and x_i varies, to yield $\langle (\delta N)^2 \rangle$ as a function of ΔT.

Appendix VI-B contains the derivation of the form that $\langle (\delta N)^2 \rangle$ is expected to take as a function of ΔT for identical rectangular shot noise pulses of duration τ and frequency of occurrence λ. The result is

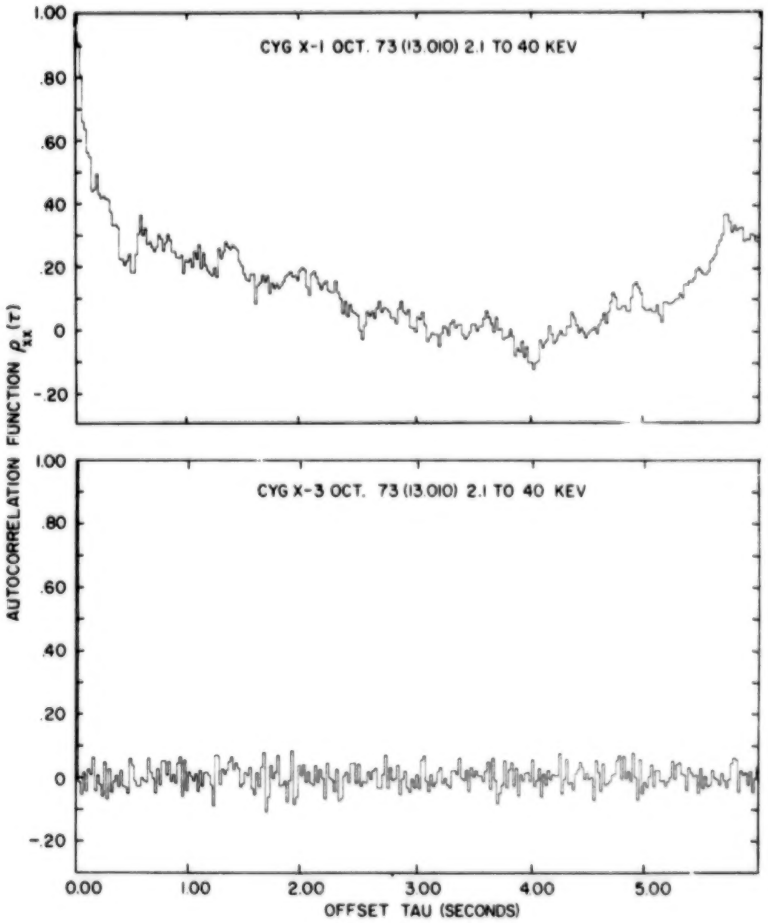

Figure VI-6. Autocorrelation $\rho(\tau)$ versus lag parameter τ for Cyg X-1 and Cyg X-3 data. The upper plot is from Cyg X-1 data and the lower plot is from Cyg X-3 data.

$$\mathrm{MSD} \equiv \frac{\langle (\delta N)^2 \rangle}{\Delta T} = \begin{cases} R\left[1 + (1-\epsilon)^2 \dfrac{R\Delta T}{\lambda \tau}\right] & \Delta T \ll \tau \\ R[1 + (1-\epsilon)^2 R/\lambda] & \Delta T \gg \tau \end{cases},$$

where R is the mean count rate per second on source and ϵ is the background signal to total signal ratio. Hence, if shot noise exists at the source, for bins small with respect to shot pulse width, the ratio MSD should increase linearly with ΔT from the value MSD = R. However, when ΔT is large with respect to the pulse width, MSD is expected to be independent of ΔT and elevated above MSD = R by the amount $(1-\epsilon)^2 R^2/\lambda$.

If shot noise were not present, then $\tau = 0$. But to give any count rate at all, the rate of such zero-width pulses would have to become infinite in such a way as to have $\lambda\tau$ be a constant. In this case we only have $\Delta T \gg \tau$, and since $1/\lambda \to 0$,

$$\frac{\langle (\delta N)^2 \rangle}{\Delta T} = R.$$

This is the result to be expected for Poisson-distributed counts: the variance equals the mean. Hence the reason for comparing to the MSD = R level.

Figure VI-7 shows the plot of MSD versus ΔT for Cyg X-1 and Cyg X-3. The points for Cyg X-3 scatter about its mean rate with increased scatter as expected as increasing ΔT reduces the number of terms involved in the calculation of MSD. On the other hand, the points for Cyg X-1 increase with bin width and appear to level off for large ΔT. This is solid evidence for the shot noise process occurring at Cyg X-1. Comparing the MSD plot to our theory gives values for λ and τ in agreement (at least for τ) with the autocorrelation function shape.

Bursts

Definition

Since the discovery of Cyg X-1 and its chaotic temporal behavior, searches have been made for very short time-scale fluctuations that would be evidence for the compact nature of this object. The exposure to Cyg X-1 we have been using as an example contains several 1-ms bursts. Figure VI-8 shows 80-ms of data binned every 640 μs. Quite obvious in this data are at least three bursts of $\simeq$1 ms duration, which implies an emission region of radius less than

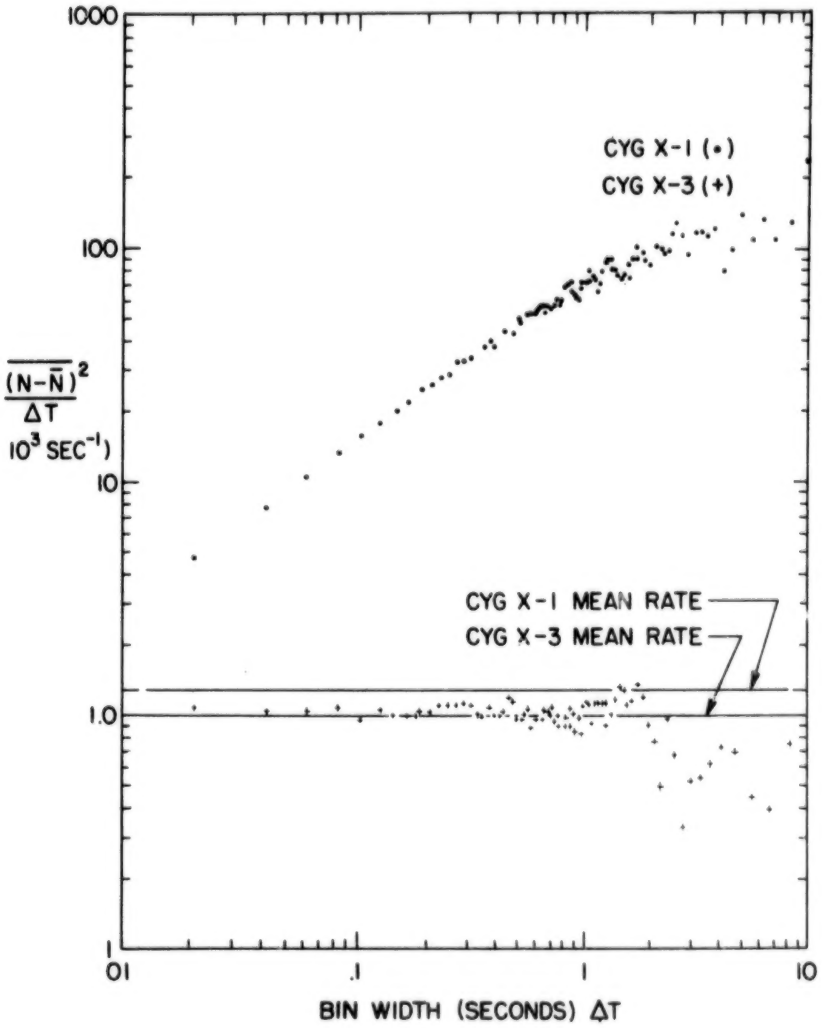

Figure VI-7. Mean square deviation divided by bin width versus bin width for Cyg X-1 (•) and Cyg X-3 (+) data (Source: Boldt et al., 1975).

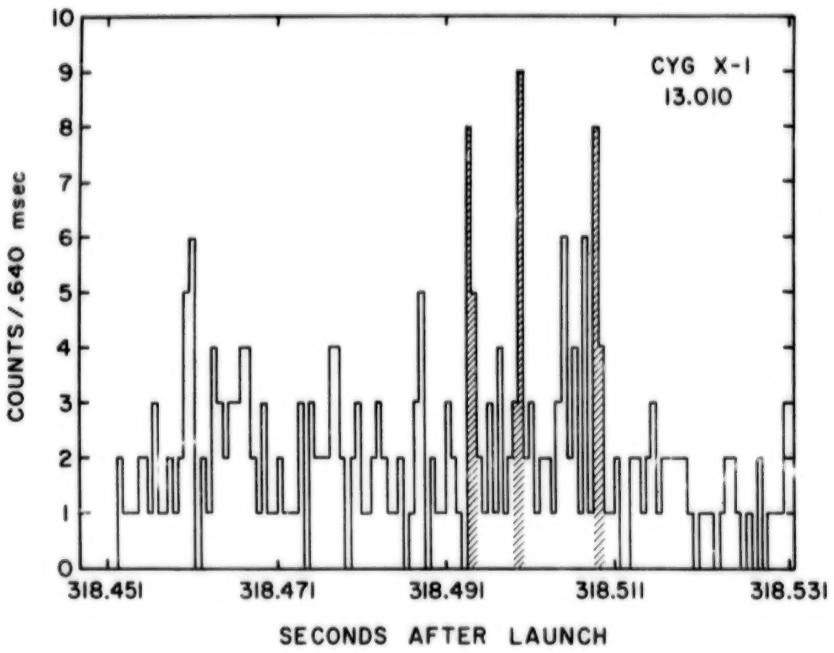

Figure VI-8. Eighty-two milliseconds of scan temporal data from the October 4, 1973 exposure to Cyg X-1, containing 3-millisecond bursts (shaded) (Source: Rothschild et al., 1974).

100 km for a 10 $M_\odot$ black hole. Hence, proving that these bursts are statistically significant is of utmost importance.

In computing statistical significance, Poisson statistics are employed. One of the parameters in the Poisson probability function is the mean rate λ. Just looking at the data will show that no single λ will do (in the Poisson sense of $\lambda = \sigma^2$) for describing the entire exposure. Hence the exposure must be broken into intervals where the data do not vary radically from the local mean. This implies using as short an interval as possible. On the other hand the shorter the interval the less the counts and, consequently, the larger the statistical uncertainties. A compromise must be reached between the two factors. Since our data could conveniently be binned every .4096 second, and since the flare that contained the three bursts was of approximately the same duration, the exposure was divided into 120 contiguous intervals of .4096 second, and then each interval could be divided into 320 bins of 1.28-millisecond bins. This implies that the statistical uncertainty on the predicted number of events is about 6%. In each interval the mean number of counts

per bin was calculated and the number of counts for each bin was noted. The expectation value N(n) for the number of 1.28-ms bins containing n counts was determined for each interval by using the local mean count per bin and Poisson statistics. In each interval a count n^* was picked such that the expectation value for the number of bursts $N^* \equiv$

$$N^* \equiv \sum_{n \geq n^*} N(n)$$

was less than or equal to .01, where n^* was the lowest possible integer. All bins in the interval were then examined to see how many had $n \geqslant n^*$. The limit .01 was chosen such that when the results from all 120 intervals were combined, the expected number of bursts due to statistics would be about 1. The result of this analysis, summed over all 120 intervals, was that in six intervals there existed at least one burst for which $n \geqslant n^*$. These six intervals contained eight bursts whereas the expectation value for the entire exposure is .73. Hence we have shown that on eight occasions throughout the exposure, including the three seen in Figure VI-8, bursts occurred when Poisson statistics would predict less than 1. This establishes the fact that Cyg X-1 occasionally bursts for a millisecond or thereabouts, and incidentally the luminosity can increase by a factor of from 4 to 7 over the mean luminosity at these times.

In order to search for bursts of other durations the bin width was varied, and the result was that there were no significant new bursts of shorter or longer duration up to about 5 ms. Similarly the duration of the interval over which the local mean rate was determined was varied from .1 to .4 second without a change in the number of bursts. Hence the interval duration did not affect the determination of bursts in the range mentioned above. One thing further should be pointed out. Since the probability that a large number of counts (a burst) occurs is directly dependent on the local mean rate, the sensitivity for revealing bursts drops with increased local mean rate. Thus this method of determining bursts is biased against finding bursts in flares or times of enhanced activity as opposed to lower-intensity periods. This makes the observation of the three bursts during the flare at $\simeq$318 seconds after launch even more significant.

Width

The next question to be resolved is the pulse width. Our binning in the burst analysis was restricted by the telemetry format. Can we get the true burst width from the data? If this were a periodic phenomenon there would be

no problem – we would just make a light curve phased to the period, as for Her X-1, and the mean pulse shape would appear. But here there is no periodicity, nothing to synchronize one burst with the next. Since a given burst contains about 10 counts in four bins, the statistics prevents us from getting a reliable pulse shape by synchronizing on, say, the largest bin. Hence, we have chosen to synchronize on the centroid of each burst. The eight bursts were binned as finely as possible (320 μs) with the centroids aligned. This is shown in Figure VI-9.

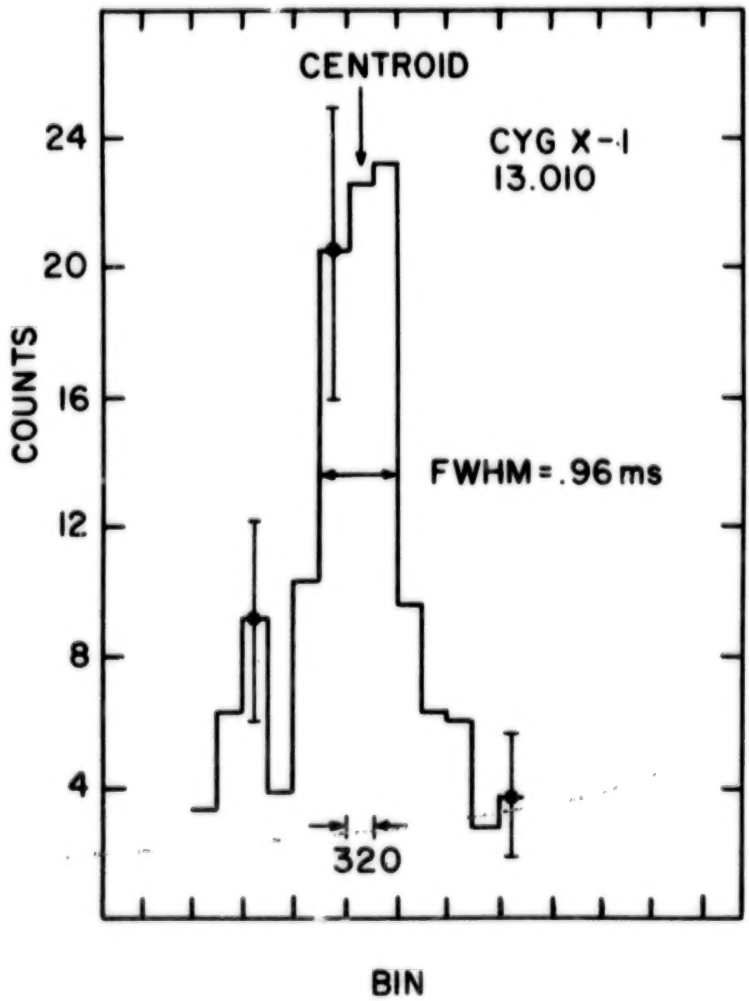

Figure VI-9. Centroid-aligned burst profile histogram. Error bars show statistical error only.

The full width at half maximum, corrected for background, is – to the nearest channel – three channels, or .96 ms. With the small number of counts comprising the graph, not much can be said for structure within the bursts or really about pulse shape. We can say that it is consistent with a rectangular pulse, but cannot rule out absolutely a triangular or exponential shape. What is needed is finer temporal resolution and more bursts and a larger area of detectors. This was partially accomplished on the next rocket flight a year later, when the resolution was 160 μs so that the bursts would cover six or seven bins, even though the counts per bin would be halved. The bursts were seen again, but in lesser numbers than expected on the basis of the first flight. Also, no two or more occurred near each other. In any case the centroid-aligned pulse profile was calculated. Since the error bars are quite large the pulse profile is still consistent with a rectangular pulse of 1-ms duration. Even with the finer binning, the width, full width at half maximum, is – to the nearest channel – 1.12 ms. Combining the results of the two flights on 320 μs binning gives again $\simeq$1 ms as the best guess width of the rectangular pulses.

Obviously a long exposure with a detector of large area is needed to get a good pulse profile (and also to get a good spectrum). The main concern here is counts above background. As opposed to radio pulsar studies, for which long times are needed, here we need area, i.e., a large number of counts per burst with respect to background, not a large number of bursts (even though that would not be unwelcome).

Ringing

The next question to ask of the data is, "Do the bursts come in bunches or alone?" Except for the three that occurred within 20 ms in the first flight, all are singles if we just inspect the data by eye. But what if there is an enhancement at some interval before or after each burst that is of the same order of magnitude as the background?

This effect will be enhanced, if it exists, by combining all of the bursts as we did to get the pulse profile. We can then display this plot for hundreds of milliseconds (or any arbitrary time) before and after the bursts to look for structure. If the limits are ±T seconds about the burst and two bursts are separated by less than T seconds, then the second of the two should be included in the background and not included in the composite burst. This is to insure that all bins of the background come frm the same number of bursts. This was done for both flights, and the result for the first flight is displayed in Figure VI-10, which shows plus and minus 16 ms centered on the aligned bursts. The large scatter due to statistics can lead the eye to see a variety of

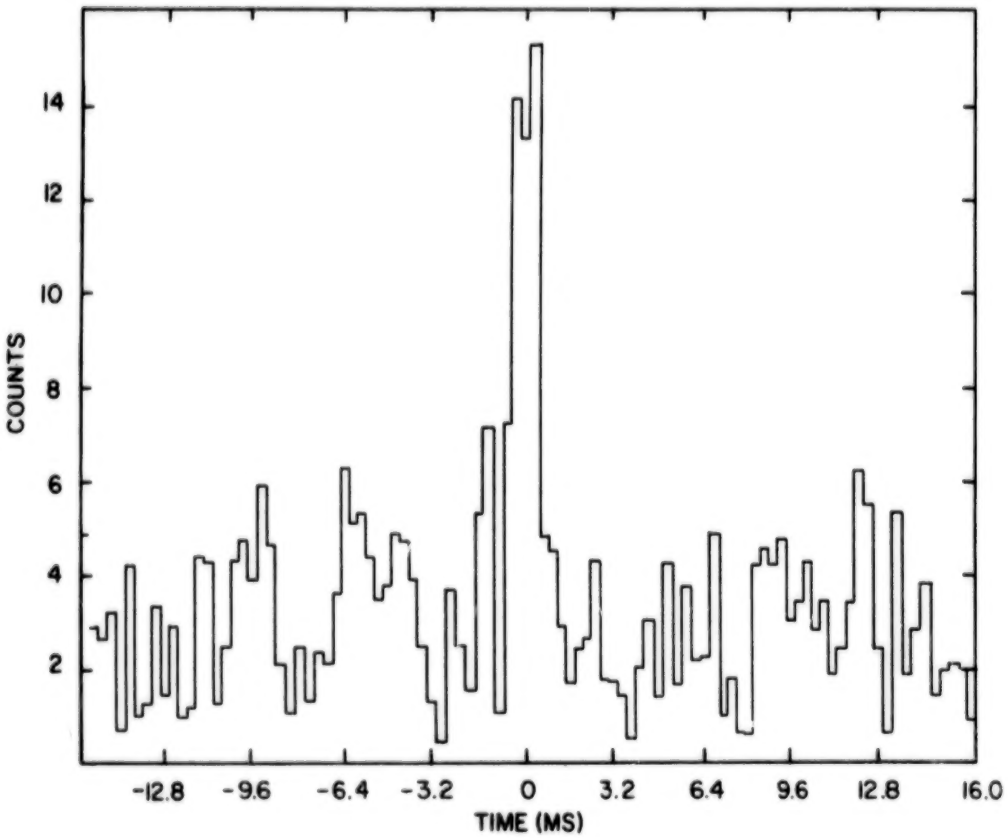

Figure VI-10. Centroid-aligned burst profile including data from ±16 ms about the centroid. The bins are 320 μs.

things, but a χ^2 test shows the background on either side of the bursts to be consistent with a constant.

Since the scatter in the points goes as $\sqrt{N}$ and the number of counts in the peak goes as N, it is advantageous to gather more bursts. When the bursts of the second flight are added in, the statistics only change by about a factor of $\sqrt{2}$. Hence, the scatter is still large.

WHAT DO THE RESULTS MEAN?

The answer to this question could be as detailed and theoretical as desired. The intent of this section is to try to describe generally the situation at these three sources, and how various types of analysis lead us to those conclusions.

For Her X-1 the situation is basically clear, but muddied by details. The power spectrum gave us the period of the pulsar. The light curve gave us the mean pulse shape. From the earlier chapters we have learned that pulsars have a beam of sorts that sweeps past us to create the pulse. Since two of the bumps are 180° apart in the pulse profile, the "light house" must have two beams shining in opposite directions. Since there are generally two magnetic poles at a magnetized object, the fact that the light curve is double peaked is not surprising. The third bump indicates either another beam or some structure to one of the two polar beams.

If we could watch Her X-1 for days on end, we would note a 1.7 day period present in both the rate data and in the measured pulsar period. This is just the binary motion of the stars. We would also notice that this source had another periodicity or two, and then the situation becomes complicated. The pulse shape changes with binary phase and the emission is only present for 9 out of 35 days. Hence this "well understood source is not so well understood after all.

From all our tests Cyg X-3 is a random source of x-rays. Its autocorrelation function is zero for $\tau \neq 0$. It contains no bursts that cannot be accounted for by the Poisson probability distribution. Its power spectrum is featureless on our time scale. Longer observations show it to exhibit a 4.8 hour sinusoidal variation. But this apparent simplicity is deceptive. Its spectrum varies dramatically, its mean intensity seems to have various levels. And intense radio flares, so far uncorrelated with its x-ray or infrared emission, are seen.

And then there is Cyg X-1. Our observation of bursts indicates a radius of less than 100 km. Optical observations predict a mass in excess of 5 $M_\odot$. It

certainly appears to be a black hole. If so, the x-rays we see are coming from the inner portions of the accretion disk. Thus the shot noise character of its intensity is telling us something about the processes occurring there. In Appendix VI-A, the mean, variance, power spectrum and autocorrelation for shot noise are derived as functions of the pulse shape. It is seen that the observed autocorrelation function shape can be predicted from the assumption of exponentially shaped pulses. We can get other parameters of the system also. The fit to the autocorrelation function gives the exponential time constant. This, combined with the mean ($\lambda A\tau_0$) and the variance ($\lambda A^2\tau_0/2$) give the pulse rate λ and pulse height A. These turn out to be about 20 per second with fall time about 1/3 - 1/2 second, and with about 65 x-ray counts detected per pulse. This is true only for the regime $\Delta T << \tau$.

The process of aligning centroids to give a light curve for bursts yielded no finer temporal structure. This is only based on a dozen or so bursts, and statistical uncertainties are large. The different metrics (Schwartzschild and Kerr) predict minimum burst durations. As yet, no distinction between metrics can be made. If and when shorter duration time structure is seen, perhaps the parameters of the metric can be found.

APPENDIX VI-A

Derivation of autocorrelation function, spectral density, and probability density functions for shot noise processes.

This derivation will proceed in three steps. First is the derivation of the autocorrelation function for Poisson impulses. Second we will convolve this result with the shape of an individual shot pulse to reveal both the autocorrelation function and the spectral density of shot noise. Finally, the probability density function will be derived.

First, a few definitions.

$\mu_x = E[x(t)]$ = mean of x(t),

σ_x^2 = variance of x(t),

f(x) = probability density function of x(t),

$\rho_{xx}(t_1, t_2)$ or $\rho_{xx}(\tau)$ } = autocorrelation function of x(t),

$\gamma_{xx}(t_1, t_2)$ or $\gamma_{xx}(\tau)$ } = autocovariance function of x(t)

$\Gamma_{xx}(f)$ = power spectrum of x(t)

$R_{xx}(f)$ = spectral density of x(t)

We know from probability and statistics (e.g., see Papoulis 1965, or Jenkins and Watts 1969) that

$$f(x)\,dx = P[x \leqslant x(t) \leqslant x + dx],$$

$$\mu_x = E[x(t)] = \frac{1}{N} \sum_{i=1}^{N} x_i$$

$$\sigma_x^2 = \frac{1}{N} \sum_{i=1}^{N} (x_i - \mu_x)^2$$

The mean and variance characterize a set of data when all the points, x_i, are independent of each other. This generally is not the case in nature. Two other quantities are needed: the autocovariance and autocorrelation functions. They are defined as:

$$\gamma_{xx}(t_1, t_2) = E\left\{[x(t_1) - \mu_x) \cdot (x(t_2) - \mu_x]\right\},$$

$$\rho_{xx}(t_1, t_2) = \gamma_{xx}(t_1, t_2)/\sigma_x(t_1)\,\sigma_x(t_2)$$

Some temporal features are more easily recognized through the power spectrum,

$$\Gamma_{xx}(\omega) = \int_{-\infty}^{\infty} e^{-i\omega\tau}\, \gamma_{xx}(\tau)\, d\tau,$$

where $\omega = 2\pi/\tau$ and $\gamma_{xx}(\tau)$ will be defined later, but is just $\gamma_{xx}(t_1, t_2)$ for $t_1 = \quad _2 = t + \tau$. The above can be inverted, if $\gamma_{xx}(\tau)$ is measurable, to give

$$\gamma_{xx}(\tau) = \frac{1}{2\pi} \int_{-\infty}^{\infty} \Gamma_{xx}(\omega)\, e^{i\omega\tau}\, d\omega.$$

Then for stationary processes, $\mu \neq \mu(t)$,

$$\rho_{xx}(\tau) = \frac{\gamma_{xx}(\tau)}{\sigma_x^2}$$

and

$$R_{xx}(\omega) = \int_{-\infty}^{\infty} e^{-i\omega\tau}\, \rho_{xx}(\tau)\, d\tau.$$

So much for definitions. Much of what follows is quite general and has wide applications, but the underlying goal is to describe successfully the temporal character of Cyg X-1 and other sources that display a shot noise type of count rate. Hence we shall consider a process whose intensity profile is a composite of overlapping and randomly occurring pulses of defined shape.

In order to achieve this result we start with the Poisson process that governs the number of shot pulses in any time interval. Consider a group of points t_i randomly distributed on the interval (0, t) with mean rate of λ. The probability of finding k points in this interval is just

$$e^{-\lambda t}\frac{(\lambda t)^k}{k!}$$

Form the random variable x(t), which is defined as the number of points in the interval (0, t). Then the difference $x(t_a) - x(t_b)$ is also a random variable and is the number of counts in (t_b, t_a).

Temporarily, let us denote $x(t_a) - x(t_b)$ by $\omega(t_a, t_b)$. Then it is easy to show that

$$E[\omega(t_a, t_b)] \equiv E[x(t_a) - x(t_b)] = \lambda \cdot (t_a - t_b) = \mu_\omega(t_a, t_b),$$

and similarly

$$E[\omega^2(t_a, t_b)] = \lambda^2(t_a - t_b)^2 + \lambda(t_a - t_b);$$

hence

$$\sigma^2_\omega(t_a, t_b) = \lambda(t_a - t_b).$$

Thus, this new random variable is also Poisson distributed. Pick four times such that $t_a > t_b > t_c > t_d$. The intervals (t_b, t_a) and (t_d, t_c) are non-overlapping and consequently independent. The auto covariance can then be written as

$$\gamma_{xx}(t_a - t_b, t_c - t_d) = E\left\{[\omega(t_a, t_b) - \mu_\omega(t_a, t_b)] \cdot [\omega(t_c, t_d) - \mu_\omega(t_c, t_d]\right\}$$

$$= E[\omega(t_a, t_b) \cdot \omega(t_c, t_d)] - \mu_\omega(t_a, t_b)\,\mu_\omega(t_c, t_d);$$

thus

$$\gamma_{xx}(t_a - t_b, t_c - t_d) = E[\omega(t_a, t_b) \cdot \omega(t_c, t_d)] - \gamma^2(t_a - t_b)(t_c - t_d),$$

Let us now evaluate the expectation value:

$$E\left\{[x(t_a) - x(t_b)]\ [x(t_c) - x(t_d)]\right\} = \lambda^2(t_a - t_b)(t_c - t_d),$$

since for two independent random variables the mean of the product is the product of the means. Thus in the non-overlap regime

$$\gamma_{xx}(t_a - t_b, t_c - t_d) = 0,$$

which makes sense. If, however, the intervals overlap, i.e., $t_a > t_c > t_b > t_d$, then intervals (t_b, t_a) and (t_d, t_c) overlap and are not independent. Adding and subtracting $x(t_c)$ and $x(t_b)$ appropriately and regrouping terms gives

$$E\left\{[x(t_a) - x(t_b)]\ [x(t_c) - x(t_d)]\right\} = E[\omega(t_a, t_c)\,\omega(t_c, t_b)]$$

$$- E[\omega(t_a, t_c)\omega(t_b, t_d)] + E[\omega^2(t_c, t_b)]$$

$$+ E[\omega(t_c, t_b)\omega(t_b, t_d)].$$

These are now nonoverlapping intervals and we can apply the formulas discussed above:

$$E[\omega(t_a, t_b)\,\omega(t_c, t_d)] = \lambda^2(t_c - t_d)\cdot(t_a - t_b) + \lambda(t_c - t_b).$$

This is identical to the non-overlap case plus a term dependent upon the overlap. Then

$$\gamma_{xx}(t_a - t_b, t_c - t_d) = \lambda(t_c\ t_b).$$

If this is generalized by setting $t_a = t_1$, $t_b = 0$, $t_c = t_2$, and $t_d = 0$, we get

$$E[x(t)] = \lambda t, \text{ where } t = t_1 \text{ or } t_2;$$

$$\gamma_{xx}(t_1, t_2) = \left\{\begin{matrix} \lambda t_2 & t_1 \geq t_2 \\ \lambda t_1 & t_2 \geq t_1 \end{matrix}\right\}$$

Now form a new random variable that eventually will be the derivative of x(t) with respect to t:

$$y(t) = \frac{1}{\epsilon}\,[x(t + \epsilon) - x(t)], \qquad \epsilon > 0.$$

y(t) is Poisson distributed and represents $1/\epsilon$ times the number of points in $(t, t + \epsilon)$. Let us now calculate the mean and autocovariance of y(t).

$$E[y(t)] = \frac{1}{\epsilon} E[x(t+\epsilon)] - \frac{1}{\epsilon} E[x(t)]$$

$$= \frac{1}{\epsilon}\lambda(t+\epsilon) - \frac{1}{\epsilon}\lambda t$$

$$= \lambda.$$

In order to calculate $\gamma_{yy}(t_1, t_2)$, we must first determine the amount of overlap.

(1) For $t_1 > t_2 + \epsilon$, (non-overlap)

$$\gamma_{yy}(t_1, t_2) = 0.$$

(2) For $t_2 + \epsilon > t_1 > t_2$, (overlap)

$$\gamma_{yy}(t_1, t_2) = \frac{1}{\epsilon^2}\gamma_{xx}(t_1 + \epsilon - t_1, t_2 + \epsilon - t_2)$$

$$= \frac{1}{\epsilon^2}[\lambda(t_2 + \epsilon) - \lambda t_1]$$

$$= \frac{1}{\epsilon}\lambda - \frac{1}{\epsilon^2}\lambda(t_1 - t_2).$$

Generalizing this gives

$$\gamma_{yy}(t_1, t_2) = \left\{ \begin{array}{ll} 0 & |t_1 - t_2| > \epsilon \\ \frac{1}{\epsilon}\lambda - \frac{1}{\epsilon^2}\lambda|t_1 - t_2| & |t_1 - t_2| < \epsilon \end{array} \right\}$$

Finally, form the random variable z(t) as

$$z(t) = \frac{dx(t)}{dt} = \lim_{\epsilon \to 0} y(t)$$

Performing this limiting process yields

$$E[z(t)] = \lambda$$

$$\gamma_{zz}(t_1, t_2) = \lambda\delta(t_1 - t_2),$$

since $|t_1 - t_2|$ must also go to zero when $\epsilon \to 0$; hence the introduction of the delta function.

This result can be put in a form more readily utilized. Most autocovariances are a function of a shift parameter τ. Let $t_2 = t$ and $t_1 = t + \tau$. Then

$$\gamma_{zz}(\tau) = \gamma_{zz}(t_1, t_2) = \gamma_{zz}(t, t + \tau)$$

thus

$$\gamma_{zz}(\tau) = \lambda\delta(\tau).$$

From this we immediately get the variance σ_z^2 by setting $\tau = 0$:

$$\sigma_z^2 = \lambda$$

Hence z(t) is also Poisson distributed. The autocorrelation function is then

$$\rho_{zz}(\tau) = \delta(\tau).$$

The power spectrum becomes

$$\Gamma_{zz}(\omega) = \lambda \int_{-\infty}^{\infty} \delta(\tau)\, e^{-i\omega\tau} d\tau = \lambda.$$

Now we need to fold in the actual pulse profile. Let h(t) be this pulse shape and let s(t) be the cumulative effect of shot pulses that occur randomly. Then we say

$$s(t) = \sum_i h(t - t_i),$$

where t_i are randomly distributed points with uniform density (in time) λ. The t_i are then described by z(t):

$$z(t) = \sum_i \delta(t - t_i)$$

How do we relate the two? They are related mathematically through a convolution:

$$s(t) = \int_{-\infty}^{\infty} (t - a)\, h(a)\, da.$$

Assuming h(t) is a real process and obeys casualty (h(t) = 0 for $t < 0$), this becomes

$$s(t) = \int_{0}^{\infty} (t - a)\, h(a)\, da.$$

A quantity we will have need for later is the Fourier transform of h(t).

$$H(i\omega) = \int_{-\infty}^{\infty} h(t)\, e^{-i\omega\tau}\, dt.$$

Note that

$$H(0) = \int_{-\infty}^{\infty} h(t)\, dt.$$

First, calculate the mean of s(t), assuming λ is a constant in time.

$$E[s(t)] = \int_{0}^{\infty} E[z(t - a)]\, h(a)\, da.$$

The expectation can go inside the integral since it is performed over t, not a. But expectations are constants in time, or so we assumed when we assumed λ constant; thus

$$E[z(t - a)] = E[z(t)] = \mu_z,$$

and so we have

$$E[s(t)] = \mu_z \int_0^\infty h(a)\, da$$

$$= \mu_z\, H(0).$$

What about the autocovariance? By expanding its definition we see that for an arbitrary function f(t)

$$\gamma_{ff}(\tau) = E[f(t) \cdot f(t+\tau) - \mu f(t) - \mu f(t+\tau) + \mu^2]$$

$$= E[f(t) \cdot f(t+\tau)] - \mu\ E[f(t)] + E[f(t+\tau)] + \mu^2$$

$$= E[f(t) \cdot f(t+\tau)] - \mu^2;$$

hence multiply s(t) by $z(t-\tau)$. Thus, since $z(t-\tau)$ is not a function of a,

$$s(t)\, z(t-\tau) = \int_0^\infty z(t-a)\, z(t-\tau)\, h(a)\, da.$$

Take the expectation of both sides:

$$E[s(t)\, z(t-\tau)] = \int_0^\infty E[z(t-a)\, z(t-\tau)]\, h(a)\, da$$

Change variables on the right side: $t' = t - a$, $t - \tau = t' + (a - \tau)$. Then the expectation value inside the integral becomes

$$E[z(t-a)\, z(t-\tau)] = E[z(t')\, z(t' + (a-\tau))];$$

but this yields

$$E[z(t-a)\, z(t-\tau)] = \gamma_{zz}(a-\tau) + \mu_z^2,$$

and since $\gamma_{zz}(a-\tau) = \gamma_{zz}(\tau - a)$, we get

$$E[s(t)\, z(t-\tau)] = \int_0^\infty [\gamma_{zz}(\tau - a) + \mu_z^2]\, h(a)\, da.$$

But the left hand side is the cross covariance between s(t) and z(t). Then

$$E[s(t)\, z(t-\tau)] = \gamma_{sz}(\tau) + \mu_s\, \mu_z,$$

so we get

$$\gamma_{sz}(\tau) = \int_0^\infty \gamma_{zz}(\tau - a)\, h(a)\, da + \mu_z^2\, H(0) - \mu_s\, \mu_z.$$

Or, using the symbol * to denote convolution,

$$\gamma_{sz}(\tau) = \gamma_{zz}(\tau) * h(\tau) + \mu_z^2\, H(0) - \mu_s\, \mu_z.$$

But we know that

$$\mu_s = \mu_z\, H(0);$$

thus the last two terms cancel to give

$$\gamma_{sz}(\tau) = \gamma_{zz}(\tau) * h(\tau).$$

Similarly, we can show that

$$\gamma_{ss}(\tau) = \gamma_{sz}(\tau) * h(-\tau).$$

Combining these two results yields the desired relation between the autocovariance of s(t) and that for z(t), which has already been calculated. We have

$$\gamma_{ss}(\tau) = \gamma_{zz}(\tau) * h(-\tau) * h(\tau).$$

Now let us proceed to the power spectrum. By definition

$$\Gamma_{zz}(\omega) = \int_{-\infty}^{\infty} e^{-i\omega\tau}\, \gamma_{zz}(\tau)\, d\tau.$$

Similarly

$$\Gamma_{zs}(\omega) = \int_{-\infty}^{\infty} e^{-i\omega\tau}\, \gamma_{zs}(\tau)\, d\tau$$

$$= \int_{-\infty}^{\infty} e^{-i\omega\tau} \left[\int_{-\infty}^{\infty} \gamma_{zz}(\tau - a)\, h(a)\, da \right] d\tau$$

$$= \int_{-\infty}^{\infty} h(a) \left[\int_{-\infty}^{\infty} e^{-i\omega\tau}\, \gamma_{zz}(\tau - a)\, d\tau \right] da$$

For the integral in brackets, let $\beta = \tau - a$; then

$$\Gamma_{zs}(\omega) = \int_{-\infty}^{\infty} h(a) \left[\int_{-\infty}^{\infty} e^{-i\omega(\beta+a)}\, \gamma_{zz}(\beta)\, d\beta \right] da$$

$$= \int_{-\infty}^{\infty} h(a)\, e^{-i\omega a} \left[\int_{-\infty}^{\infty} e^{-i\omega\beta}\, \gamma_{zz}(\beta)\, d\beta \right] da$$

$$= \int_{-\infty}^{\infty} h(a)\, e^{-i\omega a}\, \Gamma_{zz}(\omega)\, da$$

$$= \Gamma_{zz}(\omega)\, H(i\omega).$$

Similarly, we can show that

$$\Gamma_{ss}(\omega) = \Gamma_{zs}(\omega)\, H^{*}(i\omega).$$

Combining these results gives

$$\Gamma_{ss}(\omega) = \Gamma_{zz}(\omega)\, |H(i\omega)|^2.$$

We now have all we need to compute the various functions associated with s(t).

$$\mu_s = \lambda\, H(0),$$

$$\Gamma_{ss}(\omega) = \lambda\, |H(i\omega)|^2,$$

$$\gamma_{ss}(\tau) = \frac{1}{2\pi} \int_{-\infty}^{\infty} \lambda\, |H(i\omega)|^2\, e^{i\omega\tau}\, d\omega.$$

This integral is the inverse transform of $|H(i\omega)|^2$ which is just $h(t) * h(-t)$, since the transform changes multiplication to convolution. Then

$$\gamma_{ss}(\tau) = \lambda \int_0^{\infty} h(\tau + \beta)\, h(\beta)\, d\beta.$$

This gives us

$$\sigma_s^2 = \lambda \int_0^{\infty} h^2(\beta)\, d\beta.$$

The expressions for μ_s and σ_s^2 form Campbell's theorem.

$$\rho_{ss}(\tau) = \frac{\displaystyle\int_0^{\infty} h(\tau + \beta)\, h(\beta)\, d\beta}{\displaystyle\int_0^{\infty} h^2(\beta)\, d\beta}$$

Now we need just supply the proper form of h(t) that describes the shot noise process.

Example: rectangular pulse h(t)

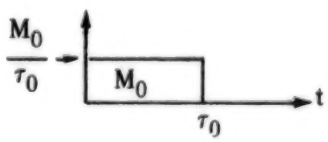

$$h(t) = \begin{cases} M_0/\tau_0, & 0 \leqslant t \leqslant \tau_0 \\ 0 & \text{otherwise} \end{cases}$$

Ther. we get

$$\mu_s = \lambda M_0,$$

$$\sigma_s^2 = \lambda M_0 \left(\frac{M_0}{\tau_0}\right),$$

$$H(i\omega) = \left(\frac{M_0}{\tau_0}\right) \left[\frac{1 - e^{-i\omega\tau_0}}{i\omega}\right]$$

$$|H(i\omega)|^2 = 2\left(\frac{M_0}{\tau_0}\right)^2 \left[\frac{1 - \cos \omega \tau_0}{\omega^2}\right],$$

$$\Gamma_{ss}(\omega) = 2\lambda \left(\frac{M_0}{\tau_0}\right)^2 \left[\frac{1 - \cos \omega \tau_0}{\omega^2}\right]$$

We must determine the proper integration limits for calculating $\gamma_{ss}(\tau)$. For $h(\beta)$ to be non zero, $0 \leqslant \beta \leqslant \tau_0$. For $h(\tau + \beta)$ to be non zero, $-\tau \leqslant \beta \leqslant \tau_0 - \tau$. Hence the integral is nonzero for $0 \leqslant \beta \leqslant \tau_0 - \tau$. Hence

$$\gamma_{ss}(\tau) = \begin{cases} \lambda\left(\frac{M_0}{\tau_0}\right)^2 (\tau_0 - \tau) & 0 \leqslant \tau \leqslant \tau_0 \\ 0 & \text{otherwise} \end{cases},$$

and finally we get

$$\rho_{ss}(\tau) = \begin{cases} 1 - \tau/\tau_0 & 0 \leqslant \tau \leqslant \tau_0 \\ 0 & \text{otherwise} \end{cases}.$$

Example: exponential pulse

$$h(t) = \begin{cases} Ae^{-t/\tau_0} & 0 \leqslant t \\ 0 & t < 0 \end{cases}$$

$$\mu_s = \lambda A \tau_0,$$

$$\sigma_s^2 = \frac{1}{2} \lambda A^2 \tau_0,$$

$$\Gamma_{ss}(\omega) = \lambda A^2 \frac{\tau_0^2}{1 + \omega^2 \tau_0^2}$$

$$\gamma_{ss}(\tau) = \frac{1}{2} \lambda A^2 \tau_0 e^{-\tau/\tau_0},$$

$$\rho_{ss}(\tau) = e^{-\tau/\tau_0},$$

which is just the shape of the autocorrelation plot shown for Cyg X-1.

Can we determine the probability density function and its Fourier transform, the characteristic function? First of all, by definition of stationary processes,

$$P\{s < s(t) \leqslant s + ds\} = f(s)\, ds,$$

and this is time inedpendent. Let us assume the process h(t) only lasts for a time T. Then

$$h(t) = 0 \text{ for } t < 0 \text{ and for } t > T,$$

In the exponential of the second example, we could let $T = 10\,\tau_0$ or $100\,\tau_0$ and be fine. Then let

$$X_1(t) = h(t - t_1),$$

where t_1 is a random variable uniformly distributed on $(t - T, t)$. (Remember we are looking for effects of things that have already happened; hence t - T.) The probability density of $X_1(t)$ is $g_1(x)$, where

$$g_1(x)\, dx = P\{x < X_1(t) \leqslant x + dx\}.$$

Now consider

$$x_2(t) = h(t - t_1) + h(t - t_2).$$

The probability density of $X_2(t)$ is $g_2(x)$, which is the convolution of $g_1(x)$ with itself, i.e.

$$g_2(x) = g_1(x) * g_1(x).$$

Extending this to k terms,

$$X_k(t) = \sum_{i=1}^{k} h(t - t_k)$$

and

$$g_k(x) = g_{k-1}(x) * g_1(x)$$

$$= g_1(x) * \cdots * g_1(x) \text{ k terms.}$$

Just for the sake of completeness, define

$$g_0(x) \equiv \delta(x)$$

Thus if there are k shot pulses in the interval $(t - T, t)$, $g_k(s)$ is the probability density of $s(t)$. This can be written as

$$f[s(t) \mid n(t - T, t) = k] = g_k(s)$$

where $n(a, b)$ is a random variable equal to the number of points in (a, b). Since everything is randomly distributed,

$$s(t) = X_k(t),$$

Then the probability density function for shot noise, $f(s)$, is given by

$$f(s) = f[s|n = 0]\ P\{n = 0\} + f[s|n = 1]\ P\{n = 1\} + \cdots + f[s|n = k]\ P\{n = k\}$$

where $P\{n = k\}$ is the Poisson probability, i.e.

$$P\{n = k\} = e^{-\lambda T} \frac{(\lambda T)^k}{k!}$$

So we get

$$f(s) = e^{-\lambda T}\left[g_0(s) + g_1(s) \cdot \lambda T + g_2(s) \cdot \frac{1}{2}(\lambda T)^2 + \cdots + g_k(s)\frac{(\lambda T)^k}{k!} + \cdots\right].$$

All we need now are the $g_i(s)$. If we change variables such that $\eta = t - t_1$, then $x_1(t) = h(\eta)$ where η is a random variable on (0, T). Thus we know the form of $x_1(t)$. We also know

$$g_1(x)\,dx = P\{x < x_1(t) \leqslant x + dx\},$$

and since η is uniformly distributed over (0, T), the probability of $x_1(t)$ being in a band of width dx is just dt/T where dt is the interval corresponding to dx. Hence we can say

$$g_1(x)\,dx = dt/T$$

or

$$g_1(x)\frac{dx}{dt}\,dt = dt/T,$$

which implies that

$$g_1(x) = \frac{1}{T} \cdot \frac{1}{dx/dt} = \frac{1}{T} \cdot \frac{1}{\dfrac{dh(\beta)}{d\beta}}.$$

It can also be shown that (Papoules 1965, p. 566) the characteristic function $\Phi(\omega)$ for shot noise is

$$\Phi(\omega) = e^{\lambda}\int_0^T e^{i\omega h(a)} - 1\,da.$$

Then we can get f(s) from the inversion

$$f(s) = \frac{1}{2\pi}\int_{-\infty}^{\infty} \Phi(\omega)\, e^{-i\omega s}\,d\omega.$$

The integrals start to get troublesome about here, so we shall end.

APPENDIX VI-B

DERIVATION OF VARIANCE AS A FUNCTION OF BIN WIDTH

In order to derive the variance as a function of bin width the following terminology will be used:

M_0 = mean counts per burst of duration τ

ΔT = temporal width of data bin

λ = mean shot burst rate

N_i = total counts in data bin i

M_{ij} = counts from burst j in data bin i

n_i = number of bursts in bin i

B_i = background counts in bin i

R = mean on-source count rate

R_B = mean background count rate.

First of all,

$$R = \langle N \rangle / \Delta T, \quad R_B = \langle B \rangle / \Delta T, \quad \epsilon = R_B / R.$$

Then summing all the contributions to data bin i,

$$N_i = \sum_{j=1}^{n_i} M_{ij} + B_i. \tag{B1}$$

The variance is then given by

$$(\delta N_i)^2 = \sum_{j=1}^{n_i} \left(\frac{\partial N_i}{\partial M_{ij}}\right)^2 (\delta M_{ij})^2 + \left(\frac{\partial N_i}{\partial B_i}\right)^2 (\delta B_i)^2 + \left(\frac{\partial N_i}{\partial n_i}\right)^2 (\delta n_i)^2. \tag{B2}$$

Let us evaluate the partial derivatives:

$$\frac{\partial N_i}{\partial M_{ij}} = 1, \quad \frac{\partial N_i}{\partial B_i} = 1, \quad \frac{\partial N_i}{\partial n_i} = M_i$$

Let us show this to be true. The first is obviously true, since the coefficient of all M_{ij} in the sum is one. Hence, the partial derivative with respect to it is just one. The second partial is one trivially. The third is not so obvious. However, we can treat the partial derivative of a sum similarly to the partial of an integral between fixed limits, i e.

$$\frac{\partial N_i}{\partial n_i} = \frac{\partial}{\partial n_i} \int_0^{n_i} M_i(y)\, dy,$$

where $M_i(y)$ is the contribution to the i^{th} data bin from the y^{th} burst. This yields

$$\frac{\partial N_i}{\partial n_i} = M_i(n_i) - M_i(0) = M_i, \tag{B3}$$

Since $M_i(0) = 0$. The interpretation of M_i is that this is the mean counts per burst for the i^{th} data bin. This is not to be confused with the overall mean counts per burst $\langle M \rangle$. We immediately can write

$$N_i = n_i M_i + B_i.$$

The variances of M_{ij} and B_i are given by Poisson statistics as

$$(\delta M_{ij})^2 = M_{ij} \text{ and } (\delta B_i) = B_i.$$

We then can write the variance as

$$(\delta N_i)^2 = \sum_{j=1}^{n_i} M_{ij} + B_i + M_i (\delta n_i)^2$$

$$= n_i M_i + B_i + M_i (\delta n_i)^2$$

$$= N_i + M_i (\delta n_i)^2.$$

If we average this over the entire exposure, we get

$$\langle(\delta N)^2\rangle = \langle N\rangle + \langle M_i\,(\delta n_i)^2\rangle.$$

If we assume the burst amplitude to be independent of burst frequency, we get

$$\langle(\delta N)^2\rangle = \langle N\rangle + \langle M(\delta n)^2\rangle.$$

Here we must enter some assumptions as to the process involved. We choose the interpretation that the overall count rate is composed of randomly occurring, overlapping pulses whose cumulative effect exceeds that of the background and other processes that generate structureless counts. This can be quantified as follows:

(a) $\langle(\delta n)^2\rangle = \langle n\rangle$,

(b) $\langle(\delta M)^2\rangle \ll \langle M\rangle^2$,

(c) $M_i = \langle M\rangle + \delta M$.

The first of these just states that the bursts are Poisson distributed; i.e., shot noise-like. The second requires that the shot noise process is the dominate process in generating the data. The last statement just shows how M_i varies from the mean $\langle M\rangle$. Incorporating this into Equation B3 yields

$$\begin{aligned}\langle(\delta n)^2\rangle &= \langle N\rangle + \langle(\langle M\rangle + \delta M)^2\,(\delta n)^2\rangle \\ &= \langle N\rangle + \langle(\langle M\rangle^2\,(\delta n)^2 + 2\langle M\rangle\,\delta M(\delta n)^2 + (\delta M)^2\,(\delta n)^2 \\ &\cong \langle N\rangle + \langle M\rangle^2\,(\delta n)^2 \\ &\cong \langle N\rangle + \langle M\rangle^2\,\langle n\rangle. \qquad \text{(B4)}\end{aligned}$$

Let us now further assume rectangular pulses of width τ and total counts M_0. There are two temporal regions in which we can make definite statements $\Delta T \ll \tau$ and $\Delta T \gg \tau$.

$\underline{\Delta T \ll \tau}$:

Here the data bin width is small compared to the burst width. Then assuming stationary mean values, we have

$$\langle M \rangle = M_0 \frac{\Delta T}{\tau} \tag{B5}$$

$$\langle n \rangle = \lambda\tau \tag{B6}$$

Plugging this into Equation (4) gives us

$$\langle (\delta n)^2 \rangle = \langle N \rangle + M_0^2 \cdot \left(\frac{\Delta T}{\tau}\right)^2 \cdot (\lambda\tau)$$

$$= R\Delta T + \frac{(R - R_B)^2\, \Delta T}{(\lambda\tau)^2} \cdot \left(\frac{\Delta T}{\tau}\right)^2 \cdot (\lambda\tau),$$

since

$$M_i = \frac{N_i - B_i}{n} \quad \text{and} \quad M_0 \Delta T = \frac{R\Delta T - R_B \Delta T}{n}.$$

Thus we get, after some algebra,

$$\langle (\delta N)^2 \rangle = R\Delta T \left[1 + (1 - \epsilon)^2 \frac{R\Delta T}{\lambda\tau}\right]$$

or

$$\frac{\langle (\delta N)^2 \rangle}{\Delta T} = R \left[1 + (1 - \epsilon)^2 \frac{R\Delta T}{\lambda\tau}\right]. \tag{B7}$$

The other temporal region is for the data bin width large compared to the pulse width. Then

$\underline{\Delta >> \tau}$

$$\langle M \rangle = M_0 \tag{B8}$$

$$\langle n \rangle = \lambda\Delta T \tag{B9}$$

This yields, after similar manipulation of equations,

$$\frac{\langle (\delta N)^2 \rangle}{\Delta T} = R \quad 1 + (1 - \epsilon)^2 \frac{R}{\lambda}. \tag{B10}$$

The obvious features of these two regions is that for data bins small with respect to pulse width, the mean square deviation over bin width increases with bin width from the Poisson prediction of $\langle N \rangle$. For data bins large with respect

to pulse width, the mean square deviation over bin width is constant but elevated above the Poisson prediction by $(1 - \epsilon)^2 R^2/\lambda$. This gives us a direct means for measuring the shot noise parameters of an x-ray source. If the data are not continuous or cannot readily be put in the form of pure counts, we can use intensities as long as we use the proper variance. Let I be the intensity, analogous to R above, and let $(\mathrm{var})_s$ be the expected statistical variance. Then instead of considering mean square deviation over width, we can use observed variance over expected variance from Poisson statistics. This gives the added advantage that truly random sources will yield unity for this ratio. Then

$$I_i = N_i/\Delta T,$$

$$\frac{\langle (\delta N)^2 \rangle}{\langle N \rangle} = \frac{\langle (\delta I)^2 \rangle}{[(\mathrm{var})_s I]},$$

and for the two regimes

$$\frac{\langle (\delta I)^2 \rangle}{(\mathrm{var})_s I} = \begin{cases} 1 + \dfrac{\langle I \rangle \Delta T}{\lambda' \tau} & \Delta T \ll \tau \\ 1 + \dfrac{\langle I \rangle}{\lambda'} & \Delta T \gg \tau \end{cases},$$

where

$$\lambda' = \frac{\lambda}{(1 - \epsilon)^2}.$$

BIBLIOGRAPHY

Boldt, E. Holt, S., Rothschild, R., and Serlemitsos, P., 1975, Proceedings of the International Conference on X-Rays in Space, 1, 69 (U. of Calgary: Calgary).

Bracewell, R. M., 1965, The Fourier Transform and Its Applications, (McGraw-Hill: New York).

Brigham, E. O., 1974, The Fast Fourier Transform, (Prentice-Hall: Englewood Cliffs, New Jersey).

Freeman, J. J., 1958, Principles of Noise, (J. Wiley & Sons: London).

Holt, S. S. Boldt, E. A., Rothschild, R. E., Saba, J. L. R., and Serlemitsos, P. J., 1974, Ap. J. (Letters), 190, L109.

Jenkins, G. M. and Watts, D. G., 1969, Spectral Analysis and Its Applications, (Holden-Day: San Francisco).

Papoulis, A., 1965, Probability, Random Variables, and Stochastic Processes, (McGraw-Hill, New York).

Rothschild, R. E., Boldt, E. A., Holt, S. S., and Serlemitsos, P. J., 1974, Ap. J. (Letters), 189, L13.

Terrell, N. J., 1972, Ap. J. (Letters), 174, L35.

Wax, N., ed. 1954, Noise and Stochastic Processes, (Dover: New York).

Weisskopf, M. C., Kahn, S. M., and Sutherland, P. G., 1975, Ap. J. (Letters) 199, L147.

Blank
Page

CHAPTER VII
RECOGNITION OF COMPACT ASTROPHYSICAL OBJECTS
THE BINARY PULSAR PSR 1913 + 16

Steven Detweiler
University of Maryland
College Park, Maryland

In the summer of 1974 Hulse and Taylor (1975) from the University of Massachusetts made the important discovery of a radio pulsar (PSR 1913+16) in a binary system. Hopefully, in the near future this system will allow unprecedented tests of general relativity and will afford new insight into the evolution of close binary systems.

THE PARAMETERS OF PSR 1913+16

The important parameters of the pulsar and its binary system are given in Table VII-1, and a schematic diagram of the velocity curve is given in Figure VII-1.

Table VII-1
Parameters of PSR 1913+16

P	Period of Pulsar	.05902995 S
$\lvert\dot{P}\rvert$	Absolute value of time derivative of P	$<10^{-16}$
DM	Dispersion measure	167 ± 5 cm^{-3}pc
	Variation with phase	<10 cm^{-3} pc
p	Period of binary	$27906.981 \pm .002$ S
ϵ	Eccentricity	$0.61723 \pm .00003$ S
ω	Longitude of periastron	179°
$\dot{\omega}$	Precession	$4.24 \pm .04$ °/year
a sin i	Projected semi-major axis	7.004×10^5 km $\sim 1R_\odot$
$f = \frac{(M_c \sin i)^3}{(M_p + M_c)^2}$	Mass function	$.1313\ M_\odot$
–	No eclipse observed	–

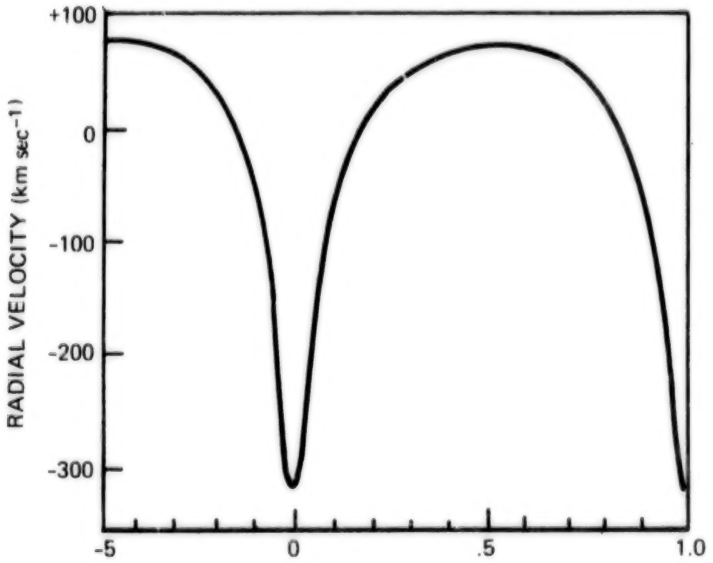

Figure VII-1. The velocity of the binary pulsar as a function of the orbital phase (Source: Hulse and Taylor, 1975).

Two bits of qualitative information are immediately apparent from the velocity curve: (1) The eccentricity of the orbit must be large, as is implied by the sharp dip in the velocity curve; the pulsar is moving toward us at a high speed for a short amount of time. (2) The longitude of the periastron, ω, must be close to 180°; this may be inferred from the high degree of symmetry about the dip in the velocity curve.

The period of the pulsar, P, is only .06 s, making it faster than all other known pulsars but the Crab. The time derivative of the period, $\dot{P}$, has not yet been determined but the upper limit of 10^{-16} is usually small.

Two facts that will be useful in the discussion of the nature of the companion of PSR 1913+16 are that no eclipses are observed and that there is no significant correlation between variations in the dispersion measure and the orbital phase.

With an orbital period of only 7.75 hours and a projected semi-major axis of the orbit (a sin i), of one solar radius, this binary system will clearly exhibit measurable general relativistic effects. In addition, the evidence implies that the companion to the pulsar is also a collapsed object; thus, the effects of the tidal interaction are likely to be at least an order of magnitude smaller than the general relativistic effects.

THE NATURE OF THE COMPANION[1]

We temporarily assume that the companion is a main sequence star; this section then shows that such an assumption is untenable.

It is obvious that the radius of the companion, R_c, must be less than the separation of the two components at periastron, r_s. Thus

$$R_c < r_s = (a \sin i)(1 - \epsilon)\left(\frac{M_c \sin i}{f}\right)^{1/2}, \qquad (1)$$

when f is the observed mass function of the system (cf. Aiken 1964, for a description of the classical problems concerning the determination of the parameters of a binary system). In addition, no eclipse of the system is observed; thus, R_c must be less than the projected stellar separation, r_e, when the pulsar is at superior conjunction, i.e.

$$R_c < r_e = [(1 + \epsilon)/(1 + \epsilon \sin \omega)]\ r_s \cos i. \qquad (2)$$

With the assumption that the companion is a main sequence star the two inequalities on R_c may be converted to inequalities on M_c by using a known mass-radius relationship for main sequence stars,

$$\log (R_c/R_\odot) = \log A + B \log (M_c/M_\odot). \qquad (3)$$

The constants A and B are determined by the specific model chosen for the main sequence stars. Now Inequalities 1 and 2, treated as inequalities on M_c, may be used with the measured values of a sin i and f to put limits on the four quantities M_p, M_c, a, and sin i. (For details see Masters and Roberts, 1975).

It is found that for all acceptable values of these parameters there would be a classical advance of the periastron of at least 3°/orbit. This shift of the periastron would be due to the quadrupole moment of the companion induced by the tidal interaction with the pulsar. The observed value is about three orders of magnitude smaller than this. Table VII-2 gives the relative magnitudes for different causes of the apsidal advance. Thus the advance of the periastron gives us strong evidence that the companion is not on the main sequence.

Inequality 1 could even be made stronger. The lack of x-rays and the lack of correlation between dispersion measure and orbital phase shows that there is no evidence of mass transfer or accretion; thus the companion must be inside its Roche lobe.

---

[1] This section is taken mainly from Masters and Roberts (1975).

Table VII-2
Order of Magnitude of Shift in the Periastron

Quadrupole moment of main sequence companion	$\gtrsim 3°$/orbit
General relativistic effect	$\sim 2°$/year
Quadrupole moment of fast rotating white dwarf companion	$\lesssim 2°$/year
Quadrupole moment of neutron star companion	$< 10^{-3}$ °/year
Quadrupole moment of Helium Main sequence companion	~ 2 °/year

There does exist one difficulty with the above conclusion: If the companion is a helium burning main sequence star (large centeal density and small radius) it is possible that the classical apsidal advance may be as small as the measured 4 °/year. While such a possibility cannot yet be ruled out on observational evidence, the experts[2] consider it unlikely on evolutionary grounds.

THE DETERMINATION OF THE MASSES OF THE BINARY SYSTEM

The Advance of the Periastron

The measured values of a sin i and f yield two equations for the four unknown parameters a, sin i, M_p and M_c. In order to determine the two masses explicitly it is necessary to find at least two more equations governing the four unknowns. For these purposes, we make the likely assumptions that the companion is a compact object and that general relativity is the correct theory of gravity in this regime of physics.

The general relativistic shift in the periastron is given by

$$\delta\omega = \frac{6\pi}{(1-\epsilon^2)} \frac{GM_c}{ac^2} \text{ per orbit.} \qquad (4)$$

[2]Informal discussion at the 1975 Enrico Fermi Summer School

If the measured 4 °/year is caused solely by the general relativistic effect then Equation 4 yields a third relationship between the four unknowns. If a and sin i are eliminated from the system it follows that the total mass of the system is

$$M_p + M_c = 2.87\ M_\odot . \tag{5}$$

If a and M_p are eliminated, then

$$M_c \sin i = 1.03\ M_\odot . \tag{6}$$

The possible relationships between the masses and sin i are given in Figure VII-2.

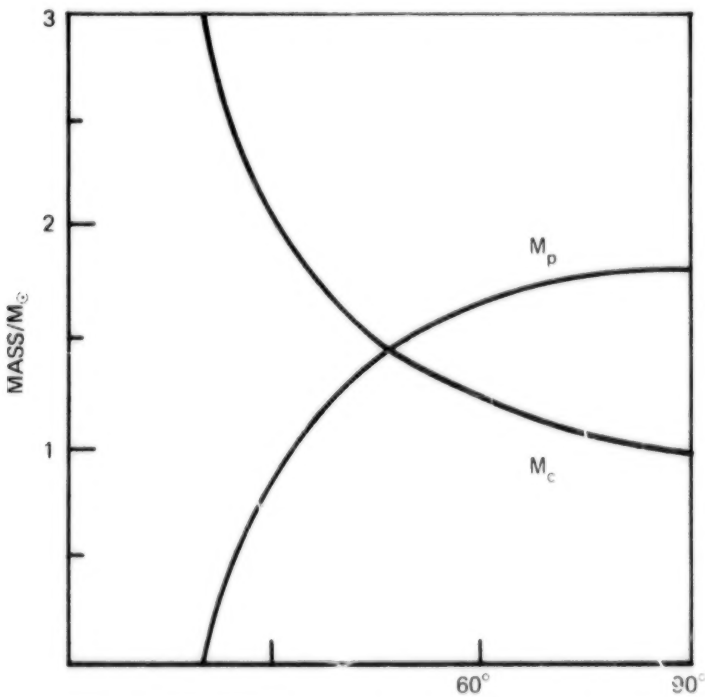

Figure VII-2. The masses of components of the binary system as a function of i (Source: notes from the Enrico Fermi Summer School, 1975).

The assumption that the entire shift in the periastron is due to the general relativistic effect does not necessarily follow from the assumption that the companion is compact. If it is a rapidly rotating white dwarf (one revolution

per 100 seconds or faster) then its rotationally induced quadrupole moment may be large enough to give an apsidal advance comparable to the general relativistic advance. We will assume that this is not the case – though it is a distinct possibility.

Second Order Doppler Shift and the Gravitational Redshift

The ratio of the observed period of the pulsar, P_{ob}, to the emitted period, P, is given by

$$\frac{P_{ob}}{P} = 1 + \frac{\vec{V}\cdot\vec{n}}{c} + \frac{1}{2}\frac{V^2}{c^2} + \frac{GM_c}{rc^2} + \text{higher order terms}, \qquad (7)$$

where r is the separation of the stars, $\vec{V}$ is the orbital velocity of the pulsar, and $\vec{n}$ is a unit vector pointing from the observer to the emitter.

The term proportional to V/c is just the first order Doppler shift and is sufficient for determining the mass function of the system. The last two terms are the second order Doppler shift and the gravitational redshift which are on the order of 10^{-6}.

When the equations for elliptic motion (Aiken, 1964; Blandford and Teukolsky, 1975) are assumed, Equation 7 takes the form

$$\frac{P_{ob}}{P} = 1 + K[\cos(\omega + \theta) + \epsilon\cos\omega] + \beta\cos\theta + \gamma, \qquad (8)$$

where θ is the true anomaly and the constants K, β and γ are given by

$$K = \frac{2\pi a \sin i}{cp(1-\epsilon^2)^{1/2}}, \qquad (9)$$

$$\beta = \frac{GM_c^2(M_p + 2M_c)\epsilon}{c^2(M_p + M_c)^2 a(1-\epsilon^2)}, \qquad (10)$$

and

$$\gamma = \frac{\beta}{\epsilon} - \frac{GM_c^3}{2c^2(M_p + M_c)^2 a}. \qquad (11)$$

K comes from the first order effect and γ cannot be determined without knowing the true period of the pulsar. Thus the next observational goal will be to determine the constant β, yielding a fourth equation for the four unknowns and thus finally determining the masses of the system.

Unfortunately present estimates (Blandford and Teukolsky, 1975) are that it will take about five more years of observations to determine β.

EFFECTS OF GENERAL RELATIVITY

Gravitational Radiation

Once the masses are determined the effects of the gravitational radiation from the binary system may be looked for.

The losses of energy and angular momentum to gravitational radiation will induce a small change in the period of the binary given by (Peters, 1964; Wagoner, 1975)

$$\frac{1}{p}\frac{dp}{dt} = \frac{96}{5}\frac{G^3 M_p M_c (M_p + M_c)}{c^5 a^4} \tag{12}$$

where

$$F(\epsilon) = (1 - \epsilon^2)^{-7/2}\left(1 + \frac{73}{24}\epsilon^2 + \frac{37}{96}\epsilon^4\right). \tag{13}$$

For our system this reduces to

$$\frac{1}{p}\frac{dp}{dt} = -6.3 \times 10^{-11}\frac{X(1 + X)^3}{\sin^5 i} \tag{14}$$

where

$$X = M_p/M_c \tag{15}$$

or approximately one part in 10^{10} per year, corresponding to a net loss in orbital energy of about 10^{30} erg s^{-1}. It is estimated that this effect will be measurable in 5-10 years (Blandford and Teukolsky, 1975).

The measurement of $1/p\ dp/dt$ yields a fifth equation for the unknowns a, sin i, M_p and M_c and thus yields an important check on the consistency of our analysis. If the consistency is upheld, then this system will provide

verification of three widely different relativistic effects: (A) precession of the periastron, Equation (4); (B) gravitational red shift and second order Doppler shift, Equation (8); and (C) gravitational radiation, Equation (12).

If the system of equations is found to be inconsistent, then either some aspect of general relativity may be suspect or the assumption of the nature of the companion may be wrong (it may be a rapidly rotating white dwarf).

Precession of the Spin Axis of the Pulsar

One final general relativistic effect is the coupling of the spin with the orbital angular momentum. This coupling may give a precession of the spin axis of the pulsar on the order of 2 °/year (Esposito and Harrison, 1975). This may cause the plane of the pulsar beam to precess off of the earth, effectively *shutting off the observations of the pulsars* in a time scale of ten years – although it might reappear 200 years later.

BIBLIOGRAPHY

Aiken, R. G., 1964, The Binary Stars, Dover: New York, pp. 79, 158.

Blandford, R. and Teukolsky, S. A., 1975, Ap. J. (Letters) 198, L27.

Esposito, L. W. and Harrison, E. R., 1975, Ap. J. (Letters), 196, L1.

Hulse, R. A. and Taylor, F. H., 1975, Ap. J. (Letters) 195, L51.

Masters, A. R. and Roberts, D. H., 1975, Ap. J. (Letters), 195, L107.

Peters, P. C. 1964, Phys. Rev., 136, B1224

Wagoner, V., 1975, Ap. J. (Letters), 196, L63.

CHAPTER VIII
PULSAR THEORY

William K. Rose
Philip Hardee
University of Maryland
College Park, Maryland

It is generally accepted that pulsars are spinning, magnetized neutron stars with surface magnetic fields of approximately 10^{12} gauss. The mean pulse envelope of NP 0532 at various wavelengths is shown in Figure VIII-1. The simplest physical model consistent with this interpretation of the observed properties of pulsars assumes that a neutron star has a dipole magnetic field and is surrounded by a vacuum. However, as will be shown below, this model is not physically self-consistent since the vacuum solutions of Maxwell's equations indicate that there is an electric field sufficiently strong to pull charged particles from the surface of the neutron star and thereby produce a plasma.

The electromagnetic field on a charge inside the highly conducting neutron star must vanish. This requirement implies

$$\mathbf{E} + \frac{(\Omega \times \mathbf{r}) \times \mathbf{B}}{c} = 0, \tag{1}$$

where $\vec{\Omega}$ is the angular velocity. From Equation 1 it follows that the components of E are

$$\left.\begin{aligned} E_r &= -\frac{Br\Omega}{c}\sin^2\theta, \\ E_\theta &= -\frac{Br\Omega}{c}\cos\theta\sin\theta = \frac{Br\Omega}{3c}\frac{\partial P_2(\cos\theta)}{\partial\theta}, \\ E_\phi &= 0, \end{aligned}\right\} \tag{2}$$

where we have assumed that the magnetic and rotational axes are aligned.

Next we solve for a time-independent solution outside the neutron star and then match boundary conditions at the surface. If the field is time-independent, it follows from Maxwell's equations that

$$\nabla \times \mathbf{E} = 0. \tag{3}$$

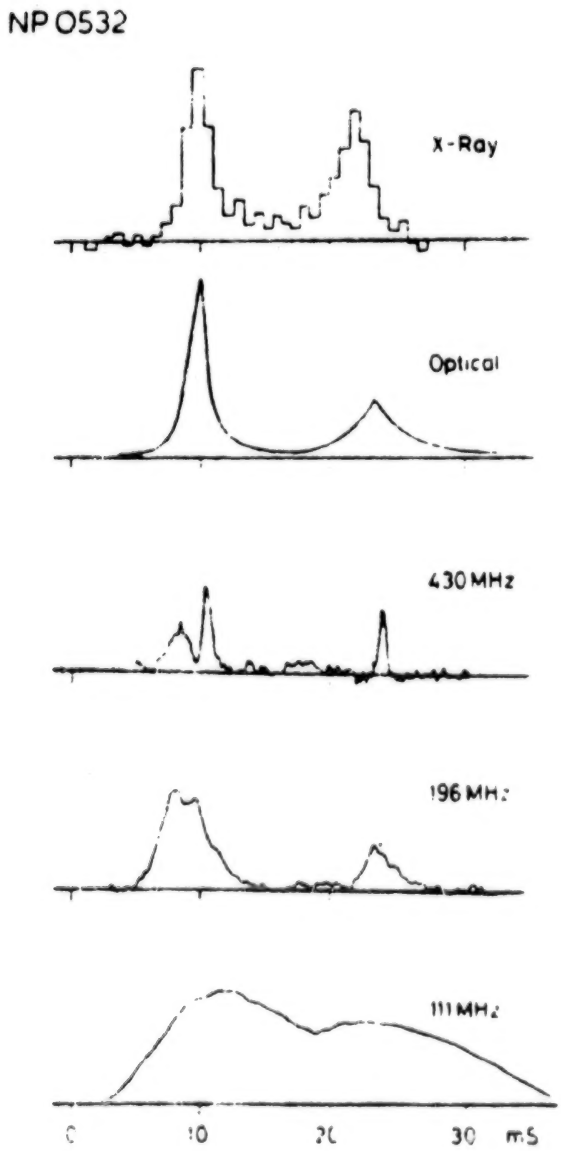

Figure VIII-1. Mean pulse envelope of the Crab pulsar at radio, optical, and x-ray wavelengths (Source: Hewish, 1970).

and therefore

$$\mathbf{E} = -\nabla\Phi. \tag{4}$$

The assumption that the neutron star is surrounded by a vacuum implies

$$\nabla \cdot \mathbf{E} = \nabla^2 \Phi = 0, \tag{5}$$

and therefore we have a standard problem in electrostatics. The boundary condition at infinity is that ϕ vanish as $r \to \infty$. This condition implies

$$\Phi = \sum_{\ell=0}^{\infty} C_\ell r^{-(\ell+1)} P_\ell(\cos\theta). \tag{6}$$

The corresponding boundary condition at the surface of the neutron star is that the tangential components of E be continuous. This condition is satisfied in a trivial manner for E_ϕ. The continuity condition for E_θ implies

$$\frac{B_s R\Omega}{3c} \frac{\partial P_2(\cos\theta)}{\partial\theta} = -\frac{1}{R}\frac{\partial\Phi}{\partial\theta} = \sum_{\ell=0}^{\infty} C_\ell R^{-(\ell+2)} \frac{\partial P_\ell(\cos\theta)}{\partial\theta} \tag{7}$$

where R is the radius of the neutron star. The coefficient $C_0 = 0$ since the neutron star is assumed to have no net charge. From Equation 7 it follows that

$$\left.\begin{aligned} C_2 &= -\frac{B_s R^5 \Omega}{3c} \\ C_\ell &= 0 \quad \ell = 0, 1, \ell > 2. \end{aligned}\right\} \tag{8}$$

It follows from equations (6) and (8) that the vacuum exterior electric field is

$$\left.\begin{aligned} E_r &= -\frac{\partial\Phi}{\partial r} = -\frac{R^5 B_s}{2cr^4}(3\cos^2\theta - 1), \\ E_\theta &= -\frac{1}{r}\frac{\partial\Phi}{\partial\theta} = -\frac{R^5 B_s}{cr^4}\cos\theta\sin\theta \end{aligned}\right\} \tag{9}$$

Since $\nabla \times \mathbf{B} = 0$ and $\nabla \cdot \mathbf{B} = 0$ outside the neutron star, we can proceed as above solving for the external magnetic field. It follows that

$$\left.\begin{aligned} B_r &= B_s \frac{R^3}{r^3} \cos\theta, \\ B_\theta &= \frac{1}{2} B_s \frac{R^3}{r^3} \sin\theta, \\ B_\phi &= 0. \end{aligned}\right\} \tag{10}$$

At the neutron star's surface, the gravitational force in the same direction is

$$\frac{ZeE \cdot B_s}{mg \cdot B_s} = \frac{\Omega R^3 B_s}{mc} \frac{Ze}{GM} \cos^2\theta \tag{11}$$

which, for $M = 1\ M_\odot$ and $B_s = 10^{12}$ gauss is $\sim 10^7$ for iron nuclei and $\sim 10^{12}$ for electrons. Therefore, charged particles are likely to be pulled from the surface of a neutron star, unless strongly bound to the surface by other forces.

The above discussion implies that it is plausible to assume that there is a plasma surrounding a neutron star and that charged particles generally experience no net force in this circumstellar plasma. If this assumption is made, then it follows from Equation 1 that

$$\mathbf{E} \cdot \mathbf{B} = 0 \tag{12}$$

in the region surrounding a neutron star as well as its interior. Equation 12 is equivalent to assuming that $E = 0$ in the corotating frame of reference. In order to satisfy Equation 1 the charges must redistribute themselves so that

$$\nabla \cdot \left(\frac{\mathbf{u}}{c} \times \mathbf{B}\right) = 4\pi e(n_- - n_+),$$

or

$$n_- - n_+ \simeq \frac{\Omega \cdot \mathbf{B}}{2\pi e c}, \tag{13}$$

where we have assumed that the positively charged particles have unit charge. Close to the light cylinder ($R_L = r \sin\theta = c/\Omega$) relativistic effects are important and it can be shown that the local charge density is

$$n_- - n_+ = \frac{\Omega \cdot B}{2\pi ec} \frac{1}{\left[1 - \frac{\Omega^2 r^2 \sin^2 \theta}{c^2}\right]} \tag{14}$$

The electric field produced by the above distribution of charge density is a quadrupole electric field since $\Omega \cdot B$ changes sign (see Figure VIII-2).

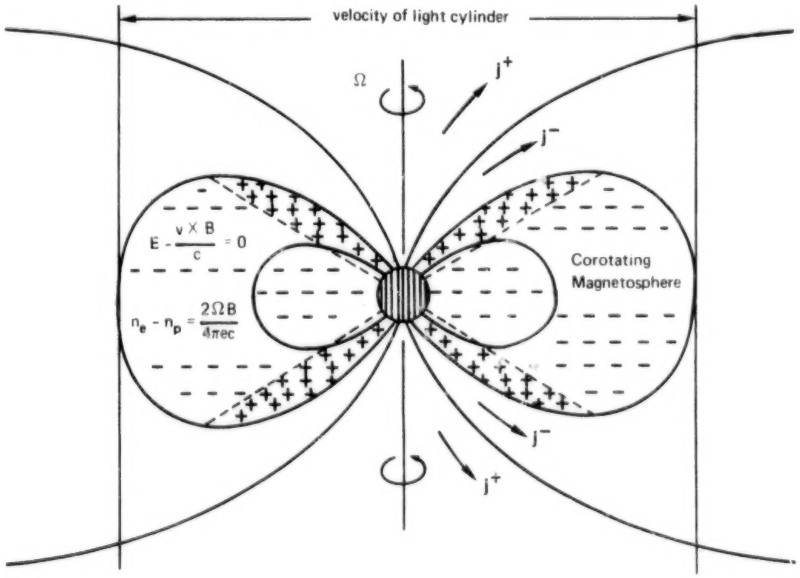

Figure VIII-2. A neutron star magnetosphere for the case where the magnetic and rotation axes are aligned

It is convenient to divide the magnetic field lines outside the neutron star into those that pass through the light cylinder and those that close within it. The co-rotating magnetosphere is defined to include those magnetic field lines that close within the light cylinder. To estimate the boundary of the magnetosphere we assume that the poloidal magnetic field is a dipole field. For this case the field lines are described by the equation

$$r = \text{const.} \times \sin^2 \theta, \tag{15}$$

and therefore the boundary of the magnetosphere includes magnetic field lines such that

$$\sin\theta_s = \left(\frac{\Omega R}{c}\right)^{1/2} \tag{16}$$

CONTENTS

	Page
Foreword	iii 1/A7
Chapter I - STELLAR EVOLUTION FROM MAIN SEQUENCE STAR TO WHITE DWARF, NEUTRON STAR OR BLACK HOLE by William K. Rose	1 1/A9
Introduction	1 1/A9
Main-Sequence Stars	3 1/A11
Red Giants	4 1/A12
Planetary Nebulae and the Final State of the Sun	9 1/B3
Production of Magnetic Fields in Stellar Interiors	10 1/B4
Stellar Collapse to Neutron Star on Black Hole	13 1/B7
Chapter II - PULSARS by D. C. Backer	15 1/B9
Introduction	15 1/B9
Spin Properties	17 1/B11
Average Waveform	21 1/C1
Radio Spectrum	24 1/C4
Fluctuation Waveform	29 1/C9
Interstellar Medium	40 1/D6
Conclusion	43 1/D9
Short Topical Bibliography	46 1/D12
Appendix II-A - Listing of Data on 147 Pulsars	49 1/E1
Chapter III - BINARY STARS AND COMPACT X-RAY SOURCES by William K. Rose	55 1/E7
Binary Stars	55 1/E7
Stellar Evolution in Close Binary Systems	59 1/E11
Novae	61 1/E13
Mass Accretion onto Neutron Stars	64 1/F2
Mass Accretion onto Black Holes	68 1/F6
Bibliography	74 1/F12

Page

Chapter IV - X-RAY SIGNATURES OF COMPACT OBJECTS
by Elihu Boldt 75 1/F13

Introduction 75 1/F13
X-Ray Scales for Compact Objects 76 1/F14
Electromagnetic Radiation Limits 77 1/G1
Accretion 81 1/G5
Radiative Transfer 82 1/G6
Some Observations 85 1/G9
Acknowledgments 96 2/A9

Chapter V - GAMMA RAYS FROM COMPACT OBJECTS
by Hakki Ögelman 99 2/A12

Introduction 99 2/A12
Observations 101 2/A14
Pulsar Environments and Gamma Ray Production 109 2/B8
Contribution of Pulsars to the Galactic Gamma Ray Emission 115 2/B14
Bibliography 122 2/C7

Chapter VI - TEMPORAL ANALYSIS OF X-RAY DATA
by Richard Rothschild 125 2/C10

What do the Data Look Like? 125 2/C10
What do we do with the Data? 127 2/C12
What do the Results Mean? 149 2/E6
Appendix VI-A 151 2/E8
Appendix VI-B 166 2/F9
Bibliography 170 2/F13

Chapter VII - RECOGNITION OF COMPACT ASTROPHYSICAL OBJECTS IN THE BINARY PULSAR PSR 1913 + 16
by Steven Detweiler 173 2/G2

The Parameters of PSR 1913 + 16 ..... 173 2/G2
The Nature of the Companion 175 2/G4
The Determination of the Masses of the Binary System 176 2/G5
Effects of General Relativity 179 2/G8
Bibliography 180 2/G9

Page

Chapter VIII - PULSAR THEORY
by William K. Rose and Philip Hardee 181 2/G10

Bibliography 194 3/A12

Magnetic fields with directions $\leq \theta_s$ at the surface of the neutron star are open field lines that extend out to infinity (i.e., to large distances from the neutron star).

Since the electric field on the surface of the neutron star is known (see Equation 2), we can calculate the potential difference between any two points on the surface. We find

$$V_B - V_A = \frac{B_s R\Omega}{2c} (\sin^2\theta_B - \sin^2\theta_A). \tag{17}$$

The potential difference between the magnetic pole and θ_s is

$$\Delta V = \frac{1}{2}\left(\frac{\Omega R}{c}\right)^2 RB_s. \tag{18}$$

Since the potential varies along the surface of the neutron star, the potential of a point on the surface cannot in general be the same as the potential at large distances, and consequently charges will move along magnetic lines of force as they do along wires. In order to maintain charge neutrality there must exist a critical angle θ_s between the magnetic pole θ_s at which the potential is the same as at large distances. It follows that the current flow out along open field lines has one sign in the polar regions ($\theta < \theta_s$) and the opposite sign in the surrounding sheath ($\theta_c < \theta < \theta_s$). The most energetic particles may attain energies as high as

$$E_{max} \simeq \frac{1}{2} e\Delta V \simeq 3 \times 10^{12} \frac{R_6^3 B_{12}}{P^2}, \tag{19}$$

where R_6 is the radius of the neutron star in units of 10^6 cm, B_{12} is the surface magnetic field in units of 10^{12} gauss and P is the period of the pulsar in seconds. We note that the limiting energy is not strongly dependent on the model details such as the relative orientation of **B** and Ω.

The total magnetic flux that passes beyond the light cylinder is

$$\Phi = \pi r_P^2 B_s \cdot e_r, \tag{20}$$

where B_s is the surface magnetic field and πr_P^2 is the area of the polar caps from which magnetic lines of force penetrate the light cylinder. It follows from Equations 13 and 20 that the maximum current from a polar cap is

$$|I_{max}| \simeq c\pi r_P^2 \frac{\Omega \cdot B_s}{2\pi c} \simeq \frac{\Phi\Omega}{2\pi} \tag{21}$$

As the above current flows from negatively charged to positively charged regions, it crosses magnetic field lines and consequently a torque is exerted on the rotating neutron star. This torque acts to lower the rotational energy at the rate

$$\frac{dE}{dt} \leqslant I_{max}\Delta V \simeq \left(\frac{\Phi\Omega}{2\pi}\right)\left(\frac{\Omega^2 R^3 B_s}{2c^2}\right). \tag{22}$$

Equations 15, 16 and 20 allow us to rewrite this expression as

$$\frac{dE}{dt} \leqslant \frac{B_s^2 \Omega^4 R^6}{c^3}. \tag{23}$$

We note that other modes of energy loss such as magnetic dipole radiation may be responsible for the loss of a pulsar's rotational energy.

In our above discussion we have assumed that the presence of electric forces greater than gravity will cause charged particles to be removed from the surface of a neutron star. However, the physical properties of matter are modified in a very significant manner when the magnetic field is as strong as 10^{12} gauss. In such magnetic fields matter will distribute itself in long molecular chains along the magnetic lines of force. The ions, which consist of nuclei (probably Fe^{56}) and some core electrons, form a one dimensional lattice along the magnetic field while the remaining electrons distribute themselves in an outer sheath. These molecular chains are very strongly bound to each other as a result of strong electric fields. For the case of Fe^{56} the binding energy per ion is $\simeq$14 keV in a magnetic field of $\simeq 2 \times 10^{12}$ gauss. The Fermi energy of the sheath electrons is $\simeq$750 eV and the lattice spacing $\simeq 10^{-9}$ cm. The electric field that is required to pull ions from such a chain is $\simeq$14 keV/ZeΔx where Z = 26 for iron and Δx is the spacing of the one dimensional lattice. It follows that the electric field necessary to unbind ions is $\simeq 10^{12}$ V cm^{-1}, which is generally less than the electric field that is predicted to exist on the surface of a neutron star,

$$E_{surface} \simeq \frac{\Omega R B_s}{c} \simeq \frac{10^{11}}{P} \text{ volts cm}^{-1}, \tag{24}$$

where P is the rotation period of the pulsar. We can conclude that unless the pulsar surface temperature is relatively high ($kT_{surface} \geqslant 2$ keV), ions should remain bound to the surface. On the other hand, electrons can be much more easily pulled from the surface of a neutron star. This circumstance implies that electrical discharges will occur on the surface of a pulsar. Such electrical discharges are likely to be the cause of the observed pulsed radiation from pulsars.

Let us consider a neutron star whose magnetic and spin axes are oriented so that the induced electric charge is positive over its polar caps. This distribution of charge is realized when the magnetic axis is antiparallel to the spin axis. In this case any positive charge flowing away from the polar regions will not be replaced, since the ions are strongly bound to the surface of the neutron star. For this reason, a potential gap will develop at the poles. From Poisson's equation, it follows that the potential differences across the gap is

$$\Delta V \simeq \frac{\Omega B}{c} h^2, \tag{25}$$

where h is the gap thickness. Equation 25 remains valid as long as the gap thickness is appreciably less than the radius of the polar cap. The maximum potential that can exist across this gap is given by Equation 18.

If a gap develops, its dimension will very rapidly increase with a speed close to that of light. However, since the potential difference across the gap varies as h^2 (see Equation 25), the gap will soon be discharged by the formation of electron-positron pairs. Let us examine more closely how this electron-positron discharge might be produced. Electrons accelerated in the gap above the polar caps will produce curvature radiation since they are constrained to move along magnetic lines of force. The characteristic energy of photons produced by such curvature radiation is

$$\hbar\omega \simeq \frac{3}{2}\gamma^3 \frac{\hbar c}{r_c}, \tag{26}$$

where r_c is the radius of curvature of the magnetic field. Close to the poles of a neutron star r_c should be 10^6 cm. When the gap potential is such that $e\Delta V \geqslant 10^{11}$ eV, the photons that are generated by means of curvature radiation will be sufficiently energetic that they will create new electron-positron pairs on nearby magnetic lines of force. If the discharge is sufficiently well developed, these secondary electron-positron pairs will produce new pairs and an electron-positron avalanche will be created. The discharge will eventually become self-limiting after a sufficient number of electrons are pulled back

onto the positively charged polar caps. The gap voltage that is sufficient to produce an electron-positron avalanche is $\simeq 10^{12}$ eV. Higher voltage drops may arise, since the gap thickness increases at nearly the speed of light.

A crucial physical parameter in determining the mean free path of a gamma ray in a magnetic field is

$$\chi = \frac{\hbar\omega}{2mc^2} \frac{B_\perp}{B_{crit}}, \tag{27}$$

where $B_{crit} = m^2c^3/e\hbar = 4.4 \times 10^{13}$ gauss and $B_\perp = B \sin\theta$ is the component of the magnetic field perpendicular to the motion of the gamma ray. Since the initial direction of the gamma rays is nearly parallel to the magnetic field (i.e., $B_\perp \leqslant B/\gamma$), the parameter χ will be $\ll 1$ and the mean free path of the gamma ray is (Erber 1966).

$$\lambda = \frac{4.4}{(e^2/\hbar c)} \frac{\hbar}{mc} \frac{B_{crit}}{B_\perp} \exp\left(\frac{4}{3\chi}\right). \tag{28}$$

It is plausible to assume that the mean free path λ is comparable to the gap thickness h at the time an electron-positron avalanche is produced. We note that since the gamma rays are emitted almost parallel to magnetic lines of force, they must travel a distance comparable to the radius of curvature r_c before $B_\perp$ becomes comparable to B.

Charged particles will achieve energies of $\gamma \sim 10^6$ inside the gap. Once beyond the gap they will experience no acceleration (i.e., $E \cdot B = 0$). Then, however, curvature radiation will produce gamma rays and electron-positron pairs with energies $\gamma \simeq 10^2 - 10^3$ (i.e., $\simeq$50 - 500 MeV). It is possible that the observed pulsed gamma ray emission at energies $\geqslant$35 MeV is caused by this process. We note that radiative energy losses from curvature radiation will prevent electrons or positrons from attaining energies much greater than $\gamma \sim 10^6$.

Our discussion above has led us to conclude that relativistic beams of electrons and positrons should stream out from the polar regions of pulsars. It is plausible that the observed emission from pulsars should be produced by such beams of particles. Moreover, since collective effects are important in understanding laboratory plasmas, it is quite reasonable to suppose that they also play a fundamental role in determining the observed properties of pulsars.

At radio wavelengths, pulsars are observed to have very high radio brightness temperatures (i.e., $T_b \simeq 10^{25} - 10^{30}$ K). A coherent radiation process is

required to attain such high brightness temperatures. The bunching of charged particles (electrons and positrons) is a plausible mechanism for producing coherent radio emission. It has been suggested that the two-stream instability is responsible for the bunching of charged particles. The two-stream instability is excited by a charged beam of particles passing through a stationary plasma. In our case the plasma is an electron-positron plasma. In order for the two stream instability to cause bunching, the growth rate of the instability must be greater than the damping caused by coherent curvature radiation.

The relativistic dispersion relation for the two-stream instability can be expressed as (Montgomery and Tidman, 1964)

$$\frac{\omega_p^2}{\gamma_p^3 (\omega - kU_p)^2} + \frac{\omega_b^2}{\gamma_b^3 (\omega - kU_b)^2} = 1, \tag{29}$$

where

$$\omega_p^2 = \frac{4\pi n_p e^2}{m} \text{ and } \omega_b^2 = \frac{4\pi n_b e^2}{m}$$

are the plasma frequencies of the electron-positron plasma and the ultra-relativistic beam respectively. It can be shown that the maximum linear growth rate for the two-stream instability is

$$\Gamma_\ell = |\,\mathrm{Im}(\omega)| = \frac{3^{1/2}}{2^{4/3}} \left(\frac{n_b}{n_p}\right)^{1/3} \frac{\gamma_p}{\gamma_b}\, \omega_p. \tag{30}$$

Equation 30 implies that the rate of energy gain per cm^3 caused by the two-stream instability is

$$\left(\frac{dE}{dt}\right)_{gain} = 2\Gamma_\ell \frac{\delta E^2}{8\pi}, \tag{31}$$

where $\delta E^2/8\pi$ is the electrostatic energy density in the bunches.

In order to compute the corresponding energy loss caused by coherent curvature radiation we must determine the wave number and phase velocity of the fastest growing wave. The wave number and phase velocity that correspond to the wave with the maximum growth rate given in Equation 30 are

$$k = 2\pi/\lambda = \frac{\omega_p}{\Delta u \gamma_p^{3/2}} \tag{32}$$

and

$$u_\phi = u_b\left(1 - 2^{-4/3}\left(\frac{n_b}{n_p}\right)^{1/3}\frac{\gamma_b}{\gamma_p}\frac{\Delta u}{u_b}\right) \tag{33}$$

respectively. The quantity Δu is defined as

$$\Delta u = u_b - u_p. \tag{34}$$

The longitudinal waves excited by the two-stream instability will cause bunching of charged particles. Since all of the above expressions have been evaluated in the observer's frame of reference, the bunches have a characteristic dimension $\simeq \lambda/2$ and move with the velocity u_ϕ in this frame of reference. It follows that the rate of energy loss per cm^3 due to coherent curvature radiation from a bunch of electrons (or positrons) is

$$\left(\frac{dE}{dt}\right)_{loss} = -\frac{2}{3}\frac{ce\delta n\left(\frac{\lambda}{2}\right)^3\gamma_\phi^4}{\Omega_c^2}, \tag{35}$$

where

$$\gamma_\phi = \frac{1}{\sqrt{1 - \frac{u_\phi^2}{c^2}}},$$

r_c is the radius of curvature, and δn is the number of electrons (or positrons) per cm^3 in a bunch.

From Poisson's equation we find

$$k\delta E = 4\pi e\delta n. \tag{36}$$

It follows from Equations 35 and 36 that the rate of energy loss from curvature radiation is

$$\left(\frac{dE}{dt}\right)_{loss} = \pi\frac{\lambda c}{r_c^2}\gamma_\phi^4\frac{\delta E^2}{8\pi}. \tag{37}$$

Since both the rate of energy loss and energy gain are proportional to the electrostatic energy density, we can define a damping rate by the expression

$$\Gamma_{\text{damping}} = \frac{\pi}{2}\frac{\lambda c}{r_c^2}\gamma_\phi^4 . \tag{38}$$

The condition that the two stream instability develop becomes

$$\Gamma_\ell > \Gamma_{\text{damping}} . \tag{39}$$

This condition for bunching makes it implausible for a beam of positrons (or electrons) as energetic as $\gamma \sim 10^6$ to excite charge bunches. However, it does not rule out the possibility that electrons (and/or positrons) with $\gamma \sim 10^3$ can excite bunches as they penetrate a lower energy electron-positron plasma. One additional condition necessary for the two-stream instability to be excited is the requirement that the electron and/or positron beams be separated in energy. If the energy distribution of particles in the beam is monotonically decreasing, then no two-stream instability will develop.

The two-stream instability is only one of a number of plasma instabilities that may be excited by charged relativistic particles moving through a plasma. The transverse electromagnetic instability (ordinary mode instability) is an example of a plasma instability that may have important application to pulsar theory. Recent studies of relativistic electron beams have shown that the ordinary mode instability can cause the filamentation of electron beams moving through a plasma. The filamentation of the electron beam is caused by a perturbed magnetic field that is perpendicular to the streaming motion of the beam.

It can be shown (e.g., Hardee and Rose, 1974) that the condition for the excitation of those transverse electromagnetic waves is

$$\frac{\omega_b^2}{\gamma_b} > \frac{\Omega^2}{\gamma_b^2} \left(\Omega = \frac{eB}{mc}\right) \tag{40}$$

for the case of an electron (or positron) beam moving along a magnetic field embedded in an electron-positron plasma. The ordinary mode instability produces a purely growing mode whose maximum growth can be shown to be

$$\omega_{I_{\max}}^2 \lesssim \frac{\omega_p^2}{\gamma_b} . \tag{41}$$

The maximum growth rate is achieved for beam and background plasma of equal density. If we compare the growth rate for the ordinary mode instability with that for the two-stream instability given in Equation 30, we see that

the ordinary mode instability, if the necessary condition for its excitation (Equation 40) is realized, can develop more rapidly for a relativistic beam than can the two-stream instability.

Close to the surface of a neutron star the magnetic field strength is very strong and consequently the plasma should be stable against the excitation of the ordinary mode instability. However, since the magnetic field outside the surface of a neutron star should scale as $B = B_s (R/r)^3$ and the particle density as $n = n_s (R/r)^3$, particle densities sufficiently high to drive the ordinary mode instability may arise inside the light cylinder (i.e., $R_L \simeq 1.5 \times 10^8$ cm for the crab pulsar). The excitation of the ordinary mode instability implies that a particle moving along a magnetic field will see a transverse magnetic field excited by the instability. The presence of a magnetic field transverse to the direction of motion of the particle (electron or positron) will cause it to radiate by means of the synchrotron process. It is plausible that the x-ray and optical pulses observed from the crab pulsar are produced in this manner.

If the initial particle distribution is of a two-stream type, then in the regime where

$$\omega_b^2/\gamma_b << \Omega^2/\gamma_b^2 \tag{42}$$

there exists an electrostatic two-stream instability and an associated low-frequency transverse wave. The phase propagation of the transverse wave occurs at any angle (other than zero) with respect to the ambient magnetic field. The group velocity, however, is along the ambient magnetic field. It has been suggested (Hardee and Rose, 1976) that the observed radio pulses from pulsars may be caused by the focusing of these transverse waves along the open field lines extending from the polar cap to the light cylinder.

BIBLIOGRAPHY

Bludman, S. A., Watson, K. M. and Rosenbluth, M. N., 1960, Phys. Fluids, 3, 747 747.

Chen, H. -H., Ruderman, M. A. and Sutherland, P. G., 1974, Ap. J., 191, 473.

Erber, T., 1966, Rev. Mod. Phys., 38, 626.

Goldreich, P. and Julian, W. H., 1969, Ap. J., 157, 869.

Hardee, P. and Rose, W. K., 1974, Ap. J. (Letters), 194, L35.

Hardee, P., and Rose, W. K., 1976, Ap. J., 210, 533.

Hewish, A., 1970, Ann. Rev. Ay. and Ap. 8, 265.

Hewish, A., 1975, Rev. Mod. Phys. 47, 571.

Hinata, S., 1975, preprint.

Michel, F. C., 1974, Ap. J., 192, 713.

Montgomery, D. C., and Tidman, D. A., 1964, Plasma Kinetic Theory (New York: McGraw Hill).

Ruderman, M. A., 1972, Ann. Rev. Astr. and Ap., 10, 427.

Ruderman, M. A., and Sutherland, P. G., 1975, Ap. J., 196, 51.

Sturrock, P. A., 1971, Ap. J., 164, 529.

*U.S. GOVERNMENT PRINTING OFFICE: 1977 - 735-004/21

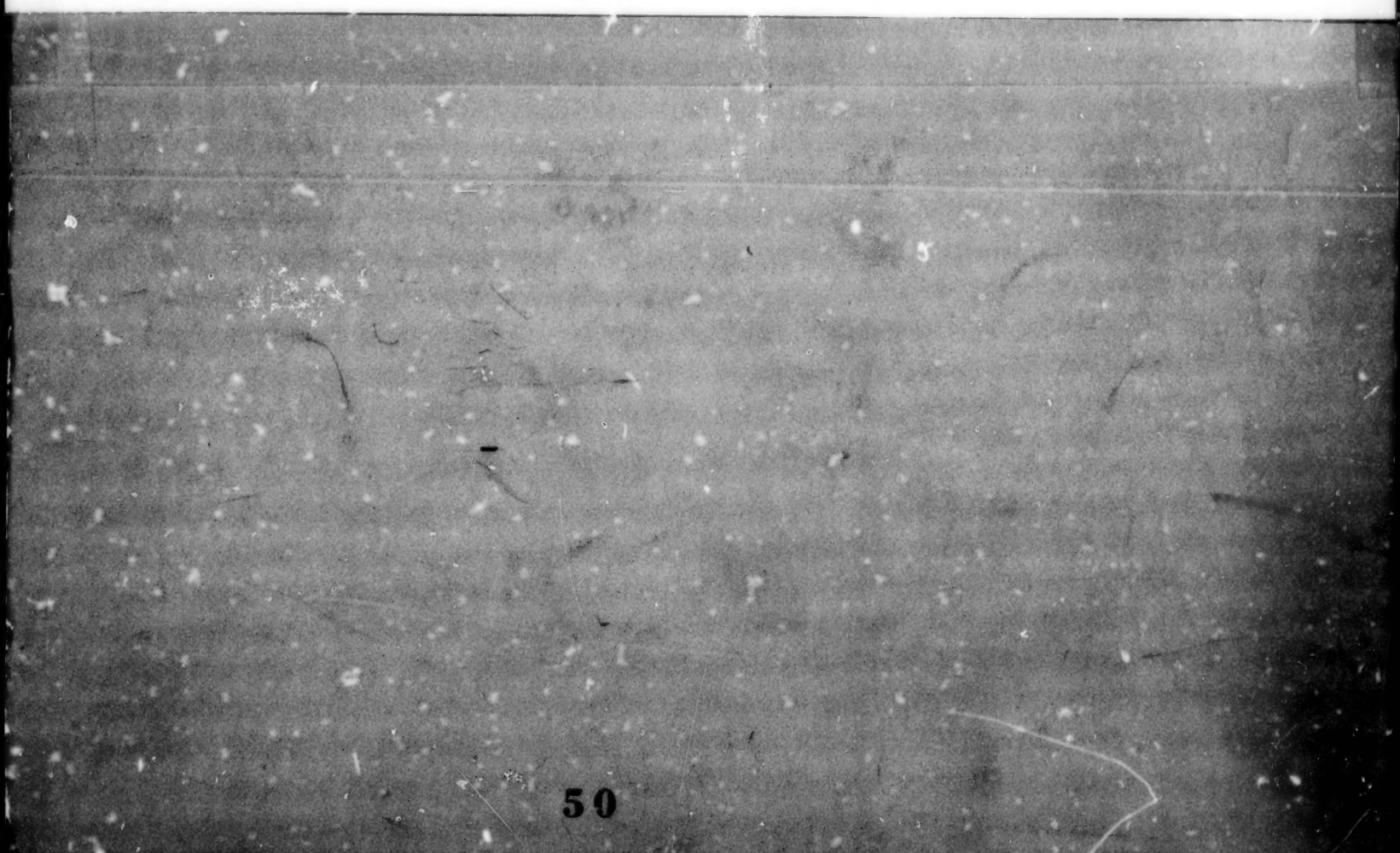

END

3.24.78